Technische Universität München
Lehrstuhl E23 für Technische Physik
Walther-Meißner-Institut für Tieftemperaturforschung
der Bayerischen Akademie der Wissenschaften

Control and Manipulation of Magnonic Spin Currents in Magnetic Insulators

Tobias Wimmer

Vollständiger Abdruck der von der Fakultät für Physik der Technischen Universität München zur Erlangung des akademischen Grades eines

Doktors der Naturwissenschaften

genehmigten Dissertation.

Vorsitzender:	Prof. Dr. Johannes Knolle
Prüfer der Dissertation:	1. Prof. Dr. Rudolf Gross
	2. Prof. Dr. Christian Back

Die Dissertation wurde am 14.07.2021 bei der Technischen Universität München eingereicht und durch die Fakultät für Physik am 22.10.2021 angenommen.

Tobias Wimmer
Control and Manipulation of Magnonic Spin Currents in Magnetic Insulators
Dissertation, November 20, 2021
Reviewers: Prof. Dr. Rudolf Gross and Prof. Dr. Christian Back

Technische Universität München
Lehrstuhl E23 für Technische Physik
Walther-Meißner-Institut für Tieftemperaturforschung
der Bayerischen Akademie der Wissenschaften
Walther-Meißner-Straße 8
85748 and Garching

A puppet is free as long as he loves his strings.
— Sam Harris

To my beloved mother and father

Abstract

Electric currents are usually referred to as the directed flow of electric charge, carried e.g. by electrons or ions. Spin currents, on the other hand, represent the directed flow of spin angular momentum, typically carried by the electron spin or the angular momentum of *magnons*, the quantized excitations of a spin lattice. A fundamental difference between these types of currents lies within the basic characteristics of charge and spin. While the former is described by a scalar quantity, the latter is usually treated as a 3-dimensional vector with a corresponding magnetic dipole field. The complexity of spin currents is thus significantly increased, making their investigation challenging, but also versatile and rich.

The dedicated goal of this thesis is to establish efficient ways to control and manipulate pure spin currents in magnetic insulators. Since electrically insulating materials do not allow for the flow of electrical charge, these spin currents cannot be associated by the flow of spin-carrying charge carriers. Nevertheless, pure spin currents - i.e. spin currents not associated with any flow of charge - can be present in magnetically ordered insulators and are carried by the quantized excitations of the spin lattice, which we refer to as *spin waves* or *magnons*. The basic setting for our experiments is the electrical and thermal injection/detection of magnon-based spin currents by applying/measuring electric fields and temperature gradients in bilayer samples consisting of heavy metals and magnetic insulators. In these structures, magnon transport can be investigated for a vast range of geometric and external conditions. The control of this magnon transport was achieved by various approaches. First, we utilized a ferromagnetic metal to inject spin currents into magnetic insulators, which allows for an improved control as compared to the sample configuration based on non-magnetic heavy metals. The corresponding magnon transport measurements enabled the determination of the charge-to-spin conversion efficiency in the ferromagnetic metal. Secondly, we have employed strong magnon-based spin current injection into a magnetic insulator as to non-linearly increase the magnon conductivity of a magnon transistor device, similar to the well-known electronic transistor functionality. As a key result, our experiments revealed a full compensation of the intrinsic magnetic damping of the magnetic insulator and even indicated the formation of a magnon Bose-Einstein condensate. Subsequently, we could demonstrate a coherent control

of antiferromagnetic magnon excitations by an external magnetic field, allowing for the controlled interconversion between right-/left-circularly as well as linearly polarized magnon excitations. Last but not least, we were able to experimentally verify a theoretical prediction stating that the charge-to-spin conversion efficiency for temperature gradient-driven charge currents vanishes in the heavy metal Pt at low temperatures.

Kurzfassung

Unter elektrischen Strömen versteht man üblicherweise den gerichteten Fluss von elektrischer Ladung, welche beispielsweise von Elektronen oder Ionen getragen wird. Spinströme hingegen stellen den gerichteten Fluss von Spin-Drehimpulsen dar, getragen z. B. vom Elektronenspin oder dem Drehimpuls von *Magnonen*, den quantisierten Anregungen eines Spin-Gitters. Ein grundlegender Unterschied zwischen diesen Arten von Strömen liegt in den grundlegenden Eigenschaften von Ladung und Spin. Während Erstere durch eine skalare Größe beschrieben wird, wird Letztere meist als 3-dimensionaler Vektor mit einem entsprechenden magnetischen Dipolfeld behandelt. Die Komplexität von Spinströmen wird dadurch deutlich erhöht, was ihre Untersuchung anspruchsvoll, aber auch vielseitig und reichhaltig macht.

Das erklärte Ziel dieser Arbeit ist es, effiziente Wege zur Kontrolle und Manipulation reiner Spinströme in magnetischen Isolatoren zu etablieren. Da der Fluss elektrischer Ladung in isolierenden Materialien blockiert ist, können diese Spinströme nicht mit dem Fluss von spin-behafteten Ladungsträgern assoziiert werden. Dennoch können reine Spinströme - d.h. Spinströme, die nicht mit einem Ladungsfluss verbunden sind - in magnetisch geordneten Isolatoren existieren und werden von den quantisierten Anregungen des Spin-Gitters getragen, die wir als *Spinwellen* oder *Magnonen* bezeichnen. Das zugrundeliegende System für unsere Experimente ist die elektrische und thermische Injektion/Detektion von magnon-basierten Spinströmen durch Anlegen/Messen von elektrischen Feldern und Temperaturgradienten in Doppelschichtproben, bestehend aus Schwermetallen und magnetischen Isolatoren. In diesen Strukturen kann der Magnonentransport sowohl für verschiedenste strukturelle Geometrien als auch äußeren Bedingungen untersucht werden. Die Kontrolle dieses Magnonentransports wurde durch verschiedene Ansätze erreicht. Zunächst verwendeten wir ein ferromagnetisches Metall um Spinströme in magnetische Isolatoren zu injizieren, welches eine verbesserte Kontrolle im Vergleich zur Probenkonfiguration auf Basis von nicht-magnetischen Schwermetallen ermöglicht. Die entsprechenden Magnonentransportmessungen ermöglichten die Bestimmung der Ladung-zu-Spin-Konversionseffizienz in dem ferromagnetischen Metall. Darüber hinaus haben wir eine starke magnon-basierte Spinstrominjektion in einen magnetischen Isolator eingesetzt, um die Magnon-Leitfähigkeit eines Magnon-Transistor Bauelements

nichtlinear zu erhöhen, ähnlich wie bei der bekannten elektronischen Transistor-Funktionalität. Als Schlüsselergebnis zeigten unsere Experimente eine vollständige Kompensation der intrinsischen magnetischen Dämpfung des magnetischen Isolators und deuteten sogar auf die Bildung eines Magnon Bose-Einstein Kondensats hin. Des Weiteren ist es uns gelungen, eine kohärente Steuerung von antiferromagnetischen Magnon-Anregungen durch ein externes Magnetfeld zu demonstrieren, die eine kontrollierte Interkonversion zwischen rechts/links-zirkular und linear polarisierten Magnonen ermöglicht. Zu guter Letzt konnten wir eine theoretische Vorhersage experimentell verifizieren, die besagt, dass die Ladungs-zu-Spin-Umwandlungseffizienz für temperaturgradienten-getriebene Ladungsströme in dem Schwermetall Pt bei tiefen Temperaturen verschwindet.

Contents

Introduction

1

> 'That which can be asserted without evidence,
> can be dismissed without evidence.' [1]

This quote from the famous british-american journalist and writer Christopher Hitchens is also known as 'Hitchens Razor', an epistemological razor stating that 'the burden of proof regarding the truthfulness of a claim lies with the one who makes the claim' [2]. It does quite concisely state one of the, if not the most important principle of the modern scientific method. Of course, this principle does also apply for the opposite extreme, which was formulated quite neatly by the US-american astronomer Carl Sagan in 1980: 'Extraordinary claims demand exraordinary evidence' [3]. Hence, any claim about the true nature of reality needs to be put to the test. If the claim under test is, however, not proven to be bullet-proof against all its reasonable objections, it shall be dismissed. It is exactly this rather rigorous and inevitable concept that ensures the great success of science as well as its quick progress. In this regard, a further extremely important characteristic of the scientific method is its yet unmatched adaptability, enabling the aforementioned progress in the first place. Depending on the most convincing evidence, science adapts itself immediately, a feature which is unfortunately far less pronounced in non-scientific areas. The latter is portrayed rather plainly in non-adaptive ideological worldviews, the consequences of which have impeded scientific progress throughout history.

The sciencific progress in solid state physics has caused major technological advances, the most important of which are undeniably the logic devices based on complementary metal-oxide semiconductors (CMOS). These semiconductor devices are the building blocks for computer technology and become ever faster and denser in accordance with the famous Moore's law [4]. The natural saturation of this empirical law is suspected for years [5], wherefore appropriate alternatives for data storage and processing become ever more pressing. One very promising step into this direction is represented by spintronics research. This research field aims at making use of the spin degree of freedom (cf. Ch. 2) and the intrinsic properties of magnetic materials. The gigahertz magnetization dynamics of the latter constitutes one key feature for ultra-fast switching devices. Moreover, pure spin currents as compared to electronic currents might be beneficial in terms of energy dissipation and therefore potentially enable easier down-scaling. In this context, the concept of pure spin currents without actually moving electrons becomes of particular interest. An experimental realization of this is made possible in a material class called magnetic insulators, which enable the propagation of

wave-type excitations within the magnetic order - a concept commonly known as *spin waves*. The quantized spin waves - also referred to as *magnons* in the associated quantum mechanical description - are the main focus of the subfield called *magnonics* [6]. A large part of the field of magnonics deals with the excitation, detection and control of spin waves. Developing efficient ways for the control of spin currents is a key goal of this thesis. More specifically, we focus on the incoherent transport of a broad spectral range of magnons, allowing for a diffusive treatment of the magnon transport somewhat similar to the well-known electronic case. This type of spin transport experiment is conducted with bilayer structures consisting of heavy metals (HMs) attached to magnetic insulators (MIs) by using at least two seperate HM electrodes deposited on different kinds of MIs. Here, one electrode acts as a charge-to-spin converter transforming an electrical current applied to the HM electrode into a spin current, employing it as a spin current injector for the MI. The second electrode is used as a detector upon exploitation of the inverse spin-to-charge conversion process. Due to the insulating nature of the MI, the injected/detected spin current in the HMs is carried by magnons. The manipulation and control of the diffusive magnon transport in the MI is the main goal of the present work. For this purpose, we have used two substantially different MIs. First, the evergreen of magnetism research: the ferrimagnetic insulator yttrium iron garnet ($Y_3Fe_5O_{12}$, YIG), still offering the lowest magnetic damping of spin waves to this day [7] and thus enabling transport of spin waves over long distances [8, 9]. Second, we employ the antiferromagnetic insulator (AFI) called hematite (α-Fe_2O_3). AFIs are particularly interesting due to their rather different magnetization/spin wave dynamics as compared to their ferro-/ferrimagnetic counterparts.

Recalling the principles that allow for scientific progress stated above, we are confident to have addressed all of the above mentioned requirements for a serious and meaningful scientific work. Notable scientific contributions of this thesis include: (i) a study on the influence of a ferromagnetic spin injector/detector on the magnon transport in YIG, which could be utilized for the determination of the spin-to-charge conversion efficiency in the ferromagnetic metal electrode, (ii) a non-linear spin current induced modulation of the magnon conductivity in YIG that we related to magnetic damping compensation and possibly the formation of a magnon Bose-Einstein condensate, (iii) the first experimental observation of the antiferromagnetic magnon Hanle effect described via a special theoretical framework considering the antiferromagnetic pseudospin dynamics [10], and (iv) the observation of the transverse spin Nernst magnetothermopower in an AFI/HM heterostructure enabling the observation of a vanishing spin Nernst angle in Pt at low temperatures. The most remarkable results have undoubtedly been aquired in (ii) and (iii). Here, we took advantage of electronics-inspired control mechanisms

and showed that they can be successfully implemented in a magnon-based setting.

The organization of this thesis is described in the following.

The basic theoretical foundations relevant for this work are given in Ch. 2. After discussing the basic features of the electron spin, we cover the foundations of spin waves in magnetically ordered materials as well as the general features of spin transport in metals. Furthermore, spin current generation in non-magnetic and magnetic metals is discussed. The most important part deals with spin transfer across heavy metal (HM)/magnetic insulator (MI) interfaces, which is of crucial importance for the magnon excitation and detection via metallic electrodes attached to magnetic systems. Based on this interfacial spin transport, we discuss the spin Hall magnetoresistance (SMR) and finally the magnon excitation, detection and transport in two-terminal HM/MI heterostructures.

Chapter 3 introduces the experimental details for this work. This includes the discussion of the relevant features of the ferrimagnetic insulator yttrium iron garnet (YIG) and the antiferromagnetic insulator hematite (α-Fe_2O_3). Moreover, we explain the sample fabrication and measurement techniques.

In Ch. 4, we investigate the spin current injection in YIG via the feromagnetic metal alloy $Co_{25}Fe_{75}$ (CoFe). Here, we demonstrate an efficient spin current injection via the anomalous spin Hall effect, but a vanishing contribution from the conventional spin Hall effect. By utilizing a multiterminal spin injection/detection device consisting of three heavy metal Pt electrodes and one ferromagnetic CoFe electrode on YIG, we could extract the anomalous spin Hall angle of CoFe via pure magnon transport measurements, which typically requires more complicated experiments. The results presented here have been published in T. Wimmer, B. Coester, S. Geprägs, R. Gross, S.T.B. Goennenwein, H. Huebl, M. Althammer, *Anomalous spin Hall angle of a metallic ferromagnet determined by a multiterminal spin injection/detection device*, Applied Physics Letters **115**, 092404 (2019).

The modulation of magnon conductivity via DC spin current injection in ultrathin YIG is explored in Ch. 5. We examine the low and large current bias regime, where the latter reveals spin current induced non-linear magnetization dynamics measured by a drastic increase in magnon conductivity. The characteristic change of magnon conductivity is related to the magnetic damping compensation in YIG. Moreover, we extensively discuss the possibility of a DC spin current induced formation of a magon Bose-Einstein condensate and the associated supposed zero resistance spin superfluid magnon transport. We perform micromagnetic simulations to access the spectral distribution of the excited magnetization dynamics and thus shed light on the microscopic pocesses in the YIG. A large part of the corre-

sponding results has been published in T. Wimmer, M. Althammer, L. Liensberger, N. Vlietstra, S. Geprägs, M. Weiler, R. Gross, H. Huebl, *Spin Transport in a Magnetic Insulator with Zero Effective Damping*, Physical Review Letters **123**, 257201 (2019).

The characteristics of the antiferromagnetic magnon transport in ultra-thin hematite films are addressed in Ch. 6. Here, we report on the first observation of the antiferromagnetic magnon Hanle effect, which we rationalize by an antiferromagnetic magnon pseudospin description employed for the respective magnon excitations and their dynamics. The magnon Hanle effect allows for coherent interconversion of right-/left-circularly and linearly polarized magnon excitations via the application of an external magnetic field. The experimental results of this work have been published in T. Wimmer, A. Kamra, J. Gückelhorn, M. Opel, S. Geprägs, R. Gross, H. Huebl, M. Althammer, *Observation of Antiferromagnetic Magnon Pseudospin Dynamics and the Hanle Effect*, Physical Review Letters **125**, 247204 (2020), whereas the details of the theoretical framework of the antiferromagnetic pseudospin can be accessed in A. Kamra, T. Wimmer, H. Huebl, M. Althammer, *Antiferromagnetic magnon pseudospin: Dynamics and diffusive transport*, Physical Review B **102**, 174445 (2020).

In the second part of Ch. 6, we investigate the thermally induced magnon transport in hematite. In contrast to the electrically induced magnon transport, it does not show any pseudospin dynamics. More importantly, however, we also observe a temperature gradient induced magnetothermopower effect, which we identify as the tranverse spin Nernst magnetothermopower (TSNM). Our results reveal that the TSNM is sensitive to the antiferromagnetic Néel order rather than the field induced net magnetization. More importantly, we observe a vanishing TSNM signal at low temperatures which we explain by a theoretical calculation of the spin Nernst conductivity in Pt. This study gives compelling evidence for the suppression of the spin Nernst angle in Pt at low temperatures.

An outlook to recent and future experiments regarding the control and manipulation of magnon transport is given in Ch. 7. We here touch on the topics of how the thermal magnon transport signals might indicate the formation of a magnon BEC. We further address recent experiments on the microwave induced modulation of magnon conductivity in YIG. Last but not least, we present ideas for an electric field control of antiferromagnetic magnon pseudospin dynamics.

To conclude this thesis, we review our main results in Ch. 8.

Theoretical Background

2

The fundamental property of *spin* is inherent to a large number of particles observed in nature. In the most general sense, spin refers to the property of an object that breaks its rotational symmetry, i.e. looks or behaves differently when observed from a different angle. The physical consequences of spin are therefore associated with an intrinsic angular momentum that breaks this symmetry. Regarding the spin of the negatively charged electron, it was first observed by Stern and Gerlach [14, 15] that this angular momentum manifests itself as a tiny magnetic moment. Early interpretations therefore assumed the electron to be spinning, thus explaining the observed magnetic moment as a consequence of a supposedly rotating electric charge density. Different to this classical expectation of a spinning charge, however, the emergence of a magnetic moment due to spin is independent of whether the associated particle is electrically charged or neutral (as e.g. confirmed by the finite spin of neutrinos), rendering this picture to be inaccurate. Moreover, its direction is quantized and can therefore, in general, not be treated as a 3-dimensional axial vector. These properties emphasize the fundamental relativistic quantum mechanical nature of spin. Besides yet hypothetical particles predicted from particle physics beyond the standard model (supersymmetric particles) and the yet unobserved graviton, each of the verified elementary spin-carrying particles exhibit a spin magnetic moment of either $\frac{1}{2}\hbar$ or $1\hbar$ (with $\hbar$ being the reduced Planck constant). Particles with half-integer spin belong to a class called fermions, whereas integer-spin particles are referred to as bosons. A fundamental difference between these types of particles is their underlying quantum statistics, obeying either the Fermi-Dirac-statistics [16, 17] (fermions) or the Bose-Einstein-statistics [18, 19] (bosons).

The by far most intensively studied half-integer spin-carrying particle is that of the negatively charged electron. Electrons carry a spin $\hat{\boldsymbol{s}}$ with a value $\hat{\boldsymbol{s}} = \frac{\hbar}{2}\hat{\boldsymbol{\sigma}}$ [20], where $\hbar$ is the reduced Planck constant and $\hat{\boldsymbol{\sigma}}$ corresponds to the vector of Pauli spin matrices [21]. Although the quantum mechanical property of spin $\hat{\boldsymbol{s}}$ cannot be rationalized within classical physics, its value is intrinsically related to the property of a conventional angular momentum $\boldsymbol{l}(\hat{\boldsymbol{s}})$ via the spin magnetic moment $\boldsymbol{\mu}^{\mathrm{s}} = \gamma \boldsymbol{l}(\hat{\boldsymbol{s}})$ (see Fig. 2.1 for a classical impression of the electron spin). Here, $\gamma = q/(2m)$ is the gyromagnetic ratio with q the charge and m the mass of the respective spin-carrying particle. For electrons, $\gamma = -g\mu_{\mathrm{B}}/\hbar$ with g the Landé factor ($g \approx 2$ for electrons) and $\mu_{\mathrm{B}} = e\hbar/(2m_{\mathrm{e}})$ the Bohr magneton. The latter introduces the electron charge $q = -e < 0$ and the electron mass m_{e}. Note that due to the negative charge of the electron, its spin $\hat{\boldsymbol{s}}$ is aligned antiparallely to its magnetic moment $\boldsymbol{\mu}^{\mathrm{s}}$. Since electrons and their charge property play a fundamental role in

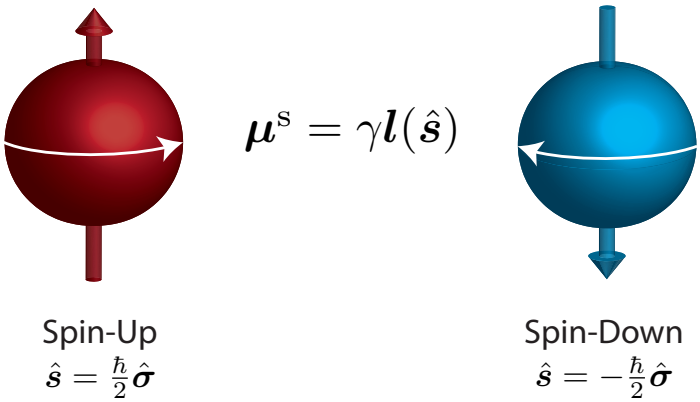

Fig. 2.1 – Classical impression of the electron spin indicated via a rotation about the particle's symmetry axis. In many cases, the physics of spin phenomena can be well described by the classical analouge of angular momentum $\boldsymbol{l}(\hat{\boldsymbol{s}})$ with an associated spin magnetic moment $\boldsymbol{\mu}^{\mathrm{S}} = \gamma \boldsymbol{l}(\hat{\boldsymbol{s}})$.

the physics of modern information technology, current research activity in the field of spintronics focusses on efficient ways to utilize the spin property of electrons.

This Chapter is dedicated to cover the theoretical principles required to understand the physics of spin transport as well as the generation and detection of pure spin currents. Furthermore, the associated spin transport effects in metallic and magnetic materials relevant for this thesis are explained. We start with an introduction to the fundamental concepts of half-integer spin systems in Ch. 2.1 and explicitly work out its correspondence to a conventional 3-dimensional angular momentum vector. On the basis of the temporal dynamics of spin and magnetization, we sketch the derivation of the spin wave dispersion relation in magnetically ordered systems in Ch. 2.2. This is followed by an introduction to spin transport concepts based on mobile electrons in metals in Ch. 2.3. We further elucidate selected aspects of spin current generation/detection in magnetic and non-magnetic metallic systems in Ch. 2.4, including one of the most important: the spin Hall effect (SHE). A very convenient way to measure an experimental trace of the SHE is the spin Hall magnetoresistance (SMR) presented in Ch. 2.6, which is typically studied in a bilayer structure consisting of a magnetic insulator (MI) and a heavy metal (HM). Spin wave excitation via the SHE and via thermal agitation in the aforementioned MI/HM bilayers are studied in Ch. 2.7. Their diffusive transport due to a spatially confined spin injection is discussed therein.

2.1 Spin-$\frac{1}{2}$ Systems

In contrast to the typical idea of the spin being a vector of angular momentum, the quantum mechanical spin operator $\hat{\boldsymbol{s}}$ behaves more complicated in many cases. Nevertheless, we almost exclusively view the spin as a classical vector in this thesis. In this Section, we will formulate how and why $\hat{\boldsymbol{s}}$ for a 1/2-valued electron spin can be mostly treated as a 3-dimensional vector in euclidean space. To this end, we will review some basic concepts about spin-1/2 systems (as represented by the electron spin) and arrive at a correspondence to a classical vector.

As mentioned above, the quantum mechanical spin operator $\hat{\boldsymbol{s}} = (\hat{s}_\mathrm{x}, \hat{s}_\mathrm{y}, \hat{s}_\mathrm{z})^\top$ for a spin-1/2 particle is given by $\hbar/2$ multiplied with the vector of Pauli spin matrices $\hat{\boldsymbol{\sigma}} = (\hat{\sigma}_\mathrm{x}, \hat{\sigma}_\mathrm{y}, \hat{\sigma}_\mathrm{z})^\top$, the components of which are given by [20, 21]

$$\hat{\sigma}_x = \begin{pmatrix} 0 & 1 \\ 1 & 0 \end{pmatrix}, \qquad \hat{\sigma}_y = \begin{pmatrix} 0 & -i \\ i & 0 \end{pmatrix}, \qquad \hat{\sigma}_z = \begin{pmatrix} 1 & 0 \\ 0 & -1 \end{pmatrix}. \tag{2.1}$$

Each of these matrices are quantum mechanical operators acting on spin states. Since the components of $\hat{\boldsymbol{\sigma}}$ satisfy the commutation relation according to $[\hat{\sigma}_i, \hat{\sigma}_j] = 2i\,\epsilon_{ijk}\hat{\sigma}_k$, where ϵ_{ijk} is the Levi-Civita tensor and the subscripts are $\{i, j, k\} \in \{x, y, z\}$, the exact determination of one particular component of $\hat{\boldsymbol{s}}$ renders the other two to be indeterminate (as usual for a quantum mechanical angular momentum operator). Considering a measurement of the spin state along the z-axis, we solve the eigenvalue equation according to

$$\hat{s}_z \left|\psi\right\rangle = s_z \left|\psi\right\rangle, \tag{2.2}$$

where $\left|\psi\right\rangle$ denote the ket-eigenstates of the $\hat{s}_z$ operator and s_z are the corresponding eigenvalues. Since the 2×2 representation of $\hat{s}_z$ is diagonal, we can immediately identify the eigenvalues $s_z = \pm\hbar/2$. It can be easily shown that the eigenvalues for the $\hat{s}_x$ and $\hat{s}_y$ operators are equal to s_z, i.e. $s_x = s_y = s_z$. We will, however, limit ourselves to the spin states related to the $\hat{s}_z$ operator in the following. The corresponding eigenstates become

$$\left|\psi\right\rangle_{s_z=+\hbar/2} = \begin{pmatrix} 1 \\ 0 \end{pmatrix} \equiv \left|\uparrow\right\rangle, \qquad \left|\psi\right\rangle_{s_z=-\hbar/2} = \begin{pmatrix} 0 \\ 1 \end{pmatrix} \equiv \left|\downarrow\right\rangle. \tag{2.3}$$

These two states are well-known as the *spin-up* and *spin-down* states of the electron spin. We can then write an arbitrary spin state $\left|\chi\right\rangle$ in the basis of the eigenstates as [22]

$$\left|\chi\right\rangle = \left|\uparrow\right\rangle \left\langle\uparrow\middle|\chi\right\rangle + \left|\downarrow\right\rangle \left\langle\downarrow\middle|\chi\right\rangle = \begin{pmatrix} \left\langle\uparrow\middle|\chi\right\rangle \\ \left\langle\downarrow\middle|\chi\right\rangle \end{pmatrix} = \begin{pmatrix} \alpha \\ \beta \end{pmatrix}, \tag{2.4}$$

where $\langle\uparrow|\chi\rangle$ ($\langle\downarrow|\chi\rangle$) is the projection of $|\chi\rangle$ along $|\uparrow\rangle$ ($|\downarrow\rangle$), which we identified with the scalar quantity α (β). Hence, we can write an arbitrary spin state as a linear combination of the eigenstates according to $|\chi\rangle = \alpha|\uparrow\rangle + \beta|\downarrow\rangle$. The preceding analysis shows that the eigenbasis of the electronic spin is 2-dimensional, which is a direct consequence of its spin quantum number being $1/2$. In the following, we will use the 2-dimensional spin-up and -down eigenstates given in Eq. (2.4) to work out its relation to a classical vector.

One important property of a classical vector is that its length is constant for arbitrary directions. To show this for the spin $1/2$-system, we calculate the absolute of the expectation value of $\hat{\boldsymbol{s}}$ for an arbitrary spin state $|\chi\rangle$ as

$$|\langle\hat{\boldsymbol{s}}\rangle| = \sqrt{\langle\chi|\hat{s}_x|\chi\rangle^2 + \langle\chi|\hat{s}_y|\chi\rangle^2 + \langle\chi|\hat{s}_z|\chi\rangle^2} = \frac{\hbar}{2}(|\alpha|^2 + |\beta|^2), \tag{2.5}$$

where $|\alpha|^2 + |\beta|^2 = 1$ for a normalized state $|\chi\rangle$ and thus $|\langle\hat{\boldsymbol{s}}\rangle| = \hbar/2$. We see that the length of the spin state is independent of α and β and thus constant for arbitrary states/directions, which is a special property of spin-$1/2$ systems. It is the first ingredient for a correspondence of the quantum mechanical spin operator $\hat{\boldsymbol{s}}$ and a conventional 3-dimensional vector. The second ingredient is that for each state $|\chi\rangle$, there should exist exactly one particular direction in 3-dimensional space. To demonstrate this, we make use of the spin rotation operator [22]

$$\begin{aligned}\mathcal{D}(\hat{\boldsymbol{n}},\phi) &= \exp\left(-\frac{i\hat{\boldsymbol{s}}\cdot\hat{\boldsymbol{n}}\phi}{\hbar}\right) = \exp\left(-\frac{i\hat{\boldsymbol{\sigma}}\cdot\hat{\boldsymbol{n}}\phi}{2}\right)\\ &= \mathbb{1}\cos\left(\frac{\phi}{2}\right) - i\hat{\boldsymbol{\sigma}}\cdot\hat{\boldsymbol{n}}\sin\left(\frac{\phi}{2}\right),\end{aligned} \tag{2.6}$$

where $\mathbb{1}$ is the 2×2 identity matrix, ϕ is the rotation angle and $\hat{\boldsymbol{n}} = (n_x, n_y, n_z)^\top$ is a unit vector representing the rotation axis. We now successively apply the rotation operator to $|\chi\rangle$ along two orthogonal rotation axes. In particular, we rotate the spin-up state $|\uparrow\rangle$ about the y-axis by the polar angle θ followed by a rotation about the z-axis by the azimuthal angle φ. We obtain [22]

$$|\chi\rangle = \mathcal{D}(\hat{\boldsymbol{z}},\varphi)\mathcal{D}(\hat{\boldsymbol{y}},\theta)|\uparrow\rangle = \begin{pmatrix}\cos\left(\frac{\theta}{2}\right)e^{-i\varphi/2}\\ \sin\left(\frac{\theta}{2}\right)e^{i\varphi/2}\end{pmatrix}, \tag{2.7}$$

where we used Eq. (2.6) and Eq. (2.3). Moreover, $\hat{\boldsymbol{y}}$ and $\hat{\boldsymbol{z}}$ are the unit vectors along y and z, respectively. Identifying the expression in Eq. (2.7) with Eq. (2.4), we find

$$\frac{\alpha}{\beta} = \frac{\cos(\theta/2)}{e^{i\varphi}\sin(\theta/2)}. \tag{2.8}$$

This relation between the eigenstate projections α and β to the polar and azimuthal rotation angles θ and φ allows for a correspondence between the vector space spanned by the Pauli spin matrices and a representation of the spin as a conven-

tional 3-dimensional vector in euclidean space. Using spherical coordinates, we introduce the dimensionless *spin polarization* vector

$$\boldsymbol{s} = \begin{pmatrix} \sin(\theta)\cos(\varphi) \\ \sin(\theta)\sin(\varphi) \\ \cos(\theta) \end{pmatrix}, \tag{2.9}$$

where θ and φ are determined via Eq. (2.8). Unless stated otherwise, the usage of the term 'spin' in this thesis usually refers to the spin polarization vector $\boldsymbol{s}$, rather than the quantum mechanical operator $\hat{\boldsymbol{s}}$. We note, that this correspondence is only valid for spin-1/2 systems due to their 2-dimensional eigenbasis. For any spin system with spin quantum number larger than 1/2, the dimensionality of the corresponding eigenbasis is larger than 2. Hence, a successive application of the rotation operator as implemented above would yield additional angles to the polar and azimuthal angles θ and φ. A corresponding euclidian vector would thus be composed of more than 3 components. The representation of $|\chi\rangle$ via the angles θ and φ in Eq. (2.7) emphasizes another peculiarity about the spin-1/2 system, which becomes immediately clear when we consider a 'full' rotation (360°) of $|\chi\rangle$ by setting $\theta = 2\pi$ (while assuming $\varphi = 0$). In contrast to the naive expectation that a full rotation should not change the original state, one finds $|\chi\rangle_{\theta=2\pi,\varphi=0} = -|\chi\rangle$, as compared to the original state being $|\chi\rangle_{\theta=\varphi=0} = +|\chi\rangle$. In fact, a rotation by $\theta = 4\pi$ (720°) is needed to return to the original state. This is a direct consequence of the half-integer eigenvalue property of the electron spins, i.e. $s_z = \pm\hbar/2$[1].

2.2 Spin Waves

The exchange interaction in magnetic materials causes neighbouring spins to orient themselves in a parallel (antiparallel) fashion in ferromagnetic (antiferromagnetic) materials. The summation over the magnetic moments of each spin allows one to define the magnetization

$$\boldsymbol{M} = \frac{1}{V} \sum_{\boldsymbol{\mu}_j^{\mathrm{s}} \in V} \boldsymbol{\mu}_j^{\mathrm{s}}, \tag{2.10}$$

which describes total magnetic moment per unit volume V with its direction given by the unit vector $\boldsymbol{m} = \boldsymbol{M}/M_{\mathrm{s}}$, where M_{s} is the saturation magnetization. Since the exchange interaction itself is completely isotropic, the direction of the magnetization is determined by any symmetry-breaking magnetic interaction

[1] It is worth noting that the appearance of the minus sign in a 2π-rotated spin state (i.e. $|\chi\rangle_{\theta=2\pi,\varphi=0} \rightarrow -|\chi\rangle$) does not change the sign of the corresponding expectation value $\langle\hat{s}_z\rangle = \langle\chi|\hat{s}_z|\chi\rangle$, meaning that the spin polarization does not change. The difference between an unrotated and 2π-rotated state can, however, be rather drastic when these two states are superimposed, as it leads to a destructive interference nullifying the state. An experimental verification of such destructive interference of 2π-rotated states with unrotated ones was implemented via neutron interferometry in Refs. [23, 24].

(e.g. spin-orbit interaction leading to magnetocrystalline anisotropy) or external magnetic fields. The typically large strength of the exchange interaction is well pictured by a mean-field approach, where the mean interaction is decribed by an equivalent molecular magnetic field (also known as the exchange field $\mu_0 \boldsymbol{H}_{\mathrm{ex}}$), ranging in the order of $100\,\mathrm{T} - 1000\,\mathrm{T}$ for typical magnetic materials. As a result of this strong interaction, the flip of a single spin (cf. Fig. 2.2**a**) would cost a very high energy. However, excitations with much lower energy but an equal change in total angular momentum are possible via wave-like excitations of the whole spin lattice, where each single spin is disturbed only slightly (see Fig. 2.2**b**). These collective excitations of the spin lattice are denoted as *spin waves* and are capable of transporting spin without moving charge carriers.

For the sake of an adequate introduction to spin wave dynamics, it is useful to address the dynamics of a magnetic spin moment $\boldsymbol{\mu}^{\mathrm{s}}$ in a (uniform) magnetic field $\mu_0 \boldsymbol{H}$. In general, the magnetic moment experiences a torque $\boldsymbol{\tau} = \boldsymbol{\mu}^{\mathrm{s}} \times \mu_0 \boldsymbol{H}$ when the field is non-collinear with the magnetic moment [25]. Recalling the definition of the spin magnetic moment $\boldsymbol{\mu}^{\mathrm{s}} = \gamma \boldsymbol{l}(\hat{\boldsymbol{s}})$ and further using the definition of the torque being the time derivative of the angular momentum, i.e. $\boldsymbol{\tau} = \partial \boldsymbol{l} / \partial t$, we obtain[2]

$$\frac{\partial \boldsymbol{\mu}^{\mathrm{s}}}{\partial t} = \gamma \boldsymbol{\mu}^{\mathrm{s}} \times \mu_0 \boldsymbol{H}, \tag{2.11}$$

which describes a precessional motion of the spin magnetic moment $\boldsymbol{\mu}^{\mathrm{s}}$ around the magnetic field $\boldsymbol{H}$. This rotating motion is induced by a finite misalignment of $\boldsymbol{\mu}^{\mathrm{s}}$ with respect to $\boldsymbol{H}$, completely analog to the dynamics of gyroscopes in gravitational fields. Equation (2.11) can be generalized to be applied to magnetization dynamics by simply substituting $\boldsymbol{\mu}^{\mathrm{s}}$ with the magnetization $\boldsymbol{M}$ and the magnetic field $\mu_0 \boldsymbol{H}$ with the effective magnetic field $\mu_0 \boldsymbol{H}_{\mathrm{eff}}$. In most cases, the latter is comprised of [26]

$$\boldsymbol{H}_{\mathrm{eff}} = \boldsymbol{H} + \boldsymbol{H}_{\mathrm{ani}} + \boldsymbol{H}_{\mathrm{D}} + \boldsymbol{H}_{\mathrm{ex}}, \tag{2.12}$$

where we introduced the external magnetic field $\mu_0 \boldsymbol{H}$, the crystalline magnetic anisotropy field $\mu_0 \boldsymbol{H}_{\mathrm{ani}}$, the demagnetization field $\mu_0 \boldsymbol{H}_{\mathrm{D}}$ and the exchange field $\mu_0 \boldsymbol{H}_{\mathrm{ex}}$. Additional internal magnetic fields stemming from more complex magnetic interactions might be added for certain materials. For the sake of a more realistic description of the magnetization dynamics in a magnetic material, T. L. Gilbert developed a phenomenological description of a damped magnetization precession

[2] Note that we defined $\gamma < 0$ accounting for the oppositely oriented spin angular momentum and magnetic spin moment according to $\boldsymbol{\mu}^{\mathrm{s}} = \gamma \boldsymbol{l}(\hat{\boldsymbol{s}})$ introduced in the beginning of Ch. 2. This is important for the actual direction of the precessional motion.

in 1955 [27]. The incorporation of this damping term leads to the Landau-Lifshitz-Gilbert (LLG) equation [27]

$$\frac{\partial \boldsymbol{m}}{\partial t} = \gamma \boldsymbol{m} \times \mu_0 \boldsymbol{H}_{\text{eff}} - \alpha_{\text{G}} \boldsymbol{m} \times \frac{\partial \boldsymbol{m}}{\partial t}, \tag{2.13}$$

where we used $\boldsymbol{m} = \boldsymbol{M}/M_{\text{s}}$ and we introduced the phenomenological dimensionless *Gilbert damping* parameter α_{G}. The damping parameter α_{G} does not contain microscopic information about the nature of the damping, but rather projects any possible damping mechanism within the magnetic material into one phenomenogical value. Due to the additional damping term, a finite misalignment of the effective field $\boldsymbol{H}_{\text{eff}}$ and magnetization direction $\boldsymbol{m}$ leads to a spiraling motion of the precession which will eventually stop when it is aligned with the effective field. As indicated above, spin waves are excited by slight misalignments of the individual spins in a lattice with respect to the effective field $\mu_0 \boldsymbol{H}_{\text{eff}}$. This leads to a precessional motion of each spin as illustrated in Fig. 2.2**c** and **d**. Introducing a finite phase difference between the precessional oscillations results in a wave-like propagation of spin through the lattice. Low magnetic damping values allow for long distance spin wave propagation [8, 28].

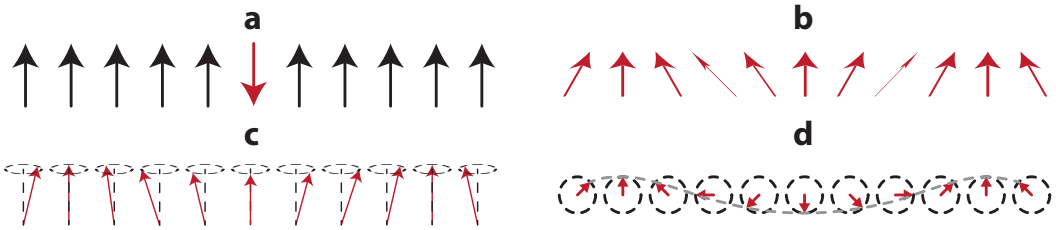

Fig. 2.2 – **a** Single spin flip in a chain of exchange coupled spins. **b** One single spin flip excitation is dispersed over the whole spin chain, thereby decreasing the exchange energy compared to the single spin flip. **c** Side view of a spin wave indicating the precession of each spin and a finite phase difference between the spins. **d** Top view of the spin wave showing the transverse components of the spins. The wavelength of the excitation is indicated and depends on the phase difference between the spins.

In magnetic crystals, spin waves are treated as quantized excitations of the magnetic order and are generally known as *magnons* (in analogy to the excitations of the electromagnetic field called photons). In a quantum mechanical particle picture, a single magnon excitation refers to an entity with the lowest possible energy above the ground state. Due to the directional quantization of the electron spin (with an arbitrary quantization axis), the excitations of an exchange coupled spin lattice can only occur in integers of $1\hbar$. In a simple picture, this can be explained as an inversion of a single spin state in the ensemble of exchange coupled spin moments arranged in a periodic structure (see Fig. 2.2**a**). Hence, for the typical case of coupled electron spins with spin magnetic moment $\hbar/2$, a single spin flip excitation corresponds to a magnon spin with the proposed magnitude $1\hbar$. Magnons therefore belong to the particle class of bosons and obey

the Bose-Einstein statistics. As mentioned above, a complete inversion of one spin would, however, lead to a rather unfavorable configuration in terms of the exchange energy. It is thus much more favorable to delocalize one spin flip over a larger number of spins, each of which is only slightly tilted with respect to each other (Fig. 2.2**b**). The wavelength λ/wavevector $\boldsymbol{k}$ of this spin excitation is determined by the relative phase between the neighbouring spins precessing in the exchange field (see Fig. 2.2**c** and **d**). For the extreme case of an inifinite wavelength/vanishing wavevector, the complete spin ensemble (i.e. magnetization $\boldsymbol{M}$) tilts uniformly with respect to the easy-axis anisotropy direction. Hence, the energy of a single magnon with $\boldsymbol{k} = 0$ is given by the anisotropy energy and the Zeeman energy when an external magnetic field $\boldsymbol{H}$ is applied. In general, short wavelengths/large wavevectors lead to a larger tilt between neighbouring spins and therefore increase the exchange energy. For large wavelengths/short wavevectors, the tilt between neighbouring spins is very small and the exchange energy plays a secondary role. In this regime, the long-range dipolar coupling between widely separated spins (with larger tilt) dominates over the very short-ranged exchange interaction between neighbouring spins. Overall, the mathematical dependence of the magnon energy/frequency on the wavevector is given by the dispersion relation which can be derived by solving the LLG Equation (2.13) and calculating the resonance frequency ω_m. A reasonably simple form of the magnon dispersion for thin films including isotropic exchange interaction ($\boldsymbol{H}_\mathrm{ex}$), anisotropic dipolar coupling due to demagnetization ($\boldsymbol{H}_\mathrm{D}$) and an external magnetic field ($\boldsymbol{H}$) was derived by B. A. Kalinikos and A. N. Slavin and is given by [29, 30]

$$\omega_\mathrm{m}(\boldsymbol{k}) = \left\{ \begin{array}{l} \left[\gamma\mu_0 H + \frac{J_\mathrm{s}}{\hbar}k^2 + \gamma\mu_0 M_\mathrm{s} P(k)\right] \\ \times \left[\gamma\mu_0 H + \frac{J_\mathrm{s}}{\hbar}k^2 + \gamma\mu_0 M_\mathrm{s}(1 - P(k))\sin^2\phi\right] \end{array} \right\}^{1/2}, \tag{2.14}$$

which assumes an in-plane magnetized ferromagnet and a uniform precession along the film thickness d. Furthermore, μ_0 is the vaccuum magnetic permeability, M_s denotes the saturation magnetization of the respective magnetic system, $k = |\boldsymbol{k}| = k_x^2 + k_y^2 + k_z^2$ and J_s is the spin wave stiffness parameter. The angle ϕ indicates the relative orientation between the spin wave propagation direction $\boldsymbol{k}$ and the magnetization $\boldsymbol{M}$ within the plane of the film. Furthermore, the correction factor $P(k) = (1 - \mathrm{e}^{-kd})/(kd)$ accounts for thin films with thickness d. For magnetic thin films and small wavevectors, the dipolar interaction plays a central role and determines the dispersion due to dipolar fields contained in the demagnetization field $\boldsymbol{H}_\mathrm{D}$. For large thicknesses $d \to \infty$ (the bulk limit), $P(k) = 0$. We have neglected crystalline magnetic anisotropy contributions in Eq. (2.14), i.e. $\boldsymbol{H}_\mathrm{ani} = 0$. By further completely disregarding the anisotropic dipolar effects in the dispersion relation, we obtain the simplest isotropic form according to $\epsilon_\mathrm{m}(\boldsymbol{k}) = \hbar\omega_\mathrm{m}(\boldsymbol{k}) = \hbar\gamma\mu_0 H + J_\mathrm{s}k^2$, which is a good approximation for large $\boldsymbol{k}$.

In a semiclassical analysis of this quadratic dispersion, the inverse of the spin wave stiffness J_s can be identified with the effective magnon mass $m_m = \hbar^2 \left[\frac{d^2\epsilon_m(\boldsymbol{k})}{dk^2}\right]^{-1} = \hbar^2/(2J_s)$. As discussed in Ch. 2.7, our magnon transport experiments studied in this thesis are dominated by the large wavevector $\boldsymbol{k}$ magnons governed by the exchange interaction, thus justifying the assumption of a simple isotropic, quadratic dispersion. Typical frequencies of magnons in the small wavevector regime are in the order of a few GHz, whereas the large wavevector magnons even reach the THz-regime. Antiferromagnetic spin excitations in general exhibit even faster dynamics due to their strong coupling [31, 32], starting from a few 100 GHz even in the low wavevector regime.

2.3 Spin Transport in Metals

While the generation of electric potentials (and thus electric currents) via the separation of positive and negative electric charges represents a standard procedure these days, a yet ongoing subject of spintronics research is the efficient generation of pure spin currents. The driving force for spin currents are gradients in the spin chemical potential emerging e.g. as a result of a spatial separation of electronic spin-up and -down states. Although the creation of spin currents is a more challenging task compared to electric current generation, great progress towards efficient methods have been discovered in recent decades. In the following, we will review the basics of electronic spin currents and their diffusive transport in metals.

2.3.1 Spin Currents

In general, a particle current density can be expressed as $\boldsymbol{j} = n\langle\boldsymbol{v}\rangle$, where n is the particle density and $\langle\boldsymbol{v}\rangle$ the associated thermodynamic expectation value of the particle velocity operator $\boldsymbol{v}$. Charge, heat and spin current densities can therefore be expressed by multiplying $\boldsymbol{j}$ with the corresponding quantity transported by the particles. For charge and heat current densities $\boldsymbol{j}_c$ and $\boldsymbol{j}_h$, respectively, where the transported charge q and heat Q per particle are scalar quantities, this simply results in

$$\boldsymbol{j}_c = q\boldsymbol{j} = qn\langle\boldsymbol{v}\rangle \tag{2.15a}$$

$$\boldsymbol{j}_h = Q\boldsymbol{j} = Qn\langle\boldsymbol{v}\rangle. \tag{2.15b}$$

For spin currents, the situation is more difficult as the transported angular momentum is no longer a scalar quantity. Therefore, the spin current density has

to be expressed by the dyadic product of the particle current density $\boldsymbol{j}$ and the transported spin $\hat{\boldsymbol{s}}$ per particle, resulting in [33, 34]

$$\underline{\boldsymbol{j}}_\mathrm{s} = \langle \hat{\boldsymbol{s}} \otimes \boldsymbol{j} \rangle = \frac{\hbar}{2} n \langle \hat{\boldsymbol{\sigma}} \otimes \boldsymbol{v} \rangle = \begin{pmatrix} \boldsymbol{j}_{\mathrm{s},x} & \boldsymbol{j}_{\mathrm{s},y} & \boldsymbol{j}_{\mathrm{s},z} \end{pmatrix}^\top = \begin{pmatrix} \boldsymbol{j}_\mathrm{s}^x & \boldsymbol{j}_\mathrm{s}^y & \boldsymbol{j}_\mathrm{s}^z \end{pmatrix}, \tag{2.16}$$

where $\langle ... \rangle$ denotes the thermodynamic expectation value for a non-equilibrium state and the underline indicates that the spin current is a second rank tensor. We further used $\hat{\boldsymbol{s}} = \frac{\hbar}{2}\hat{\boldsymbol{\sigma}}$ with $\hat{\boldsymbol{\sigma}}$ the vector of the Pauli spin matrices introduced in Eq. (2.1) and we have assumed that every particle (e.g. electrons) transports a spin angular momentum of $\hbar/2$. The row vectors $\boldsymbol{j}_{\mathrm{s},i} = \frac{\hbar}{2} n \langle \hat{\sigma}_i \boldsymbol{v}^\top \rangle$ denote the flow direction of the spin current with fixed polarization $\hat{\sigma}_i$, while the column vectors $\boldsymbol{j}_\mathrm{s}^j = \frac{\hbar}{2} n \langle \hat{\boldsymbol{\sigma}} v_j \rangle$ denote the spin polarization direction with fixed current flow direction given by the velocity component v_j.

In an experimental measurement setting, the spin state manifests itself along a certain quantization axis. It is therefore useful to express the spin current only in terms of the two eigenstates corresponding to this quantization axis. For convenience, we choose the z-axis which results in spin-up $|\uparrow\rangle$ and spin-down $|\downarrow\rangle$ states (see Ch. 2.1). Calculating the expectation value as defined in Eq. (2.16) for these two spin states leads to $\boldsymbol{j}_{\mathrm{s},z}^{|\uparrow\rangle} = \frac{\hbar}{2} n \langle \uparrow | \hat{\sigma}_z \boldsymbol{v}^\top | \uparrow \rangle = \frac{\hbar}{2} n \langle \boldsymbol{v}^\top \rangle^\uparrow \equiv \boldsymbol{j}_\mathrm{s}^\uparrow$ and $\boldsymbol{j}_{\mathrm{s},z}^{|\downarrow\rangle} = \frac{\hbar}{2} n \langle \downarrow | \hat{\sigma}_z \boldsymbol{v}^\top | \downarrow \rangle = -\frac{\hbar}{2} n \langle \boldsymbol{v}^\top \rangle^\downarrow \equiv \boldsymbol{j}_\mathrm{s}^\downarrow$, respectively. Here, $\langle \boldsymbol{v}^\top \rangle^\uparrow$ and $\langle \boldsymbol{v}^\top \rangle^\downarrow$ are the expectation values for the particle velocities of spin-up and spin-down states[3]. This corresponds to a particle current density transporting the spin angular momentum of either $\hbar/2$ or $-\hbar/2$, which is the expected result when only one particular spin direction is considered. Along our arbitrarily chosen quantization axis, we can express the total spin current within a two-fluid model as the sum of spin-up and -down currents as

$$\boldsymbol{j}_\mathrm{s} = \boldsymbol{j}_\mathrm{s}^\uparrow + \boldsymbol{j}_\mathrm{s}^\downarrow = \frac{\hbar}{2} n (\langle \boldsymbol{v} \rangle^\uparrow - \langle \boldsymbol{v} \rangle^\downarrow) = -\frac{\hbar}{2e} (\boldsymbol{j}_\mathrm{c}^\uparrow - \boldsymbol{j}_\mathrm{c}^\downarrow), \tag{2.17}$$

where we related the spin currents to electrical currents via $\boldsymbol{j}^{\uparrow,\downarrow} = n \langle \boldsymbol{v} \rangle^{\uparrow,\downarrow} = \boldsymbol{j}_\mathrm{c}^{\uparrow,\downarrow}/q$ using $q = -e$ for electrons. Note that we dropped the transposition of the velocity vector for convenience, making $\boldsymbol{j}_\mathrm{s}$ a conventional 3-dimensional column vector. Since the two-fluid model treats the spin-up and -down states as seperate currents, we can define two seperate chemical potentials $\mu^\uparrow$ and $\mu^\downarrow$ for the two spin species and use $\boldsymbol{j}_\mathrm{c}^{\uparrow,\downarrow} = -(-\sigma_\mathrm{e}/e) \nabla \mu^{\uparrow,\downarrow}$ according to Fick's law [26] (with σ_e denoting the electrical conductivity), resulting in [35]

$$\boldsymbol{j}_\mathrm{s} = -\frac{\hbar}{2e} \frac{\sigma_\mathrm{e}}{e} \nabla \mu_\mathrm{s}, \tag{2.18}$$

[3] In order to explicitly calculate the expectation value of the velocity operator, one needs to have exact information about the (non-equilibrium) spatial wavefunction of the system under consideration, which is omitted here for the sake of a general description.

where we have introduced the *spin chemical potential* or *spin accumulation* $\mu_s = \mu^\uparrow - \mu^\downarrow$, indicating the excess of spin-up states[4]. We can further identify the metallic spin conductivity $\sigma_s = \hbar/(2e^2)\sigma_e$. Intuitively, one can think of this electron-based spin current as the opposing flow of spin-up and -down electrons, thus compensating the net charge current flow but transporting a finite spin. Microscopically, however, this diffusive spin transport must not be imagined as a directed flow of electrons, but rather by a random walk biased by a spatially inhomogenous spin distribution. Hence, assuming that the electron density is conserved throughout the material, a finite excess spin density evolves within the electron system, the direction of which is governed by the gradient in Eq. (2.18). Such a spin current therefore does not carry any charge and is considered as a *pure spin current*.

For some situations, only one particular direction of the particle flow is of interest, which is usually the case when we discuss spin transport across an interface. In such configurations, one can again express the spin current density by a vector with its direction defining the polarization direction of the spin current (column vector in Eq. (2.16)). This is used e.g. below in Eq. (2.28), where a spin current in a particular direction is discussed, and in Eq. (2.43), where the spin current across an interface is described.

2.3.2 Spin Diffusion

Having discussed the peculiarities of spin currents, we now turn to the derivation of the spatial and temporal behaviour of the spin chemical potential μ_s itself, which drives the spin current as defined in Eq. (2.18) in the first place. To this end, we start with the continuity equation for the spin density ρ_s reading as [36]

$$\frac{\partial \rho_s}{\partial t} + \nabla \cdot \boldsymbol{j}_s = -\Gamma_s \rho_s, \tag{2.19}$$

where $\rho_s = \rho^\uparrow - \rho^\downarrow$ with $\rho^\uparrow$ ($\rho^\downarrow$) the spin density for spin-up (spin-down) electron states[5]. Furthermore, $\Gamma_s = 1/\tau_s$ is the spin relaxation rate accounting for the finite lifetime τ_s of either spin-up or -down states due to spin-flip scattering events. One might notice that Eq. (2.19) is different from conventional continuity equations, where the right-hand side is supposed to be zero. This non-vanishing term on the right-hand side is due to finite spin-flip scattering, leading to a non-conservation of the non-equilibrium spin density ρ_s. The total number of excess spin (either spin-up or -down, depending on the sign of ρ_s) is therefore not a conserved quantity

[4] Since the chemical potentials are given in units of energy (i.e. Joule J), this results in a spin current density given in units of 'spin angular momentum ($\hbar$) per area and second', i.e. $\mathrm{Js/(m^2 s)} = \mathrm{J/m^2}$.

[5] Generally, the spin density ρ_s must be considered as a vectorial quantity. However, we keep the analysis simple by only considering the spin density along an arbitrary quantization axis, thus allowing for a description within the two-fluid model.

and its relaxation must be taken into account in the continuity equation. In order to arrive at a differential equation for μ_s, we have to calculate the spin density according to

$$\rho_s = \frac{\hbar}{2} n_s = \frac{\hbar}{2} \int_0^\infty D(\epsilon) \left[n_F(\epsilon, \mu^\uparrow, T) - n_F(\epsilon, \mu^\downarrow, T) \right] \mathrm{d}\epsilon, \tag{2.20}$$

where $n_s = n^\uparrow - n^\downarrow$ is the difference between the electron density of spin-up and spin-down states and we assumed each electron to carry a spin angular momentum of $\hbar/2$. These electron spin densities are calculated via an integral over the electron density of states $D(\epsilon)$ (per volume and energy) weighted by the Fermi-Dirac distribution functions $n_F(\epsilon, \mu^{\uparrow,\downarrow}, T) = \left[\exp\left((\epsilon - \mu^{\uparrow,\downarrow})/(k_B T)\right) + 1\right]^{-1}$ for the electronic spin-up and spin-down states with single particle energy ϵ at temperature T. A difference between the spin-up and spin-down densities is introduced by a non-vanishing spin chemical potential μ_s. For the evaluation of Eq. (2.20), we use the fact that the electron density must be a conserved quantity for any temperature T. Hence, we can evaluate ρ_s at $T = 0$, which transforms the Fermi-Dirac distribution to a simple step function according to $n_F(\epsilon, \mu^{\uparrow,\downarrow}, T = 0) = \Theta(\mu^{\uparrow,\downarrow} - \epsilon)$ with $\Theta(x)$ the Heaviside function. We thus obtain

$$\begin{aligned} \rho_s &= \frac{\hbar}{2} \int_0^\infty D(\epsilon) \left[\Theta(\mu^\uparrow - \epsilon) - \Theta(\mu^\downarrow - \epsilon) \right] \mathrm{d}\epsilon \\ &= \frac{\hbar}{2} \int_{\mu^\downarrow}^{E_F} D(\epsilon)\, \mathrm{d}\epsilon + \frac{\hbar}{2} \int_{E_F}^{\mu^\uparrow} D(\epsilon)\, \mathrm{d}\epsilon, \end{aligned} \tag{2.21}$$

where $E_F = (\mu^\uparrow + \mu^\downarrow)/2$ is the Fermi energy. Considering a sufficiently small spin chemical potential μ_s, we can further assume the density of states to be constant across the energy range $\mu^\downarrow < \epsilon < \mu^\uparrow$, ultimately leading to

$$\rho_s = \frac{\hbar}{2} [D(E_F)(E_F - \mu^\downarrow) + D(E_F)(\mu^\uparrow - E_F)] = \frac{\hbar}{2} D(E_F) \mu_s. \tag{2.22}$$

With these simplifications, the spin density becomes a linear function of μ_s. This is a prerequisite for the derivation of the spin diffusion equation in the following. The prefactor before μ_s in Eq. (2.22) can be also more generally written as a derivative according to $\partial\rho_s/\partial\mu_s$, thus not implying a certain approximation used for the calcualation of the spin density. Based on the continuity Equation (2.19), this allows us to write down a rather simple differential equation for μ_s. Substituting Eqs. (2.18) and (2.22) into (2.19), we arrive at [37–39]

$$\frac{\partial \mu_s}{\partial t} - D_s \nabla^2 \mu_s = -\frac{\mu_s}{\tau_s}, \tag{2.23}$$

where $D_s = \hbar/(2e) \cdot \sigma_e / e \left(\frac{\partial \rho_s}{\partial \mu_s}\right)^{-1} = \sigma_s \left(\frac{\partial \rho_s}{\partial \mu_s}\right)^{-1}$ is the spin diffusion constant and we used $\sigma_s = \hbar/(2e^2)\, \sigma_e$ as introduced before. The associated spin diffusion length

is given by $l_s = \sqrt{D_s \tau_s}$ and takes typical values of a few nm up to a few µm. Experimentally determined values for l_s often vary strongly between different measurement methods and therefore have to be taken with care. Additional complications like crystalline quality, impurities or correction factors [40, 41] also lead to the broad range of values observed for supposedly identical materials.

An important difference of diffusive spin transport compared to the diffusive electron transport is the non-conservation of the spin density/spin chemical potential (in contrast to the electron particle conservation), which is represented by the loss term on the right hand side of Eq. (2.19) and Eq. (2.23)[6]. This represents one of the most striking challenges to be overcome by spintronics research. One possible way to tackle this task in the context of spin excitations in magnetic insulators is discussed in Chapter 5 of this thesis.

2.4 Pure Spin Current Generation in Metals

The perequisite of generating pure spin currents in metallic systems is the spatial separation of oppositely oriented spin states. To achieve such inhomogeneity in the most general sense, we require a material that breaks the time reversal symmetry in spin space. Such symmetry breaking is induced by any kind of external or internal magnetic field acting on the spins. Two of the very common spin-based interactions in condensed matter physics leading to internal magnetic fields are the spin-orbit coupling (SOC) and the exchange interaction responsible for ferromagnetism. Heavy metallic systems with large SOC or ferromagnetic metals therefore serve as prototypes for the implementation of spin dependent effects due to time reversal symmetry breaking. In the following, we introduce two of the most important instances of such spin dependent effects leading to efficient pure spin current generation, which are generally referred to as the *spin Hall effect* in non-magnetic metals as well as the *anomalous spin Hall effect* in ferromagnetic metals.

2.4.1 Non-Magnetic Metals

Firstly introduced by Dyakonov and Perel [42] and later reformulated by Hirsch [43], the spin Hall effect (SHE) triggered a wide variety of research activity and proposals for spintronic applications to this day [44]. The application of an electrically induced charge current $\boldsymbol{j_c} = \sigma_e \nabla \mu_e / e$ (with μ_e the electrochemical potential) to a metallic system with sufficient SOC leads to spin dependent scattering of the flowing electron spins due to both intrinsic bandstructure physics [45] and extrinsic impurity scattering [46–48] contributions. As a result, the spin-up and

[6] We note that the spin non-conservation does not imply the spin to disappear spontaneously, but rather to change its direction during scattering events. In the two-fluid model, such spin-flip event appears as if a spin is disappearing spontaneously from the respective fluid. The property of spin itself is, however, conserved.

-down electrons acquire a transverse velocity component in opposite directions, facilitating the emergence of a transverse spin current $\boldsymbol{j}_\mathbf{s}$ (see Fig. 2.3**a** and **b**)[7]. Phenomenologically, the conversion efficiency of this process is given by the dimensionless spin Hall angle θ_{SH}. Dictated by Onsager reciprocity, exactly the same physics also leads to the inverse spin Hall effect (ISHE), allowing to convert a spin current $\boldsymbol{j}_\mathrm{s}$ into a charge current $\boldsymbol{j}_\mathrm{c}$. The corresponding equations of these effects are given by [49]

$$\boldsymbol{j}_\mathrm{s} = \theta_{\mathrm{SH}} \frac{\hbar}{2e} \boldsymbol{j}_\mathrm{c} \times \boldsymbol{s}, \tag{2.24}$$

$$\boldsymbol{j}_\mathrm{c} = -\theta_{\mathrm{SH}} \frac{2e}{\hbar} \boldsymbol{j}_\mathrm{s} \times \boldsymbol{s}, \tag{2.25}$$

where $\boldsymbol{s}$ denotes the dimensionless spin polarization vector (as defined in Ch. 2.1) of the associated spin current $\boldsymbol{j}_\mathrm{s}$. Since the quantization axis of the spin states in a non-magnetic material is arbitrary, any spin polarization $\boldsymbol{s}$ with components perpendicular to the charge/spin current will be deflected according to Eqs. (2.24) and (2.25). The first experimental evidence of the SHE has been observed by Kato *et al.* in a semiconductor [50] and has since been observed in various other materials like heavy metals [51], topological insulators [52] or Weyl semimetals [53]. Typical heavy metals used for various spin Hall related physics are platinum (Pt), tungsten (W) or tantal (Ta). In this thesis, we exclusively use Pt as a non-magnetic spin Hall active material, which was previously determined to exhibit a spin Hall angle of $\theta_{\mathrm{SH}} = 0.11$ [54]. We note that similar to the spin diffusion length l_s, the spin Hall angle θ_{SH} suffers from the same issues regarding its experimental determination. A broad range of values can therefore be found in literature [51].

According to the Seebeck effect, charge currents can also be thermally induced via finite temperature gradients ∇T, leading to a charge current of the form $\boldsymbol{j}_\mathrm{c} = -\sigma_\mathrm{e} S_\mathrm{e} \nabla T$ (where S_e is the conventional Seebeck coefficient) [26]. As observed for the first time in 2017 [55] and shortly after reproduced in other works [56–58], the interconversion of a temperature gradient-driven charge current $\boldsymbol{j}_\mathrm{c} \propto -\nabla T$ into a spin current $\boldsymbol{j}_\mathrm{s}$ (and vice versa) is known as the *spin Nernst effect* (SNE) and inverse spin Nernst effect (SNE). Equivalent to the SHE and ISHE, it is given by

$$\boldsymbol{j}_\mathrm{s} = \theta_{\mathrm{SN}} \frac{\hbar}{2e} \boldsymbol{j}_\mathrm{c} \times \boldsymbol{s}, \tag{2.26}$$

$$\boldsymbol{j}_\mathrm{c} = -\theta_{\mathrm{SN}} \frac{2e}{\hbar} \boldsymbol{j}_\mathrm{s} \times \boldsymbol{s}, \tag{2.27}$$

[7] It is worth noting that the identification of the SHE as a *Hall effect* is slightly misleading, since Hall effects are usually considered as the generation of a transverse current originating from a longitudinal current, where both of the currents refer to the same transport quantity. For the SHE, however, the longitudinal current transports charge, while the emerging transverse current transports spin. It is thus an effect stemming from spin-to-charge coupling which is fundamentally different to conventional Hall effects.

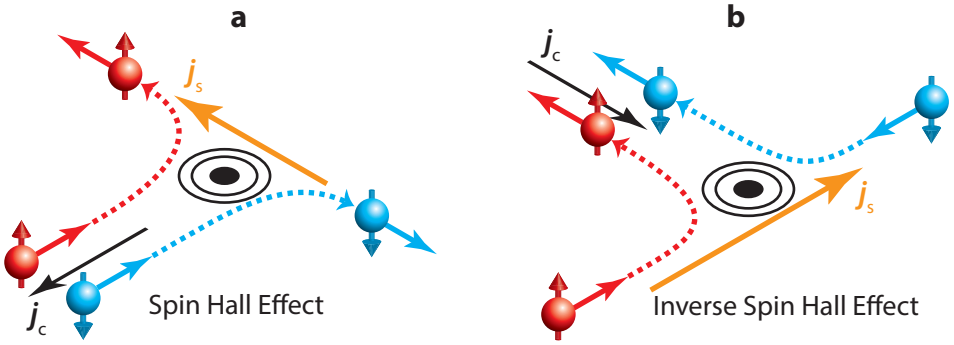

Fig. 2.3 – In metallic systems with strong SOC, a spin dependent scattering of conduction electrons emerges. The scattering center is indicated by the black dot with rings. **a** An applied charge current j_c gives rise to a transverse pure spin current due to the spin Hall effect (SHE). **b** The inverse spin Hall effect (ISHE) describes the reciprocal process where a transverse charge current j_c is caused by a spin current j_s.

where θ_{SN} is the charge-to-spin (and spin-to-charge) conversion efficiency for thermally induced charge currents referred to as the *spin Nernst angle*. It should be noted that the spin Nernst angle θ_{SN} and the spin Hall angle θ_{SH} have different microscopic origins [59–61] and can even differ in sign for identical materials such as Pt [55].

2.4.2 Magnetic Metals

Driving conventional charge currents in magnetic conductors offers a simple way to generate spin polarized currents, i.e. charge currents with finite spin polarization. While this concept has been employed for decades in the form of spin-transfer torque (STT) devices [62], ferromagnets also offer a zoo of pure spin current properties without accompanying charge flow. Their finite magnetic order represents an additional breaking of symmetry leading to a rich spin current generation as recently put forward both theoretically [63,64] and experimentally [11, 65–69]. As detailed in Ref. [64], the general form of a spin current in a ferromagnet flowing along the $\hat{z}$ direction can be expressed as

$$\boldsymbol{j}_s^z = \frac{\hbar}{2e}\left[\theta_{\parallel}[\boldsymbol{m}\cdot(\hat{\boldsymbol{z}}\times\boldsymbol{j}_c)]\boldsymbol{m} + \theta_{\perp}\boldsymbol{m}\times[(\hat{\boldsymbol{z}}\times\boldsymbol{j}_c)\times\boldsymbol{m}] + \theta_{\perp}^{R}\boldsymbol{m}\times(\hat{\boldsymbol{z}}\times\boldsymbol{j}_c)\right], \quad (2.28)$$

where the vector $\boldsymbol{j}_s^z$ denotes the spin polarization direction with fixed spin current direction along $\hat{z}$ as introduced in Eq. (2.16). The resulting spin current direction vector is thus given by $\boldsymbol{j}_{s,i} = j_{s,i}^z\hat{\boldsymbol{z}}$, where $j_{s,i}^z$ denotes the vector components of Eq. (2.28). Further, $\theta_{\parallel}$, $\theta_{\perp}$ and $\theta_{\perp}^{R}$ are spin Hall angle-like conversion efficiencies characterizing contributions associated to spin currents polarized along the magnetization ($\boldsymbol{s} \parallel \boldsymbol{m}$ via the longitudinal component $\theta_{\parallel}$) and transverse to the magnetization ($\boldsymbol{s} \perp \boldsymbol{m}$ via the orthogonal components $\theta_{\perp}$ and $\theta_{\perp}^{R}$). Naively, one would have expected any transverse spin components to dephase quickly due to the rapid and incoherent precession of the spin in the exchange field of the

magnetic order. The SOC, however, acts as an additional effective field that stabilizes these transverse components [63]. The emerging spin currents $\boldsymbol{j}_{\mathrm{s},i} \parallel \hat{\boldsymbol{z}}$ when $\boldsymbol{j}_\mathrm{c} = j_\mathrm{c}\hat{\boldsymbol{y}}$ are exemplarily depicted for $\boldsymbol{j}_\mathrm{c} \perp \boldsymbol{m} \parallel \hat{\boldsymbol{x}}$ and $\boldsymbol{j}_\mathrm{c} \parallel \boldsymbol{m} \parallel \hat{\boldsymbol{y}}$ in Fig. 2.4**a** and **b**, respectively.

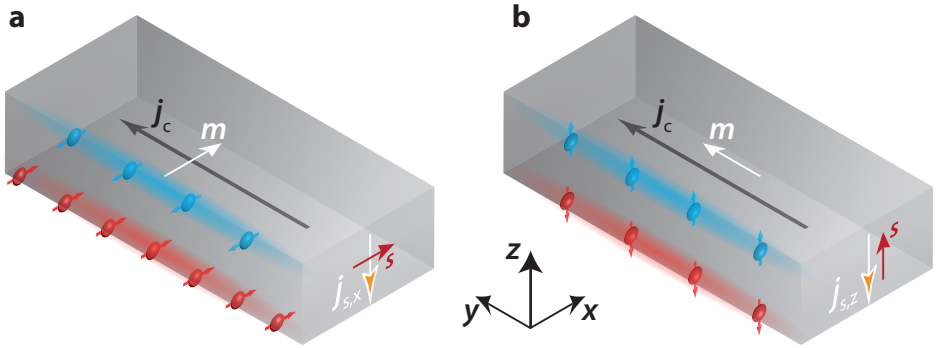

Fig. 2.4 – Illustration of spin dependent scattering effects in magnetic conductors with large SOC. **a** For the anomalous spin Hall effect, $\boldsymbol{m}$ is orthogonal to both $\boldsymbol{j}_\mathrm{c}$ and $\boldsymbol{j}_\mathrm{s}$ while $\boldsymbol{s} \parallel \boldsymbol{m}$. Due to the finite spin polarization of the charge carriers, an electric field along $\hat{\boldsymbol{z}}$ accompanies the spin chemical potential μ_s. **b** For $\boldsymbol{m} \parallel \boldsymbol{j}_\mathrm{c}$, a spin current with spin polarization along $\hat{\boldsymbol{z}}$ builds up at the edges with $\boldsymbol{m} \perp \boldsymbol{s}$. This contribution is referred to as the magnetic spin Hall effect. The spin Hall effect is also active for this configuration but not shown explicitly. Figure reproduced from [70].

When $\boldsymbol{m} \parallel \hat{\boldsymbol{x}}$ (Fig. 2.4**a**), the emerging spin current $\boldsymbol{j}_{\mathrm{s},x} = j^z_{\mathrm{s},x}\hat{\boldsymbol{z}}$ is restricted to the contribution associated with $\theta_\parallel$, while the transverse components $\theta_\perp = \theta^\mathrm{R}_\perp = 0$. As a result, it exhibits a spin polarization $\boldsymbol{s} \parallel \boldsymbol{m}$ and is characterized by the sum of the magnetization-independent spin Hall effect and the magnetization-dependent spin anomalous Hall effect: $\theta_\parallel = \theta_\mathrm{SH} + \theta_\mathrm{ASH}$ [63] with θ_ASH the anomalous spin Hall angle unique to ferromagnetic conductors. The situation further mimics the conventional spin Hall effect symmetry in the sense that $\boldsymbol{j}_\mathrm{c}$, $\boldsymbol{m} \parallel \boldsymbol{s}$ and $\boldsymbol{j}_{\mathrm{s},x}$ are all orthogonal to each other.

For $\boldsymbol{m} \parallel \hat{\boldsymbol{y}}$ (Fig. 2.4**b**), both transverse components associated with $\theta_\perp$ and $\theta^\mathrm{R}_\perp$ are finite, while the longitudinal component $\theta_\parallel = 0$. On the one hand, there is the magnetization-independent spin current with spin polarization $\boldsymbol{s} \parallel \hat{\boldsymbol{y}}$ associated with $\theta_\perp = \theta_\mathrm{SH}$ due to the SHE (which is omitted in Fig. 2.4**b**). On the other hand, a second contribution with $\boldsymbol{s} \parallel \hat{\boldsymbol{z}}$ related to $\theta^\mathrm{R}_\perp$ emerges, thus giving rise to an out-of-plane polarized spin current $\boldsymbol{j}_{\mathrm{s},z} = j^z_{\mathrm{s},z}\hat{\boldsymbol{z}}$. This type of spin current is unique to ferromagnetic conductors and is referred to as the magnetic spin Hall effect in recent literature [71–73]. Since we do not consider out-of-plane magnetized ferromagnets in the context of this thesis, we omit the the third case where $\boldsymbol{m} \parallel \hat{\boldsymbol{z}}$.

2.5 Spin Transport Across Metal/Magnetic Insulator Interfaces

The combination of MIs with conducting HM materials with large SOC opens up a vast variety of interesting physics. Such bilayers are particularly interesting with respect to charge current-induced spin current generation in the metal layer, since the insulating nature of the magnetic layer suppresses typically unwanted current shunting in these bilayer systems. The interaction of spin currents in the HM with the magnetic order in the MI is summarized within the widely studied phenomenon of STT [62]. For the exertion of spin torques in this thesis, we employ pure spin currents originating from SOC in metallic layers, which are therefore more accurately referred to as spin orbit torques (SOT) [74].

The following review of spin transport across MI/HM interfaces discusses the interactions of the unit magnetic order vector $\boldsymbol{n}$ in a MI[8] with an incident electron spin current density polarized along $\boldsymbol{s}$ in the HM. The proportion of electron spins capable of transferring spin angular momentum to the magnetic order $\boldsymbol{n}$ across the HM/MI interface can be described by the complex *spin mixing conductance* [75–77]

$$g^{\uparrow\downarrow} = \frac{1}{A}\sum_{nm}(\delta_{nm} - r^{\uparrow}_{nm}(r^{\downarrow}_{nm})^{*}) = g_{\mathrm{r}}^{\uparrow\downarrow} + i g_{\mathrm{i}}^{\uparrow\downarrow}, \tag{2.29}$$

which is calculated from the interfacial reflection amplitudes $r^{\uparrow}_{nm}$ ($r^{\downarrow}_{nm}$) of electronic spin-up (spin-down) wavefunctions describing the scattering from energy mode m to n. It is further normalized to the respective interfacial area A and thus given in units of $1/\mathrm{m}^2$. Moreover, $\sum_{nm}\delta_{nm} = M$ denotes the total number of open quantum transport channels across the interface (at the Fermi energy) which depends on the available conduction electron modes and thus on their geometrical confinement in the HM[9] [79]. The spin mixing conductance is a measure of the number of spin-flip scattering events happening for an ensemble of electron spins impinging on a given magnet/metal interface when $\boldsymbol{n} \perp \boldsymbol{s}$ [80, 81]. Due to angular momentum conservation, these spin flips lead to a transfer of spin angular momentum to the magnetic order manifesting as a torque acting on $\boldsymbol{n}$, hence $g^{\uparrow\downarrow}$ gives information about the interfacial spin torque transparency [62, 82–85]. Other interfacial conductances that conserve the spin during the scattering event do not transfer any angular momentum and are therefore not of relevance for the spin mixing conductance [75].

[8] In contrast to the definition of a magnetization vector $\boldsymbol{M}$ used in Ch. 2.2 and Ch. 2.4.2, we here define the more general, normalized magnetic order vector $\boldsymbol{n} = \frac{\boldsymbol{N}}{|\boldsymbol{N}|}$, indicating the possibility of more complex magnetic sublattice configurations comprised in $\boldsymbol{n}$.

[9] Considering that the electrons are confined to a long lead along x with a finite cross-section in the y-z-plane, the corresponding energy of the electrons might be generally written as $\epsilon_n = \hbar k_x^2/(2m_{\mathrm{e}}) + E_n$, where the first term represents the continuous kinetic energy along the lead and E_n represents the energy quantization due to the confinement in the transverse direction. For $n \in \{1, 2, 3, ...\}$, two states (spin-up and -down) are occupied for each $\epsilon_n < E_{\mathrm{F}}$, from which the avalaible transport channels M can be deduced. The quantized conductance value for each channel (for one particular spin direction) is given by the conductance quantum $G_0 = e^2/h$ [78].

As defined in Eq. (2.29), $g^{\uparrow\downarrow}$ is composed of a real ($g_r^{\uparrow\downarrow}$) and imaginary ($g_i^{\uparrow\downarrow}$) part, completely analogue to electrical transport, where the complex electrical interface impedance is described by a real component, the resistance, and an imaginary component, the reactance. We will discuss the physical interpretation and relation to the electrical case of these real and imaginary components later in this Section. It should be noted that the theoretical derivation of $g^{\uparrow\downarrow}$ in Refs. [75–77] only considers conducting magnets as opposed to magnetic insulators discussed in this thesis. Despite of the lack of conduction electrons in the MI, the formalism based on the interfacial scattering of conduction electrons in the HM still works well in these systems, which is based on the fact that the spin-mixing conductance is mostly determined by the local magnetic moments/exchange fields at the interface, i.e. only the first few layers of the magnet contribute [82, 86, 87]. We want to raise awareness that for the case of MIs disussed here, there are no finite transmission amplitudes $t_{nm}^{\uparrow,\downarrow}$ for electrons traversing through the MI and thus scattering into the HM, which should otherwise be added as a term $-\sum_{nm} t_{nm}^{\uparrow}(t_{nm}^{\downarrow})^*$ to the spin mixing conductance [75]. In fact, the assumption of vanishing transmission coefficients is typically also valid for conducting magnets as long as the thickness t of the magnet under consideration is larger than the spin coherence length $\lambda_{sc} = \pi/\left|k_F^{\uparrow} - k_F^{\downarrow}\right|$, where $k_F^{\uparrow}/k_F^{\downarrow}$ denotes the Fermi wavevector for spin-up/spin-down states [77].

The preceding description of spin transfer across an HM/MI interface implicitly assumes a perfect alignment of the magnetic order $\boldsymbol{n}$ along a certain axis, which is a valid assumption for temperatures $T \approx 0$. Allowing for $T > 0$, however, results in fluctuations of the magnetic order leading to deviations from the average relative orientation of $\boldsymbol{s}$ and $\boldsymbol{n}$. In the following, we will discuss the resulting corrections to the zero temperature spin mixing conductance $g^{\uparrow\downarrow}$ as well as introduce other purely temperature-induced interfacial spin transfer coefficients, the latter of which are of particular importance for this thesis.

Finite Temperature Spin Transfer for $\boldsymbol{s} \perp \boldsymbol{n}$

When the relative orientation is $\boldsymbol{s} \perp \boldsymbol{n}$, the spin mixing conductance must be corrected for finite temperature induced magnon bandstructure effects via the corresponding magnon density of states $g(\epsilon_m)$ and the Bose-Einstein distribution function $n_B(\epsilon_m, \mu, T) = (\exp[(\epsilon_m - \mu)/(k_B T)] - 1)^{-1}$ with the single particle magnon energy ϵ_m, the chemical potential μ and temperature T[10]. The result-

[10] The single particle magnon energy is given by the dispersion relation (cf. Ch. 2.2), which in its simplest form is given by $\epsilon_m(\boldsymbol{k}) = \hbar\omega_m(\boldsymbol{k}) = J_s k^2 + \Delta$. Here Δ is the magnon gap which is typically induced by internal magnetic anisotropy fields and/or externally applied magnetic fields.

ing *effective spin mixing conductance* including these temperature induced effects reads [88]

$$\tilde{g}_{\mathrm{r}}^{\uparrow\downarrow} = \left(1 - 2\frac{n_{\mathrm{m}}}{s}\right) g_{\mathrm{r}}^{\uparrow\downarrow} + \frac{2g_{\mathrm{r}}^{\uparrow\downarrow}}{s}\frac{\partial}{\partial\mu_{\mathrm{s}}} M_{\uparrow\downarrow}, \tag{2.30}$$

$$\tilde{g}_{\mathrm{i}}^{\uparrow\downarrow} = \left(1 - \frac{n_{\mathrm{m}}}{s}\right) g_{\mathrm{i}}^{\uparrow\downarrow}, \tag{2.31}$$

with

$$M_{\uparrow\downarrow} = \int_0^\infty \mathrm{d}\epsilon_{\mathrm{m}}\, g(\epsilon_{\mathrm{m}})(\epsilon_{\mathrm{m}} - \mu_{\mathrm{s}}) \left[n_{\mathrm{B}}(\epsilon_{\mathrm{m}}, \mu_{\mathrm{m}}, T_{\mathrm{m}}) - n_{\mathrm{B}}(\epsilon_{\mathrm{m}}, \mu_{\mathrm{s}}, T_{\mathrm{e}})\right], \tag{2.32}$$

where n_{m}/s indicates the ratio of the thermal magnon density n_{m} and the equilibrium spin density $s = S/a^3$ with S being the total (dimensionless) spin number in a unit cell of volume a^3. Furthermore, T_{m} and T_{e} are the temperatures of the magnon system in the MI and the electron system in the HM, respectively. One of the most crucial parameters is the magnon chemical potential μ_{m}, which is introduced in the equilibrium Bose-Einstein distribution function to account for non-equilibrium magnetic excitations, i.e. magnons, of the magnetic order [36, 88]. The introduction of a finite chemical potential μ_{m} into the equilibrium distribution function for magnons requires a very efficient and fast local equilibration of the magnon system, otherwise the assumption of an equilibrium-type distribution function is not valid[11] [88]. We immediately see that the ratio n_{m}/s in Eqs. (2.30) and (2.31) is introduced by finite temperature leading to thermal magnons which reduce the $T = 0$ spin mixing conductance $g^{\uparrow\downarrow}$. The contribution from Eq. (2.32) can be roughly understood as the total energy difference between the non-equilibrium magnons and the electronic spin accumulation at the interface. Hence, the derivative $\partial_{\mu_{\mathrm{s}}} M_{\uparrow\downarrow}$ is roughly equal to the non-equilibrium spin density difference Δn_{s} at the interface, such that the ratio $\Delta n_{\mathrm{s}}/s$ measures the relative change in spin torque due to the non-equilibrium spin density at the interface.

Finite Temperature Spin Transfer for $\boldsymbol{s} \parallel \boldsymbol{n}$

The finite temperature fluctuations also have an important influence for the interfacial spin transfer when the case of parallel orientation $\boldsymbol{n} \parallel \boldsymbol{s}$ is considered. Although the incident spin current polarization $\boldsymbol{s}$ cannot exert a static torque on $\boldsymbol{n}$ in this configuration, it can couple to the magnetic fluctuations as they represent an effective (transient) misalignment of $\boldsymbol{s}$ and $\boldsymbol{n}$, thus allowing for a finite torque. The resulting spin transfer across the interface is driven by the chemical potential difference $\Delta\mu = \mu_{\mathrm{m}} - \mu_{\mathrm{s}}$. Moreover, considering a finite interfacial temperature difference $\delta T = T_{\mathrm{m}} - T_{\mathrm{e}}$, spin is injected independent of $\boldsymbol{s}$ with spin polarization

[11] In actual thermal equilibrium, the magnon chemical potential $\mu_{\mathrm{m}} = 0$ since their particle number is not conserved.

along $\boldsymbol{n}$. The corresponding interfacial spin transfer efficiencies are termed as the *spin conductance* g and the *spin Seebeck coefficient* S and can be expressed as [88]

$$g = \frac{g_{\mathrm{r}}^{\uparrow\downarrow}}{\pi s} \frac{\partial}{\partial \mu_{\mathrm{m}}} M_{\uparrow\uparrow}, \tag{2.33}$$

$$S = \frac{g_{\mathrm{r}}^{\uparrow\downarrow}}{\pi s} \frac{\partial}{\partial T_{\mathrm{m}}} M_{\uparrow\uparrow}, \tag{2.34}$$

with

$$M_{\uparrow\uparrow} = \int_0^\infty \mathrm{d}\epsilon_{\mathrm{m}}\, g(\epsilon_{\mathrm{m}}) \epsilon_{\mathrm{m}} \left[n_{\mathrm{B}}(\epsilon_{\mathrm{m}}, \mu_{\mathrm{m}}, T_{\mathrm{m}}) - n_{\mathrm{B}}(\epsilon_{\mathrm{m}}, 0, T_{\mathrm{e}}) \right]. \tag{2.35}$$

Equations (2.33) and (2.34) represent purely thermally activated coefficients as they vanish for $T = T_{\mathrm{m}} = T_{\mathrm{e}} = 0$, while the effective spin mixing conductance shown in Eqs. (2.30) and (2.31) reduce to their familiar $T = 0$ value introduced in Eq. (2.29). The integral in Eq. (2.35) measures the total energy of the non-equilibrium magnon accumulation in the MI. Hence, the derivatives $\partial_{\mu_{\mathrm{m}}}$ and $\partial_{T_{\mathrm{m}}}$ of $M_{\uparrow\uparrow}$ in Eqs. (2.33) and (2.34) can be identified with the total non-equilibrium magnon density and non-equilibrium entropy density induced by a finite magnon chemical potential μ_{m} and temperature difference δT, respectively[12].

The interfacial spin transfer coefficients $\tilde{g}_{\mathrm{r}}^{\uparrow\downarrow}$, $\tilde{g}_{\mathrm{i}}^{\uparrow\downarrow}$, g and S can be explicitly calculated when we assume the simplest form of magnon dispersion according to $\epsilon_{\mathrm{m}}(\boldsymbol{k}) = \hbar\omega_{\mathrm{m}}(\boldsymbol{k}) = J_{\mathrm{s}} k^2 + \Delta$ (cf. Ch. 2.2). For the sake of simplicity, we will neglect the magnon gap Δ in the dispersion, which is a valid assumption for the limit of large temperatures $T \gg \Delta/k_{\mathrm{B}}$ [36]. The resulting magnon density of states then becomes $g(\epsilon_{\mathrm{m}}) = \frac{1}{4\pi^2} J_{\mathrm{s}}^{-3/2} \sqrt{\epsilon_{\mathrm{m}}}$. Using this, we can calculate explicit expressions for the integrals in Eqs. (2.32)-(2.35). While these integrals do have exact solutions, it is much more insightful to evaluate them in linear response, such that the spin transfer coefficients become independent of the driving forces. We thus obtain

$$\tilde{g}_{\mathrm{r}}^{\uparrow\downarrow} = \left(1 - 2\frac{n_{\mathrm{m}}}{s}\right) g_{\mathrm{r}}^{\uparrow\downarrow} - \frac{3 g_{\mathrm{r}}^{\uparrow\downarrow}}{s\Lambda^3} \zeta(3/2), \tag{2.36}$$

$$\tilde{g}_{\mathrm{i}}^{\uparrow\downarrow} = \left(1 - \frac{n_{\mathrm{m}}}{s}\right) g_{\mathrm{i}}^{\uparrow\downarrow}, \tag{2.37}$$

$$g = \frac{3 g_{\mathrm{r}}^{\uparrow\downarrow}}{2\pi s \Lambda^3} \zeta(3/2), \tag{2.38}$$

$$S = \frac{15 g_{\mathrm{r}}^{\uparrow\downarrow}}{4\pi s \Lambda^3} k_{\mathrm{B}} \zeta(5/2), \tag{2.39}$$

where $\zeta(x)$ is the Riemann-Zeta function and we introduced the thermal magnon (de-Broglie) wavelength $\Lambda = \sqrt{4\pi J_{\mathrm{s}}/(k_{\mathrm{B}} T)}$ [36]. In the calculation, we assumed an

[12] The identification of these quantities can be rationalized when we consider the total internal energy of the system and express it in terms of the grand canonical potential differential (at constant volume) $\mathrm{d}\Omega = -\mathcal{S}\,\mathrm{d}T - N\,\mathrm{d}\mu$ with $\mathcal{S}$ the entropy and N the particle number. The corresponding partial derivatives then become $\partial_\mu \Omega = -N$ and $\partial_T \Omega = -\mathcal{S}$.

efficient equilibration of the magnon system with the phonon bath, such that $T_\mathrm{m} = T_\mathrm{p} = T$ (with T_p the phonon temperature). This shows that the leading temperature dependence of the spin transfer coefficients is $\propto T^{3/2}$. By further using the explicit expression of the thermal magnon density $n_\mathrm{m} = \int_0^\infty \mathrm{d}\epsilon_\mathrm{m}\, g(\epsilon_\mathrm{m}) n_\mathrm{B}(\epsilon_\mathrm{m}, 0, T) = \Lambda^{-3}\zeta(3/2)$, we can reformulate $\tilde{g}_\mathrm{r}^{\uparrow\downarrow}$, g and S according to

$$\tilde{g}_\mathrm{r}^{\uparrow\downarrow} = \left(1 - 5\frac{n_\mathrm{m}}{s}\right) g_\mathrm{r}^{\uparrow\downarrow}, \tag{2.40}$$

$$g = \frac{3 g_\mathrm{r}^{\uparrow\downarrow}}{2\pi}\frac{n_\mathrm{m}}{s}, \tag{2.41}$$

$$S = \frac{15 g_\mathrm{r}^{\uparrow\downarrow}}{4\pi}\frac{\zeta(5/2)}{\zeta(3/2)} k_\mathrm{B}\frac{n_\mathrm{m}}{s}. \tag{2.42}$$

In this form, one can immediately see that all of the temperature induced corrections to the interfacial transport coefficients scale with the ratio of the thermally excited magnon density and the equilibrium spin density n_m/s.

We can now finally give an expression for the total spin current across an HM/MI interface including finite temperature effects. In Fig. 2.5**a-c**, a bilayer consisting of an MI with unit magnetic order vector $\boldsymbol{n}$ adjacent to a HM is depicted. For arbitrary directions of $\boldsymbol{n}$ and the spin polarization vector $\boldsymbol{s}$, the interfacial spin current across the interface (along $\hat{\boldsymbol{z}}$) according to Ref. [88] reads as[13]

$$\begin{aligned}\boldsymbol{j}_\mathrm{s,int}^z = &\frac{1}{4\pi}\left(\tilde{g}_\mathrm{i}^{\uparrow\downarrow} + \tilde{g}_\mathrm{r}^{\uparrow\downarrow}\boldsymbol{n}\times\right)\left(\boldsymbol{n}\times\mu_\mathrm{s}^0\boldsymbol{s} - \hbar\dot{\boldsymbol{n}}\right)\\ &+ \left[g(\mu_\mathrm{m}^0 - \mu_\mathrm{s}^0\boldsymbol{s}\cdot\boldsymbol{n}) + S(T_\mathrm{m} - T_\mathrm{e})\right]\boldsymbol{n},\end{aligned} \tag{2.43}$$

where the vector $\boldsymbol{j}_\mathrm{s,int}^z$ denotes the spin polarization direction with fixed spin current direction along $\hat{\boldsymbol{z}}$ as introduced in Eq. (2.16). For convenience, we denote the corresponding spin current direction vector as $\boldsymbol{j}_\mathrm{s,int} = j_{\mathrm{s,int}_i}^z\hat{\boldsymbol{z}}$, where $j_{\mathrm{s,int}_i}^z$ refers to the vector components $i \in x, y, z$ of Eq. (2.43). We have further defined the interfacial spin chemical potential μ_s^0 and interfacial magnon chemical potential μ_m^0, both of which denote the associated chemical potentials directly at the location of the interface and have to be derived from the spin/magnon diffusion Equations (2.23)/(2.60) assuming appropriate boundary conditions.

For the sake of a more intuitive understanding of the underlying physics involved in Eq. (2.43), we now discuss the individual terms in more detail. We first consider the contributions related to the $\boldsymbol{n}\times\mu_\mathrm{s}^0\boldsymbol{s}$ terms in the first line of Eq. (2.43). Evidently, these terms are only non-zero for $\boldsymbol{n}\perp\boldsymbol{s}$. In this case, the spin current carrying electrons scatter elastically off the interface performing a spin flip. Due to conservation of angular momentum, the excess spin angular momentum of $\hbar$ produced by the spin flip is transferred to the magnetic order by exerting the

[13] Different to Equation (4) of Ref. [88], we chose an opposed sign for the spin polarization $\boldsymbol{s}$ in Eq. (2.43), since we consider the actual spin direction as opposed to the associated magnetic moment.

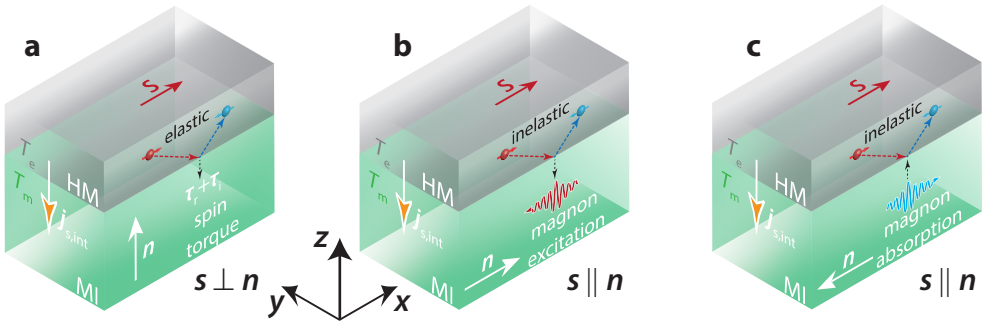

Fig. 2.5 – Interfacial spin-flip scattering processes of electron spins in a HM attached to a MI for finite temperature T. **a** For $\boldsymbol{s} \perp \boldsymbol{n}$, electrons scatter off the interface elastically while flipping their spin and emit their spin angular momentum to the MI. The magnetic order $\boldsymbol{n}$ therefore experiences the torques $\boldsymbol{\tau}_\mathrm{r}$ and $\boldsymbol{\tau}_\mathrm{i}$ according to Eq. (2.43). **a**,**b** The case $\boldsymbol{s} \parallel \boldsymbol{n}$ is shown for a parallel (**b**) and antiparallel (**c**) configuration. In both cases the electrons scatter off the interface inelastically while flipping their spin due to an interaction with the thermal magnon spectrum in the MI. As a result of conservation of spin angular momentum, magnons are excited in **b** and absorbed by the electron spin in **c**. Independent of the electron spins in the HM, a spin current can be injected thermally via a temperature difference between T_m and T_e.

torques $\boldsymbol{\tau}_\mathrm{r} \propto \tilde{g}_\mathrm{r}^{\uparrow\downarrow} \boldsymbol{n} \times (\boldsymbol{n} \times \boldsymbol{s})$ and $\boldsymbol{\tau}_\mathrm{i} \propto \tilde{g}_\mathrm{i}^{\uparrow\downarrow} (\boldsymbol{n} \times \boldsymbol{s})$. In a classical picture, the torque $\boldsymbol{\tau}_\mathrm{r}$ (commonly known as the Slonczewski-torque [89–91] or damping-like torque) is related to the dephasing of the scattered electron spin $\boldsymbol{s}$ due to its precession in the exchange field of $\boldsymbol{n}$ [62, 83] (see Fig. 2.6**a**). Since the scattered conduction electrons possess any wavevectors permitted by the Fermi surface, the phase of their precession is mostly random. The superposition of all possible electron scattering events therefore results in a loss of transverse spin momentum, which is transferred to the magnetic order by the torque $\boldsymbol{\tau}_\mathrm{r}$ (see Fig. 2.5**a**). In analogy to electrical transport, the dissipation of the spin magnetic moment via dephasing in the exchange field corresponds to the real part of the electrical interface impedance, i.e. the resistance. Both $\tilde{g}_\mathrm{r}^{\uparrow\downarrow}$ and the electrical resistance quantify the disspation of either spin angular momentum or moving electrical charge, respectively. The second torque contribution $\boldsymbol{\tau}_\mathrm{i}$ is also known as the field-like torque and results from an incomplete dephasing during the aforementioned precession of spin in the exchange field (see Fig. 2.6**b**). Consequently, the scattered spins retain a finite spin moment along their original direction $\boldsymbol{s}$ and thus exert a torque directly to $\boldsymbol{n}$, giving rise to the symmetry of $\boldsymbol{\tau}_\mathrm{i} \propto \boldsymbol{n} \times \boldsymbol{s}$. Comparing this to the more familiar electrical case, we can relate the lack of dephasing and thus dissipationless spin precession to the imaginary part of the electrical impedance, i.e. the reactance. Both $\tilde{g}_\mathrm{i}^{\uparrow\downarrow}$ and the reactance are measures for the dissipationless part of the transport of spin and charge, respectively. We note that the terms 'damping-like' ($\boldsymbol{\tau}_\mathrm{r}$) and 'field-like' ($\boldsymbol{\tau}_\mathrm{i}$) torque arise from the equivalent vector symmetries known from the Landau-Lifshitz-Gilbert equation [27, 92] introduced in Eq. (2.13), in particular from the Gilbert damping term and the term describing the precessional motion of magnetization in the effective field, respectively. The terms associated with the

time derivative $\dot{\boldsymbol{n}}$ in Eq. (2.43) account for the spin pumping contributions due to a coherent precession of the magnetic order [77, 93–98].

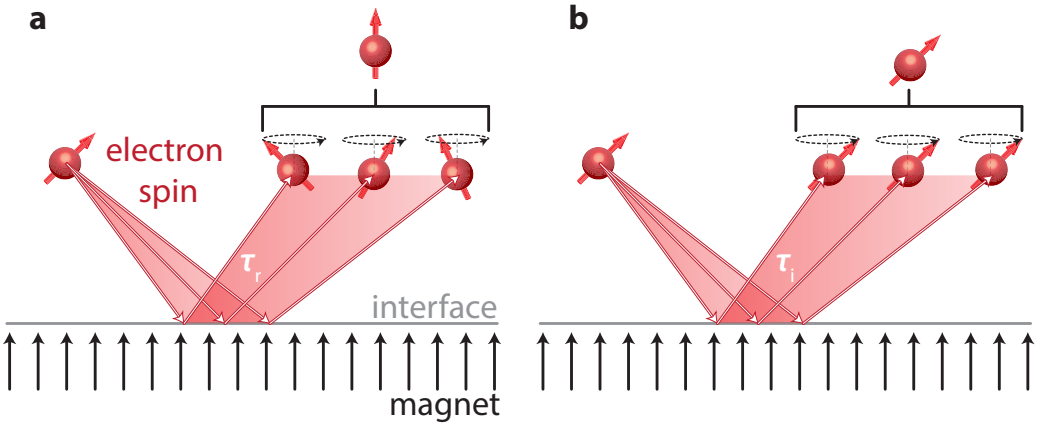

Fig. 2.6 – Classical illustration of spin torque at a magnetic interface. **a** The contribution $\boldsymbol{\tau}_r$ associated with the real part $g_r^{\uparrow\downarrow}$ of the spin mixing conductance is explained by the dephasing of scattered spins at the interface due to their precession in the exchange field. The scattered spins thereby lose their transverse spin momentum which is transferred to the magnetic order. **b** The torque $\boldsymbol{\tau}_i$ associated with the imaginary part $g_i^{\uparrow\downarrow}$ emerges due to an incomplete dephasing of the electron spins. Consequently, their spin is transferred as a direct torque to the magnetic order. Figure reproduced from [99].

The contribution proportional to the spin conductance g in the second line of Eq. (2.43) accounts for inelastic spin flip scattering events of the spin polarized electrons when $\boldsymbol{n} \parallel \boldsymbol{s}$ [88] (Fig. 2.5**b**, **c**). In this process, the scattered electrons partly release energy and transfer their spin angular momentum to excite or absorb a magnon in the thermal spectrum, giving rise to a non-equilibrium magnon accumulation/depletion at the interface (depending on whether $\boldsymbol{n}$ is parallel/antiparallel to $\boldsymbol{s}$) characterized by μ_m^0. Since this spin-flip scattering event is based on the interaction of an electronic spin with a thermally excited magnon state in the magnet, such spin injection is only possible at finite temperatures. Similarly, the term associated with S is also a finite temperature effect and is driven by a temperature difference between the magnon system with temperature T_m and the electron system with temperature T_e. The spin polarization of the corresponding spin current is given by $\boldsymbol{n}$ and is active for arbitrary relative orientations of $\boldsymbol{n}$ to $\boldsymbol{s}$. This temperature driven spin current across a MI/HM bilayer is generally known as the spin Seebeck effect (SSE) [100, 101].

2.6 Spin Hall Magnetoresistance

The spin Hall magnetoresistance (SMR) [33, 54, 102] appears as a resistance modulation in a heavy metal (HM) with finite spin Hall angle θ_{SH} attached to a magnetic insulator (MI). The physical origin of the effect is sketched in Fig. 2.7**a** and **b**. Upon applying a charge current to the HM layer along $\hat{\boldsymbol{x}}$, a spin current along $\hat{\boldsymbol{z}}$ with spin polarization $\boldsymbol{s} \parallel \hat{\boldsymbol{y}}$ emerges as a consequence of the spin Hall effect (cf. Ch. 2.4, Eq. (2.24)). Depending on the relative orientation of the magnetic order $\boldsymbol{n}$ with respect to $\boldsymbol{s}$, the interfacial spin current behaves in accordance with Eq. (2.43). For the sake of simplicity, we disregard finite temperature effects for the discussion of the SMR in the following [33, 103]. The effective spin mixing conductance thus reduces to its well-known zero temperature limit $\tilde{g}^{\uparrow\downarrow} = g^{\uparrow\downarrow}$, whereas the spin conductance and spin Seebeck coefficient vanish ($g = S = 0$). Eventually, the remaining equation for the interfacial spin current along $\hat{\boldsymbol{z}}$ reads

$$\boldsymbol{j}^{z}_{\mathrm{s,int}}(T=0) = \frac{1}{4\pi}\left(g_{\mathrm{i}}^{\uparrow\downarrow} + g_{\mathrm{r}}^{\uparrow\downarrow}\boldsymbol{n}\times\right)\left(\mu_{\mathrm{s}}^{0}\boldsymbol{s}\times\boldsymbol{n}\right), \tag{2.44}$$

where we assumed no coherent precession of $\boldsymbol{n}$, i.e. $\dot{\boldsymbol{n}} = 0$. We see that the interfacial spin current is now exclusively dependent on the real and imaginary part of the conventional spin mixing conductance $g^{\uparrow\downarrow}$. The interfacial spin current $\boldsymbol{j}^{z}_{\mathrm{s,int}}(T=0)$ is therefore zero when $\boldsymbol{n} \parallel \boldsymbol{s}$ (Fig. 2.7**a**) but finite for $\boldsymbol{n} \perp s$ (Fig. 2.7**b**). By changing the orientation of $\boldsymbol{n}$ relative to the injected spin polarization $\boldsymbol{s}$ (and thus also relative to the charge current direction $\boldsymbol{j}_{\mathrm{c}}$), we effectively change the boundary condition for $\boldsymbol{j}_{\mathrm{s,int}}$. This change finds its expression in a modulation of the longitudinal and transvere electrical resistivity ρ of the heavy metal layer, an effect which is generally known as the SMR. In this thesis, we restrict ourselves to the longitudinal resistivity modulation, which we discuss in more detail in the following. For $\boldsymbol{n} \parallel \boldsymbol{s}$, the SHE-induced spin current $\boldsymbol{j}_{\mathrm{s}}$ cannot enter the magnet (open circuit conditions) and thus a spin accumulation μ_{s}^{0} builds up at the interface (see Fig. 2.7**a**), which is similar to the creation of an opposing electric field in the case of charge transport. According to Eq. (2.18), the gradient $-\nabla\mu_{\mathrm{s}}$ drives an opposing spin current $\boldsymbol{j}_{\mathrm{s,back}}$ along the thickness of the HM, such that the total spin current $\boldsymbol{j}_{\mathrm{s,tot}} = \boldsymbol{j}_{\mathrm{s}} + \boldsymbol{j}_{\mathrm{s,back}} = 0$ (steady state condition). The complete blocking of the spin current across the HM/MI interface results in a resistivity equivalent to that of a bare HM layer. When the SHE-induced spin current can enter the magnetic material for $\boldsymbol{n} \perp \boldsymbol{s}$, a part of the initial charge current is dissipated/absorbed by the magnetic material via the spin torque on $\boldsymbol{n}$ (see Fig. 2.7**b**) and the subsequent dephasing of the transverse spin excitations in the MI. Consequently, the resistance of the HM layer adjacent to the MI is larger for this configuration as compared to that of a bare HM layer, where this spin dissipation channel is unavailable.

For the sake of a generally applicable nomenclature, we redefine the coordinate system shown in Fig. 2.7. Hence, we replace $\hat{\boldsymbol{x}}$ by the charge current direction

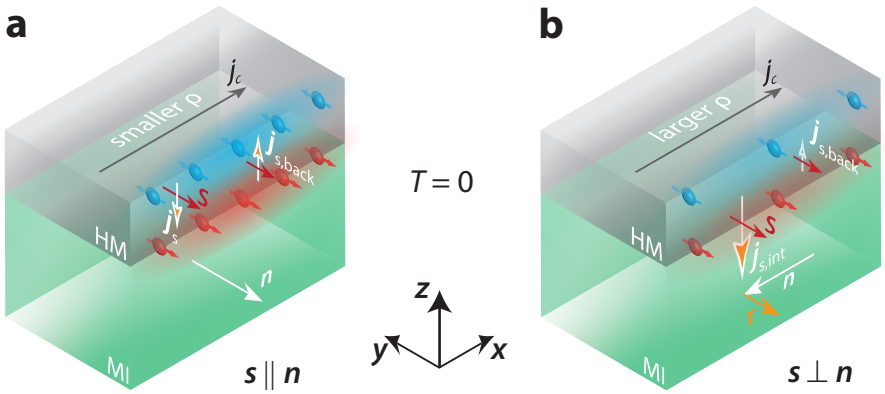

Fig. 2.7 – Dependence of the electrical resistivity ρ in a HM on the orientation of the magnetic order $\boldsymbol{n}$ in an attached MI. For the sake of simplicity, we here consider the case of $T = 0$. **a** For $\boldsymbol{s} \parallel \boldsymbol{n}$, the SHE-induced spin current $\boldsymbol{j}_\mathrm{s}$ cannot enter the MI. In steady state, the build up of the interfacial spin accumulation μ_s^0 leads to a diffusive spin current $\boldsymbol{j}_\mathrm{s,back}$ according to Eq. (2.18). The configuration is thus equivalent to a bare HM layer. **b** For $\boldsymbol{s} \perp \boldsymbol{n}$, the spin current enters the MI by exerting a torque $\boldsymbol{\tau} = \boldsymbol{\tau}_\mathrm{r} + \boldsymbol{\tau}_\mathrm{i}$. The spin accumulation at the interface is therefore decreased compared to the previous case and only a fraction of the incident spin current is compensated by the backflow drift current $\boldsymbol{j}_\mathrm{s,back}$, leading to a larger ρ.

$\boldsymbol{j}$ and $\hat{\boldsymbol{y}}$ by the in-plane direction transverse to $\boldsymbol{j}$ defined as $\boldsymbol{t} = \hat{\boldsymbol{z}} \times \boldsymbol{j}$. Taken together, the longitudinal resistivity ρ_long in a HM/MI bilayer as a function of the orientation of $\boldsymbol{n}$ becomes [102]

$$\rho_\mathrm{long} = \rho_0 + \Delta\rho(1 - {n_t}^2), \tag{2.45}$$

where ρ_0 corresponds to the resistivity of a bare HM layer and $\Delta\rho = \rho_\parallel - \rho_\perp$ is the SMR-induced resistivity change with $\rho_\parallel$ and $\rho_\perp$ being the HM resistances for $\boldsymbol{n} \parallel \boldsymbol{j}_\mathrm{c}$ and $\boldsymbol{n} \perp \boldsymbol{j}_\mathrm{c}$. For the $T = 0$ case considered here, $\rho_0 = \rho_\perp$. Finally, $n_t = \boldsymbol{n} \cdot \boldsymbol{t}$ denotes the projection of $\boldsymbol{n}$ along $\boldsymbol{t}$. Assuming $g_\mathrm{r}^{\uparrow\downarrow} \gg g_\mathrm{i}^{\uparrow\downarrow}$, the relative SMR amplitude can be calculated from the miscroscopic parameters as [33, 34]

$$\frac{\Delta\rho}{\rho_0} = \frac{{\theta_\mathrm{SH}}^2 (2 l_\mathrm{s}^2 \rho_\mathrm{e})(t_\mathrm{HM})^{-1} g_\mathrm{r}^{\uparrow\downarrow} \tanh^2\left(\frac{t_\mathrm{HM}}{2 l_\mathrm{s}}\right)}{\frac{h}{e^2} + 2 l_\mathrm{s} \rho_\mathrm{e} g_\mathrm{r}^{\uparrow\downarrow} \coth\left(\frac{t_\mathrm{HM}}{l_\mathrm{s}}\right)}, \tag{2.46}$$

where $\rho_\mathrm{e} = 1/\sigma_\mathrm{e}$ is the electrical resistivity of the HM and l_s its spin diffusion length. Measuring the SMR as a function of the HM thickness t_HM thus allows the determination of $|\theta_\mathrm{SH}|$ and l_s for a known $g_\mathrm{r}^{\uparrow\downarrow}$ [54, 104]. Vice versa, the SMR is also a great tool to determine $g_\mathrm{r}^{\uparrow\downarrow}$ for a given HM/MI interface when the HM parameters are well known, such as for platinum [104]. In this thesis, we use the SMR exclusively as a characterization tool and also restrict ourselves to yttrium iron garnet/platinum interfaces for which the assumption $g_\mathrm{r}^{\uparrow\downarrow} \gg g_\mathrm{i}^{\uparrow\downarrow}$ always holds [54, 82, 105]. In general, this assumption is however not valid. Recent studies in Pt attached to an europium-based MI for example even suggest $g_\mathrm{i}^{\uparrow\downarrow} \gg g_\mathrm{r}^{\uparrow\downarrow}$ [106].

Lifting the assumption that $T = 0$ results in a finite interfacial spin current injection into the magnet at finite temperature even for $\boldsymbol{n} \parallel \boldsymbol{s}$ since the finite temperature spin conductance $g > 0$. Due to the strong temperature dependence of g explicitly evaluated in Eq. (2.38), however, it is reasonable to assume $g^{\uparrow\downarrow} \gg g$ even at room temperature in most cases [36]. The above description of the SMR effect at $T = 0$ therefore represents an excellent approximation also for finite temperatures [54].

2.7 Charge Current Induced Magnon Excitation and Transport in Magnetic Insulator/Heavy Metal Bilayers

As introduced in Eq. (2.43), spin injection via a spin accumulation in metals adjacent to magnetic insulators is manifold and depends on both temperature as well as the relative orientation of the injected spin $\boldsymbol{s}$ and magnetic order vector $\boldsymbol{n}$. While we considered the zero temperature case for interfacial spin injection in the context of the SMR in Ch. 2.6, we here focus on finite temperatures enabling non-zero spin injection for $\boldsymbol{n} \parallel \boldsymbol{s}$ via the spin convertance g and for arbitrary directions of $\boldsymbol{n}$ via the spin Seebeck conductance S (cf. Eq. (2.43)). Although a spin torque from $\boldsymbol{s}$ on the magnetic order $\boldsymbol{n}$ is only present for $\boldsymbol{n} \perp \boldsymbol{s}$ (i.e. $\boldsymbol{s} \times \boldsymbol{n} \neq 0$), a finite (transient) misalignment between $\boldsymbol{s}$ and $\boldsymbol{n}$ is introduced via thermal fluctuations of $\boldsymbol{n}$, i.e. magnons, even for $\boldsymbol{n} \parallel \boldsymbol{s}$. Therefore, the electronic spin current couples to the thermal magnon spectrum for this configuration (cf. Ch. 2.5). It is important to emphasize that the injected spin excitations for $\boldsymbol{n} \parallel \boldsymbol{s}$ correspond to longitudinal excitations (i.e. along $\boldsymbol{n}$) of the magnetic order, which persist in the material according to the characteristic magnon lifetime τ_m scaling inversely with the magnon damping α_G given for a particular magnetic material. For $\boldsymbol{s} \perp \boldsymbol{n}$, the spin excitations correspond to transverse excitations of $\boldsymbol{n}$ and therefore dephase on a very short time/length scale due to fast precession in the strong exchange field [36, 107][14]. Magnons belong to longitudinal excitations of $\boldsymbol{n}$ by definition (cf. Ch. 2.2) and are therefore only excited in the $\boldsymbol{n} \parallel \boldsymbol{s}$ configuration. Considering the interfacial magnon flux $j_\mathrm{m,int} = \boldsymbol{j}^z_\mathrm{s,int} \cdot (-\boldsymbol{n})$[15] for $T > 0$, we obtain [88]

$$j_\mathrm{m,int} = -g(\mu^0_\mathrm{m} - \mu^0_\mathrm{s}\boldsymbol{s} \cdot \boldsymbol{n}) - S(T_\mathrm{m} - T_\mathrm{e}). \tag{2.47}$$

[14] The dephasing of transverse spin excitations in magnetic materials can be quantified by the spin coherence length λ_sc. For the case of transversely polarized electron spins entering a conducting magnet with peperpendicular magnetic order, it can be easily expressed as $\lambda_\mathrm{sc} = \pi/\left|k^\uparrow_\mathrm{F} - k^\downarrow_\mathrm{F}\right|$ [77, 108], where $k^{\uparrow,\downarrow}_\mathrm{F}$ are the Fermi wavevectors of the electronic spin-up and spin-down bands, respectively. Magnets with strong exhange splitting therefore have very short spin coherence lengths $\lambda_\mathrm{sc} \sim$ Å. A similar length scale can therefore be assumed for the case of transverse spin excitations in a MI.

[15] The minus sign between $j_\mathrm{m,int}$ and $\boldsymbol{j}^z_\mathrm{s,int}$ stems from the fact that the magnon magnetic moment is oriented antiparallely to the spin polarization $\boldsymbol{s}$. Hence, the magnon current carries magnetic moment along $-\boldsymbol{n}$.

This interfacial magnon current is composed of two contributions, which we refer to as the SHE-induced magnon injection (characterized by g) and thermally induced magnon injection (characterized by S). In the subsequent Section, these two components will be discussed in the context of a magnon injection/detection device in more detail.

2.7.1 Magnon Injection and Detection via Heavy Metal Electrodes

The main platform utilized for the magnon spin transport experiments in this thesis is discussed herein. The corresponding device is based on two HM electrodes attached to a MI as depicted in Fig. 2.8**a**. The left and right HM electrodes are used for the electrical injection as well as detection of magnons via the SHE and ISHE, respectively. This concept was initially introduced theoretically by Zhang and Zhang [109, 110] and later implemented experimentally by Cornelissen *et al.* [8] closely followed by Goennenwein *et al.* [9]. The injector serves as a spin current source by applying a charge current $\boldsymbol{j}_\mathrm{c}$ along the electrode and exploit the SHE to convert it to a transverse spin current $\boldsymbol{j}_\mathrm{s}$. As a result, spin polarized electrons approach the HM/MI interface. For $\boldsymbol{s} \parallel \boldsymbol{n}$, the spin current couples to the thermally occupied magnon states of the spectrum via g, resulting in a magnon current injection according to the first term of Eq. (2.47). In general, for multi-sublattice magnetic insulators with ferri- or antiferromagnetic order, the magnon system exhibits a non-trivial bandstructure [111]. In particular, due to the opposing magnetic sublattices in these systems, different chiralities and hence magnon polarizations exist simultaneously [13, 32, 111–115]. To generalize the spin current-induced magnon injection to a larger class of magnetic materials, we consider two magnon modes with opposite chiralities denoted as α- and β-modes. The α-mode refers to magnon excitations with magnetic moments opposite to $\boldsymbol{n}$, whereas the β-mode excitations are oriented along $\boldsymbol{n}$ [116]. For a parallel (antiparallel) orientation of $\boldsymbol{n}$ and $\boldsymbol{s}$, α-modes are excited (depleted), while β-modes are depleted (excited) [16]. A reversal of either $\boldsymbol{n}$ or $\boldsymbol{j}_\mathrm{c}$ (due to the SHE symmetry) can therefore switch between excitation or depletion of a particular magnon mode. The simultaneous excitation of one polarization of magnons and the depletion of the oppositely polarized ones effectively add up and lead to the same sign of the associated magnon spin current [117]. Due to the spatially confined magnon injection, a localized non-equilibrium magnon accumulation μ_m emerges and results in diffusive magnon currents driven by gradients in μ_m [8] (the associated magnon transport characteristics are discussed in detail in the subsequent Section). The diffusing magnon accumulation is converted to a spin accumulation μ_s at the interface of the detector which induces a spin current

[16] Note that due to the negative charge ($-e$) of electrons and thus the negative gyromagnetic ratio γ, the spin magnetic moment is opposite to the spin direction $\boldsymbol{s}$.

according to Eq. (2.18). Finally, this spin current is converted into a charge current via the ISHE flowing along the same direction as the injector current. In open circuit conditions, the current can be measured as a voltage drop V_{det} across the detector electrode (cf. Ch. 3.3 and 3.4). Due to the spin-to-charge conversion in the injector and the reciprocal process in the detector, the symmetry of the SHE is applied twice in the process. Hence, the injected and detected spin direction $\boldsymbol{s}$ (in turn given by the direction of $\boldsymbol{j}_{\mathrm{c}}$) determines the sign of the measured voltage signal, independent of whether $\boldsymbol{s}$ is parallel or antiparallel to $\boldsymbol{n}$. By changing the orientation of $\boldsymbol{n}$ with respect to $\boldsymbol{s}$, as typically conducted in angle dependent magnetotransport measurements, a 180°-symmetric modulation of the signal is expected.

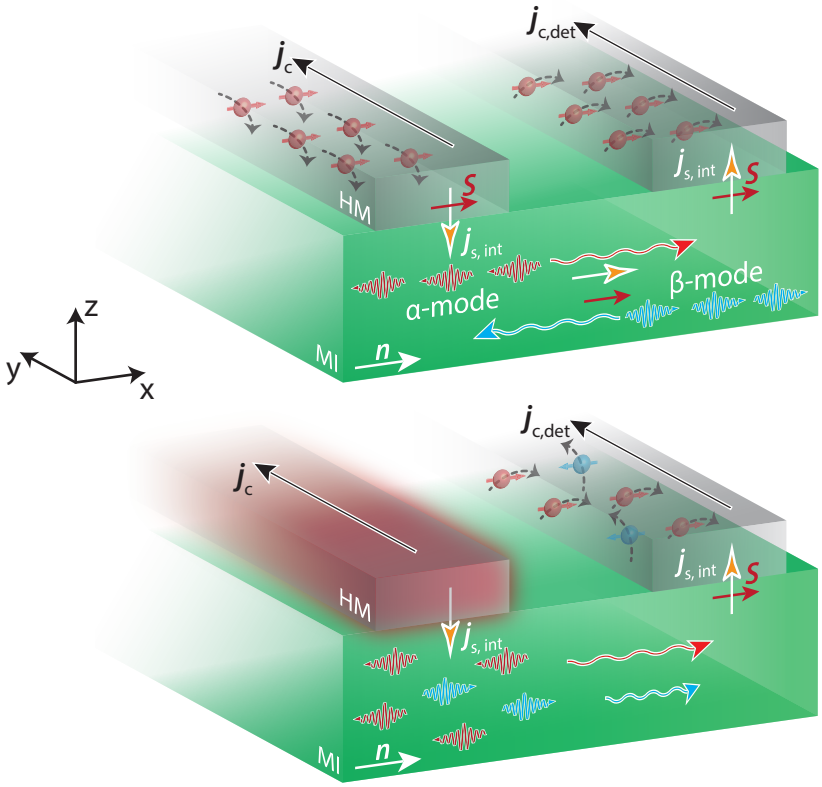

Fig. 2.8 – Magnon excitation and detection in two-terminal HM/MI heterostructures. A charge current $\boldsymbol{j}_{\mathrm{c}}$ in the left injector electrode injects magnons electrically (**a**) and thermally (**b**). The emerging magnon spin current in the MI is then converted to a charge current $\boldsymbol{j}_{\mathrm{c,det}}$ by the inverse SHE in the right detector. We consider the general case for ferri-/antiferro-magnetic systems hosting α- and β-modes with opposite chirality. **a** The SHE-induced spin current $\boldsymbol{j}_{\mathrm{s}}$ injects spin into the MI. For the given parallel orientation between $\boldsymbol{s}$ and $\boldsymbol{n}$, α-modes are excited, whereas β-modes are depleted (provided the presence of a finite thermal occupation of α- and β-modes in the MI). Both modes thus contribute positively to the emerging magnon spin current. **b** As a consequence of the current-induced Joule heating at the injector, both modes are excited simultaneously in the MI. An effective magnon spin current is thus only present for a finite imbalance regarding the occupation of the two opposing modes.

An additional magnon injection process is based on the Joule heating occuring inevitably as a consequence of the charge current applied to the injector (see Fig. 2.8**b**). Equation (2.43) accounts for this effect by the spin Seebeck coefficient S and a finite temperature difference between T_m and T_e at the interface induced by the current heating. Since the heating-induced injection is independent of $\boldsymbol{s}$, the magnon polarization is exclusively determined by the direction of $\boldsymbol{n}$. For the general case of two oppositely polarized magnon modes present in the system, both modes are excited simultaneously with an efficiency according to their thermal occupation [111, 112]. In case of collinear easy-axis antiferomagnets, the opposing magnon modes are degenerate and the effective thermally excited spin adds up to zero. Lifting the degeneracy results in a finite excess spin accumulation along $\boldsymbol{n}$ and therefore finite magnon spin transport. Such energy splitting is either induced by applying a field along the easy axis [114, 118], or by forcing a non-collinearity with an external field applied perpendicular to the sublattice magnetizations [117]. Non-trivial intrinsic magnetic interactions like the anisotropic exchange (usually known as the Dzyaloshinskii-Moriya interaction [119, 120]), dipolar interactions or certain anisotropies can also lead to an energy splitting of the magnon modes in more complex antiferromagnets [10, 32, 121]. For ferrimagnetic systems with opposing, but non-degenerate magnon modes the thermal occupation number of the individual magnon bands determines the effectively transported spin (particularly important for compensated ferrimagnets [112, 113]). In most conventional ferrimagnets, however, the magnetic structure can be treated as a single sublattice, quasi-ferromagnetic system, rendering the incorporation of both magnon modes redundant. The transport of thermally injected magnons is initiated due to a local increase in the magnon chemical potential as well as the magnon temperature [36, 122]. Consequently, magnon transport is driven by a gradient in μ_m as well as T_m (see Ch. 2.7.2 for details). Indeed, it was shown from multiple experimental studies that the long distance transport of thermally excited magnons has significant contributions from gradients in μ_m and T_m [122–124]. The temperature difference between phonons and magnons in the bulk of the material, on the other hand, plays a secondary role for magnon transport [36, 122, 125]. Moreover, the heating at the injector also changes the temperature profile across the complete device due to pure heat currents, which induces an interfacial temperature difference between T_m and T_e at the detector and drives an interfacial spin Seebeck current according to Eq. (2.43). This local spin Seebeck-type contribution due to a temperature difference at the detector was, however, estimated to have a minor effect on the transport signals [124]. Overall, the thermal contribution of the magnon transport is expected to be mainly composed of bulk magnon currents induced by gradients in the magnon chemical potential and temperature. The superposition of these effects is sensed in the detector via the inverse SHE. Since the thermal magnon transport voltage at the detector simply follows the orientation of $\boldsymbol{n}$, only the ISHE symmetry at the detector gives rise to an angle dependence, resulting in a

360°-symmetric angular modulation of the signal. Thermally induced voltage signals at the detector can therefore be easily distinguished from the 180°-symmetric electrical signals.

2.7.2 Magnon Transport

Due to the incoherent excitation processes of thermal magnons discussed in the preceding Section, the non-equilibrium magnon accumulation μ_m is expected to exhibit a broad range of mean free paths. Instead of describing spin wave propagation of certain frequency and wavevector, one must therefore take into account the transport of a large magnon ensemble with broad spectral range. To this end, we use the theoretical framework of Boltzmann transport theory describing the spatial and temporal dynamics of non-equilibrium distribution functions [36, 109, 110]. The following introduction to diffusive magnon transport closely follows the analysis conducted in Ref. [70], first established in Ref. [36].

For a simple (exchange dominated) quadratic magnon dispersion $\epsilon_\mathrm{m}(\boldsymbol{k}) = \hbar\omega_\mathrm{m}(\boldsymbol{k}) = \hbar\gamma\mu_0 H + J_\mathrm{s}k^2$, the Boltzmann transport equation for the position vector $\boldsymbol{r}$, wavevector $\boldsymbol{k}$ and time t dependent magnon distribution function $f(\boldsymbol{r}, \boldsymbol{k}, t)$ reads[17]

$$\frac{\partial f}{\partial t} + \frac{1}{\hbar}\frac{\partial \epsilon_\mathrm{m}(\boldsymbol{k})}{\partial \boldsymbol{k}} \cdot \nabla_{\boldsymbol{r}} f = \left.\frac{\partial f}{\partial t}\right|_\mathrm{scatt}, \tag{2.48}$$

where $\left.\frac{\partial f}{\partial t}\right|_\mathrm{scatt}$ accounts for the equilibration of f via magnon scattering. Note, that we have disregarded a contribution due to magnon relaxation into the HM attached to the MI. We now apply the well-known relaxation time approximation for the scattering rate according to

$$\left.\frac{\partial f}{\partial t}\right|_\mathrm{scatt} = -\sum_i \frac{f - \overline{f}_i}{\tau_i} \tag{2.49}$$

with $\overline{f}_i$ the quasi-equilibrium distribution function of a subsystem i to which the magnons relax into and τ_i the corresponding relaxation times with $i \in \{\mathrm{mm}, \mathrm{mp}, \mathrm{el}, \mathrm{mr}\}$. As detailed in Ref. [36], the subscripts denote different characteristic magnon relaxation mechanisms referring to either magnon number conserving scattering events or magnon number non-conserving events. Magnon-conserving scattering events are parametrized by magnon-magnon scattering ($i = \mathrm{mm}$), magnon-conserving magnon-phonon scattering ($i = \mathrm{mp}$) and the elastic magnon-defect scattering ($i = \mathrm{el}$). Magnon non-conserving processes are

[17] We have neglected the additional 'field-term' $1/\hbar\nabla_{\boldsymbol{r}}\epsilon_\mathrm{m}(\boldsymbol{k}) \cdot \nabla_{\boldsymbol{k}} f(\boldsymbol{r}, \boldsymbol{k}, t)$ in the Boltzmann equation [26], since we have $\nabla_{\boldsymbol{r}}\epsilon_\mathrm{m}(\boldsymbol{k}) = 0$ in our case. The latter expression might become non-zero when the magnon energy is altered by an energy $\delta\epsilon_\mathrm{m} = -\boldsymbol{m}_\mathrm{m} \cdot \boldsymbol{B}$ via a magnetic flux density $\boldsymbol{B} = \mu_0 \boldsymbol{H}$ interacting with the magnon magnetic moment $\boldsymbol{m}_\mathrm{m}$, resulting in a magnetic force $\boldsymbol{F}_\mathrm{m} = -\nabla_{\boldsymbol{r}}\delta\epsilon_\mathrm{m} = \nabla_{\boldsymbol{r}}(\boldsymbol{m}_\mathrm{m} \cdot \boldsymbol{B})$. Since we work with spatially homogeneous magnetic fields in our experiment, however, we expect $\boldsymbol{F}_\mathrm{m} = -\nabla_{\boldsymbol{r}}\delta\epsilon_\mathrm{m} = 0$ [126].

captured by the magnetic Gilbert damping α_G which corresponds to magnon scattering with the phonon bath ($i = \mathrm{mr}$). Assuming thermal magnons with energy at $k_B T$, the relaxation time of the latter can thus be approximated by $\tau_{\mathrm{mr}} \approx \hbar/(\alpha_G k_B T)$. For most magnetic systems relevant for this type of magnon transport, we can assume $\tau_{\mathrm{mr}} \gg \tau_{\mathrm{mm}}, \tau_{\mathrm{mp}}$, whereas τ_{mp} governs the relaxation regarding magnon-conserving scattering. For the widely used ferrimagnetic insulator yttrium iron garnet, τ_{mr} has been estimated to be about 2-3 orders of magnitude larger than the magnon-conserving scattering times [36]. The latter therefore dominates magnon scattering for this system. Furthermore, the quasi-equilibrium distributions $\overline{f}_i$ are given by Bose-Einstein distribution functions of the form $n_B(\epsilon_m, \mu_m, T) = (\exp[(\epsilon_m(\boldsymbol{k}) - \mu_m)/k_B T] - 1)^{-1}$, in particular [36]

$$\overline{f}_{\mathrm{mm}} = n_B(\epsilon_m, \mu_m, T_m), \tag{2.50a}$$
$$\overline{f}_{\mathrm{mp}} = n_B(\epsilon_m, \mu_m, T_p), \tag{2.50b}$$
$$\overline{f}_{\mathrm{el}} = n_B(\epsilon_m, \mu_m, T_m), \tag{2.50c}$$
$$\overline{f}_{\mathrm{mr}} = n_B(\epsilon_m, 0, T_p). \tag{2.50d}$$

For magnon-conserving relaxation with $i \in \{\mathrm{mm}, \mathrm{mp}, \mathrm{el}\}$, $\overline{f}_i$ is characterized by $\mu_m \neq 0$ (magnon accumulation unaffected), while for magnon non-conserving relaxation with $i \in \{\mathrm{mr}\}$ it follows $\mu_m = 0$ (magnon accumulation relaxed). The magnon temperature T_m has been substituted into the equilibrium distribution $\overline{f}_i$ for $i \in \{\mathrm{mm}, \mathrm{el}\}$ (representing magnon relaxation within the magnon system), while the phonon temperature T_p was substituted into $\overline{f}_i$ for $i \in \{\mathrm{mr}, \mathrm{mp}\}$ (due to magnon relaxation into the phonon bath). In our rather simplified analysis here, however, we assume $T = T_p = T_m$ (referring to the assumption that the magnons are equilibrated with the phonons at all times). This is a reasonable assumption as the magnon temperature equilibration to the phonon bath occurs on typical length scales of $\sim 1\,\mathrm{nm}$ [36, 125]. For steady state conditions, Eq. (2.48) can be solved by the linear addition of a non-equilibrium distribution $g(\boldsymbol{k})$ and equilibrium distribution according to $f(\boldsymbol{r}, \boldsymbol{k}, t) = g(\boldsymbol{k}) + n_B(\epsilon_m(\boldsymbol{k}), \mu_m(\boldsymbol{r}), T(\boldsymbol{r}))$, where $n_B = (\exp[(\epsilon_m(\boldsymbol{k}) - \mu_m(\boldsymbol{r}))/k_B T(\boldsymbol{r})] - 1)^{-1}$ is the Bose-Einstein distribution function with space-dependent magnon chemical potential $\mu_m(\boldsymbol{r})$ and temperature $T(\boldsymbol{r})$. Substituting this ansatz together with the corresponding relaxation times and equilibrium subsystem distributions $\overline{f}_i$ into Eqs. (2.48) and (2.49), the non-equilibrium distribution evaluates to

$$\begin{aligned} g(\boldsymbol{k}) = \tau_m &\left(-\frac{\partial n_B(\epsilon_m(\boldsymbol{k}), \mu_m, T)}{\partial \epsilon_m(\boldsymbol{k})}\right) \frac{1}{\hbar} \frac{\partial \epsilon_m(\boldsymbol{k})}{\partial \boldsymbol{k}} \\ &\times \left[-\nabla \mu_m(\boldsymbol{r}) - \frac{\epsilon_m(\boldsymbol{k}) - \mu_m}{T} \nabla T(\boldsymbol{r})\right], \end{aligned} \tag{2.51}$$

where $(\tau_\mathrm{m})^{-1} = \sum_i (\tau_i)^{-1}$ is the total magnon scattering time. To arrive at this result, we assumed $\tau_\mathrm{mr} \gg \tau_\mathrm{m}$, representing a reasonable assumption as stated above. Having determined the non-equilibrium $\boldsymbol{k}$-vector distribution of the magnons (under the assumption of a non-uniform spatial distribution of both μ_m and T), the associated magnon spin current density can be written as

$$\boldsymbol{j}_\mathrm{m} = \hbar \int \frac{\mathrm{d}\boldsymbol{k}}{(2\pi)^3} g(\boldsymbol{k}) \frac{1}{\hbar} \frac{\partial \epsilon_\mathrm{m}(\boldsymbol{k})}{\partial \boldsymbol{k}}, \tag{2.52}$$

where we assumed each magnon to carry a spin of $\hbar$, leading to a magnon current given in units of $\mathrm{J/m^2}$ equivalent to the unit we chose for spin currents. The energy carried by each magnon is given by $\epsilon_\mathrm{m}(\boldsymbol{k}) - \mu_\mathrm{m}$, leading to a heat current density according to

$$\boldsymbol{j}_\mathrm{h} = \int \frac{\mathrm{d}\boldsymbol{k}}{(2\pi)^3} g(\boldsymbol{k}) (\epsilon_\mathrm{m}(\boldsymbol{k}) - \mu_\mathrm{m}) \frac{1}{\hbar} \frac{\partial \epsilon_\mathrm{m}(\boldsymbol{k})}{\partial \boldsymbol{k}}, \tag{2.53}$$

which is given in units of $\mathrm{J/(m^2 s)}$. As already indicative in Eq. (2.51), the magnon spin and heat currents are driven by $\nabla \mu_\mathrm{m}$ and ∇T, resulting in the transport equations

$$\begin{pmatrix} \boldsymbol{j}_\mathrm{m} \\ \boldsymbol{j}_\mathrm{h} \end{pmatrix} = - \begin{pmatrix} \sigma_\mathrm{m} & \hbar L/T \\ L & \kappa_\mathrm{m} \end{pmatrix} \begin{pmatrix} \nabla \mu_\mathrm{m} \\ \nabla T \end{pmatrix}, \tag{2.54}$$

where the 2×2 matrix contains the linear response transport coefficients, i.e. the magnon conductivity σ_m, the bulk spin Seebeck coefficient L[18] and the magnon heat conductivity κ_m. These coefficients can be derived by evaluating the $\boldsymbol{k}$-vector integration in Eqs. (2.52) and (2.53) in linear response. For a simple quadratic magnon dispersion $\epsilon_\mathrm{m}(\boldsymbol{k}) = J_\mathrm{s} k^2$ with vanishing magnon gap Δ (which is a valid approximation for large temperatures $k_\mathrm{B} T \gg \Delta$), we obtain[19]

$$\sigma_\mathrm{m} = 2.4556 \frac{8}{\sqrt{2\pi}} \frac{\tau_\mathrm{m} J_\mathrm{s}}{\hbar \Lambda^3} = 3\hbar \frac{n_\mathrm{m} \tau_\mathrm{m}}{m_\mathrm{m}}, \tag{2.55}$$

$$L = 1.57622 \frac{16}{\sqrt{2\pi}} \frac{\tau_\mathrm{m} J_\mathrm{s} k_\mathrm{B} T}{\hbar^2 \Lambda^3} = 3.85134 \cdot k_\mathrm{B} T \frac{n_\mathrm{m} \tau_\mathrm{m}}{m_\mathrm{m}}, \tag{2.56}$$

$$\kappa_\mathrm{m} = 2.31681 \frac{32}{\sqrt{2\pi}} \frac{\tau_\mathrm{m} J_\mathrm{s} k_\mathrm{B}^2 T}{\hbar^2 \Lambda^3} = 11.3218 \cdot k_\mathrm{B}^2 T \frac{n_\mathrm{m} \tau_\mathrm{m}}{m_\mathrm{m}}, \tag{2.57}$$

[18] Note that the bulk spin Seebeck coefficient L [127] represents the response function to temperature gradients and magnon chemical potential gradients for magnon currents and heat currents in a MI, respectively. It should not be confused with the interfacial spin Seebeck coefficient S introduced in Eq. (2.43), which measures the spin transfer efficiency across a HM/MI interface due to a finite temperature difference.

[19] For the evaluation of Eqs. (2.52) and (2.53), we switch to an integral over ϵ_m and identify $\frac{\partial n_\mathrm{B}(\epsilon_\mathrm{m}, \mu_\mathrm{m}, T)}{\partial \epsilon_\mathrm{m}} \frac{\partial \epsilon_\mathrm{m}}{\partial k} = -\frac{2\sqrt{J_\mathrm{s} \epsilon_\mathrm{m}}}{k_\mathrm{B} T} \frac{1}{4} \operatorname{csch}^2((\epsilon_\mathrm{m} - \mu_\mathrm{m})/(2k_\mathrm{B} T))$. We then substitute $x = (\epsilon_\mathrm{m} - \mu_\mathrm{m})/(2k_\mathrm{B} T)$ for the integration.

where we assumed $\mu_m \approx 0$ for linear response solutions. The numerical prefactors stem from integrals of the form $\int_0^\infty dx\, x^{n/2}\, \mathrm{csch}^2(x)$ with $n \geq 3$ and we used the effective magnon mass $m_m = \hbar^2/(2J_s)$ introduced in Ch. 2.2. The magnon conductivity σ_m, bulk spin Seebeck coefficient L and magnon heat conductivity κ_m are given in units of $1/m$, $1/(m \cdot s)$ and $J/(K \cdot m \cdot s)$, respectively. We note that σ_m in Eq. (2.55) shares a striking similarity to the conventional Drude model [128, 129] for electrical transport. In the conventional Drude-model, the electrical conductivity is given by $\sigma_e = e^2 n\tau/m_e$ with n, τ and m_e the electron density, scattering time and mass, respectively[20]. For the experiments conducted in this thesis, we almost exclusively consider the magnon spin current $\boldsymbol{j}_m$ driven by the magnon chemical potential gradient $\nabla\mu_m$. Indeed, temperature driven magnon spin currents have been characterized as a minor correction for sufficiently large length scales, at least for the SHE-induced signals [36, 115]. The thermally induced magnon transport, on the other hand, does exhibit considerable contributions from temperature gradients via the bulk spin Seebeck coefficient L [123, 124]. Since the thermal signals are not the main focus in this work, we omit a further analysis of the heat currents or temperature driven effects in the following. In order to get access to the spatial profile of μ_m for a given boundary condition in our magnetic system, we ought to derive the corresponding magnon spin diffusion equation. To this end, we exploit the continuity equation for $\boldsymbol{j}_m$ according to

$$\frac{\partial \rho_m}{\partial t} + \nabla \cdot \boldsymbol{j}_m = -\Gamma_{mr}\, \rho_m, \tag{2.58}$$

where Γ_{mr} is the magnon relaxation rate and ρ_m refers to the non-equilibrium magnon spin density given in units of Js/m^3. Note, that the right side of the magnon continuity equation is non-zero, reflecting their non-conserved nature parametrized by Γ_{mr}. Calculating ρ_m in linear response results in

$$\begin{aligned} \rho_m = \hbar \Delta n_m &= \hbar \int_0^\infty d\epsilon_m\, g(\epsilon_m) \left[n_B(\epsilon_m, \mu_m, T) - n_B(\epsilon_m, 0, T) \right] \\ &\approx \hbar \frac{\zeta(1/2)}{\Lambda^3 k_B T} \mu_m, \end{aligned} \tag{2.59}$$

where Δn_m is the non-equilibrium magnon number density and we identify $\partial\rho_m/\partial\mu_m = \hbar\zeta(1/2)/(\Lambda^3 k_B T)$. Combining Eqs. (2.54), (2.58) and (2.59) finally leads to the magnon spin diffusion equation

$$\frac{\partial \mu_m}{\partial t} - D_m \nabla^2 \mu_m = -\frac{\mu_m}{\tau_{mr}}, \tag{2.60}$$

where $D_m = \sigma_m \left(\partial\rho_m/\partial\mu_m\right)^{-1}$ is the magnon diffusion constant and $\tau_{mr} = \Gamma_{mr}^{-1}$ is the magnon spin lifetime parametrizing the scattering time for magnon non-

[20] Since the magnon current density is defined as $\boldsymbol{j}_m = -\sigma_m \nabla\mu_m$ as compared to electrical currents with $\boldsymbol{j}_c = -(-\sigma_e/e)\nabla\mu$, the transport quantities e and $\hbar$ appear with different powers in the electrical conductivity and magnon conductivity, respectively.

conserving processes as introduced before. In analogy to the spin diffusion equation discussed in Ch. 2.3, we can define the magnon diffusion length $\lambda_\mathrm{m} = \sqrt{D_\mathrm{m}\tau_\mathrm{mr}}$, up to which the magnon number is mostly conserved[21]. An analytical solution to Eq. (2.60) in steady state (by setting $\partial\mu_\mathrm{m}/\partial t = 0$) is only possible in one dimension, but is sufficient to highlight the most important features of the spatial characteristics of diffusive magnon transport. To this end, we consider a magnon transport structure as depicted in Fig. 2.8. Following Ref. [8], we further consider the one-dimensional magnon transport along the spatial coordinate x and apply the boundary conditions $\mu_\mathrm{m}(x=0) = \mu_\mathrm{m}^0$ and $\mu_\mathrm{m}(x=d) = 0$ with μ_m^0 being the magnon accumulation at $x = 0$ and d the distance between injector and detector. The latter boundary condition assumes a complete absorption of the magnon accumulation at the detector. As a result, we obtain for the magnon spin current $j_\mathrm{m}(d) = -D_\mathrm{m}\frac{\partial\mu_\mathrm{m}(d)}{\partial d} = -2D_\mathrm{m}\frac{\mu_\mathrm{m}^0}{\lambda_\mathrm{m}}\exp(d/\lambda_\mathrm{m})/(1-\exp(2d/\lambda_\mathrm{m}))$, which is plotted as a function of d/λ_m in Fig. 2.9 (black solid line). Evaluating the limiting case for $d \ll \lambda_\mathrm{m}$ gives a spatial decay of the current according to $1/(2d)$ (green dashed line), which corresponds to an electron-like diffusion without relaxation of magnon spin. It can thus be treated equivalently to an ohmic-like charge transport, i.e. a linear relation between $\boldsymbol{j}_\mathrm{m}$ and $\nabla\mu_\mathrm{m}$ via a constant σ_m can be assumed. For $d \gg \lambda_\mathrm{m}$, the magnon number n_m (and thus σ_m) decreases, leading to an exponential transport scaling as $\exp(-d/\lambda_\mathrm{m})$ (orange dashed line). Distance dependent measurements of the magnon transport signal measured with devices as depicted in Fig. 2.8 therefore allow an easily-accessible way to quantify λ_m in magnetic insulators.

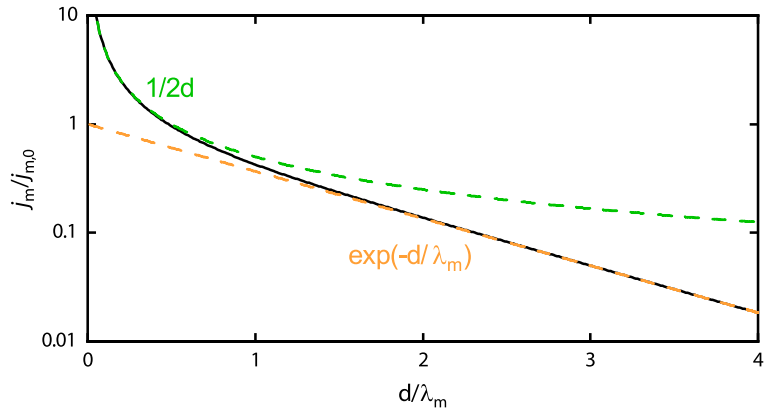

Fig. 2.9 – Expected decay of the normalized magnon spin current j_m as a function of the injector-detector distance d derived from the magnon diffusion Equation (2.60). For $d \ll \lambda_\mathrm{m}$, the decay can be well described by a $1/(2d)$ relation, wheras for $d \gg \lambda_\mathrm{m}$ an exponential decay according to $\exp(-x/\lambda_\mathrm{m})$ ensues.

[21] Using the average thermal magnon velocity $v_\mathrm{th} = \frac{1}{n_\mathrm{m}}\int_0^\infty \mathrm{d}\epsilon_\mathrm{m}\, g(\epsilon_\mathrm{m}) n_\mathrm{B}(\epsilon_\mathrm{m}, 0, T) 1/\hbar \frac{\partial\epsilon_\mathrm{m}}{\partial \boldsymbol{k}} = 2\pi^{3/2}\sqrt{J_\mathrm{s} k_\mathrm{B} T}/(3\zeta(3/2)\hbar)$, we can express the magnon diffusion length as $\lambda_\mathrm{m} \sim v_\mathrm{th}\sqrt{\tau_\mathrm{m}\tau_\mathrm{mr}}$ (omitting numerical prefactors).

We want to point out that the above description is essentially also applicable to antiferromagnetic insulators (AFIs). As for that matter, individually defined magnon spin chemical potentials and temperatures of the two oppositely polarized α- and β-modes have to be considered (cf. Ch. 2.7.1) [116]. While the magnon transport in an easy-axis antiferromagnet can be well described with the magnon chemical potential based approach discussed above [117], much more complicated transport ensues for non-trivial antiferromagnetic spin textures [13]. This additional complexity is induced by magnetic interactions that break the rotational symmetry about the magnetic order $\boldsymbol{n}$ of the AFI. Such symmetry breaking results in a coupling between the oppositely polarized magnon modes and allows for arbitrary superposition states of the two basis modes. The transport of such a coupled antiferromagnetic magnon system can be very conveniently described via the concept of magnonic pseudospin [10]. The theoretical and experimental features of this antiferromagnetic pseudospin transport are investigated in detail in Ch. 6.

Experimental Details

3

In this Chapter, we present the experimental details necessary for the comprehension of the results discussed in the subsequent Chapters. Starting from the used material systems in Ch. 3.1, we also introduce the nanofabrication of the samples in Ch. 3.2 as well as the experimental setup and measurements techniques in Chs. 3.3 and 3.4, respectively.

3.1 Material Systems

Mainly, two insulating magnetic materials have been investigated in this work: the ferrimagnet yttrium iron garnet (YIG) and the antiferromagnet hematite. In the following, we present the detailed crystalline and magnetic properties of both materials.

3.1.1 Ferrimagnetic Insulator Yttrium Iron Garnet

The crystal structure of the magnetic insulator $Y_3Fe_5O_{12}$ is body-centered-cubic (bcc) featuring a conventional unit cell with a lattice constant $a = 12.38\,\text{Å}$ [130, 131] that contains 4 times the formula unit [132]. The yttrium Y^{3+} ions are dodecahedrally coordinated and due to its completely filled shells the electron configuration carries no net magnetic moment. The finite net magnetic moment in YIG therefore originates from two octahedrally coordinated Fe^{3+} ions (FeA) and three tetrahedrally coordinated Fe^{3+} ions (FeD) per formula unit. A simulation of the middle layer of the YIG unit cell is shown in Fig. 3.1. Each of the magnetic iron ions carries a finite spin number of $S = 5/2$. The magnetic sublattices corresponding to the FeA and FeD moments are antiferromagnetically exchange coupled within the sublattices with exchange energies $J_{AA} = -0.92 \times 10^{-21}\,\text{J}$ and $J_{DD} = -3.24 \times 10^{-21}\,\text{J}$ [7], while the inter-sublattice exchange with $J_{AD} = -9.6 \times 10^{-21}\,\text{J}$ [7] is also antiferromagnetic. Since the latter is by far dominating, the intra-sublattice spins orient themselves parallel to each other to satisfy the dominating inter-sublattice exchange, making the overall spin structure simply equal to two antiferromagnetically coupled sublattices (cf. Fig. 3.1). Due to this strong antiparallel coupling of the sublattices, which persists up to external magnetic fields of 250 T [133,134], YIG is mostly treated as a single sublattice ferromagnet with its total magnetization $\boldsymbol{M}$ characterized by its net magnetization $\boldsymbol{M}_{\text{Fe,net}} = \boldsymbol{M}_{\text{FeA}} + \boldsymbol{M}_{\text{FeD}}$. The strong antiferromagnetic coupling is also responsible for the large magnetic ordering temperature (Curie Temperature) $T_C = 559\,\text{K}$. The magnetic anisotropy of YIG is governed by a crystalline cubic anisotropy [135], which determines the magnetic easy and hard axes for the magnetization direction. The corresponding anisotropy

field is in the order of a few mT in bulk crystals [136]. All YIG crystals studied in this thesis are in the thin-film limit ($\leq 1\,\mu m$), leading to the existence of an additional shape anisotropy with a magnetic hard axis pointing out-of-plane.

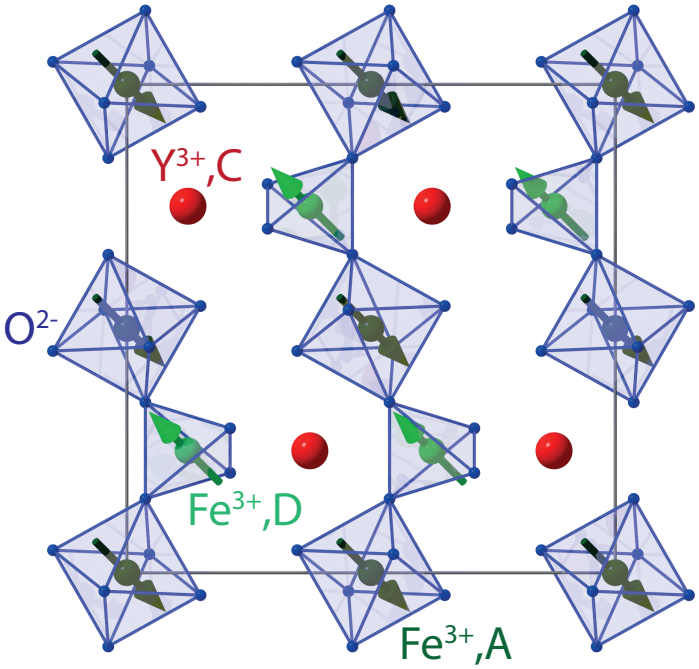

Fig. 3.1 – Simulation of the middle layer of the cubic unit cell of YIG. The magnetic sublattices are composed of octahedrally coordinated Fe^{3+} ions (FeA) and tetrahedrally coordinated Fe^{3+} ions (FeD) (courtesy of Stephan Geprägs, WMI).

Most prominently, YIG is known for its record low magnetic damping coefficient reaching values of $\alpha_G = 4 \times 10^{-5}$ in bulk crystals [136–138]. In general, thin films of YIG exhibit larger values of approximately 1×10^{-4} due to surface defects and inhomogeneities [137, 139, 140]. In Chapter 5, we study the ultra-thin limit in the order of $\sim 10\,nm$, which are grown via pulsed laser deposition (PLD) at the Walther-Meißner-Institut (WMI). Here, the magnetic damping increases to the low 1×10^{-3} regime. The generally low magnetic damping in YIG films enables the efficient and long-distance transport of spin for both incoherently [8, 9] and coherently excited spin waves [141].

3.1.2 Antiferromagnetic Insulator Hematite

The antiferromagnetic insulator hematite (α-Fe_2O_3) crystallizes in the so-called corundum structure with a conventional unit cell featuring the lattice constants $a = 5.04\,\text{Å}$ and $c = 13.77\,\text{Å}$ [142], containing 6 times the formula unit. This structure may also be described as a slightly distorted hexagonal system of oxygen atoms, where only every sixth layer along the hexagonal [0001]-direction is lying directly on top of each other. The Fe^{3+} ions are situated in between the (0001) oxygen layers in the octahedral interstices (spanned by the oxygen ions), of which only two-thirds are occupied in each layer, thus lowering the symmetry to a trigonal structure. The corresponding crystal structure is simulated in Fig. 3.2**a** in side view, where the trigonal unit cell of the crystal is indicated by the thick connector lines. A top view of the crystal is shown in Fig. 3.2**b**.

The first five nearest neighbours of the magnetic Fe^{3+} ions with $S = 5/2$ exhibit the relevant exchange coupling strengths [143]. Among them, the dominating energies are given by the antiferromagnetic exchange couplings of the third and fourth nearest neighbours with $J_3 = -4.69 \times 10^{-22}\,\text{J}$ and $J_4 = -3.17 \times 10^{-22}\,\text{J}$ [143], respectively [143]. This roughly gives an equivalent exchange field of $\mu_0 H_\text{E} = 900\,\text{T}$ [143, 144]. Due to its antiferromagnetic nature, the orientation of the two sublattice magnetizations $\boldsymbol{m}_1$ and $\boldsymbol{m}_2$ of hematite is characterized by the Néel vector $\boldsymbol{n} = \boldsymbol{m}_1 - \boldsymbol{m}_2$.

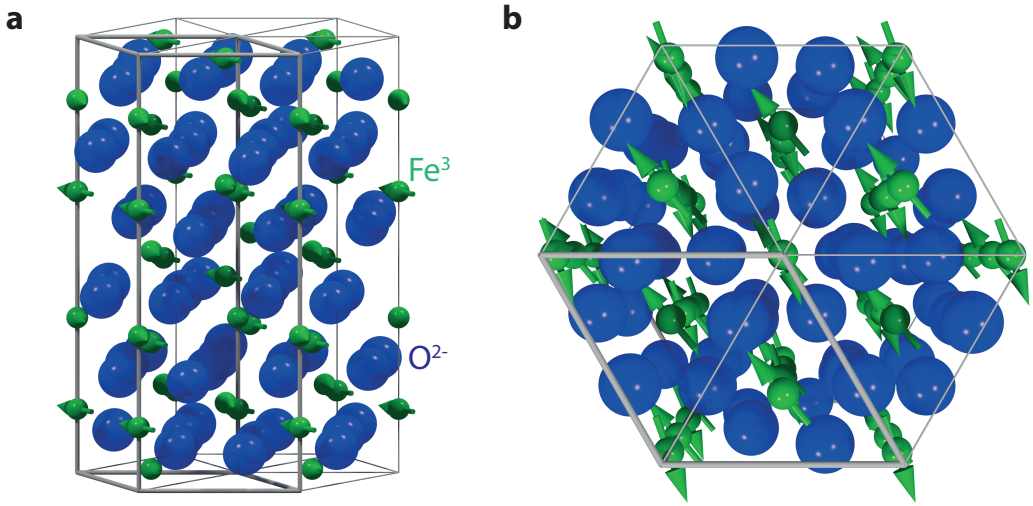

Fig. 3.2 – Simulation of the corundum crystal structure of α-Fe_2O_3. Side (**a**) and top (**b**) view of the structure are shown. The trigonal unit cell is indicated by the thick connector lines, three of which make up the hexagonal conventional cell (courtesy of Stephan Geprägs, WMI).

In bulk crystals, hematite exhibits a Néel temperature of $T_\text{N} = 953\,\text{K}$ and undergoes a spin reorientation, the so-called Morin transition, at $T_\text{M} \approx 263\,\text{K}$ [142, 145]. This transition is characterized by a sign change of the uniaxial magnetic anisotropy, resulting in a transition from a magnetic easy (0001)-plane above T_M to a magnetic easy (0001)-axis below T_M. Additionally, the sublattice magnetizations

lying in the (0001)-plane above T_M are subject to a slight canting due to the finite Dzyaloshisnkii-Moriya-Interaction (DMI) with the DMI-vector pointing along the (0001)-direction. The canting leads to a finite net magnetic moment $\boldsymbol{m}_{net}$ perpendicular to the Néel order $\boldsymbol{n}$. The trigonal symmetry of the crystal also leads to a threefold crystalline anisotropy in the easy-plane phase [146], resulting in the formation of an equal distribution of 120°-domains in the film.

In this thesis, we investigate hematite thin films in the ultra-thin limit of the order of $\sim$ 10 nm to $\sim$ 100 nm grown on sapphire substrates (Al_2O_3) via PLD at the WMI. In this limit, our films exhibit no Morin transition over the investigated temperature range of 100 K to 300 K. Instead, our films remain in the easy-plane phase for all temperatures, therefore showing a finite magnetic moment due to the DMI-induced canting of the sublattices. To verify this magnetic behaviour, we performed SQUID (superconducting quantum interference device) magnetometry using a 90 nm-thick film (which ensures a larger magnetic moment as compared to the thinner 15 nm-thick film used in Ch. 6) prepared using the same parameters as the film investigated in Ch. 6. The measured magnetic moment in the (0001)-plane is shown as a function of the in-plane magnetic field in Fig. 3.3 for several temperatures. For each measurement, a linear (diamagnetic) background was subtracted from the data. Clearly, the data shows a finite magnetic moment as well as a hysteretic behaviour. This finding supports the finite canting of the sublattice moments, which is only present for $T > T_M$ (above the Morin-transition) due to the perpendicular configuration of the in-plane oriented magnetic sublattice spins and the out-of-plane oriented DMI vector [142]. The hysteretic behaviour can be explained by the three-fold easy-plane anisotropy due to the crystal structure with trigonal symmetry [142], leading to the formation of 120° domain walls [147, 148]. Increasing magnetic fields $\mu_0 H$ lead to a growth of domains with a perpendicular orientation of their Néel vector $\mathbf{n}$ to $\mathbf{H}$ with a monodomainization field of $\mu_0 H_{MD} = 600$ mT [148]. This monodomainization field agrees reasonably well with our magnetic hysteresis curve, exhibiting a closure of the hysteresis at approximately 700 mT. Hence, the measured hysteresis behaviour supports the expected domain configuration of the hematite above the Morin transition [146, 149].

Different to the expected behaviour of bulk hematite, we do not observe any indication of a Morin transition in the temperature range from 100 K to 300 K. This feature is not yet entirely clear. Although recent reports also indicate a strong decrease (up to a complete absence) of the Morin transition temperature T_M for thin film hematite [150, 151] and relate this to strain-induced change of the magnetic anisotropy, we cannot support this explanation for our films. This is due to the fact that we observe a complete relaxation of the hematite films grown on the sapphire substrates - even for films as thin as $\sim$ 5 nm. Hence, strain induced changes should play a minor role. A more accurate explanation might be an unintended Al doping of the hematite during the growth process, the reason being an interdiffusion of Al

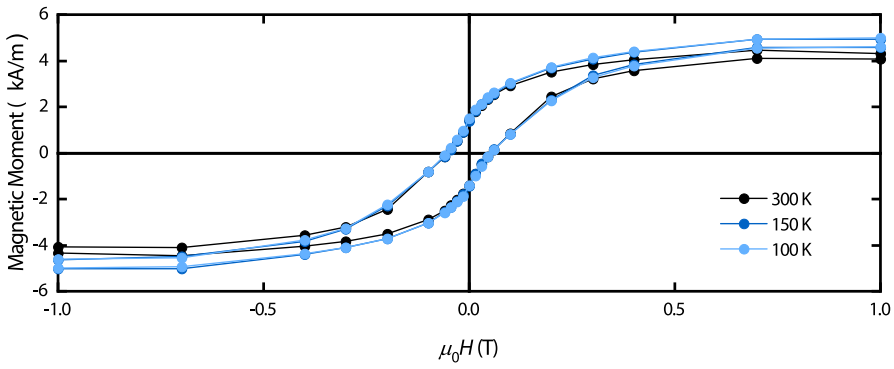

Fig. 3.3 – In-plane SQUID magnetometry measurement of a 90 nm-thick film of (0001)-oriented hematite. The magnetic hysteresis curves are recorded for different temperatures. Clearly, we observe the weak ferromagnetic moment corresponding to the small canting of the magnetic sublattices above T_M.

stemming from the Al_2O_3 (sapphire) substrate. As shown previously in Ref. [146], the Morin transition temperature does indeed significantly decrease when hematite is doped with Al. In the thin film regime considered here, even a slight doping of Al atoms may have a large impact due to the large relative increase thereof. A verification of this explanation, however, requires an element-specific measurement of the Al content in the hematite, which is beyond the scope of this work.

3.2 Sample Fabrication and Layout

The magnon transport experiments presented in Chapter 5 utilize YIG thin films grown via PLD on a (100)-oriented Gadolinium-Gallium-Garnet (GGG) substrate. Furthermore, we use a commercially availabe YIG film grown via liquid phase epitaxy (LPE) in Chapter 4. The antiferromagnetic insulator hematite (α-Fe_2O_3) used in Chapter 6 is also grown via PLD on a (0001)-oriented sapphire (Al_2O_3) substrate at the WMI. In order to inject and detect magnon spin currents into our magnetic insulators, we employ the spin Hall effect (SHE) in either heavy non-magnetic metals or ferromagnetic metals (cf. Ch. 2.4). To this end, we apply these thin metallic films via sputter deposition on the magnetic insulators and pattern them into nanowires via electron beam lithography[22] and lift-off techniques.

The magnetic insulator samples are cleaned in acetone and isopropanol (IPA) in an ultrasonic bath for at least 2 min in each solution. Then, after the samples are blow-dried with nitrogen, they are spin coated with different resist layers and baked on a hotplate after each coating (fabrication parameters and resist types are summarized in Table 3.1). Note, that due to the insulating nature of the substrates

[22] For electron beam lithography, the *NanoBeam nB5* system from *NanoBeam Ltd.* is used, which we operate at a beam voltage of 80 kV.

a conductive resist (*PMMA-Electra 92*[23], see 3.1) has to be applied on top of each of the resist layers to avoid surface charging effects that significantly deteriorate the writing process. After writing the sample, the conductive resist has first to be removed by rinsing it in deionized water (H_2O) for approximately $\sim$ 20 sec and blow-drying therafter. For each resist used in this work, the samples are then developed in the *AR 600-56* developer from Allresist (developing times are listed in Table 3.1), after which the developing reaction is stopped by rinsing the sample twice in IPA for 30 sec altogether. Lift-off is conducted by applying the samples in an acetone bath heated up to 70° and leaving them in the the solution for at least 15 min. After gently pipetting the sample to enhance the lift-off effect, it is finally put into the ultrasonic bath for 1 min at the lowest possible ultrasonic power level to remove any metallic residues.

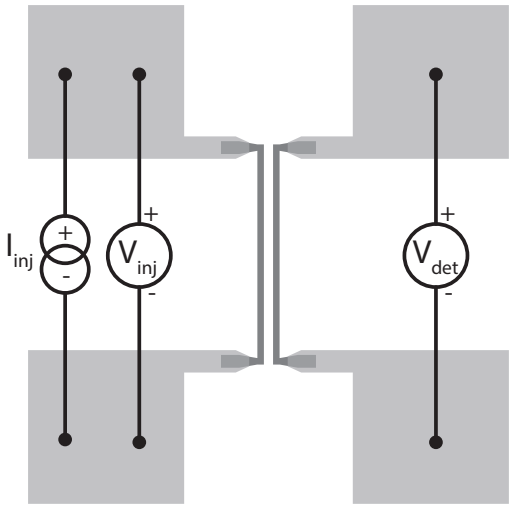

Fig. 3.4 – Schematic illustration of a patterned structure with two nanostrips. Light gray colored shapes are the Al bondpads and leads, dark gray shapes are the nanostrips made of different materials. The left strip is typically used as the injector, whereas the right strip is employed as the detector.

A typical structure consisting of two nanostrip electrodes (injector and detector) is shown in Fig. 3.4. In detail, the whole fabrication process consists of (at least) three deposition/lithography steps: in the first step, we typically apply $\sim$ 45 nm of Platinum (Pt) onto our films via sputter deposition. These are patterned into alignment/-focus markers situated on the corners of the sample. The markers are used for focussing of the electron beam as well as for aligning the structures of the subsequent nanostructures. Different metallic films are then patterned into strips of lengths between 50 µm to 162 µm and widths between 100 nm to 1 µm. Subsequently, we apply a $\sim$ 50 nm thick layer of Aluminum (Al) which is patterned into leads and bonding pads to connect the nanostrips electrically. The detailed fabrication/lithography parameters as well as the applied resists are summarized in Table 3.1.

[23] Model: AR-PC 5090.02

	alignment/focus markers
resist layers	*PMMA/MA33%/PMMA-Electra 92*
spin coating	4000 rpm, 1 min/4000 rpm, 1 min
bake temperature	170°/90°
bake time	2 min/2 min
base dose	$3.0\,\mathrm{C\,m^{-2}}$
development time	90 sec
	nanostrip electrodes and leads/bondpads
resist layers	*PMMA 600K/PMMA 950K/PMMA-Electra 92*
spin coating	4000 rpm, 1 min/4000 rpm, 1 min/4000 rpm, 1 min
bake temperature	170°/170°/90°
bake time	5 min/5 min/2 min
base dose	$5.6\,\mathrm{C\,m^{-2}}$(for GGG)/$7.4\,\mathrm{C\,m^{-2}}$(for Al_2O_3)
development time	120 sec

Tab. 3.1 – Summary of the lithography parameters for the fabrication of nanostructured electrodes allowing the injection and detection of magnon spin in magnetic insulators.

3.3 Experimental Setup

The finalized nanostructured samples are glued on a chip carrier and wire bonded in a 4-point configuration as depicted in Fig. 3.4. For measurements, the sample is attached to a dipstick equipped with DC measurement wires and placed in a variable temperature insert (VTI) ($2\,\mathrm{K} \leq T \leq 300\,\mathrm{K}$) of a superconducting magnet cryostat at the WMI. There are three different superconducting magnet cryostat setups available at the WMI: (i) a 3D-vector magnet consisting of three superconducting Helmholtz coils reaching magnetic field strengths of up to $\mu_0 H = 2.5\,\mathrm{T}$ in the horizontal plane and up to $\mu_0 H = 6\,\mathrm{T}$ in the vertical direction, (ii) a superconducting solenoid with a field strength of up to $\mu_0 H = 7\,\mathrm{T}$ with the possibity to rotate the sample via an electronic stepper motor and (iii) a superconducting solenoid capable of large field strengths of up to $\mu_0 H = 15\,\mathrm{T}$. For the standard magnon transport measurements, we apply a charge current I_{inj} of either DC-type (Ch. 3.4.1) or low frequency AC-type (Ch. 3.4.2) to the injector electrode and measure the voltage output at the detector. For the DC measurements, we usually also record the local voltage drop V_{inj} at the injector, which allows us to characterize various magnetoresistance contributions such as the SMR (see Ch. 2.6). Typically, we perform angle dependent magnetotransport measurements on our samples by rotating either the external magnetic field $\mu_0 H$ around the sample (setup (i)) or the sample itself within a static magnetic field (setup (ii)). Rotations can be done in three different orthogonal planes. In this thesis, however, we exclusively investigate *in plane* rotations around the axis normal to the film plane.

3.4 Measurement Techniques

The current densities J_{inj} applied to the nanostrip injectors are in the order of $1 \times 10^{10}\,\mathrm{A\,m^{-2}} \leq J_{\mathrm{inj}} \leq 5 \times 10^{11}\,\mathrm{A\,m^{-2}}$, resulting in typical power densities of $5 \times 10^{9}\,\mathrm{W\,m^{-2}}$ to $1.25 \times 10^{13}\,\mathrm{W\,m^{-2}}$. Thus, besides electrically excited effects due the charge current flow, also thermal effects due to the dissipated power become significant in our measurements. In order to discern electrically and thermally excited effects, two main measurement techniques have been implemented for magnetotransport measurements, which are presented in the following.

3.4.1 DC Technique: Current Reversal Method

Via this method, DC currents of positive ($+I_{\mathrm{inj}}$) and negative ($-I_{\mathrm{inj}}$) polarity are applied subsequently to the injector. The corresponding voltage drops $V^{+}_{\mathrm{inj/det}}$ and $V^{-}_{\mathrm{inj/det}}$ at the injector/detector are recorded accordingly. Since electrical voltage contributions $V^{\mathrm{el}}_{\mathrm{inj/det}}$ switch sign under polarity change (i.e. $V^{\mathrm{el}}_{\mathrm{inj/det}}$ is proportional to odd powers of I_{inj}) and thermal voltages $V^{\mathrm{th}}_{\mathrm{inj/det}}$ are even under current reversal (i.e. $V^{\mathrm{th}}_{\mathrm{inj/det}}$ is proportional to even powers of I_{inj}) we can calculate the contributions as

$$V^{\mathrm{el}}_{\mathrm{inj/det}} = \frac{V^{+}_{\mathrm{inj/det}} - V^{-}_{\mathrm{inj/det}}}{2} \tag{3.1}$$

$$V^{\mathrm{th}}_{\mathrm{inj/det}} = \frac{V^{+}_{\mathrm{inj/det}} + V^{-}_{\mathrm{inj/det}}}{2}. \tag{3.2}$$

For the usual DC transport measurements, we use a Keithley 2400 Sourcemeter to feed current through the injector and measure the respective voltages at both the injector and detector with a Keithley 2182 Nanovoltmeter [24]. To enhance signal-to-noise ratio, we repeat the current reversal for (typically) $n_{\mathrm{rev}} = 5$ times for each external parameter setting (i.e. magnetic field magnitude, direction, current amplitude etc.). The electrical and thermal voltage contributions are calculated via Eqs. (3.1) and (3.2) and the arithmetic mean over the $n_{\mathrm{rev}} = 5$ cycles is taken for each contribution. Another advantage of this method is the correction of thermal drifts that arise on a timescale of seconds, which might be related to e.g. the rotation of the dipstick in the He exchange gas of the cryostat.

[24] Typical settings for the Keithley 2182 voltage measurements are: *resolution*: 7.5 digits, *repeating filter count*: 30, *number of power line cycles*: 2.

3.4.2 AC Technique: Lock-In Detection

Instead of applying DC currents of different polarity, another method is to apply low-frequency AC currents to the injector and measure the frequency-sensitive voltage response at the detector via a lock-in detection scheme. For this purpose, we apply AC currents in the frequency range between $\sim 7\,\mathrm{Hz}$ to $\sim 13\,\mathrm{Hz}$. In particular, we choose the frequency f such that $f \neq n \cdot 50\,\mathrm{Hz}$ (with $n \in \mathbb{N}$), ensueing that it does not coincide with multiples of the frequency of the AC power outlets. Furthermore, we use very low frequency 'quasi-DC' currents, assuring that we have negligible capacitive/inductive coupling between the nanostrips, which otherwise might overshadow the magnon transport signals.

In the experiment, we apply a sinusoidal AC current $I_{\mathrm{inj}}(t) = I_0 \sin(\omega t)$ with $\omega = 2\pi f$ and I_0 the injected peak current amplitude. Correspondingly, the emerging current at the detector oscillates with the same frequency and can be written as $I_{\mathrm{det}}(t) = I_1 \sin(\omega t + \phi)$, where I_1 is the detector current amplitude and ϕ is a finite phase delay observed in our experiments, which will be discussed later in this Section. The measured voltage response $V_{\mathrm{det}}(t)$ at the detector can then generally be written as

$$V_{\mathrm{det}}(t) = R_1 I_{\mathrm{det}}(t) + R_2 I_{\mathrm{det}}^2(t) + R_3 I_{\mathrm{det}}^3(t) + \mathcal{O}(I_{\mathrm{det}}^4(t)), \tag{3.3}$$

where we only consider powers up to third order. The coefficients R_1, R_2 and R_3 parametrize the conversion processes involved in the magnon transport from injector to detector. With the lock-in detection method, the n^{th} harmonic voltage signal $V^{n\omega}$ is measured by multiplying $V_{\mathrm{det}}(t)$ with two sinusoidal reference signals $\propto \sin(n\omega t)$ and $\propto \cos(n\omega t)$ (i.e. shifted by 90°) that are in phase with the injected current $I_{\mathrm{inj}}(t)$. In the next stage, the multiplied signals are integrated over a time interval $T \gg 1/\omega$ via low-pass filtering. Thus, $V^{n\omega}$ is given by the two quadratures

$$V_{\mathrm{X}}^{n\omega} = \frac{\sqrt{2}}{T} \int_t^{t+T} \sin\left(n\omega t'\right) V_{\mathrm{det}}(t')\, \mathrm{d}t', \tag{3.4}$$

$$V_{\mathrm{Y}}^{n\omega} = \frac{\sqrt{2}}{T} \int_t^{t+T} \cos\left(n\omega t'\right) V_{\mathrm{det}}(t')\, \mathrm{d}t' \tag{3.5}$$

denoted by the subscripts X and Y. Plugging Eq. (3.3) into Eqs. (3.4) and (3.5), the first three harmonic voltages become

$$V_{\mathrm{X}}^{1\omega} = \frac{1}{\sqrt{2}} \left(I_1 R_1 + \frac{3}{4} I_1^3 R_3 \right) \cos(\phi) \qquad V_{\mathrm{Y}}^{1\omega} = \frac{1}{\sqrt{2}} \left(I_1 R_1 + \frac{3}{4} I_1^3 R_3 \right) \sin(\phi) \tag{3.6}$$

$$V_{\mathrm{X}}^{2\omega} = \frac{1}{2\sqrt{2}} I_1^2 R_2 \sin(2\phi) \qquad V_{\mathrm{Y}}^{2\omega} = -\frac{1}{2\sqrt{2}} I_1^2 R_2 \cos(2\phi) \tag{3.7}$$

$$V_X^{3\omega} = \frac{1}{4\sqrt{2}} I_1^3 R_3 \cos(3\phi) \qquad V_Y^{3\omega} = \frac{1}{4\sqrt{2}} I_1^3 R_3 \sin(3\phi). \tag{3.8}$$

Evidently, the first harmonic voltage signals (Eqs. (3.6)) correspond to effects that are odd under current reversal (i.e. odd powers in I_{det}), while the second harmonic contributions (Eqs. (3.7)) represent effects that are even under current reversal (i.e. even powers in I_{det}). Notably, there is a finite third harmonic voltage contribution present in the first harmonic voltage signals. In most experiments, however, we observe $V_X^{3\omega} = V_Y^{3\omega} = 0$ for sufficiently small injector currents I_{inj}, inferring that $R_3 = 0$. Hence, the lock-in detection represents a very sensitive and suitable tool to distinguish between electrically and thermally generated effects in magnetotransport measurements.

The finite phase delay ϕ that we have considered in the detector current $I_{\mathrm{det}}(t)$ leads to a distribution of the signal into both the X and Y quadratures of the harmonic voltages. In order to account for the full signal response in only one of the quadratures, we apply a rotation matrix to our signals and thus calculate the rotated quadratures X' and Y':

$$\begin{pmatrix} V_{X'}^{n\omega} \\ V_{Y'}^{n\omega} \end{pmatrix} = \begin{pmatrix} \cos n\phi & \sin n\phi \\ -\sin n\phi & \cos n\phi \end{pmatrix} \begin{pmatrix} V_X^{n\omega} \\ V_Y^{n\omega} \end{pmatrix}. \tag{3.9}$$

The phase delay ϕ is iteratively determined by applying the rotation matrix to the first harmonic voltages ($n = 1$) for different values of ϕ until there is no finite signal left in the Y quadrature. Notably, the n^{th} harmonic voltages have to be rotated by $n\phi$ to get the full signal response in either of the two quadratures (cf. Eqs. (3.6)-(3.8)).

We use a HF2LI 50 MHz Lock-In Amplifier from Zurich Instruments to simultaneously record the first, second and third harmonic voltage at the detector. The voltage signals are preamplified by a SR560 Low Noise Preamplifier. Furthermore, the AC injector current is generated by a Keithley 6221 DC and AC Current Source, which is triggered by the digital output of the HF2LI. Hence, the current source and the reference signal of the lock-in are synchronized to ensure no drifting of the relative phase between source and reference. Although the source and the reference signal are supposed to be in phase, a finite phase delay can still be present due to different trigger conditions of the Keithley 6221 Source and the HF2LI. Moreover, the phase delay could also be accumulated at the voltage preamplifier. Finally, one could think of a phase shift stemming from the magnon transport between injector and detector. The exact identification of the origin of ϕ, however, requires a careful consideration of all of the possible sources, which is not necessary for the analysis of the data presented in this thesis.

4 Manipulation of Magnon Transport in YIG via the Magnetic Metal Alloy $Co_{25}Fe_{75}$

The spin Hall effect (SHE) is at the origin of a plethora of transport effects relevant for spintronic applications [12, 43, 54, 65, 152–156]. Its efficiency to convert charge to spin currents is conveniently expressed in terms of the phenomenological spin Hall angle θ_{SH}, the microscopic origin of which is rooted in the spin-orbit interaction causing spin-selective scattering of charge carriers [44, 155]. Many ferromagnetic metals exhibit a strong spin-orbit coupling, which manifests itself in various electrical transport effects, among them the anomalous Hall effect (AHE) [157]. The AHE hinges on the same physical principles as the SHE [153, 155]. While the transverse charge current arising in the AHE has been studied for more than a century, the pure spin current part has only very recently received broad attention [65, 68, 69, 152, 158, 159]. Generally speaking, the time reversal symmetry breaking due to the finite magnetic order in ferromagnetic crystals leads to magnetization dependent spin currents and thus allows for a convenient control of spin currents by magnetic fields [63, 69, 160].

Recent developments in magnetotransport experiments with incoherent magnons (the quantized excitations of the spin lattice) [8, 9, 161, 162] offer a suitable platform for the investigation of the SHE and the anomalous spin Hall effect (ASHE) in ferromagnets [65, 66, 152, 163, 164]. In a recent work, Das et al. reported spin injection and detection in YIG via the ASHE [157] using Py electrodes [65]. Here, a tunable spin injection/detection efficiency of the permalloy (Py) electrodes via the orientation of the magnetization in Py was observed. This is attributed to the gradually increasing anomalous spin Hall effect (ASHE) in Py, which is enhanced as the external magnetic field is saturating the magnetization. Moreover, it was found that Py exhibits a finite contribution purely stemming from the spin Hall effect (SHE), rather than only the ASHE (see also Ch. 2.4.2).

In this Chapter, we investigate the influence of spin current injection and detection into YIG via the ferromagnetic metal-alloy cobalt-iron ($Co_{25}Fe_{75}$) [28, 165]. In particular, we report on the determination of the anomalous spin Hall angle θ_{ASH} in $Co_{25}Fe_{75}$ (CoFe) [165] via all-electrical magnon transport measurements in the magnetic insulator YIG (cf. Ch. 2.7). For this purpose, we utilize a multi-terminal structure with four metallic electrodes – one made of CoFe and three made of Pt – deposited onto a YIG thin film. Our experiments reveal a negative anomalous spin Hall angle in the ferromagnetic CoFe, but a vanishing contribution of the magnetization-independent spin Hall angle. Upon applying a spin-resistor

model to our multiterminal spin transport structure, we are able to independently determine the magnon conductivity in YIG, the spin conductance at the YIG/CoFe interface and eventually the (negative) anomalous spin Hall angle of CoFe as a function of its spin diffusion length in a single multiterminal structure.

We start this Chapter with an introduction to the experimental details as well as preliminary measurements for pre-characterization of the sample in Ch. 4.1. We proceed with the determination of the anomalous spin Hall angle of CoFe via our multiterminal spin transport device in Ch. 4.2. We ultimately discuss yet unclear asymmetric features of the magnon transport when using ferromagnetic metals as spin injectors/detectors in Ch. 4.3. A summary and conclusion of the obtained results is given in Ch. 4.4

The vast majority of text and Figures in this Chapter is taken from the article published in T. Wimmer, B. Coester, S. Geprägs, R. Gross, S.T.B. Goennenwein, H. Huebl, M. Althammer, *Anomalous spin Hall angle of a metallic ferromagnet determined by a multiterminal spin injection/detection device*, Applied Physics Letters **115**, 092404 (2019).

4.1 Experimental Details and Preliminary Measurements

The following subsections introduce the sample layout, a quantification of the spin conductance across YIG/Pt interfaces and the extraction of the magnon diffusion length via distance dependent measurements.

4.1.1 Sample Layout

Our device consists of a 1 µm thick, commercially availabe YIG film grown on a GGG ($Gd_3Ga_5O_{12}$) substrate via liquid phase epitaxy (cf. Ch. 3.1.1). Both Pt and CoFe electrodes were deposited by DC sputtering and patterned via electron beam lithography and lift-off as schematically depicted in Fig. 4.1 (see Ch. 3.2 for details of the fabrication procedure). The CoFe electrode was additionally capped with a 2.5 nm thick Al layer to prevent oxidation. In a further step, Al leads and bondpads were deposited to connect the device electrically. Each electrode has a width of $w = 500\,\text{nm}$ and a thickness of $t_{\text{Pt}} = t_{\text{CoFe}} = 7\,\text{nm}$. The lengths of the strips are $l_{\text{Pt1}} = l_{\text{Pt3}} = 148\,\mu\text{m}$ for the outer electrodes and $l_{\text{Pt2}} = l_{\text{CoFe}} = 162\,\mu\text{m}$ for the inner ones. As indicated in Fig. 4.1, the center-to-center distances between the metal strips are $d_{\text{Pt}} = 1.6\,\mu\text{m}$ and $d_{\text{CoFe}} = 0.8\,\mu\text{m}$ (cf. Fig. 4.1). If not stated otherwise, we apply a charge current $I_{\text{inj}} = 0.5\,\text{mA}$ to the Pt2 electrode (the injector) and detect the magnon transport signal as the detector voltage V_{det} at the Pt1, Pt3 and CoFe electrodes (see Fig. 4.1). In order to distinguish between electrically (via the SHE) and thermally (via Joule heating) injected magnons, we utilize the current reversal method described in Ch. 3.4.1. Here, we focus on the magnon transport

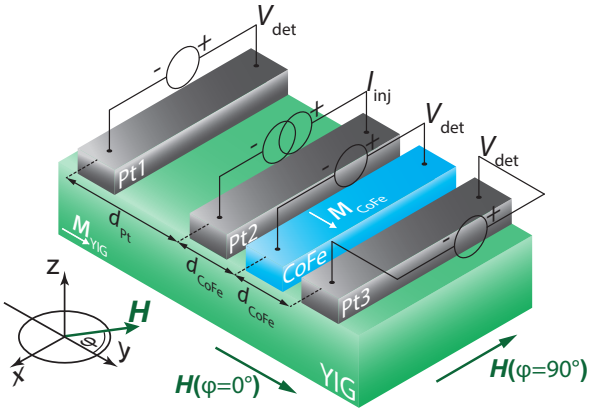

Fig. 4.1 – Sketch of the device configuration, the electrical connection scheme and the coordinate system. A charge current I_{inj} is fed through the Pt2 electrode, resulting in a spin current injection into YIG via the SHE. The lateral diffusion of the magnon spin current is electrically detected at the Pt electrodes ('Pt1' and 'Pt3') and the ferromagnetic metal electrode ('CoFe') as the detector voltage V_{det}. The center-to-center distances between each of the Pt electrodes is constant, such that $d_{\mathrm{Pt}} = 2d_{\mathrm{CoFe}}$. The shape anisotropy due to the particular structure of the CoFe electrode makes $\boldsymbol{H} \parallel \boldsymbol{x}$ ($\varphi = \pm 90°$) an easy axis.

	Symbol	Value	Unit
Pt strip thickness	t_{Pt}	7	nm
CoFe strip thickness	t_{CoFe}	7	nm
Pt & CoFe strip widths	w	500	nm
Pt spin diffusion length [54]	$l_{\mathrm{s}}^{\mathrm{Pt}}$	1.5	nm
Pt spin Hall angle [54]	$\theta_{\mathrm{SH}}^{\mathrm{Pt}}$	0.11	
Pt2 conductivity	σ_{Pt2}	2.64×10^6	$1/\Omega\mathrm{m}$
CoFe conductivity	σ_{CoFe}	1.50×10^6	$1/\Omega\mathrm{m}$
YIG thickness	t_{YIG}	1	μm

Tab. 4.1 – Material parameters of the YIG/Pt+CoFe device depicted in Fig. 4.1 at $T = 280\,\mathrm{K}$.

signal $V_{\mathrm{det}}^{\mathrm{el}}$ via the electrical SHE-induced spin current injection. All measurements are conducted in a superconducting magnet cryostat at a constant temperature of $T = 280\,\mathrm{K}$. In order to compare between different detector signals, we define a normalized signal amplitude as $R_{\mathrm{det}}^{\mathrm{el}} = (V_{\mathrm{det}}^{\mathrm{el}}/I_{\mathrm{inj}}) \cdot (A_{\mathrm{inj}}/A_{\mathrm{det}})$, which accounts for the different interface areas A_{inj} (A_{det}) of the injector and detectors [161].

4.1.2 Spin Conductance of YIG/Pt Interfaces

As introduced in Ch. 2.5, more specifically in Eq. (2.38), the thermally activated interfacial spin conductance g (which governs the magnon current across the YIG/Pt interface) directly relates to the real part of the spin mixing conductance according to $g = 3\zeta(3/2)g_{\mathrm{r}}^{\uparrow\downarrow}/(2\pi s\Lambda^3) \propto T^{3/2}$. In order to determine the spin conductance g_{Pt} of the YIG/Pt interfaces, we deduce the real part of the Pt/YIG spin mixing conductance $g_{\mathrm{Pt}}^{\uparrow\downarrow}$ from spin Hall magnetoresistance (SMR) measurements in the Pt electrodes. The magnitude of the SMR is given by the relative resistivity change $\Delta R_{\mathrm{long}}/R_{\mathrm{long}}$ in the Pt electrode measured between the in-plane

YIG magnetization pointing parallel and perpendicular to the current direction (cf. Ch. 2.6). We employ the theoretical equation for the SMR magnitude described in Ch. 2.6 [33]

$$\frac{\Delta R_{\mathrm{long}}}{R_{\mathrm{long}}} = \frac{\theta_{\mathrm{SH}}^{\mathrm{Pt}\,2} l_{\mathrm{s}}^{\mathrm{Pt}}}{t_{\mathrm{Pt}}} \frac{2 l_{\mathrm{s}}^{\mathrm{Pt}} g_{\mathrm{Pt}}^{\uparrow\downarrow} \tanh^2\left(\frac{t_{\mathrm{Pt}}}{2 l_{\mathrm{s}}^{\mathrm{Pt}}}\right)}{\sigma_{\mathrm{Pt2}} + 2 l_{\mathrm{s}}^{\mathrm{Pt}} g_{\mathrm{Pt}}^{\uparrow\downarrow} \coth\left(\frac{t_{\mathrm{Pt}}}{l_{\mathrm{s}}^{\mathrm{Pt}}}\right)}, \tag{4.1}$$

where we redefined the (real part of the) spin mixing conductance according to $g_{\mathrm{Pt}}^{\uparrow\downarrow} = G_0 g_{\mathrm{r}}^{\uparrow\downarrow}$ with $G_0 = e^2/h$ the conductance quantum (for one spin direction) [34, 78]. Hence, $g_{\mathrm{Pt}}^{\uparrow\downarrow}$ is given in units of an electrical conductance $\mathrm{S\,m^{-2}}$. Furthermore, σ_{Pt2} is the electrical conductivity of the Pt2 electrode. We measured the longitudinal resistance R_{long} at the Pt2 electrode as a function of the magnetic field orientation φ for various magnetic fields, as shown in Fig. 4.2**a**. The resistance change ΔR_{long} is determined by fitting a $\Delta R_{\mathrm{long}} \sin^2(\varphi)$ function to the magnetization orientation dependent data (under the assumption that the magnetization in the YIG is always aligned parallel to the external magnetic field), and is normalized to the high resistance value R_{long}. The resulting SMR magnitude is shown as a function of the external magnetic field in Fig. 4.2**b**. As expected from theory [33], we do not see any significant field dependence of the SMR. In order to obtain a representative value, we calculate an average over the whole field range measured and find $\Delta R_{\mathrm{long}}/R_{\mathrm{long}} = 7.38 \times 10^{-5}$. Hence, we can calculate the spin mixing conductance from Eq. (4.1). Using the values listed in Tab. 4.1, we obtain $g_{\mathrm{Pt}}^{\uparrow\downarrow} = 2.68 \times 10^{13}\,\mathrm{S\,m^{-2}}$. According to Eq. (2.38), the magnon excitation efficiency (given by the spin conductance g_{Pt}) relates to the spin mixing conductance as $g_{\mathrm{Pt}} = 3 g_{\mathrm{Pt}}^{\uparrow\downarrow} \zeta(3/2)/(2\pi s \Lambda^3) \approx 1.61 \times 10^{12}\,\mathrm{S\,m^{-2}}$ for YIG at room temperature. This value is then used throughout the calculations conducted in the subsequent Sections.

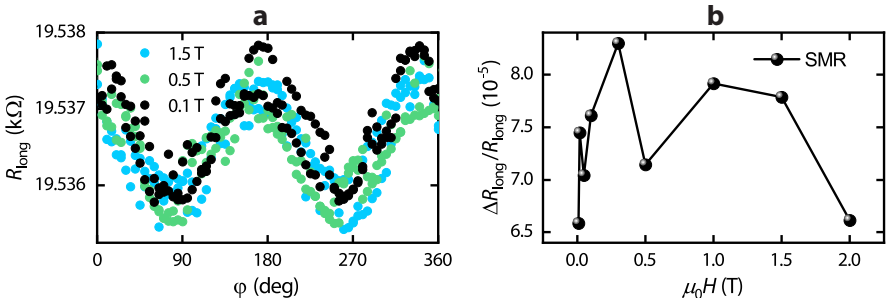

Fig. 4.2 – **a** Longitudinal resistance R_{long} measured on the Pt2 electrode as a function of the magnetic field orientation φ for different magnetic field magnitudes. **b** SMR magnitude $\Delta R_{\mathrm{long}}/R_{\mathrm{long}}$ as a function of magnetic field.

4.1.3 Magnon Diffusion Length

In Ch. 4.2, we apply a spin-resistor model to our magnon transport structure, which is only valid if the magnon diffusion length of our YIG film is larger than the distances between the respective electrodes considered. We thus determine the magnon diffusion length λ_m of a comparable 1 µm thick YIG film from the same wafer as the one shown in Fig. 4.1. For this purpose, we structured simple two-electrode devices consisting of Pt strips with a thickness of 7 nm on the YIG film with various values of their separation d (here d denotes the edge-to-edge distance between the electrodes). In Fig. 4.3**a**, the magnon transport signal amplitude $\Delta V_{\mathrm{det}}^{\mathrm{el}}$ is plotted versus d for different external magnetic fields. As indicated by the green and gray areas in the plot, we observe two different distance regimes, which decay on different length scales. We therefore show the short (orange shaded area) and long (gray shaded area) distance regimes on an enlarged scale in Fig. 4.3**b** and **c**, respectively. Here, the two regimes are fitted separately with single exponential fits of the form $\Delta V_{\mathrm{det0}}^{\mathrm{el}} e^{-d/\lambda_m}$, where $\Delta V_{\mathrm{det0}}^{\mathrm{el}}$ denotes the amplitude for zero distance. For the short (long) distance regime we find the diffusion length to vary from $\lambda_m \approx 1.0\,\mu$m to $0.8\,\mu$m ($\lambda_m \approx 6.4\,\mu$m to $1.8\,\mu$m) for magnetic fields from $\mu_0 H = 0.1\,$T to $7\,$T. Since the long distances correspond to the diffusive regime [36], we compare the diffusion lengths extracted for the long distance regime to the electrode separations studied in the subsequent Sections and find that $\lambda_m > d_{\mathrm{Pt}} = 1.6\,\mu$m for the whole field range considered. Hence, we conclude that the application of a spin-resistor model to our magnon transport device is valid.

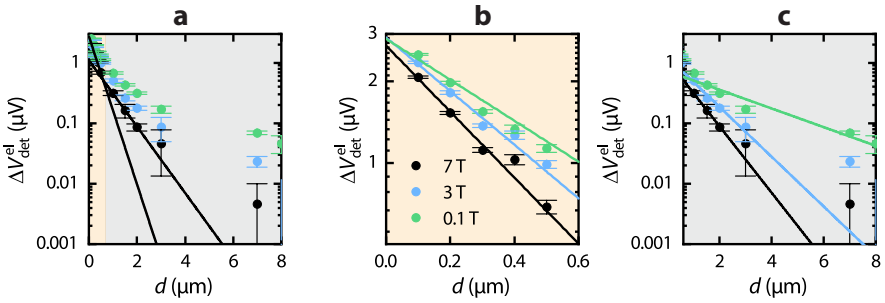

Fig. 4.3 – **a** Magnon transport signal $\Delta V_{\mathrm{det}}^{\mathrm{el}}$ plotted versus the injector-detector separation d on a logarithmic scale. The data is measured for a comparable 1 µm thick, LPE-grown YIG film taken from the same wafer as the one shown in Fig. 4.1. The straight lines indicate the different behavior observed on different length scales. Short (long) distance regimes are indicated by the orange (grey) shaded areas. Panels **b** and **c** show an enlarged view of the short and long distance regimes with exponential fits, respectively.

4.2 Determination of the Anomalous Spin Hall Angle of CoFe via Magnon Transport Measurements

To characterize the magnon transport in our device, we measure $R_{\mathrm{det}}^{\mathrm{el}}$ as a function of the magnetic field orientation φ for various in-plane field magnitudes $\mu_0 H$. Corresponding data are shown in Fig. 4.4 **a-c** for three different external magnetic fields. First, panel **a** shows the reference measurement using Pt1 as the detector. In accordance with Refs. [8, 9, 166], we observe a $\sin^2(\varphi)$-dependence of $R_{\mathrm{det}}^{\mathrm{el}}$ with an amplitude which is decreasing with increasing external magnetic field strengths. The origin of this reduction stems from the field-dependence of the magnon injection/detection at the YIG/Pt interface and the field-dependent magnon diffusion length λ_{m} [166]. We do not expect any effects from field induced magnetic moments or proximity magnetism in Pt [167], since these were ruled out in YIG/Pt heterostructures at elevated temperatures [168, 169]. Second, panel **b** shows $R_{\mathrm{det}}^{\mathrm{el}}$ recorded at the Pt3 detector. Since the separation of the Pt1 and Pt3 strip to the injector strip Pt2 are the same (cf. 4.1), one would expect the same signal magnitude. However, the $R_{\mathrm{det}}^{\mathrm{el}}$ modulation recorded across the Pt3 strip is significantly smaller, which we attribute to a partial absorption of the magnon spin current in the CoFe electrode located in between the Pt2 and Pt3 electrodes. Finally, panel **c** shows $R_{\mathrm{det}}^{\mathrm{el}}$ measured at the CoFe electrode. Interestingly, the polarity of the detected voltage is inverted. Since all strips were contacted with identical polarity in the experiments (see Fig. 4.1), we conclude that the anomalous spin Hall angle $\theta_{\mathrm{ASH}}^{\mathrm{CoFe}}$ in CoFe is negative compared to the positive spin Hall angle $\theta_{\mathrm{SH}}^{\mathrm{Pt}}$ in Pt [44, 86]. This is in agreement with the negative spin Hall angles reported for both Co and Fe [158]. Unlike the magnetic field suppression observed for the Pt detector strips, we find a significant enhancement of $R_{\mathrm{det}}^{\mathrm{el}}$ for increasing magnetic fields up to $\mu_0 H = 2\,\mathrm{T}$ for the CoFe detector. We attribute this to the field-induced increase of $\theta_{\mathrm{ASH}}^{\mathrm{CoFe}}$, qualitatively similar to the results reported in Ref. [65]. The origin of this increase is simply related to an increasing alignment and saturation of the CoFe magnetization M_{CoFe} perpendicular to the strip electrode, such that the transverse spin deflection along the CoFe/YIG interface originating from the anomalous spin Hall effect becomes larger due to a larger spin polarization (cf. Eq. (2.28)). Effectively, this can be captured by an increase in the anomalous spin Hall angle $\theta_{\mathrm{ASH}}^{\mathrm{CoFe}}$. For larger magnetic fields ($\mu_0 H = 7\,\mathrm{T}$), however, we observe a suppression of the magnon transport signal. Since the CoFe magnetization M_{CoFe} saturates around $\mu_0 H = 2\,\mathrm{T}$ [165], we attribute this field suppression to the YIG magnon system in analogy to the situation observed for the Pt detectors [8]. Interestingly, we observe a distinct asymmetry in the magnitudes of the signal for strong magnetic fields $\mu_0 H > 2\,\mathrm{T}$, which is discussed in more detail in Ch. 4.3.

In Fig. 4.5**a**, we plot the anisotropic magnetoresistance (AMR) of the CoFe electrode by measuring its longitudinal resistance R_{long} as a function of the mag-

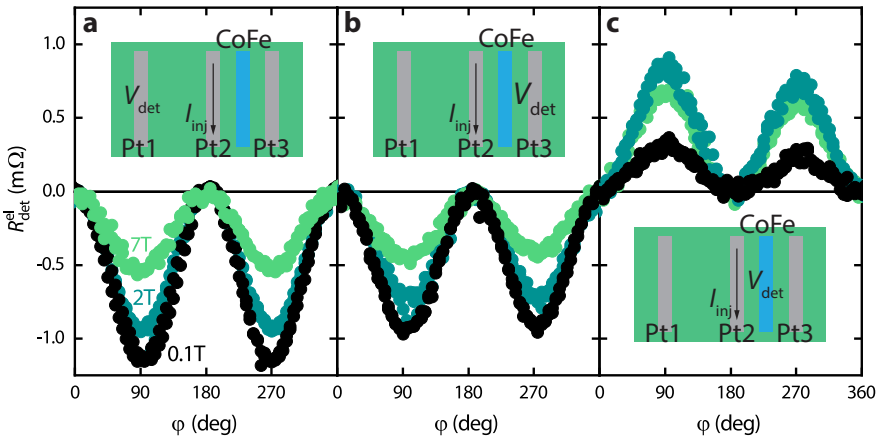

Fig. 4.4 – Normalized magnon transport signal R^{el}_{det} measured using different detector electrodes. **a** The signal at the Pt1 detector is taken as a reference measurement, with which we can characterize the magnon transport in the YIG layer with a well-known Pt injector and detector. **b** The Pt3 detector signal is somewhat smaller than the Pt1 signal owing to the finite absorption of the magnon current by the CoFe electrode in between Pt2 and Pt3. **c** The signal R^{el}_{det} associated with the detector voltage recorded at the CoFe electrode shows a sign reversal, indicating that the anomalous spin Hall angle in CoFe is negative.

netic field strength (the sweep direction is indicated by arrows). The blue (green) colored lines correspond to the field direction pointing perpendicular (parallel) to the strip length, while dark (light) colored lines correspond to the up (down) sweep of the magnetic field strength (trace and retrace, respectively). Obviously, we observe a clear AMR with a maximum (minimum) in resistance for parallel (perpendicular) field alignment with respect to the strip length at a coercive field of approximately $\pm 18\,\mathrm{mT}$. Additionally, we find a second peak at a characteristic field of roughly $\pm 11\,\mathrm{mT}$. This feature corresponds well to the switching field observed for the longitudinal resistance of the Pt2 electrode, which is shown in Fig. 4.5**b** (switching field indicated by gray dashed lines). Therefore, the peaks in the resistance of the CoFe strip around $\pm 11\,\mathrm{mT}$ can be attributed to a spin Hall magnetoresistance (SMR) [54] contribution related to the magnetization reversal in the YIG film. Most importantly, these magnetoresistance measurements show that exchange coupling between the two ferromagnetic layers is not relevant, since no exchange bias effect can be observed (which would lead to a shift of the hysteresis curves along the magnetic field axis). Figure 4.5**c**, **d** show the detector signals R^{el}_{det} as a function of the magnetic field strength measured at the Pt1 and CoFe electrodes, respectively. For the reference detector (Pt1), we find a continuous suppression of the magnon transport signal R^{el}_{det} with increasing magnetic field strength when the field is oriented perpendicular to the strips (blue data points in Fig. 4.5**c**). For a parallel alignment of the field and the strips (green data points), the signal vanishes. This response is quantitatively consistent with the field-orientation

dependent data (Fig. 4.4**a** and **b**). Figure 4.5**d** shows the magnetic field dependence of $R_{\mathrm{det}}^{\mathrm{el}}$ when the CoFe electrode is used as the detector. Here, $R_{\mathrm{det}}^{\mathrm{el}}$ is zero for $\mu_0 H = 0$ for both field orientations. When the field is oriented perpendicular to the strips, $R_{\mathrm{det}}^{\mathrm{el}}$ rapidly increases and reaches its maximum at around $\mu_0 H \approx 2\,\mathrm{T}$. Since the injection and detection efficiency of the magnons is maximized when the magnetizations M_{YIG} and M_{CoFe} are aligned perpendicular to the electrodes [65], the maximum of $R_{\mathrm{det}}^{\mathrm{el}}$ is expected when the magnetization M_{CoFe} is fully saturated perpendicularly to the strips overcoming the shape anisotropy at around 2 T [65] (see Fig. 4.5**d**). For larger magnetic fields, we again observe a field-induced suppression of the signal, which was already discussed for the orientation dependent measurements in Fig. 4.4 and originates from the field dependence of the magnon transport in YIG. Following Ref. [65], the contributions of θ_{SH} and θ_{ASH} can be separated by identifying the magnon transport signal at the switching field and the saturation field of the CoFe detector, respectively. It is, however, evident that the CoFe detector signal in Fig. 4.5**d** becomes zero for small magnetic fields, suggesting that there is no contribution from a pure SHE in CoFe, different to the results reported for Py [65, 170]. We note, however, that this observation strongly depends on whether or not the CoFe is in a multidomain state, since a net magnetization M_{CoFe} perpendicular to the electrode could be counterbalanced by a positive SHE contribution. Clearly, we can verify again the asymmetry feature when the CoFe electrode is used as a detector (see Ch. 4.3 for details).

Utilizing our multiterminal magnon transport device, we are able to extract the anomalous spin Hall angle $\theta_{\mathrm{ASH}}^{\mathrm{CoFe}}$. To this end, we model the spin transport in our device by employing the spin-resistor circuit model proposed in Ref. [36]. This approach is valid as long as the distance d between the considered electrodes is smaller than the characteristic magnon diffusion length λ_{m} in our YIG film. We verified that $d_{\mathrm{Pt}} = 2d_{\mathrm{CoFe}} < \lambda_{\mathrm{m}} \approx 6\,\mu\mathrm{m}$ for a comparable YIG film (see Ch. 4.1.3). The equivalent spin-resistor circuit diagram for the Pt2-Pt1 contact pair and the three-terminal Pt2-CoFe-Pt3 contacts are shown in Fig. 4.6**a** and **b**, respectively. Here, the individual resistors are described by three different resistances (each of which are given in units of Ω): first, $R_i^{\mathrm{s}} = l_{\mathrm{s}}^i \rho_i / [l_i w \tanh(t_i / l_{\mathrm{s}}^i)]$ is the spin resistance of electrode i (i = Pt1, CoFe, Pt3) with l_{s}^i the spin diffusion length and ρ_i the electrical resistivity. Furthermore, t_i, l_i and w denote the thickness, length and width of electrode i. Secondly, $R_{\mathrm{int},i}^{\mathrm{s}} = 1/(g_{\mathrm{i}} l_i w)$ is the interface spin resistance, with g_i the interface spin conductance of electrode i and lastly $R_{\mathrm{YIG}}^{\mathrm{s}} = d_{\mathrm{CoFe}} / \left(\frac{2e^2}{\hbar} \sigma_{\mathrm{m}} l_{\mathrm{Pt2}} t_{\mathrm{YIG}}\right)$ is the YIG spin resistance for a distance d_{CoFe} with σ_{m} the magnon conductivity and t_{YIG} the thickness of the YIG film. For convenience, we will refer to the magnon conductivity in units of electrical conductivity S/m by calculating $2e^2/\hbar \cdot \sigma_{\mathrm{m}}$. For both circuits shown in Fig. 4.6**a** and **b**, the "spin battery" of the network is characterized by the injected spin chemical potential $\mu_{\mathrm{s,inj}}^{\mathrm{Pt2}} = 2e\theta_{\mathrm{SH}}^{\mathrm{Pt}} I_{\mathrm{inj}} l_{\mathrm{s}}^{\mathrm{Pt}} [R_{\mathrm{Pt2}} / l_{\mathrm{Pt2}}] \tanh\left(t_{\mathrm{Pt}} / (2 l_{\mathrm{s}}^{\mathrm{Pt}})\right)$ [33] at the YIG/Pt2 interface (given in units of J). Here, $l_{\mathrm{s}}^{\mathrm{Pt}}$ is the spin diffusion length of Pt, $\theta_{\mathrm{SH}}^{\mathrm{Pt}}$ is the spin Hall angle

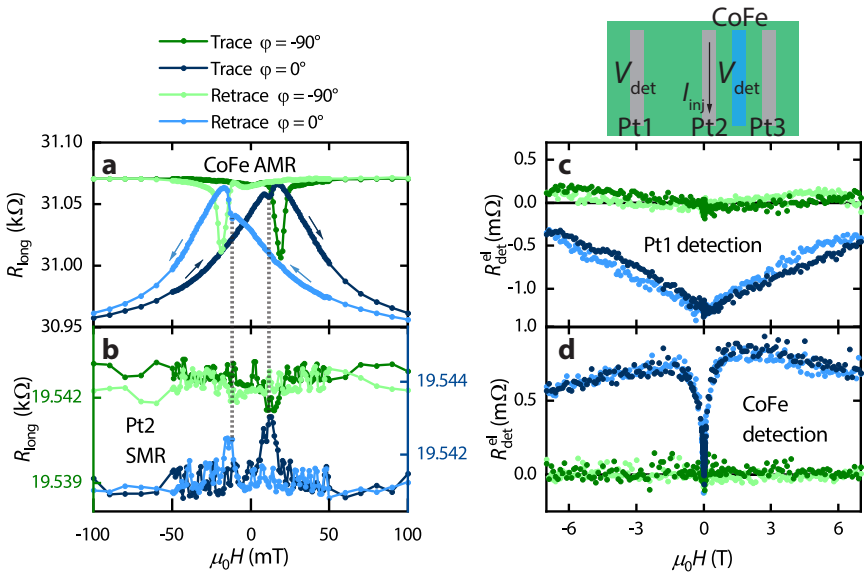

Fig. 4.5 – Longitudinal resistance R_{long} and magnon transport signal $R^{\text{el}}_{\text{det}}$ measured as a function of the magnetic field strength for field directions pointing perpendicular (blue) and parallel (green) to the strip length. Dark and light colored lines correspond to up- and down-sweep curves, respectively. **a** R_{long} measured on the CoFe electrode, showing the AMR with a switching field of $\mu_0 H = \pm 18\,\text{mT}$. Additionally, a second switching at lower fields $\mu_0 H = \pm 11\,\text{mT}$ (indicated by gray dashed lines) is observed, which corresponds to the R_{long} change measured on the Pt2 electrode (SMR) in **b**. Here, the green curves correspond to the left vertical axis, while the blue lines refer to the right axis. **c**, **d** $R^{\text{el}}_{\text{det}}$ shown as a function of the magnetic field strength measured at the Pt1 and CoFe detector, respectively.

of Pt and R_{Pt2} is the electrical resistance of the Pt2 electrode. The spin chemical potential "drop" across each detector i is given via the measured detector voltages $V^{\text{el},i}_{\text{det}}$ and reads $\mu^{i}_{\text{s,det}} = 2et_{\text{i}}/(\theta^{\text{i}}_{(\text{A})\text{SH}} l_{\text{i}}) \left(1 + [\cosh(t_i/l^{i}_{\text{s}}) - 1]^{-1}\right) V^{\text{el},i}_{\text{det}}$ [36]. For each detector i, we can then calculate the spin transfer efficiency generally as

$$\eta^{i}_{\text{s}} = \frac{\mu^{i}_{\text{s,det}}}{\mu^{\text{Pt2}}_{\text{s,inj}}}. \tag{4.2}$$

Applying Kirchhoff's laws to the spin-resistor network shown in Fig. 4.6**a**, we obtain the spin transfer efficiency of the Pt1 detector as

$$\eta^{\text{Pt1}}_{\text{s}} = \frac{R^{\text{s}}_{\text{Pt1}}}{R^{\text{s}}_{\text{Pt2}} + R^{\text{s}}_{\text{Pt1}} + R^{\text{s}}_{\text{int,Pt2}} + R^{\text{s}}_{\text{int,Pt1}} + 2R^{\text{s}}_{\text{YIG}}}, \tag{4.3}$$

while analyzing the circuit shown in Fig. 4.6**b**, we find

$$\eta^{\text{Pt3}}_{\text{s}} = \frac{R^{\text{s}}_{\text{Pt3}}\zeta}{R^{\text{s}}_{\text{tot}}(1+\zeta)}, \tag{4.4a}$$

$$\eta^{\text{CoFe}}_{\text{s}} = \frac{R^{\text{s}}_{\text{CoFe}}}{R^{\text{s}}_{\text{tot}}(1+\zeta)}, \tag{4.4b}$$

for the Pt3 and CoFe detectors. Here, $\xi = [R^{s}_{\mathrm{int,CoFe}} + R^{s}_{\mathrm{CoFe}}]/[R^{s}_{\mathrm{YIG}} + R^{s}_{\mathrm{int,Pt3}} + R^{s}_{\mathrm{Pt3}}]$ and R^{s}_{tot} is the total resistance of the spin-resistor network of Fig. 4.6**b**.

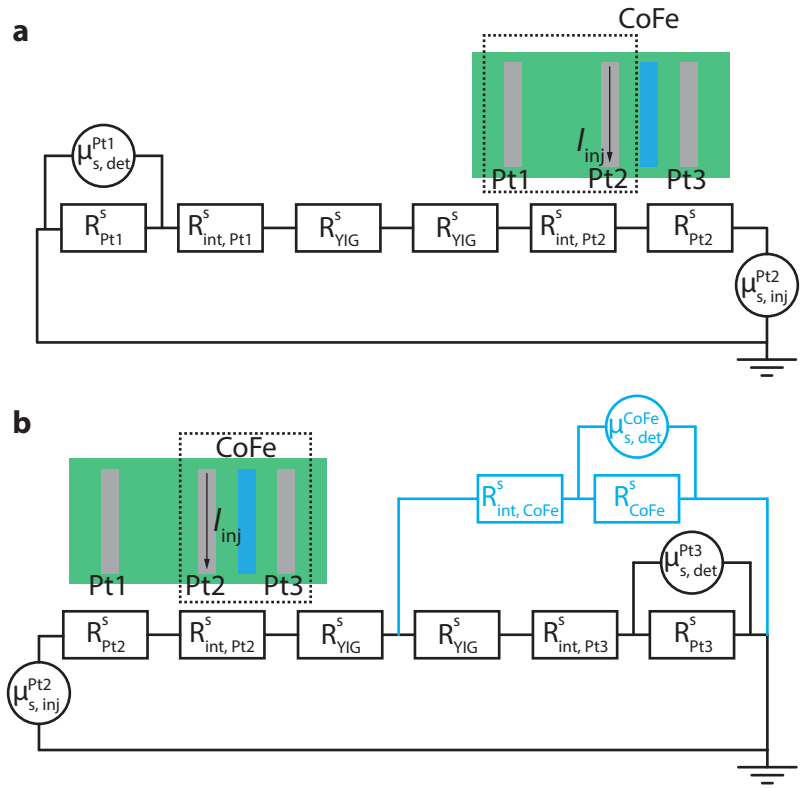

Fig. 4.6 – Equivalent spin-resistor network for **a** the Pt2-Pt1 contact pair and **b** the Pt2-CoFe-Pt3 contact configuration.

On the basis of this model, we now calculate σ_{m}, g_{CoFe} of the YIG/CoFe interface and finally $\theta^{\mathrm{CoFe}}_{\mathrm{ASH}}$ of CoFe. We obtain σ_{m} by equating Eqs. (4.2) and (4.3) for i = Pt1. The spin conductance g_{Pt} for the YIG/Pt interfaces was independently determined via longitudinal SMR measurements (see Ch. 4.1.2). We extract σ_{m} for the different magnetic field values and plot the result in Fig. 4.7**a**. For small magnetic fields of $10\,\mathrm{mT} < \mu_0 H < 50\,\mathrm{mT}$, the magnon conductivity in the YIG layer exhibits a sharp increase, which is due to the initial saturation of the magnetization. It reaches its maximum at $(2e^2)/\hbar\,\sigma_{\mathrm{m}} \approx 3.2 \times 10^4\,\mathrm{S\,m^{-1}}$ for $\mu_0 H = 50\,\mathrm{mT}$, which is roughly one order of magnitude smaller than what is reported in Ref. [171]. This difference is due to the fact that our YIG film is five times thicker than the one studied in Ref. [171]. Since the electrically excited magnon transport signal was shown to decrease monotonically with increasing thickness [124], we conclude our extracted value to be reasonable. For larger magnetic fields $\mu_0 H > 50\,\mathrm{mT}$, σ_{m} monotonically decreases as a function of magnetic field. This is expected, since the thermal magnon number of the YIG film is decreasing as the Zeeman gap opens with increasing external field. In a Drude-inspired conductivity model for magnons [172], a decreasing magnon number is directly connected to a decreasing magnon conductivity (cf. Ch. 2.7.2 and Eq. (2.55)). We want to emphasize here

that the spin resistor model (per definition) neglects magnon decay, which is parameterized by the magnon diffusion length λ_m. As the magnon diffusion length is a field dependent parameter (see Ch. 4.1.3), this implies that we project the complete field dependence onto the magnon conductivity σ_m. This, however, is justified since the distances d between the strips that we investigate in this work are smaller than the magnon diffusion length (see Ch. 4.1.3) in all cases, thus legitimizing the use of the spin resistor model. Furthermore, the spin conductance g_{Pt} (that also enters the calculation of σ_m) at the YIG/Pt interface (which is given by the real part of spin mixing conductance $g_{Pt}^{\uparrow\downarrow}$, see Ch. 4.1.2) is generally considered as a weakly field-dependent parameter [75, 86]. Moreover, for the spin Hall angle of Pt no strong dependence on magnetic field was shown either [54].

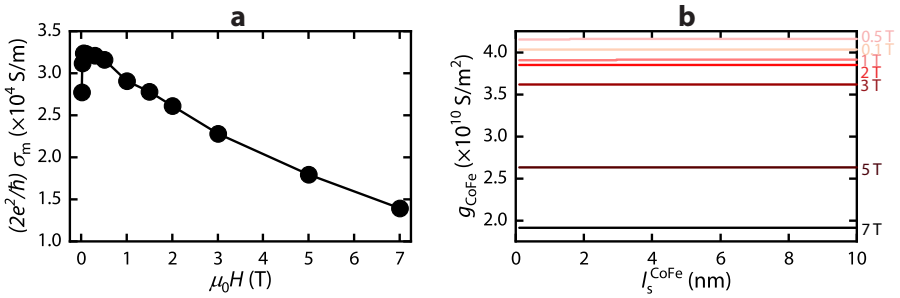

Fig. 4.7 – **a** Magnon conductivity σ_m of the YIG film as a function of magnetic field. The values were extracted within the spin-resistor model outlined in Fig. 4.6. **b** Spin conductance g_{CoFe} as a function of the spin diffusion length l_s^{CoFe} for different external magnetic fields.

In a next step, we extract the spin conductance g_{CoFe} at the YIG/CoFe interface. Since our experiment does not allow to determine the spin diffusion length l_s^{CoFe} of CoFe, we determine g_{CoFe} as a function of l_s^{CoFe} from Eqs. (4.2) and (4.4a) for $i =$ Pt3. The result is shown in Fig. 4.7**b** for different external magnetic fields. We here observe a vanishing dependence of g_{CoFe} on the spin diffusion length l_s^{CoFe} varying only by roughly $\sim 0.05\,\%$ between $l_s^{CoFe} = 0\,\text{nm}$ and $10\,\text{nm}$. We therefore treat g_{CoFe} as a constant value, independent of the spin diffusion length. However, as evident from Fig. 4.7**b**, the interface spin conductance g_{CoFe} does slightly vary with the external magnetic field by a factor of ~ 2 in the measured field range. Similar to the YIG/Pt interface spin conductance g_{Pt}, we do not expect the spin conductance g_{CoFe} at the YIG/CoFe interface to exhibit a strong external field dependence. Since our measurements of the detector voltage $V_{det}^{el,Pt3}(\mu_0 H)$ at the Pt3 electrode enter the spin-resistor model, their field dependence is projected onto g_{CoFe}, as this parameter characterizes the amount of spin current absorbed in the CoFe strip (between Pt2 and Pt3). This effect is, however, mostly counterbalanced by the field dependent magnon conductivity values (see Fig. 4.7**a**) that also enter the calculation of g_{CoFe}. As evident from Fig. 4.7**b**, this balancing effect is clearly visible for fields $\mu_0 H \leq 2\,\text{T}$ (where a vanishing field dependence of g_{CoFe} is observed), but a stronger field dependence becomes apparent for $\mu_0 H \geq 3\,\text{T}$. Since

we do not consider g_{CoFe} as a field dependent parameter [33, 76, 86], this feature might be explained by the fact that the magnon diffusion length λ_{m} is strongly suppressed for large magnetic fields (see Ch. 4.1.3), such that the spin resistor model becomes less accurate in this field regime. Hence, the calculation of g_{CoFe} might be also less accurate for $\mu_0 H \geq 3\,\mathrm{T}$. For the sake of consistency and to reduce the number of field dependent parameters, we therefore assume a constant value of $g_{\mathrm{CoFe}} = 4 \times 10^{10}\,\mathrm{S\,m^{-2}}$ for the calculation of the anomalous spin Hall angle of CoFe in the following. This value approximately corresponds to the values extracted for the field range between $\mu_0 H = 0.1\,\mathrm{T}$ and $2\,\mathrm{T}$, as shown in Fig. 4.7**b**. For the sake of completeness we also analyze the influence of varying g_{CoFe} on the determination of $\theta_{\mathrm{ASH}}^{\mathrm{CoFe}}$ in Ch. 4.2.1.

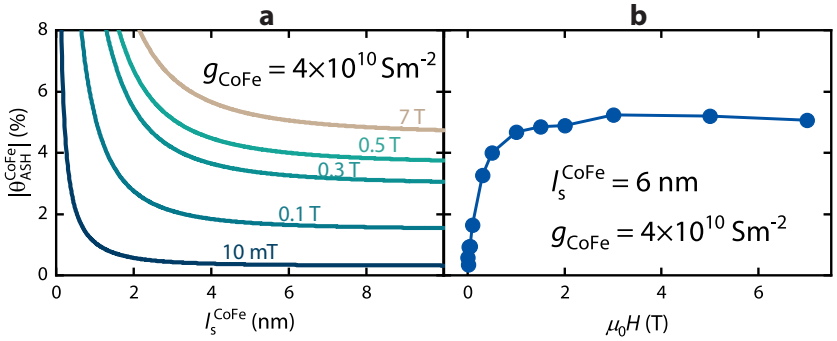

Fig. 4.8 – **a** Experimentally determined absolute value of the anomalous spin Hall angle $\theta_{\mathrm{ASH}}^{\mathrm{CoFe}}$ as a function of the spin diffusion length $l_{\mathrm{s}}^{\mathrm{CoFe}}$ for various external magnetic fields. Here, the spin conductance of the YIG/CoFe interface was set to a constant value $g_{\mathrm{CoFe}} = 4 \times 10^{10}\,\mathrm{S\,m^{-2}}$. **b** Anomalous spin Hall angle of CoFe as a function of the applied magnetic field assuming a spin diffusion length $l_{\mathrm{s}}^{\mathrm{CoFe}} = 6\,\mathrm{nm}$.

Interestingly, the spin conductance g_{CoFe} of the YIG/CoFe interface is almost two orders of magnitude smaller than g_{Pt} of the YIG/Pt interfaces. This rather drastic difference suggests that the diffusing magnons at the YIG/CoFe interface are not only transmuting into an electronic spin chemical potential by spin flip scattering processes, but also cross the interface as magnon excitations due to the ferromagnetic nature of CoFe. This additional dissipation channel for the transported YIG magnons should, naively, lead to an enhanced absorption by the ferromagnetic CoFe electrode as compared to the non-magnetic Pt, in contrast to our experimentally determined values. To potentially resolve this issue, we have to take into consideration the involved length scales for electronic and magnonic spin currents in CoFe. Based on our spin resistor model in Fig. 4.6, the spin conductance g_{CoFe} is basically determined by comparing the magnon transport signals at the Pt1 and Pt3 detectors, the difference of which indicates the amount of magnon absorption at the CoFe electrode. While the absorbed magnons in CoFe transmuting into an electronic spin current are governed by the short spin diffusion length $l_{\mathrm{s}}^{\mathrm{CoFe}}$ (in the order of a few nm [173]) and are therefore mostly dissipated across its thickness of $t_{\mathrm{CoFe}} = 7\,\mathrm{nm}$ (as experimentally verified by the

finite electrical detector signal at the CoFe electrode), the transmutation of YIG magnons into CoFe magnons is governed by the magnon diffusion length in CoFe. Considering the record low damping of thin CoFe layers demonstrated recently [165] and its correpsonding large spin wave propagation length in the order of tens of µm [28], it is reasonable to assume a non-coherent magnon diffusion length of the order of µm in CoFe. Hence, it is quite likely that the transmuted magnons are mostly reflected at the top surface of the thin CoFe electrode ($t_{\mathrm{CoFe}} = 7\,\mathrm{nm}$) and are therefore converted back into the YIG film. As a consequence, the magnon absorption in CoFe due to the magnon channel is likely to have a negligible impact on the Pt3 detector signal, which is determined by the total amount of non-equilbrium magnons at its interface. This might therefore explain the large difference between the extracted interface transparencies from our model, since the transmutation of YIG magnons into CoFe magnons would not lead to an effectively increased absorption due to the supposedly large magnon diffusion length in CoFe. Assuming that the total magnon absorption at the YIG/CoFe interface is comparable to that of YIG/Pt, the above considerations suggest a far more efficient transmutation of YIG magnons into CoFe magnons compared to the conversion into an electronic spin accumulation. In any case, the above arguments legitimize our following analysis regarding the anomalous spin Hall angle of CoFe.

Having determined both σ_{m} and g_{CoFe}, we can now quantify the anomalous spin Hall angle $\theta_{\mathrm{ASH}}^{\mathrm{CoFe}}$ by equating Eqs. (4.2) and (4.4b) for $i = \mathrm{CoFe}$. We thus extract $\theta_{\mathrm{ASH}}^{\mathrm{CoFe}}$ as a function of $l_{\mathrm{s}}^{\mathrm{CoFe}}$ from Eqs. (4.2) and (4.4b) for $i = \mathrm{CoFe}$. The result is shown in Fig. 4.8**a** for different magnetic fields. Obviously, $\theta_{\mathrm{ASH}}^{\mathrm{CoFe}}$ saturates as a function of $l_{\mathrm{s}}^{\mathrm{CoFe}}$ at around $\sim 7\,\mathrm{nm}$, which corresponds to the CoFe electrode thickness t_{CoFe}. This is reasonable, since (experimentally) we do not expect any change of $\theta_{\mathrm{ASH}}^{\mathrm{CoFe}}$ for $l_{\mathrm{s}}^{\mathrm{CoFe}} > t_{\mathrm{CoFe}}$. Finally, we estimate the field dependence of $\theta_{\mathrm{ASH}}^{\mathrm{CoFe}}$ by assuming $l_{\mathrm{s}}^{\mathrm{CoFe}} = 6\,\mathrm{nm}$, which is based on Ref. [173], where the spin diffusion length of a $Co_{60}Fe_{40}$ alloy was determined via spin absorption in lateral spin valves. Note, that the value of $l_{\mathrm{s}}^{\mathrm{CoFe}}$ only affects the quantitative values for $\theta_{\mathrm{ASH}}^{\mathrm{CoFe}}$, but the qualitative field dependence remains the same. Plotting $\theta_{\mathrm{ASH}}^{\mathrm{CoFe}}$ as a function of magnetic field in Fig. 4.8**b**, we find that $\theta_{\mathrm{ASH}}^{\mathrm{CoFe}}$ rapidly increases with increasing magnetic field (as M_{CoFe} saturates) and reaches its maximum value for about 2 T-3 T at $\sim 5\,\%$. For permalloy, a spin Hall angle of 2 % was reported [158]. Clearly, the field dependence of $\theta_{\mathrm{ASH}}^{\mathrm{CoFe}}$ in our experiment is determined by the magnetization M_{CoFe} aligning perpendicularly to the CoFe strip length (i.e. along the magnetic hard axis). As detailed in the Ch. 4.2.2, however, the application of a Stoner-Wohlfarth model with uniaxial shape anisotropy [174] does not reproduce the observed field dependence well, suggesting that the CoFe electrode is in a multidomain state for small magnetic fields. We want to emphasize that our experimental determination of $\theta_{\mathrm{ASH}}^{\mathrm{CoFe}}$ takes into account the spin conductance g_{CoFe} at the YIG/CoFe interface. Earlier estimations of θ_{ASH} in ferromagnetic metals

either assume a comparable spin conductance as for YIG/Pt interfaces [175] or do not provide any experimental data on the interfacial spin conductance [65].

4.2.1 Influence of the Spin Conductance g_{CoFe} on the Anomalous Spin Hall Angle $\theta_{\mathrm{ASH}}^{\mathrm{CoFe}}$

In order to show the effect of different spin conductances g_{CoFe} on the evolution of the anomalous spin Hall angle of CoFe, we plot $\theta_{\mathrm{ASH}}^{\mathrm{CoFe}}$ as a function of magnetic field in Fig. 4.9 for two constant values of g_{CoFe} (black and blue points), assuming a constant spin diffusion length of $l_{\mathrm{s}}^{\mathrm{CoFe}} = 6\,\mathrm{nm}$ [173]. Additionally, we plot the situation when the full field dependence $g_{\mathrm{CoFe}}(\mu_0 H)$ shown in Fig. 4.7**b** is taken into account (red data points). Assuming a small spin conductance $g_{\mathrm{CoFe}} = 2 \times 10^{10}\,\mathrm{S\,m^{-2}}$ (blue data), we find a significantly larger anomalous spin Hall angle as compared to $g_{\mathrm{CoFe}} = 4 \times 10^{10}\,\mathrm{S\,m^{-2}}$ (black data). This is expected, since a smaller spin conductance has to be counterbalanced by a larger anomalous spin Hall angle, in order to maintain the measured magnon transport signal. Figuratively speaking, g_{CoFe} determines the amount of spin current injected into the CoFe strip, while $\theta_{\mathrm{ASH}}^{\mathrm{CoFe}}$ describes the spin-to-charge current conversion process in the CoFe. Calculating $\theta_{\mathrm{ASH}}^{\mathrm{CoFe}}$ including the full field dependence $g_{\mathrm{CoFe}}(\mu_0 H)$ (red data points), we observe an increase of the anomalous spin Hall angle even beyond 2 T, where the CoFe electrode is already saturated. This, however, is implausible and we therefore attribute this artificial increase in $\theta_{\mathrm{ASH}}^{\mathrm{CoFe}}$ to the violation of the assumptions made in the spin resistor-model, i.e. that the decay of magnons can be neglected. We conclude that the assumption of a constant g_{CoFe} is well justified in the field range of $2\,\mathrm{T} < \mu_0 H < 7\,\mathrm{T}$.

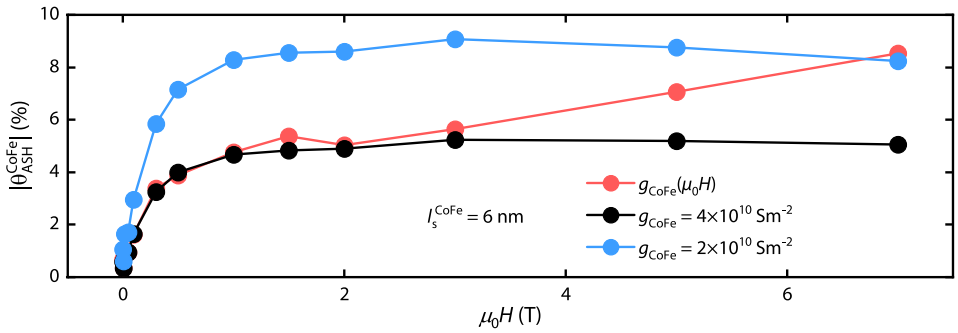

Fig. 4.9 – Anomalous spin Hall angle of CoFe for two different (constant) values of the spin conductance g_{CoFe} (black and blue data points). Additionally, the result for a field dependent spin conductance $g_{\mathrm{CoFe}}(\mu_0 H)$ is shown (red data points).

4.2.2 Shape Anisotropy of the CoFe Electrode

In this subsection, we employ the Stoner-Wohlfarth model [174] to extract the uniaxial shape anisotropy of the CoFe electrode. On the basis of this model, we furthermore attempt to reproduce the field dependence of the anomalous spin Hall angle $\theta_{\mathrm{ASH}}^{\mathrm{CoFe}}$, which is characterized by the alignment of the magnetization M_{CoFe} perpendicular to the CoFe strip (i.e. along the magnetic hard axis in the film plane). The Stoner-Wohlfarth model with uniaxial shape anisotropy (for our definition of the field direction and for in-plane orientations) reads

$$f = -\frac{1}{2}K_{\mathrm{u}}\sin^2(\theta+\varphi) - \mu_0 H M_{\mathrm{CoFe}}\cos(\theta), \tag{4.5}$$

where f is the free energy density, K_{u} is the uniaxial anisotropy constant, $\mu_0 H$ the external magnetic field strength with μ_0 the magnetic vacuum permeability, $\mu_0 M_{\mathrm{CoFe}} \approx 2.3\,\mathrm{T}$ is the saturation magnetization of CoFe [165], φ is the direction of the external magnetic field (cf. Fig. 4.1) with respect to the magnetic hard axis and θ is the angle between the magnetization and external field direction. Equation (4.5) is expanded up to second order in θ and then minimized with respect to θ. The resulting equation for θ is a function of the angle φ and reads

$$\theta(\varphi) = \frac{K_{\mathrm{u}}\cos(\varphi)\sin(\varphi)}{\mu_0 H M_{\mathrm{CoFe}} - K_{\mathrm{u}}\cos(2\varphi)}. \tag{4.6}$$

The AMR modulates as a $\sin^2(\varphi)$ function when the magnetization is rotated in the magnetic material. Introducing the finite misalignment of the external magnetic field and the magnetization, the AMR modulation can be written as $\sin^2(\varphi - \theta(\varphi))$ with Eq. (4.6). This function is fitted to the AMR measurements of the CoFe electrode for different magnetic fields in Fig. 4.10**a**. Extracting the anisotropy constant from the fits gives $K_{\mathrm{u}} \approx 90\,\mathrm{kJ\,m^{-3}}$, which results in an equivalent anisotropy field of $B_{\mathrm{ani}} = K_{\mathrm{u}}/M_{\mathrm{CoFe}} \approx 49\,\mathrm{mT}$.

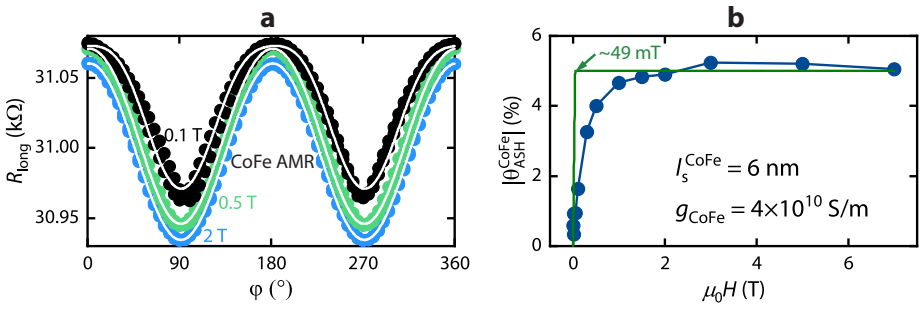

Fig. 4.10 – a Longitudinal resistance R_{long} measured at the CoFe electrode as a function of the magnetic field orientation φ (cf. Fig. 4.1), showing the anisotropic magnetoresistance behaviour. The solid lines are fits to the data. **b** Field dependence of the anomalous spin Hall angle $\theta_{\mathrm{ASH}}^{\mathrm{CoFe}}$ (same as Fig. 4.8**b** in Ch. 4.2). The green solid line is calculated on the basis of a Stoner-Wohlfarth model assuming uniaxial shape ansisotropy of the CoFe strip with an anisotropy field $B_{\mathrm{ani}} \approx 49\,\mathrm{mT}$.

Using the experimentally extracted anisotropy constant K_u, we can calculate the field dependence of the anomalous spin Hall angle θ_{ASH}^{CoFe}. For the purpose of this, Eq. (4.5) is minimized with respect to the angle θ while setting $\varphi = 0°$ (which corresponds to the magnetic hard axis of the field direction). Thus, we obtain the angle θ_{min} as a function of the external magnetic field $\mu_0 H$. Taking into account the measured anomalous spin Hall angle at large magnetic fields ($\sim 5\,\%$) and considering the projection of the magnetization along the magnetic hard axis (i.e. $\cos(\theta_{min})$), we expect a field dependence as shown by the green line in Fig. 4.10**b**. As evident, this simple model does not reproduce the observed field dependence well. We can therefore conclude that the CoFe electrode is in a multidomain state for small magnetic fields $\mu_0 H \lesssim 1\,\mathrm{T}$.

4.3 Asymmetric Magnon Transport Signals Using Spin Injection/Detection via CoFe

In Ch. 4.2, we observed a slight asymmetry between the magnon transport signals measured at the CoFe detector for the two field directions pointing perpendicular to the strips, i.e. $\varphi = 0°$ and $\varphi = 180°$. Most likely, this asymmetry is related to the magnetization behaviour of M_{CoFe} of the CoFe electrode. We therefore measured the anisotropic magnetoresistance (AMR) as a function of φ on the CoFe electrode in Fig. 4.11**a**. Additionally, we recorded the magnon transport signal as a function of φ for various injector-detector configurations in Fig. 4.11**b** - **e**. Here, each of the respective panels is indicated with 'injector - detector', denoting the considered measurement configuration. For each configuration, we show rotations with two different magnetic field magnitudes (red and blue data points), where the forth [towards larger positive φ values] (back [towards smaller φ values]) rotation is indicated by darker (lighter) colored points. Panels **b** and **c** show the case when the CoFe electrode is used as the detector, while panels **d** and **e** picture the case when the CoFe electrode serves as an injector.

We first focus on the large magnetic field ($\mu_0 H = 2\,\mathrm{T}$) rotations (red data points). Here, the AMR in CoFe (Fig. 4.11**a**) exhibits the typical $\sin^2(\varphi)$ modulation with a relative magnitude of $\sim 3\,\%$, exhibiting a lower resistance state for a perpendicular configuration of M_{CoFe} as for a parallel alignment with the strip, i.e. the electrical current direction. Disregarding the asymmetry feature for now, the magnon transport signals in Fig. 4.11**b** - **d** also show the expected behaviour. Nominally, we expect the signals of panel **b** and **c** to exhibit a comparable magnitude, since the injectors Pt2 and Pt3 are supposed to have the same edge-to-edge distance of $d = 300\,\mathrm{nm}$ to the CoFe electrode. In contrast to this, the signal amplitudes differ by roughly 45 %. Considering the distance dependence of the magnon transport in the YIG film (Fig. 4.3), we see that the transport signal varies by roughly 25 % from $d = 300\,\mathrm{nm}$ to $d = 200\,\mathrm{nm}$. Hence, this difference

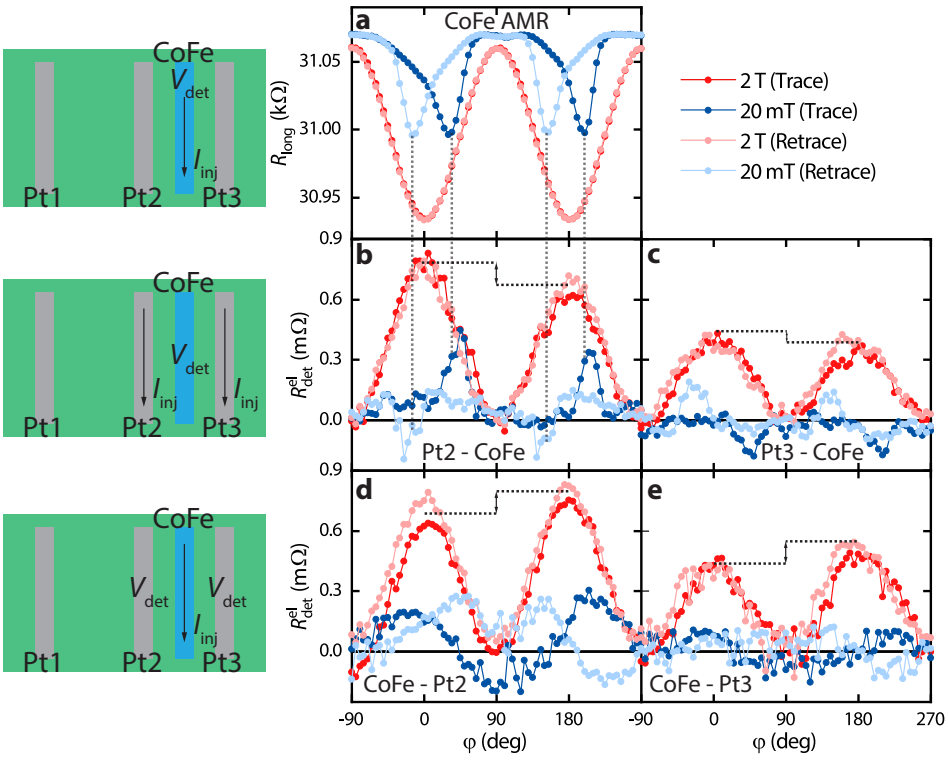

Fig. 4.11 – **a** Longitudinal resistance R_{long} (i.e. the anisotropic magnetoresistance) of the CoFe electrode measured as a function of φ. Magnon transport signal $R^{\text{el}}_{\text{det}}$ as a function of the magnetic field orientation φ. The forth (back) rotations of the magnetic field are shown in dark (light) colors. Different configurations of injector - detector combinations are used, which are indicated in the form of 'injector - detector' in each panel **b**, **c**, **d** and **e**.

can be explained by a slight displacement of the CoFe strip by $\sim 80\,\text{nm}$ in the negative y direction (see Fig. 4.1 in Ch. 4.1.1), which is likely due to an error in the alignment procedure during the fabrication of the samples. When we calculate the anomalous spin Hall angle with our spin-resistor model and include this displacement to the model, it only changes the value of $\theta^{\text{CoFe}}_{\text{ASH}}$ by 0.5 % and thus this geometry effect only plays a minor role in the quantification process. The lower panels **d** and **e** present the signals at the Pt2 and Pt3 electrode when the CoFe strip is used as the injector. Here, the difference in signal magnitude can also be attributed to the displacement of the CoFe electrode in the same quantitative way, thus supporting this claim.

A more interesting behaviour is observed for the small magnetic field ($\mu_0 H = 20\,\text{mT}$) rotations (blue data points). Here, the AMR in CoFe (Fig. 4.11**a**) exhibits a clear hysteresis due to the shape anisotropy of the electrode: the resistance switches for $\varphi > 0°$ ($\varphi > 180°$) for the forth rotation (dark blue), rather than directly at $\varphi = 0°$ ($\varphi = 180°$). As expected, this behaviour is inverted for the back rotation (light blue), showing a switching for $\varphi < 180°$ ($\varphi < 0°$). The low field magnon transport signal measured for the 'Pt2 - CoFe' configuration (Fig. 4.11**b**) exhibits several peaks in the signal modulation, which approximately correspond

to the magnetization switching of M_{CoFe} to a perpendicular state (indicated by the gray dashed vertical lines). These peaks are attributed to the increase of the magnon transport signal when the magnetization M_{CoFe} has a finite contribution perpendicular to the strip, such that the anomalous spin Hall effect (ASHE) becomes measurable along the strip. Unexpectedly, the back rotation exhibits these peaks with an inverted sign. This is most likely due to an opposing configuration of the YIG magnetization M_{YIG} and M_{CoFe} at these inverted peaks. Since the spin current polarization due to the ASHE is tunable via the magnetization direction of M_{CoFe}, and the diffusion direction of the Pt-injected magnons is determined by M_{YIG}, the sign of the resulting signal in the CoFe detector is dependent on the relative orientation of the two magnetizations. At the considered field of $\mu_0 H = 20\,\mathrm{mT}$, M_{YIG} can be assumed to closely follow the external magnetic field direction. The orientation of M_{CoFe}, however, is mostly determined by the shape anisotropy of the strip. Thus, the inverted peaks in the back rotation in Fig. 4.11**b** might be attributed to a rather complicated domain configuration in the CoFe electrode during the rotation, which can exhibit a net contribution of M_{CoFe} pointing oppositely to M_{YIG}. Here, it is important to note that in our experiments we conducted rotations over 400° in each direction and thus a slight misalignment of the external magnetic field with respect to the structure could be responsible for a different domain configuration for the two rotation directions. A similar peak structure can be observed for the 'Pt3 - CoFe' configuration in Fig. 4.11**c**. Surprisingly, however, the peaks are exactly inverted regarding the forth and back rotations, as compared to the behaviour for 'Pt2 - CoFe' configuration in Fig. 4.11**b**. Since the two measurements in panel **b** and **c** are obviously not measured in the same run, one could argue that the system was prepared differently regarding its domain configuration, resulting in a different relative orientation of M_{CoFe} and M_{YIG} during the rotation. The small magnetic field rotations for the case when the CoFe electrode is used as the injector, shown in Fig. 4.11**d** and **e**, do however not exhibit a clear modulation of the signal. All in all, the observed behaviour at small magnetic field rotations supports the picture that the shape anisotropy in the CoFe strip is the origin of the oberved features. Moreover, it supports the claim that the anomalous spin Hall angle in CoFe is responsible for the observed magnon transport signals, since the peak structure in the rotations suggests a very sensitive dependence on the relative orientation of M_{CoFe} with respect to M_{YIG}.

In the following, we focus on the asymmetry behaviour for $\mu_0 H = 2\,\mathrm{T}$ in Fig. 4.11**b** - **e** (red data points). Interestingly, the asymmetry feature for panel **b** and **c** (CoFe as detector) exhibits an inverted behaviour as compared to the lower panels **d** and **e** (CoFe as injector), suggesting that the asymmetry is reversed when the CoFe electrode is either used as an injector or detector. In order to further verify the appearance of this feature, we plot the fieldsweep measurements for the 'Pt2 - CoFe' and 'CoFe - Pt2' configurations in Fig. 4.12 **a** and **b**, respectively. As evident, we still oberve the asymmetry for magnetic fields $\mu_0 H \gtrsim 2\,\mathrm{T}$ and

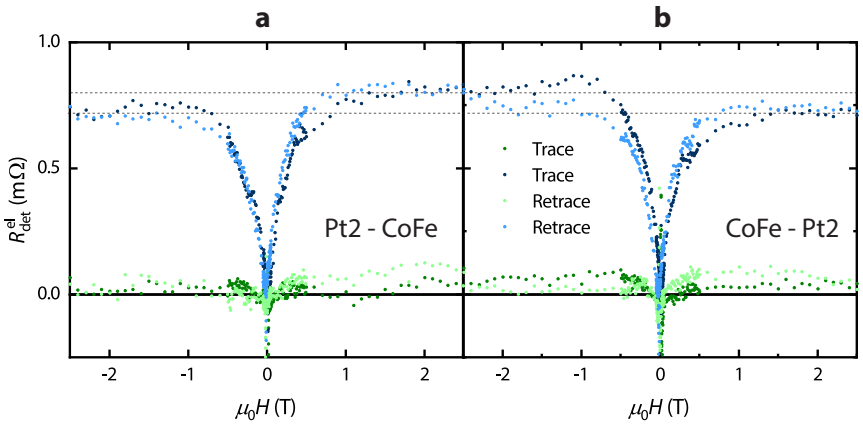

Fig. 4.12 – R^{el}_{det} measured as a function of magnetic field strength for field directions pointing perpendicular (blue) and parallel (green) to the strip length. Dark and light colored lines correspond to trace and retrace curves, respectively. In **a** the magnon transport signal for the Pt2 - CoFe (injector - detector) configuration is shown, which is inverted in **b**.

confirm the inversion of the feature when the CoFe electrode is changed from being used as a detector or injector (indicated by the horizontal gray dashed lines). Several possible sources of the observed asymmetry feature can be thought of in our device. First of all, the fact that the asymmetry is larger for high magnetic fields rules out any effects stemming from a misalignment of the YIG and CoFe magnetizations. Apart from this, the asymmetry behaviour does also not depend on the actual direction of the magnon spin current (i.e. magnon current flowing to the left or right from the CoFe injector, as measured in Fig. 4.11**d** and **e**), therefore ruling out any anisotropic dipolar magnon mode propagation effects. As theoretically proposed in Ref. [103], the observed asymmetry effect does resemble an unidirectional magnon transport effect. Here, the asymmetry is stemming from a non-linear injection of magnons but a linear depletion of the magnon system as a function of the injector current. Since our orientation dependent measurements switch between injection and depletion of the magnon system by reversing the magnetic field direction, an imbalance of the signal amplitudes similar to our results could occur. However, our current reversal method that we use for the detection of the electrically excited magnons is not sensitive to any current-induced imbalance between injection and depletion of magnons, hence ruling out non-linear magnon injection effects as well. For the same reason, we cannot attribute any effects arising from the difference in the density of states of the majority and minority spins in the ferromagnetic CoFe electrode. Due to the ASHE, the amount of electron spins on the top and bottom side of the CoFe electrode are not equal, hence one could relate the asymmetry to an asymmetric spin injection for different field directions. On the one hand, however, the current reversal method averages out this putative imbalance. On the other hand, it is not the actual amount of spins at particularly the YIG/CoFe interface that determines the spin injection but

rather the spin chemical potential, which is equal for both field directions [33, 36]. In conclusion, the asymmetry behaviour of magnon injection/detection with CoFe electrodes appears to be robust in our measurements. It is, however, not yet clear which mechanism is responsible for this interesting feature and requires further investigation.

4.4 Summary and Conclusion

The influence of using the ferromagnetic metal alloy $Co_{25}Fe_{75}$ to inject/detect magnon spin in the ferromagnetic insulator YIG has been investigated. We could verify recent observations of spin injection using Py electrodes [65], exhibiting an initial increase in the injection efficiency until the CoFe is saturated, followed by a decrease due to the field-induced decrease in thermal magnon number in the YIG. As a main result, we demonstrated the determination of the anomalous spin Hall angle $\theta_{\mathrm{ASH}}^{\mathrm{CoFe}}$ of CoFe employing a multiterminal spin injection/detection device. Using both paramagnetic Pt and ferromagnetic CoFe electrodes on the ferrimagnetic insulator YIG, we determined the magnon conductivity of YIG, the spin conductance of the YIG/CoFe interface and finally the anomalous spin Hall angle of CoFe on a single device. We based our analysis on a spin-resistor model [36] and found that the pure SHE contribution in CoFe is negligible, which is different to the finite SHE contribution reported for Py [65]. The negative anomalous spin Hall angle of CoFe was found to increase strongly by saturating M_{CoFe} with an applied magnetic field and shows a saturation value of $\sim 5\,\%$ for magnetic fields of $\mu_0 H \gtrsim 2\,\mathrm{T}$.

A yet unclear feature refers to the asymmetry of the magnon transport signals under magnetization reversal of the CoFe electrodes when using them as either injectors or detectors. Several possible sources of this asymmetry could be excluded, but an explanation of the effect is still missing. Since the effect requires a symmetry that is odd under magnetization reversal, the recently discovered magnetic spin Hall effect might be a possible source [71, 73]. Spin currents that occur due to interfacial effects could be another source for such odd magnetization dependent symmetries [160]. A more rigorous investigation of the signals, in particular including out-of-plane magnetotransport measurements, are however needed to test for this conjecture.

Using ferromagnetic metals for spin injection or detection offers a large playground for novel spin torque related physics. Due to a finite spin-orbit coupling and magnetic order in these materials, all symmetries are broken when allowing for arbitrary directions of the magnetization and the electric field/current direction, leading to rich spin current generation [63]. Spin currents unique to such systems, like the planar spin Hall spin current, have been utilized as efficient spin-orbit torque sources [68, 69]. Moreover, the signficant difference between the spin conductance g_{Pt} and g_{CoFe} measured in our experiment suggests

a considerable contribution of magnon-to-magnon interconversion at the YIG/CoFe interface. Future investigations in our CoFe/YIG devices should check for these magnetic contributions to the electric field-induced spin current generation as well as magnon transmutation, attempting to disentangle the various contributions to the spin current generation in ferromagnetic metals.

5 Full Spin Conductivity Control in a Three-terminal YIG/Pt Heterostructure

The fast and reliable transport of information represents an essential ingredient for modern technology. Independent of the particular nature of the mobile carriers used to transport this information, their efficient storage and control are crucial features for information processing systems. The indispensability of charge based DRAMs (dynamic random access memories) and the electron-based field effect transistor (FET) for modern information technology are striking examples for this. In particular, the FET embodies an almost immaculate device capable of controlling the electron conductivity over orders of magnitude.

Besides the well-established charge transport via electrons, there is broad interest in using their inherent spin degree of freedom for information processing. This makes the efficient manipulation of the associated spin currents, in particular the control over their conductivity, an important but also challenging task [176–179]. Magnons, the quantized excitations of the spin system in a magnetically ordered material, are one of the most promising candidates for transporting information encoded in the spin degree of freedom. However, in contrast to the number of charge carriers in an electronic conductor, the magnon number in a spin conductor is not conserved[25]. Inevitably, magnon mediated spin currents only prevail on a characteristic length scale, which is mainly determined by the magnetic Gilbert damping of the material. Thus, efficient ways of reducing and tuning the magnetic damping represent an important step towards magnonic spin transport devices.

Whereas the control of charge currents by electric fields is well established, the control of spin currents is still in its infancy and different methods are still under debate. One promising way to manipulate spin currents is to employ spin orbit torques (SOTs) in heavy metal (HM)/magnetic insulator (MI) bilayers[26] [156, 180–182]. Driving a charge current through the HM in contact with the MI, an antidamping-like spin torque can be exerted on the magnetization of the MI. Above a critical current, the magnetic damping is completely compensated via the SOT. For nano-structured devices, this damping compensation manifests itself in the emergence of auto-oscillations of the magnetization forming the basis of so-called spin torque oscillators [156, 180, 183, 184]. Moreover, recent experiments [181] demonstrated a 10-fold increase of the propagation length of

[25] Note that electronic charge ist also not conserved in modern charge-based storage devices such as DRAMs. The information in these volatile memory devices has to be refreshed on the ms scale.

[26] Obviously, SOTs in conducting ferromagnet/heavy metal bilayers are perfectly possible as well, we focus however on magnetic insulators in this thesis.

coherent spin-waves in a HM/MI waveguide upon application of a large charge current to the HM. Cornelissen *et al.* [172] reported that also the diffusive transport of incoherently generated magnons can be controlled by charge currents in HM/MI nanostructures.

In this Chapter, we demonstrate a proof-of-principle magnon transistor device consisting of three Pt nanostrip electrodes ('injector' (source), 'modulator' (gate) and 'detector' (drain)) attached to the ferrimagnetic insulator YIG (cf. Ch. 3.1.1), similar to the device presented in Ref. [172]. Here, magnon transport is measured between injector and detector (cf. Ch. 2.7), while the magnon conductivity is altered via injection of additional magnons by the third modulator electrode placed in between. In this manner, we achieve a damping-compensated region underneath the modulator, influencing the diffusive magnon transport from injector to detector. In a transistor language, this means that the source-drain magnon current can be manipulated by the gate electrode. Furthermore, we find various indications for the formation of a magnon Bose-Einstein condensate (BEC) that is supported by the observation of magnon transport with effectively zero resistance beneath the modulator. We shed light on the relation of the experimentally measured magnon conductivity and the excited frequency spectrum of the spin-orbit-torque induced magnetization dynamics via micromagnetic simulations.

In the following Ch. 5.1, we discuss theoretical aspects about the correlation between SOT induced magnetic damping compensation and charge current-induced magnon Bose-Einstein condensation, as well as the related magnon conductivity modulation due to electrical pumping. After introducing the sample layout and preliminary characterization measurements in Ch. 5.2, we investigate the spin transport due to the SHE-induced magnons in Ch. 5.3, and the thermally induced magnons in Ch. 5.4. Finally, an investigation of the spin-orbit-torque (SOT) induced magnetization dynamics via micromagnetic simulations employing the open source code *MuMax3* [185] is given in Ch. 5.5. A summary with concluding remarks is given in Ch. 5.6.

This Chapter extensively reuses parts of text and figures published in T. Wimmer, M. Althammer, L. Liensberger, N. Vlietstra, S. Geprägs, M. Weiler, R. Gross, H. Huebl, *Spin Transport in a Magnetic Insulator with Zero Effective Damping*, Physical Review Letters **123**, 257201 (2019).

5.1 Theoretical Considerations

The experimental results presented in the subsequent Sections can be satisfactorily rationalized via the theory of spin Hall oscillators (SHO) [91,156,180] as well as the theory of current-induced magnon BECs [186–188]. Thus, we will discuss the correlation between these two theories in Ch. 5.1.1. The subsequent Ch. 5.1.2 is concerned with the theoretical derivation of magnon conductivity changes under the influence of charge current induced spin current injection in a HM/MI bilayer.

5.1.1 Correlation between SHOs and Current Induced Magnon BEC

In general, both theoretical frameworks regarding SHOs and current induced magnon BEC basically describe a coherent oscillation of the magnetization that is dynamically sustained via SOT. While SHOs are described within a fully classical Landau-Lifshitz-Gilbert (LLG) model, the DC pumped magnon BEC theory relies on a quantum mechanical description of thermal and condensed magnons.

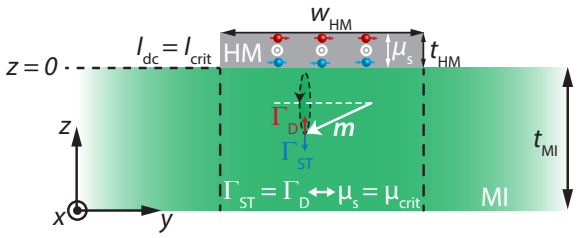

Fig. 5.1 – Schematic illustration of a MI with thickness t_{MI} in contact with a HM lead with thickness t_{HM} and width w_{MI}. A DC current I_{dc} applied to the HM leads to the build-up of the spin chemical potential μ_s due to the SHE. A spin-transfer torque Γ_{ST} is therefore acting on the precessing magnetization $\boldsymbol{m}$, which counteracts the intrinsic damping torque Γ_D. For $I_{dc} = I_{crit}$, it follows that $\Gamma_{ST} = \Gamma_D$ leading to an auto-oscillation of the magnetization. It is shown that this threshold condition is completely equivalent to the critical behaviour formulated in the theory of DC pumped magnon BEC, put forward in Ref. [187], and constitutes a mere reformulation of the torques in terms of the chemical potential energies μ_s and μ_{crit}. Note, that an antiparallel alignment of the spin direction at the interface and the magnetization $\boldsymbol{m}$ in the YIG results in a spin torque that reinforces the damping.

We start with the well-established description of SHOs. Here, auto-oscillation of the magnetization is achieved when the spin torque generated via the SHE in a HM compensates the intrinsic damping torque of an adjacent MI, which is schematically depicted in Fig. 5.1. The magnetic damping rate Γ_D (expressed in units of s^{-1}) is given by the ferromagnetic resonance (FMR) linewidth $\Delta\omega$ and reads

$$\Gamma_D = \Delta\omega = \alpha\mu_0\gamma\left(H + \frac{M_s}{2}(N_x + N_y - 2N_z)\right), \tag{5.1}$$

where α is the total magnetic damping constant, $\gamma = g\mu_B/\hbar$ the gyromagnetic ratio with the Landé factor g and the Bohr's magneton μ_B, μ_0 the vacuum permeabilty, H the external magnetic field, M_s the saturation magnetization of the MI and $N_{x,y,z}$ are the geometry-dependent demagnetization factors. For an out-of-plane magnetized thin film along z ($N_x = N_y = 0$, $N_z = 1$) in the presence of spin-pumping induced damping α_{sp}, we obtain

$$\Gamma_D^{oop} = \Delta\omega^{oop} = \left(\alpha_G + \alpha_{sp}\right)\gamma\mu_0\left(H - M_s\right), \tag{5.2}$$

while for an in-plane magnetized thin film in the x-y-plane ($N_x + N_y = 1, N_z = 0$) we find

$$\Gamma_D^{ip} = \Delta\omega^{ip} = \left(\alpha_G + \alpha_{sp}\right)\gamma\mu_0\left(H + \frac{M_s}{2}\right). \tag{5.3}$$

Here, we have set $\alpha = \alpha_G + \alpha_{sp}$ with α_G the intrinsic Gilbert damping constant [189, 190]. The anti-damping spin torque rate due to the SHE in the HM within the macrospin approximation is given by [180]

$$\Gamma_{ST} = \frac{\hbar}{2e}\frac{\gamma}{M_s t_{MI} t_{HM} w_{HM}}\mathcal{T}\theta_{SH} I_{dc} \tag{5.4}$$

with t_{MI} the film thickness of the MI layer, θ_{SH} the spin Hall angle of the HM and I_{dc} the DC current applied to the HM with thickness t_{MI} and width w_{HM}. $\mathcal{T}$ denotes the interface transparency for spin currents as put forward in Ref. [191] and reads as

$$\mathcal{T} = \frac{g_r^{\uparrow\downarrow}\tanh(\eta)}{g_r^{\uparrow\downarrow}\coth(2\eta) + \frac{h}{2e^2}\frac{\sigma_e}{l_s}}, \tag{5.5}$$

where $g_r^{\uparrow\downarrow}$ denotes the real part of the spin-mixing conductance and $\eta = t_{HM}/(2l_s)$ with the spin diffusion length l_s of the HM. In the following, we approximate $\coth(2\eta) \approx 1$ in Eq. (5.5). We further take into account that the spin mixing conductance $g_r^{\uparrow\downarrow}$ cannot be determined directly from experiments, but rather only the (real part of the) effective spin mixing conductance[27]

$$g_{eff}^{\uparrow\downarrow} = \alpha_{sp}\frac{4\pi M_s t_{MI}}{\hbar\gamma}. \tag{5.6}$$

The relation between these two is [77, 191–193]

$$g_r^{\uparrow\downarrow} = g_{eff}^{\uparrow\downarrow}\frac{\frac{h}{e^2}\frac{\sigma_e}{2l_s}}{\frac{h}{e^2}\frac{\sigma_e}{2l_s} - g_{eff}^{\uparrow\downarrow}}, \tag{5.7}$$

[27] In contrast to the finite temperature correction derived for the effective spin mixing conductance $\tilde{g}^{\uparrow\downarrow}$ defined in Ch. 2.5 (Eq. (2.36)), $g_{eff}^{\uparrow\downarrow}$ is a correction due to spin current backflow from the MI into the HM. When the HM is considered as a perfect spin sink, this correction can be neglected [77].

where e is the elementary charge, h the Planck constant, σ_e denotes the HM conductivity and l_s the spin diffusion length in the HM. When the condition $\Gamma_D = \Gamma_{ST}$ is met, the external spin torque compensates the intrinsic damping torque of the MI. Magnon modes with the lowest magnetic damping (i.e. the Gilbert damping α_G of the FMR mode) become unstable and grow exponentially in time. Hence, a coherent precession of the magnetization with zero effective damping emerges [189]. Note, that the discussed magnon excitation requires finite thermal fluctuations of the magnetization (i.e. finite temperature, cf. Ch. 2.5) as well as a finite interaction between magnons (which is given by the exchange interaction of the magnet). In the DC pumped magnon BEC theory put forward in Ref. [187], Bender *et al.* give two characteristic threshold conditions for either the magnon BEC transition and the so called 'swasing' transition[28]. For the spin chemical potential μ_s at the MI/HM interface (for an out-of-plane magnetized film), these criteria read as

$$\mu_{on}^{oop} = \left(1 + \frac{\alpha_G}{2\alpha_{sp}}\right) \hbar\Omega^{oop} \tag{5.8}$$

$$\mu_{crit}^{oop} = \left(1 + \frac{\alpha_G}{\alpha_{sp}}\right) \hbar\Omega^{oop}, \tag{5.9}$$

which only differ by a prefactor of $1/2$ before the damping ratio term α_G/α_{sp}. Here, $\Omega^{oop} = \gamma\mu_0(H - M_s)$ is the fundamental ferromagnetic resonance frequency for an out-of-plane magnetized film derived from the Kittel formula [194]

$$\Omega = \mu_0\gamma\sqrt{[H + M_s(N_x - N_z)][H + M_s(N_y - N_z)]}. \tag{5.10}$$

We note, that the ratio $\frac{\alpha_G}{\alpha_{sp}}$ in Eqs. (5.8) and (5.9) accounts for the interface spin transparency in this model. The threshold μ_{on} is defined by the onset of the condensation of magnons, i.e. by the condition $n_c = 0$ (where n_c denotes the number of condensed magnons) [187]. For $\mu_s > \mu_{on}$, a continuous condensation of magnons sets in, characterizing it as a phase transition of second order [187]. At $\mu_s = \mu_{crit}$, the damping is fully compensated by the external spin torque, which is also known as 'swasing' [91]. For μ_{crit}^{oop}, one can easily show that

$$\mu_{crit}^{oop} = \frac{\hbar}{\alpha_{sp}}\Gamma_D^{oop}, \tag{5.11}$$

meaning that the swasing threshold condition is identical to the critical condition of SHOs (i.e. the compensation of the damping rate) and therefore represents a mere reformulation of damping rates to spin chemical potentials. This can be easily

[28] The term 'swasing' stems from the artificial word SWASER firstly introduced by L. Berger in 1996 [91] in analogy to the optical LASER. The analogy is based around the fact that the spin up and down states of the conduction electrons are 'pumped' into different energy states with an energy splitting given by the spin chemical potential μ_s, which is somewhat similar to the pumping of photon states in a lasing device.

understood by considering two limiting cases: for a fully transparent interface, where $\frac{\alpha_G}{\alpha_{sp}} \ll 1$, the critical chemical potential is equal to the spin wave gap $\hbar\Omega^{oop}$. For a fully opaque interface, however, $\frac{\alpha_G}{\alpha_{sp}} \to \infty$, leading to a divergence of the threshold.

The direct proportionality of $\mu^{oop}_{on/crit}$ to the FMR frequency Ω^{oop} in Eqs. (5.8) and (5.9) is solely valid for an out-of-plane magnetized film. For the in-plane configuration, we instead have to consider the in-plane frequency linewidth[29] and obtain

$$\mu^{ip}_{on} = \left(1 + \frac{\alpha_G}{2\alpha_{sp}}\right)\hbar\gamma\mu_0\left(H + \frac{M_s}{2}\right) \tag{5.12a}$$

$$\mu^{ip}_{crit} = \frac{\hbar}{\alpha_{sp}}\Gamma^{ip}_D = \left(1 + \frac{\alpha_G}{\alpha_{sp}}\right)\hbar\gamma\mu_0\left(H + \frac{M_s}{2}\right). \tag{5.12b}$$

The spin chemical potential at the MI/HM interface induced via the SHE can be derived from the spin diffusion equation (2.23). Assuming no spin transfer at the interface, one obtains [33, 36, 110]

$$\mu^0_s = \frac{e\theta_{SH} I_{dc}}{w_{HM}\sigma_e \eta}\tanh(\eta) \tag{5.13}$$

We now combine Eq. (5.7), (5.3), (5.4) and (5.5) and find $\mu^0_s = \frac{\hbar}{\alpha_{sp}}\Gamma_{ST}$. Hence, the swasing threshold $\mu_s = \mu_{crit}$ is indeed fully identical to the SHO threshold $\Gamma_{ST} = \Gamma_D$ for in-plane and out-of plane configurations.

Ultimately, we can now solve the critical conditions for the experimentally accessible DC current I_{dc} applied to the HM. We focus on the experimentally relevant in-plane magnetized case by equating Eqs. (5.12a) and Eq. (5.12b), respectively, to Eq. (5.13). Hence, we find the critical currents (for the in-plane case)

$$I_{on} = \frac{\eta w_{HM}\sigma_e}{e\theta_{SH}}\coth(\eta)\left(1 + \frac{\alpha_G}{2\alpha_{sp}}\right)\hbar\gamma\mu_0\left(H + \frac{M_s}{2}\right), \tag{5.14a}$$

$$I_{crit} = \frac{\eta w_{HM}\sigma_e}{e\theta_{SH}}\coth(\eta)\left(1 + \frac{\alpha_G}{\alpha_{sp}}\right)\hbar\gamma\mu_0\left(H + \frac{M_s}{2}\right), \tag{5.14b}$$

which can be reformulated to current densites as $J_{on} = I_{on}/(w_{HM}t_{HM})$ and $J_{crit} = I_{on}/(w_{HM}t_{HM})$. In order to describe real experiments, we have to take into account the inhomogeneous line broadening of the MI, as demonstrated in Ref. [180]. To this end, we follow Ref. [180] and introduce an effective (frequency-dependent) damping parameter

$$\alpha_{eff} = \alpha_G + \gamma\mu_0\frac{\delta H}{2\Omega^{ip}} \tag{5.15}$$

[29] The proportionality $\mu^{oop}_{on/crit} \propto \Omega^{oop}$ in Eqs. (5.8) and (5.9) stems from the (coincidental) equality $\alpha\Omega^{oop} = \Delta\omega^{oop} = \alpha\gamma\mu_0(H - M_s)$. Therefore, the threshold conditions can be expressed via the out-of-plane FMR frequency Ω^{oop}. Since, however, $\alpha\Omega^{ip} \neq \Delta\omega^{ip}$, this does not apply for in-plane magnetized films.

where the second term accounts for the damping introduced via the inhomogenous broadening δH of the magnetic thin film, which arises due to sample inhomogeneitites resulting in enhanced two-magnon scattering processes [195]. The FMR frequency $\Omega^{\mathrm{ip}} = \gamma\mu_0\sqrt{H(H+M_\mathrm{s})}$ is calculated from Eq. (5.10) for the in-plane configuration (considering the external field H to point along the y-axis, such that $N_x = N_z = 0$ and $N_y = 1$). By substituting α_G with α_eff in Eqs. (5.14a) and (5.14b), we arrive at the final result for the critical currents.

We note, that our result for the current threshold conditions can be easily generalized to include crystalline anisotropy contributions of the MI. To this end, we simply substitute $H \to H + H_\mathrm{ani}$, where H_ani is the crystalline anisotropy field determined by the details of the crystal structure [194]. For our experimentally relevant case, we consider a cubic crystal with (100)-orientation (see Ch. 5.2.1), where the external field points along an easy axis along a [100] direction. In that case, the anisotropy field simply reduces to $H_\mathrm{ani} = 2K_{\mathrm{c}1}/M_\mathrm{s}$, where $K_{\mathrm{c}1}$ is the cubic anisotropy constant [194]. We make use of this generalization in Ch. 5.3.4.

5.1.2 Modulation of Magnon Conductivity via Electrical Pumping

We now derive how an external spin current injection (in the sense of magnon injection) influences the magnon conductivity σ_m in a MI. As derived in Ch. 2.7.2 (see Eq. (2.55)), $\sigma_\mathrm{m} = 3\hbar n_\mathrm{m}\tau_\mathrm{m}/m_\mathrm{m}$. While the effective magnon mass m_m is fixed via the dispersion relation, the magnon density n_m and magnon relaxation time τ_m can be tuned via external spin current injection [172, 188]. In the first part of the following discussion, we will derive the magnon density induced change of σ_m in a MI due to electrical pumping in an adjacent HM layer, while assuming a constant τ_m. The second part considers changes in the magnon relaxation time and its effect on σ_m by applying a very simple model considering relaxation rate compensation by the external spin torque. We further discuss a more rigorous attempt to calculate the magnon conductivity as a function of electrical spin current injection within the non-linear regime based on recent literature.

Magnon Density Induced Modulation of σ_m

A DC current density $j_\mathrm{dc} = I_\mathrm{dc}(t_\mathrm{HM}w_\mathrm{HM})^{-1}$ in a HM/MI heterostructure causes a finite spin chemical potential μ_s^0 at the HM/MI interface via the SHE. According to Eq. (2.43), this leads to an interfacial magnon spin current $\boldsymbol{j}^z_{\mathrm{s,int}} = \left[g(\mu_\mathrm{m}^0 - \mu_\mathrm{s}^0\boldsymbol{s}\cdot\boldsymbol{m}) + S\delta T\right]\boldsymbol{m}$, where $\boldsymbol{m}$ is the unit vector of the magnetization in the MI and δT is the interfacial temperature difference between magnons and electrons. Considering the MI/HM bilayer illustrated in Fig. 5.1 and further assuming only one spatial dimension along the z direction, the spatial distributions of the spin chemical potential $\boldsymbol{\mu}_\mathrm{s} = \mu_\mathrm{s}\boldsymbol{s}$ polarized along $\boldsymbol{s}$ and the magnon chemical potential

$\boldsymbol{\mu}_\mathrm{m} = \mu_\mathrm{m}\boldsymbol{m}$ along $\boldsymbol{m}$ are determined by the one-dimensional spin diffusion equations (cf. Eqs. (2.23) and (2.60))

$$\frac{\partial^2 \boldsymbol{\mu}_\mathrm{s}}{\partial z^2} = \frac{\boldsymbol{\mu}_\mathrm{s}}{l_\mathrm{s}^2}, \tag{5.16}$$

$$\frac{\partial^2 \boldsymbol{\mu}_\mathrm{m}}{\partial z^2} = \frac{\boldsymbol{\mu}_\mathrm{m}}{\lambda_\mathrm{m}^2}, \tag{5.17}$$

where we assumed steady state conditions and used the spin diffusion and magnon diffusion length $l_\mathrm{s} = \sqrt{D_\mathrm{s}\tau_\mathrm{s}}$ and $\lambda_\mathrm{m} = \sqrt{D_\mathrm{m}\tau_\mathrm{mr}}$, respectively. The general solution of these differential equations is given by $\mu_{\mathrm{s(m)}}(z) = A\exp\left[-z/\zeta_{\mathrm{s(m)}}\right] + B\exp\left[z/\zeta_{\mathrm{s(m)}}\right]$, where $\zeta_\mathrm{s} = l_\mathrm{s}$, $\zeta_\mathrm{m} = \lambda_\mathrm{m}$ and the coefficients A and B are determined by the boundary conditions. The latter are given by the spin currents at the upper boundary of the HM at $z = t_\mathrm{HM}$, the HM/MI interface at $z = 0$ and the lower boundary of the MI at $z = -t_\mathrm{MI}$. The spin currents in our HM layer are composed of a diffusive spin current and a SHE induced spin current according to Eqs. (2.18) and (2.24). As a result, the boundary conditions in the HM are given by[30]

$$-\sigma_\mathrm{s}\left.\frac{\partial \mu_\mathrm{s}(z)}{\partial z}\right|_{z=0}\boldsymbol{s} - j_\mathrm{s}^\mathrm{SH}\boldsymbol{s} = \left[g(\mu_\mathrm{m}^0 - \mu_\mathrm{s}^0\boldsymbol{s}\cdot\boldsymbol{m}) + S\delta T\right]\boldsymbol{m}, \tag{5.18}$$

$$-\sigma_\mathrm{s}\left.\frac{\partial \mu_\mathrm{s}(z)}{\partial z}\right|_{z=t_\mathrm{HM}}\boldsymbol{s} - j_\mathrm{s}^\mathrm{SH}\boldsymbol{s} = 0 \tag{5.19}$$

with $j_\mathrm{s}^\mathrm{SH} = \frac{\hbar}{2e}\theta_\mathrm{SH} j_\mathrm{dc}$ the SHE induced spin current (cf. Eq. (2.24)) due to the DC charge current density j_dc in the HM layer and $\mu_{\mathrm{s(m)}}^0 = \mu_{\mathrm{s(m)}}(z=0)$ the magnon (spin) chemical potential at the interface. The spin currents at the boundaries of the MI are

$$-\sigma_\mathrm{m}\left.\frac{\partial \mu_\mathrm{m}(z)}{\partial z}\right|_{z=0}\boldsymbol{m} = \left(g(\mu_\mathrm{m}^0 - \mu_\mathrm{s}^0\boldsymbol{s}\cdot\boldsymbol{m}) + S\delta T\right)\boldsymbol{m}, \tag{5.20}$$

$$-\sigma_\mathrm{m}\left.\frac{\partial \mu_\mathrm{m}(z)}{\partial z}\right|_{z=-t_\mathrm{MI}}\boldsymbol{m} = 0. \tag{5.21}$$

Depending on the relative orientation of $\boldsymbol{s}$ and $\boldsymbol{m}$, magnons are injected into the MI when $\boldsymbol{s}\cdot\boldsymbol{m} > 0$ and depleted from the MI when $\boldsymbol{s}\cdot\boldsymbol{m} < -1$. Applying the boundary conditions and solving the differential equations for $\boldsymbol{s}\cdot\boldsymbol{m} = +1$ (parallel orientation) and $\boldsymbol{s}\cdot\boldsymbol{m} = -1$ (antiparallel orientation), we obtain for the magnon chemical potential (polarized along m)

$$\mu_\mathrm{m}^\pm(z) = \frac{\left(\pm g j_\mathrm{s}^\mathrm{SH}(\delta_\mathrm{ms} - \lambda_\mathrm{m} l_\mathrm{s}) - \alpha_\mathrm{ms} S\delta T\right)\left(\mathrm{e}^{-z/\lambda_\mathrm{m}} + \mathrm{e}^{\eta_\mathrm{m}}\mathrm{e}^{z/\lambda_\mathrm{m}}\right)}{g\alpha_\mathrm{ms}(\mathrm{e}^{\eta_\mathrm{m}}+1) + g\beta_\mathrm{ms}(\mathrm{e}^{\eta_\mathrm{m}}-1) + \gamma_\mathrm{ms}(\mathrm{e}^{\eta_\mathrm{m}}-1)} \tag{5.22}$$

[30] In contrast to the definition of the SHE induced spin current in Eq. (2.24) and the diffusive spin current in Eq. (2.18), which are both expressed as vectors denoting the spin current flow direction, we here define them to point along the spin polarization direction $\boldsymbol{s}$, while their current flow direction is fixed along the z-direction.

with $\eta_m = 2t_{MI}/\lambda_m$, $\eta = t_{HM}/(2l_s)$ and μ_m^+ (μ_m^-) refers to the magnon chemical potential for parallel (antiparallel) orientation of $\boldsymbol{s}$ and $\boldsymbol{m}$. We have further defined the parameters

$$\alpha_{ms} = \lambda_m \sigma_s \sinh(2\eta), \tag{5.23}$$

$$\beta_{ms} = \sigma_m l_s \cosh(2\eta), \tag{5.24}$$

$$\gamma_{ms} = \sigma_m \sigma_s \sinh(2\eta), \tag{5.25}$$

$$\delta_{ms} = \lambda_m l_s \cosh(2\eta). \tag{5.26}$$

In the experiments in this Chapter, we consider a MI (YIG) with a thickness of about $\sim 10\,\mathrm{nm}$, which is very small compared to the magnon diffusion length λ_m of typically a few µm in YIG [8]. We can thus apply the valid approximation $\exp(\eta_m) \approx 1$ in Eq. (5.22). We are further mainly interested in the average magnon chemical potential $\langle \mu_m^\pm \rangle = t_{MI}^{-1} \int_{-t_{MI}}^{0} \mu_m^\pm(z)\, \mathrm{d}z$ across the thickness of the MI, for which we finally obtain

$$\langle \mu_m^\pm \rangle = \left(\pm \frac{j_s^{SH} l_s}{\sigma_s} \tanh(\eta) - \frac{S}{g} \delta T \right) \frac{\lambda_m}{t_{MI}} \sinh\left(\frac{t_{MI}}{\lambda_m} \right). \tag{5.27}$$

It is worth noting that the first term in brackets in Eq. (5.27) can be identified with $\mu_s^0/2$, i.e. half of the SHE induced interfacial spin chemical potential (assuming no interfacial spin transfer), as introduced in Eq. (5.13). For $t_{MI}/\lambda_m \ll 1$, we can make a further approximation according to $\frac{\lambda_m}{t_{MI}} \sinh\left(\frac{t_{MI}}{\lambda_m}\right) \approx 1$. As we have finally arrived at a rather simple expression for μ_m, we now express it as a function of the experimentally most relevant parameter I_{dc}. To this end, we use the fact that the temperature difference δT is generally proportional to the Joule heating power $P_J \propto I_{dc}^2$ [196], i.e. $\delta T = -c I_{dc}^2$ with c an appropriate conversion factor[31]. We then obtain

$$\langle \mu_m^\pm \rangle (I_{dc}) = \pm \frac{e \theta_{SH} l_s \tanh(\eta)}{\sigma_e t_{HM} w_{HM}} I_{dc} + \frac{S}{g} c\, I_{dc}^2, \tag{5.28}$$

where we used $\sigma_s = \hbar/(2e^2)\sigma_e$ and $j_s^{SH} = \frac{\hbar}{2e} \theta_{SH} j_{dc}$. As expected, the magnon chemical potential in linear response has a linear and quadratic contribution in I_{dc} due to the SHE- and thermally-induced injection of magnons [8, 172]. Having established how μ_m reacts to a charge current I_{dc}, we now calculate the non-

[31] Assuming $c > 0$, the minus sign in the equation $\delta T = -c I_{dc}^2$ is introduced due to $T_e > T_m$ and thus $\delta T < 0$ (when current induced heating of the HM layer is considered). Hence, we accounted for the fact that current induced heating and the associated magnon injection will always enhance the magnon chemical potential rather than reduce it (i.e. inject magnons in the MI rather than depleting them).

equilibrium magnon density $n_m(\langle\mu_m^{\pm}\rangle, T)$ (in linear approximation assuming a vanishing magnon gap Δ, compare Ch. 2.7.2) as

$$\begin{aligned} n_m(\langle\mu_m^{\pm}\rangle, T) &= \int_0^{\infty} d\epsilon_m\, g(\epsilon_m) n_B(\epsilon_m, \langle\mu_m^{\pm}\rangle, T) \\ &= n_m^0 + \frac{\zeta(1/2)}{\Lambda^3 k_B T}\langle\mu_m^{\pm}\rangle = n_m^0 + \Delta n_m, \end{aligned} \tag{5.29}$$

with $n_m^0 = \zeta(3/2)\Lambda^{-3}$ the magnon density in thermal equilibrium and $\Delta n_m = \rho_m/\hbar$ the non-equilibrium magnon number density as introduced in Ch. 2.7.2 (cf. Eq. (2.59)). We see that a finite magnon chemical potential μ_m is directly connected to an enhanced magnon density n_m. We further also find that $n_m \propto I_{dc} + I_{dc}^2$ in linear response (cf. Eq. (5.28)), meaning that we are able to tune the magnon density by a charge current in the HM similar to μ_m [8,36]. As rigorously derived in Ch. 2.7.2, the magnon conductivity in linear response theory can then be expressed as [172]

$$\begin{aligned} \sigma_m &= 3\hbar\frac{n_m\tau_m}{m_m} = 3\hbar\frac{\tau_m}{m_m}\left(n_m^0 + \Delta n_m\right) \\ &= 3\hbar\frac{\tau_m}{m_m}\left(n_m^0 + \frac{\zeta(1/2)}{\Lambda^3 k_B T}\left(\pm\frac{e\theta_{SH} l_s \tanh(\eta)}{\sigma_e t_{HM} w_{HM}} I_{dc} + \frac{S}{g} c\, I_{dc}^2\right)\right) \\ &= \sigma_m^0 \pm \Delta\sigma_{SHE} I_{dc} + \Delta\sigma_{th} I_{dc}^2, \end{aligned} \tag{5.30}$$

where τ_m is the total magnon scattering time (see Ch. 2.7.2) and m_m is the effective magnon mass. We have further introduced the magnon conductivity in thermal equilibrium σ_m^0, the SHE induced magnon conductivity change $\Delta\sigma_{SHE}$ and the thermally induced magnon conductivity change $\Delta\sigma_{th}$, which can easily be identified in Eq. (5.30). Different to electrical transport, the magnon density n_m is typically not constant. According to Eq. (5.30), a change in magnon density due to a DC current I_{dc} in an adjacent HM is expected to modify the magnon conductivity in a linear and quadratic fashion.

Magnon Relaxation Time Induced Modulation of σ_m

The rather simplified description of electrically induced magnon conductivity modulation given above assumes that the DC spin current injection via the spin chemical potential μ_s only affects the magnon density n_m, while the magnon relaxation time τ_m is unchanged. This description works well within a low bias regime where the current-induced magnon chemical potential μ_m is well below the magnon gap [172], but becomes inaccurate within the non-linear regime of spin current injection [197]. A very simple idea of how the magnon relaxation time changes due to spin current injection can be derived when we make the crude assumption that the total (inverse) of the magnon relaxation time is given by the difference of the damping and spin torque rate, i.e. $(\tau_m)^{-1} = \Gamma_D - \Gamma_{ST}$ (the minus

sign is valid when we assume spin current injection rather than depletion). The magnon conductivity (assuming constant magnon density n_m) then becomes

$$\sigma_m = 3\hbar \frac{n_m}{m_m} \left(\Gamma_D - \Gamma_{ST}\right)^{-1} = 3\hbar \frac{n_m \tau_m^0}{m_m} \left(1 - \frac{I_{dc}}{I_{crit}}\right)^{-1}, \tag{5.31}$$

where we introduced the equilibrium magnon relaxation time $\tau_m^0 = (\Gamma_D)^{-1}$ and we identified $\Gamma_{ST}/\Gamma_D = I_{dc}/I_{crit}$. This crude model demonstrates that the magnon relaxation time and thus magnon conductivity diverges as $I_{dc} \to I_{crit}$, thereby introducing a non-linearity to the current induced modulation of σ_m. In a more rigorous theory work published recently in Ref. [188], the magnon conductivity near damping compensation is calculated in a more accurate manner, especially considering non-equilibrium distributions and finite temperature effects. Here, an inverse square root dependence according to $\sigma_m \propto (1 - \mu_s/\mu_{crit})^{-1/2} \propto (1 - I_{dc}/I_{crit})^{-1/2}$ is found at room temperature. Since this expression only accounts for the SHE-induced pumping of the magnon system, we add the expected thermally-induced quadratic magnon injection due to the spin Seebeck effect (cf. Eq. (5.30)) and obtain

$$\sigma_m = \sigma_m^0 \left(1 - \frac{I_{dc}}{I_{crit}}\right)^{-1/2} + \Delta\sigma_{th} I_{dc}^2. \tag{5.32}$$

We will make use of this inverse square root dependence of electrically induced magnon conductivity modulation in Ch. 5.3.4. According to Ref. [188], the exponent in Eq. (5.32) approaches $-1/2$ for large temperatures (room temperature and above), but also surpasses -1 towards lower temperatures. Hence, our crude derivation represented by Eq. (5.31) can be considered as a lower temperature limit. In contrast to the non-linear response function given by the first term in Eq. (5.32), the thermal spin Seebeck torque contribution $\Delta\sigma_{th} I_{dc}^2$ stems from the linear response model derived in Eq. (5.30). This implicitly assumes that the spin Seebeck torque does not lead to non-linear effects in the magnetization dynamics/magnon conductivity. This assumption is in accordance with theory [187, 188], stating that the temperature induced spin Seebeck torque is not capable of magnon condensation (i.e. damping compensation) by itself since the magnon system is always accompanied by a temperature rise that prevents condensation.

We want to emphasize that the magnon conductivity modulation by electrical pumping can generally not be narrowed down to changes in either the magnon density n_m or the magnon relaxation time τ_m. In particular, the clear separation of these two quantities is only valid in the linear response regime, whereas the magnon conductivity becomes far more complex for large electrical pumping due to non-equilibrium distributions [188]. Indeed, we will see in Ch. 5.3 that in the low bias current regime, where μ_m is sufficiently small and therefore linear response

holds true, the magnon conductivity modulation is well described by changes in the magnon density according to Eq. (5.30). For large electrical pumping in the non-linear regime, on the other hand, a diverging character of σ_m is observed, which can be characterized by an infinite τ_m as indicated by the crude analysis given in Eq. (5.31). Although a clear differentiation between the two quantities is not possible in our experiment, we will mostly argue with a changing magnon density n_m in the linear regime, while we refer to a diverging magnon relaxation time τ_m in the non-linear regime.

5.2 Experimental Methods and Preliminary Measurements

In the following, we will introduce the sample geometry of the YIG/Pt bilayer and how it can be used to measure and purposefully alter the magnon conductivity. Furthermore, we present preliminary characterization measurements of our sample, including atomic force microscopy (AFM) to verify the spatial dimensions of the nanostructures, a characterization of the magnetic damping via ferromagnetic resonance (FMR) measurements, thermometry measurements to study the temperature rise due to the applied charge currents in the Pt strips, a quantification of the spin Seebeck effect driven by the induced temperature gradient at the YIG/Pt interface and finally the influence of the magnetocrystalline anisotropy on our measurements.

5.2.1 Sample Layout and Measurement Principle

The $t_{YIG} = 13.4\,nm$ thick, single crystalline (100)-oriented yttrium iron garnet ($Y_3Fe_5O_{12}$, YIG) film (cf. Ch. 3.1.1) used for the experiments presented in this Chapter was grown via pulsed laser deposition at the Walther-Meißner-Institut on a gadolinium gallium garnet ($Gd_3Ga_5O_{12}$, GGG) substrate using a substrate temperature of 450 °C, an oxygen pressure of 25 µbar, a laser fluence at the target of $2.0\,J/cm^2$ and a laser frequency of 10 Hz. The $t_{Pt} = 3.5\,nm$ thick Pt strips were deposited on the YIG thin film by DC sputtering and were patterned by e-beam lithography as described in detail in Ch. 3.2. For the experiments conducted in this Chapter, we have prepared nanostructured devices consisting of four parallel Pt nanostrips. The strips have varying center-to-center separations d and constant widths of $w = 500\,nm$ (see Fig. 5.2**a**). The lengths of the Pt strips are $l_{Pt} = 148\,\mu m/162\,\mu m$ (the two center strips are slightly longer than the outer ones). Subsequently, Ti/Al layers of 5/50 nm were deposited on the film by DC sputtering and patterned into leads for the Pt strips to contact the device electrically. An optical micrograph of the device is shown in Fig. 5.2**b**. As indicated in the Figure, only three of the four Pt strips are used for the majority of the measurements in this Chapter, which we label as 'injector', 'modulator' and 'detector'. The majority

of the measurements shown in this Chapter are also focussed on one main device with strip separation $d = 900\,\mathrm{nm}$.

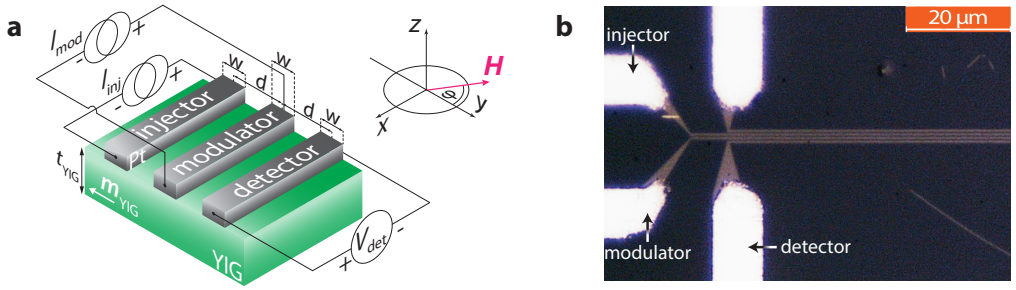

Fig. 5.2 – a Schematic depiction of the device, the electrical connection scheme and the coordinate system. An AC current $I_{\mathrm{inj}}(t) = I_0 \sin(\omega t)$ is applied to the injector, while the detector voltage V_{det} is measured via lock-in detection (see Sec. 3.4.2). Simultaneously, a DC current I_{mod} is applied to the modulator strip. **b** Optical micrograph of a section of a typical device (the electrical contacts to the injector, modulator and detector on the right hand side are not shown). Black regions correspond to the YIG surface, while the Pt strips appear in dark grey. The strips are contacted with 5 nm/50 nm thick Ti/Al leads (white). Usually, the strips are used as indicated in the figure, which corresponds to the schematic in panel **a**. The uppermost strip is utilized for some additional measurements presented within Ch. 5.3.5.

The principle of our magnon conductance measurement is inspired by recent DC magnetotransport experiments that infer magnon transport properties in YIG [8, 9, 36, 117, 161, 162, 197–199]. As shown in Fig. 5.2**a**, magnons are injected from a Pt strip (injector) into the YIG film using a low-frequency charge current $I_{\mathrm{inj}} = I_0 \sin(\omega t)$ with $I_0 = 50\,\mu\mathrm{A}$ and $\omega/(2\pi) = f = 13.131\,\mathrm{Hz}$ via both the spin Hall effect (SHE) [42, 43] and thermal excitation of magnons due to Joule heating (cf. Ch. 2.7). The diffusive transport of these magnons is quantified by electrically measuring the magnon density below a second Pt strip (detector) as the first harmonic voltage signal $V_{\mathrm{det}}^{1\omega}$ (for SHE-induced magnons) and second harmonic voltage $V_{\mathrm{det}}^{2\omega}$ (for thermally induced magnons) via lock-in detection, exploiting the inverse SHE (see Ch. 3.4.2). Cornelissen *et al.* [172] demonstrated that the magnon transport in such an arrangement can be manipulated by a DC charge current I_{mod} applied to a third (modulator) strip placed in between injector and detector (cf. Fig. 5.2**a**). As rigorously derived in Ch. 5.1.2, the magnon density n_{m} underneath the modulator is influenced by I_{mod} via two contributions: (i) SHE-induced spin accumulation at the YIG/Pt interface and (ii) Joule heating in the Pt strip. In linear response, these two contributions modulate the magnon conductivity according to $\sigma_{\mathrm{m}} \propto I_{\mathrm{mod}} + I_{\mathrm{mod}}^2$. For very large currents I_{mod} (where linear response does not apply anymore), the conductivity modulation is expected to behave in accordance with Eq. (5.32). We note, that the use of the lock-in detection technique is essential to distinguish between magnons stemming from the DC driven modulator and the AC driven injector which is picked up as a voltage signal in the detector [161, 172]. Therefore, any change in the first/second harmonic signals measured at the detector as a function of the DC modulator

current I_{mod} reflects a magnon conductivity change, rather than a mere increase of signal due to a second magnon source.

It should be emphasized that we consider the magnon transport from injector to detector to be exclusively driven by the AC magnon chemical potential gradient $\nabla\mu_{\mathrm{m}}$ induced at the injector, in fact for both SHE- as well as thermally induced spin current injection (characterized by the interfacial spin conductance g and interfacial spin Seebeck coefficient S introduced in Ch. 2.5, respectively). Indeed, it has been shown that this assumption is perfectly valid for the SHE-induced magnon transport, since temperature gradient-driven magnon currents induced by the linear (in current) spin Peltier effect (SPE) [200] have been found to be insignificant in experiments [36]. The thermally induced magnon transport, on the other hand, is significantly affected by temperature gradient-driven magnon currents since the Joule heating induced quadratic (in current) temperature rise at the injector is far more pronounced. While we will not consider this additional complexity for the thermal signals within this Chapter, we will analyze this peculiarity in more detail in Ch. 7.1, where we attempt to interpret the thermal magnon transport modulations by including temperature gradient-driven effects[32]. As for now, our assumption entails that any change in the magnon transport induced by the DC modulator current can be retraced exclusively to a change in the magnon conductivity σ_{m}. As discussed in Ch. 5.1.2, the magnon conductivity beneath the modulator electrode is altered by the DC current I_{mod}, which in turn alters the AC magnon transport signal measured at the detector. In the experiment, this change is quantified by the I_{mod} dependence of the first and second harmonic voltage readings $V_{\mathrm{det}}^{1\omega}$ and $V_{\mathrm{det}}^{2\omega}$, respectively. We thus expect

$$V_{\mathrm{det}}^{1\omega,2\omega}(I_{\mathrm{mod}}) \propto \sigma_{\mathrm{m}}(I_{\mathrm{mod}}), \tag{5.33}$$

where $\sigma_{\mathrm{m}}(I_{\mathrm{mod}})$ has been derived for the low current bias regime in Eq. (5.30), while the large current bias regime is expected to behave according to Eq. (5.32). Note, that the magnon conductivity reduces to its equilibrium value σ_{m}^{0} for $I_{\mathrm{mod}} = 0$. Unlike the conventional definition of a conductivity, which represents a local quantity describing the response function between a local current density and a local driving field (like the electric field in the case of charge transport), our experimental setting illustrated in Fig. 5.2**a** measures the detector signal as a result of the current I_{inj} at the injector. Hence, the ratio $V_{\mathrm{det}}^{1\omega,2\omega}/I_{\mathrm{inj}}$ can only be considered as a formal conductivity[33] as it does not reflect a local correlation between a current

[32] Next to temperature gradient-driven magnon spin currents, also pure phononic heat transport due to a gradient in ∇T_{p} from injector to detector is expected and can potentially generate a detector signal according to the local spin Seebeck effect. Such an effect was however estimated to be insignificant in experiments [124].

[33] We note that the ratio $V_{\mathrm{det}}^{1\omega,2\omega}/I_{\mathrm{inj}}$ has, formally, units of a resistance rather than conductance, which seems to be at odds with our discussion that the signal is proportional to the magnon conductivity σ_{m}. It must be recalled, however, that the injector current I_{inj} serves as the 'driving field' since it induces the magnon chemical potential gradient $\nabla\mu_{\mathrm{m}}$, while the measured detector

and driving field. In other words, due to the multiple conversion processes from injector to detector, i.e. charge current to electronic spin current to magnon current and vice versa, the detector signal contains much more information than just the magnon conductivity, but also the interfacial and metallic spin conductivities contribute to the resulting signal. Since we do not expect a significant DC current induced change in the latter two quantities, we view the I_{mod} dependence of $V_{\mathrm{det}}^{1\omega}$ and $V_{\mathrm{det}}^{2\omega}$ exclusively as a change of magnon conductivity. Note that we do not bother to normalize our detector voltage signals to the injector current in this Chapter, since the injector current was kept constant throughout the measurements presented.

Our measurements are conducted in a cryostat in vacuum at an ambient temperature of $T = 280\,\mathrm{K}$. The detector voltage is recorded at constant applied magnetic field $\mu_0 H$ as a function of the in-plane angle φ between the YIG magnetization direction $\boldsymbol{m}_{\mathrm{YIG}}$ (which is parallel to the applied field at the chosen magnetic field strengths) and the Pt strips in a 3D-vector magnet. All of the measurements in this Chapter are conducted at a base temperature of $T = 280\,\mathrm{K}$.

5.2.2 Atomic Force Microscopy

As argued above, the magnon conductivity can be tuned via the modulator of our spin transport device presented in Fig. 5.2**a**. In order to be able to make a quantitative statement about the effective conductivity/resistance beneath the modulator, it is crucial to know the exact widths of the Pt strips. Therefore, we performed atomic force microscopy (AFM) measurements for two different devices shown in Fig. 5.3**a** and **c**. Since the sample was glued to a chip carrier for the transport measurements, it had to be removed from the carrier for the AFM measurements, resulting in the reduced image quality of the main device shown in Fig. 5.3**c**. Nevertheless, all of the devices on the sample are prepared with equal strip widths of 500 nm defined by the electron beam lithography. We therefore measured a similar structure on the same sample using the AFM in Fig. 5.3**a**. Here, a device with center-to-center strip distances of $d = 1.3\,\mu\mathrm{m}$ is shown. To determine the strip width, we plot line cuts at four different positions perpendicular to the strips (see red lines in Fig. 5.3**a**). The corresponding line scans are shown in Fig. 5.3**b**, which are consecutively numbered from '1' to '4'. We then extract the strip width by measuring the distance between each of the edges corresponding to the borders of the strips (we here take the center of the edge flanks as the markers for measuring the distance), as indicated by the black vertical lines in Fig. 5.3**b**. In doing so, we obtain for the strip widths from left to right: w_{AFM} =540 nm, 500 nm, 550 nm, 560 nm, while the edge-to-edge strip distances

signals $V_{\mathrm{det}}^{1\omega,2\omega}$ represent a measure of the detected magnon spin current $j_{\mathrm{m}} = -\sigma_{\mathrm{m}} \nabla \mu_{\mathrm{m}}$. Hence, $V_{\mathrm{det}}^{1\omega,2\omega} / I_{\mathrm{inj}} \propto j_{\mathrm{m}} / \nabla \mu_{\mathrm{m}} \propto \sigma_{\mathrm{m}}$.

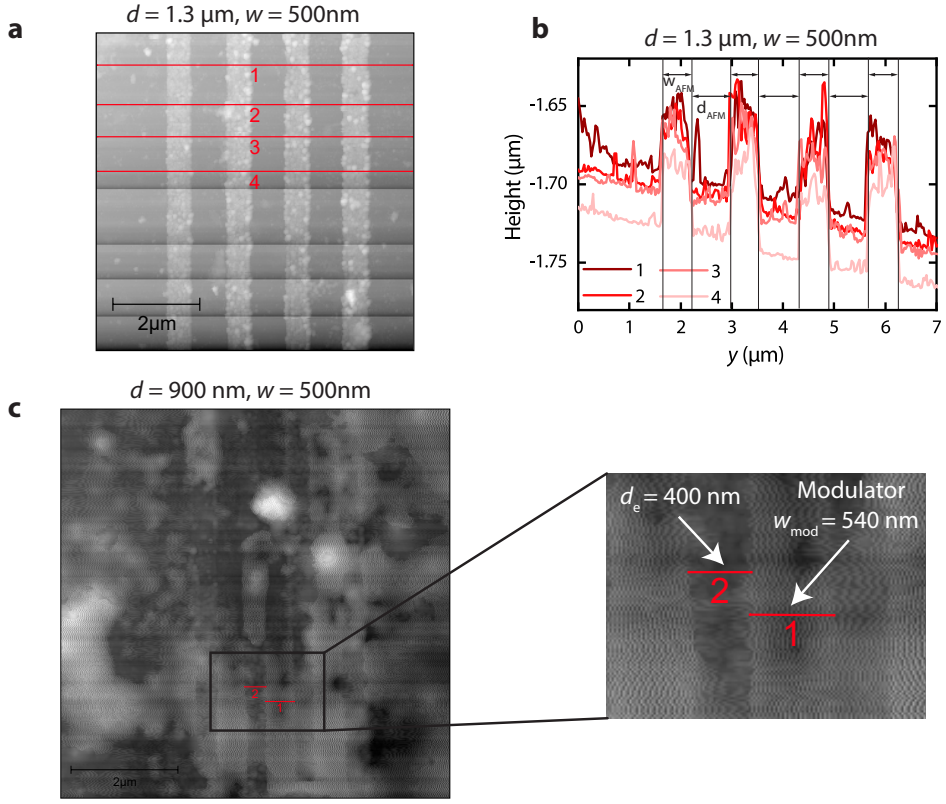

Fig. 5.3 – **a** 2D AFM scan of a device with center-to-center strip distance $d = 1.3\,\text{nm}$ and widths $w = 500\,\text{nm}$. The strips can be identified with the light grey areas. The red lines represent the line cuts, which are plotted in **b**. From the line cuts, the strip widths and distances are extracted by measuring the distance between each of the vertical black marker lines drawn in the plot. The marker lines were set at the center of each of the steep edges in the line scan. The measured height of the strips agrees well with the nominal Pt thickness $t_{\text{Pt}} = 3.5\,\text{nm}$. **c** 2D AFM scan of the main device with $d = 900\,\text{nm}$. Due to surface contaminations present on the device, the strips are less clearly visible. Still, the strip width of the modulator can be extracted via measuring the distance between the edges of the strip on the 2D scan (red line labelled with '1'), which gives a width of $w_{\text{mod}} = 540\,\text{nm}$. In order to verify that the device shows the expected strip separation, we also extracted it from the 2D scan (line labelled by '2'), giving $d_{\text{e}} = 400\,\text{nm}$.

are: $d_{\text{AFM}} = 780\,\text{nm}, 830\,\text{nm}, 800\,\text{nm}, 560\,\text{nm}$. These results suggest that the strip widths commonly exhibit a slightly larger value than defined by the electron beam lithography[34]. Although the AFM measurements of the main device with distance $d = 900\,\text{nm}$ are noisy due to increased surface contaminations (see Fig. 5.3**c**), the AFM image still allows to resolve the strips. Here, we measured the strip width of the modulator via the 2D scan rather than via line scans, which turned out to be rather noisy and therefore unreliable. Indicated by the red line labelled with '1' in Fig. 5.3**c**, the modulator width exhibits a width of $w_{\text{mod}} = 540\,\text{nm}$. We will use this value in Ch. 5.3.5 to compare it to the estimated lateral spatial extension of the

[34]This observation originates from the double layer resist system used for structuring the Pt strips via a lift-off procedure (see Ch. 3.2). Thereby, we ensure a larger undercut of the structured resists, which in turn yields better results regarding the lift-off. As a compromise we loose some resolution, which explains the slightly larger strip width measured via the AFM measurements.

damping compensated regime featuring zero spin resistance expected beneath the modulator. To verify that the device also exhibits the expected strip separation, we measure the edge-to-edge distance $d_e = 400\,\text{nm}$, which perfectly fits to the expected center-to-center distance $d = d_e + w/2 = 900\,\text{nm}$.

5.2.3 Ferromagnetic Resonance Measurements

Since the magnetic Gilbert damping α_G of the YIG film is a crucial parameter in our experiment (cf. 5.1), we employed in-plane ferromagnetic resonance (FMR) spectroscopy measurements on a bare YIG film with a comparable thickness of $t'_{YIG} = 24.5\,\text{nm}$, which was grown by pulsed laser deposition on a (100)-oriented GGG substrate at the Walther-Meißner-Institut. The same growth parameters were used as for the YIG film employed for the magnon transport measurements introduced in Ch. 5.2.1. The FMR measurements are performed under ambient conditions at room temperature ($\sim 295\,\text{K}$). In order to measure the spin pumping induced damping α_{sp}, we additionally measured the same YIG film covered with 3.5 nm of sputter deposited Pt. To this end, the thin film sample is mounted with the ferromagnetic layer facing the center conductor of a coplanar waveguide (CPW). The complete CPW assembly is placed in the homogeneous magnetic field region of an electromagnet and is connected to a vector network analyzer (VNA). Using the VNA, the complex microwave transmission parameter S_{21} of the setup is measured as a function of the applied magnetic field $\mu_0 H$ and for a series of fixed frequencies f with a fixed microwave power of 1 mW. The resonance fields $\mu_0 H_{res}$ and linewidths $\mu_0 \Delta H$ are extracted from the real and imaginary part of S_{21} via Lorentzian fits (not shown here).

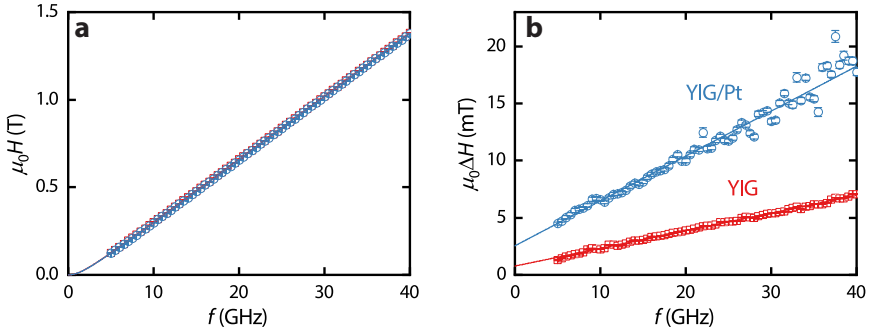

Fig. 5.4 – Ferromagnetic resonance data for a 24.5 nm thin YIG film. **a** Frequency dependence of the resonance field for the bare (red data points) and Pt covered YIG film (blue data points). The solid lines are fits by Eq. (5.34). **b** Frequency dependence of the FWHM $\mu_0 \Delta H$ of the FMR line for the bare YIG and YIG/Pt film. Solid lines are fits to Eq. (5.35).

Fig. 5.4**a** shows the frequency dependence of the FMR resonance field for the bare (red data points) and Pt covered YIG film (blue data points) extracted from the Lorentz fits to S_{21}. The solid lines are fits to the in-plane Kittel equation [194]

$$f = \frac{\gamma}{2\pi} \mu_0 \sqrt{H_{res}(H_{res} + M_s)}. \tag{5.34}$$

The fit results for M_s of the two configurations are shown in Tab. 5.1. The resonance conditions are not altered for the Pt covered YIG compared to the bare film. As obvious from Fig. 5.4**b**, however, a significant increase of the full width at half maximum (FWHM) $\mu_0\Delta H$ is observed when the film is covered with Pt. This is caused by the enhanced Gilbert damping in thin ferromagnetic films covered by normal metals due to the additional spin relaxation channel represented by the metal layer [76]. The frequency dependence of the linewidth is fitted by [28]

$$\mu_0\Delta H = \mu_0\delta H + \frac{4\pi f \alpha_{\text{tot}}}{\gamma} \tag{5.35}$$

with fitting parameters δH (the inhomogenous FMR linewidth) and α_{tot} (total damping), which are also listed in Tab. 5.1.

bare YIG ($t'_{\text{YIG}} = 24.5\,\text{nm}$)	Symbol	Value	Unit
saturation magnetization	$\mu_0 M_s$	140	mT
inhomogenous linewidth	$\mu_0\delta H$	0.77	mT
Gilbert damping	α_{tot}	2.17×10^{-3}	
Pt covered YIG			
saturation magnetization	$\mu_0 M_s$	140	mT
inhomogenous linewidth	$\mu_0\delta H$	2.54	mT
Gilbert damping	α_{tot}	5.50×10^{-3}	

Tab. 5.1 – Values of the fit parameters of Eq. ((5.34)) and ((5.35)) for the bare and Pt covered YIG film.

The difference between the Gilbert damping parameters of the YIG/Pt and the bare YIG film gives the spin pumping induced damping $\alpha'_{\text{sp}} = 3.33 \times 10^{-3}$. Since the YIG film studied for our magnon transport experiments (cf. Ch.5.2.1) is thinner by a factor of $t'_{\text{YIG}}/t_{\text{YIG}} \sim 1.8$ compared to the thickness of the film investigated in this Section, we assume an enhanced spin pumping induced damping of $\alpha_{\text{sp}} = 1.8 \cdot \alpha'_{\text{sp}} \approx 6 \times 10^{-3}$ in the following. This is a reasonable assumption due to the reciprocal relation between spin pumping induced damping and thickness of the ferromagnetic film [76]. From the derived α_{sp}, we can calculate the real part of the effective spin mixing conductance from Eq. (5.6) and obtain $g_{\text{eff}}^{\uparrow\downarrow} = 6.07 \times 10^{18}\,\text{m}^{-2}$ (here, we set $t_{\text{MI}} = t_{\text{YIG}} = 13.4\,\text{nm}$ in Eq. (5.6)). The spin mixing conductance $g_r^{\uparrow\downarrow}$ can thus be calculated from Eq. (5.7). Substituting the values for the Pt conductivity $\sigma_e = 1.74 \times 10^6\,\Omega^{-1}\,\text{m}^{-1}$ (measured for the modulator of the main device with $d = 900\,\text{nm}$) and the Pt spin diffusion length $l_s = 1.5\,\text{nm}$ [54], we obtain $g_r^{\uparrow\downarrow} = 1.02 \times 10^{19}\,\text{m}^{-2}$. This value agrees well with previous measurements of $g_r^{\uparrow\downarrow}$ in YIG/Pt interfaces [54,201]. Note that we assumed the imaginary part of the spin mixing conductance to be zero [33].

5.2.4 Thermometry

In our experiment, we apply rather large DC currents to the modulator strip to drive the magnon conductivity into a non-linear regime. The corresponding current densities applied to the DC modulator strip range up to almost $4.6 \times 10^{11}\,\mathrm{A\,m^{-2}}$ (for the highest current value of $I_{\mathrm{mod}} = 0.8\,\mathrm{mA}$ used in this thesis). The total resistance of the modulator strip at $T = 280\,\mathrm{K}$ is approximately $50\,\mathrm{k\Omega}$, resulting in a power density of almost $\sim 40\,\mathrm{kW/cm^2}$. Due to this large Joule heating present in our sample, we performed thermometry measurements on the main device ($d = 900\,\mathrm{nm}$) by measuring the Pt resistances R as a function of temperature. To this end, we applied a small DC current of $10\,\mu\mathrm{A}$ to the three strips (injector, modulator and detector) and measured the respective voltages as a function of the base temperature of the cryostat. The resulting resistance vs. temperature curves of each strip are shown in Fig. 5.5**a** and can be viewed as calibration curves using Pt thermometers. As expected for metals, a linear increase of the resistivity with increasing temperature is observed. Subsequently, we swept the modulator current from $-0.8\,\mathrm{mA}$ to $0.8\,\mathrm{mA}$ at a base temperature of $T = 280\,\mathrm{K}$ (which is equal to the base temperature used in the experiments) while applying a small current of $10\,\mu\mathrm{A}$ to the injector and detector electrodes. We then derive the local temperatures of each strip, which are plotted as a function of the modulator current in Fig. 5.5**b**. Evidently, at the maximum modulator current of $0.8\,\mathrm{mA}$, the associated Joule heating results in a temperature increase at the modulator reaching up to $366\,\mathrm{K}$. However, at this temperature, YIG can still be considered as a good electrical insulator [202]. We therefore exclude spurious electrical crosstalk effects as a possible origin of our all-electrical magnon transport signals. The injector and detector strips only reach temperatures up to $330\,\mathrm{K}$.

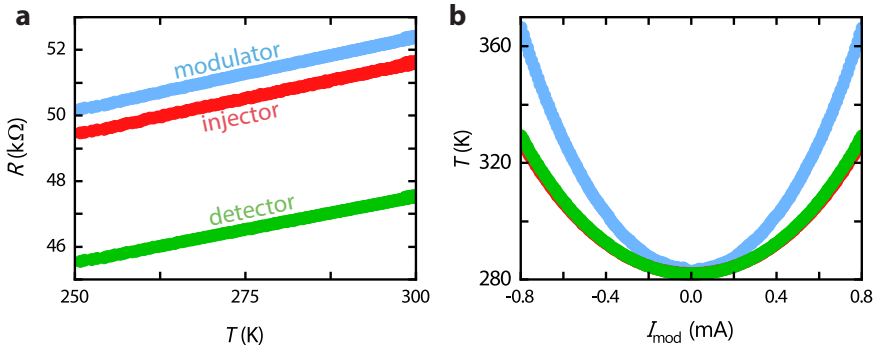

Fig. 5.5 – **a** Resistance R of injector, modulator and detector as a function of the base temperature of the sample. The linear dependencies are used as calibration curves, allowing to use the strips as local temperature sensors. **b** DC modulator current dependence of the temperature in the three Pt strips.

We also investigated the electrical insulation between injector and detector as a function of the modulator current. Over the whole current range the resistance between injector and detector is above $1\,\mathrm{G\Omega}$, which is 5 orders of magnitude larger

than the Pt resistance and comparable to the input resistance of the measurement setup. This clearly shows that any influence from enhanced electrical conduction from the YIG layer can be ruled out in our experiments [202].

5.2.5 Spin Seebeck Effect

Due to the current-induced heating discussed in the past subsection, we observe a significant temperature increase at the modulator, which also gives rise to a temperature gradient across the YIG/Pt interface. The spin Seebeck effect (SSE) describes a spin current density j_s that is driven across the interface via the temperature difference $\Delta T_{me} = T_m - T_e$ between the magnon temperature T_m in the YIG film and the electron temperature T_e in the Pt strip, which is converted to a charge current via the inverse SHE (see Fig. 5.6**a** for a schematic depiction) [100, 101, 203]. According to Bender *et al.* [187], a temperature difference ΔT_{me} causes an increase of the threshold condition μ_{on} due to the spin injection driven by the SSE[35]. These corrections are not taken into account for the description of our data. Hence, quantifying the magnitude of the SSE allows for an accurate estimation of ΔT_{me} and therefore an estimate for the impact of the SSE on the threshold conditions discussed in Ch. 5.1.

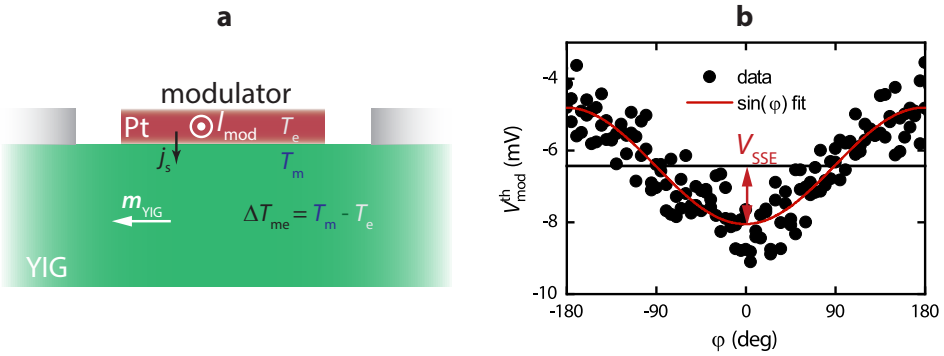

Fig. 5.6 – **a** Schematic depiction of the YIG film attached to the Pt modulator strip. The DC current I_{mod} heats the Pt strip via Joule heating, resulting in a finite temperature difference ΔT_{me} at the interface, which drives a spin current density j_s across the interface. Via the inverse SHE, this spin current is converted to a charge current in the modulator, which we measure as a voltage drop V^{th}_{mod}. **b** Spin Seebeck contribution to the voltage drop across the modulator strip as a function of the magnetic field orientation φ for a heating current of 0.55 mA and an applied magnetic field magnitude of $\mu_0 H = 50$ mT. The amplitude V_{SSE} is extracted as the amplitude of the sinusoidal fit.

Experimentally, we evaluate the temperature difference via the SSE at the modulator strip for a heating current of $I_{mod} = 0.55$ mA, which approximately corresponds to the critical current I_{crit} for an external field of 50 mT (cf. Ch. 5.3). To this end, we measured the thermal contribution of the voltage drop V^{th}_{mod} (extracted via the DC current reversal, cf. Ch. 3.4.1) across the modulator strip as a function of the magnetic field orientation φ at $\mu_0 H = 50$ mT, as shown in Fig. 5.6**b**. The

[35] With increasing temperature difference ΔT_{me}, the critical chemical potential/current is always shifted to higher values, independent of the actual sign of ΔT_{me} (see Ref. [187])

spin Seebeck voltage V_{SSE} is then extracted by fitting $V_{\mathrm{mod}}^{\mathrm{th}}(\varphi) = V_{\mathrm{SSE}} \sin(\varphi)$ to the data, which results in $V_{\mathrm{SSE}} = -1.62\,\mathrm{mV}$. From the SSE theory [100, 125], we can calculate ΔT_{me} via

$$V_{\mathrm{SSE}} = \frac{g_{\mathrm{r}}^{\uparrow\downarrow}\gamma\hbar k_{\mathrm{B}}}{2\pi M_{\mathrm{s}} V_{\mathrm{a}}} \frac{2e}{\hbar\sigma_{\mathrm{e}}} \theta_{\mathrm{SH}} l_{\mathrm{Pt}} \xi \frac{l_{\mathrm{s}}}{t_{\mathrm{Pt}}} \tanh\left(\frac{t_{\mathrm{Pt}}}{2l_{\mathrm{s}}}\right) \Delta T_{\mathrm{me}} \tag{5.36}$$

with a backflow correction factor $\xi = \left[1 + 2g_{\mathrm{r}}^{\uparrow\downarrow} l_{\mathrm{s}} \frac{e^2}{\hbar\sigma_{\mathrm{e}}} \coth\left(\frac{t_{\mathrm{Pt}}}{l_{\mathrm{s}}}\right)\right]^{-1}$ and the magnetic coherence volume $V_{\mathrm{a}} = \frac{2}{3\zeta(5/2)} \left(\frac{4\pi J_{\mathrm{s}}}{k_{\mathrm{B}} T}\right)^{3/2}$ [100, 125] with $J_{\mathrm{s}} = 8.458 \times 10^{-40}\,\mathrm{J\,m^2}$ the spin wave stiffness of YIG [7]. Considering an increased ambient temperature of $T = 320\,\mathrm{K}$ due to the current-induced heating evaluated in Ch. 5.2.4 for $I_{\mathrm{mod}} = 0.55\,\mathrm{mA}$, we find an experimentally determined temperature difference via the SSE voltage of $\Delta T_{\mathrm{me}} \approx -0.12\,\mathrm{K}$, corresponding to a thermal energy of $k_{\mathrm{B}}|\Delta T_{\mathrm{me}}| \approx 11\,\mu\mathrm{eV}$ (values for the calculation are listed in Tab. 5.2). Comparing this to Fig. 6 in Ref. [187], the SSE is found to only marginally affect the threshold condition for the BEC phase transition (for the swasing phase transition there is no effect at all). An estimate of the enhancement of the critical current density due to the thermally injected magnons from Ref. [187] gives roughly $1.7 \times 10^9\,\mathrm{A\,m^{-2}}$ ($\sim 3\,\mu\mathrm{A}$) for $\Delta T_{\mathrm{me}} = -0.12\,\mathrm{K}$, which is less than 1 % of the typical critical current densities $J_{\mathrm{on/crit}} \approx 2.9 \times 10^{11}\,\mathrm{A\,m^{-2}}$ ($I_{\mathrm{on/crit}} \approx 500\,\mu\mathrm{A}$) found in this experiment. Hence, the current-induced heating of the Pt strip is not expected to have a measurable impact on $I_{\mathrm{on/crit}}$ in our experiments.

5.2.6 Impact of Magnetocrystalline Anisotropy on Angular Dependent Spin Transport Measurements

In this Section, we quantitatively investigate the impact of the cubic magnetocrystalline anisotropy of our YIG film on the shape of the angle dependent magnon transport measurements. We start with the angle dependent magnon transport measurement between injector and detector, which is detected as the first harmonic voltage signal $V_{\mathrm{det}}^{1\omega}$. The corresponding measurement is shown in Fig. 5.7**a** (black data points). First of all, the measurement exhibits the expected 180° symmetric modulation typical for the magnon transport between two parallel Pt electrodes [8, 9]. It is obvious, however, that the measurement displays a rather triangular shape compared to the expected perfect $\cos^2(\varphi)$-like modulation, which is shown as a fit to the data (blue solid line) in Fig. 5.7**a**. This discrepancy stems from the in-plane cubic anisotropy of our (100)-oriented YIG film, leading to a slight misalignment of the external field direction φ and the magnetization direction φ_{m} of the YIG film. Since the data is measured for an external field of $\mu_0 H = 50\,\mathrm{mT}$, a visible contribution of the anisotropy to the angular depen-

dent meaurements is likely. In order to quantitatively model this behaviour, we implement the cubic anisotropy by introducing a Stoner-Wohlfarth-model as

$$f(\varphi_m) = -\mu_0 \mathbf{H} \cdot \mathbf{M} + K_{c1} m_x^2 m_y^2. \tag{5.37}$$

Here, f is the free energy density which is a function of the in-plane angle φ_m of the magnetization $\mathbf{M} = M_s[m_x, m_y] = M_s[\cos(\varphi_m), \sin(\varphi_m)]$. Furthermore, K_{c1} is the cubic anisotropy constant and the external magnetic field is written as $\mu_0\mathbf{H} = \mu_0 H[\cos(\varphi), \sin(\varphi)]$ with $\mu_0 H = 50\,\mathrm{mT}$ the magnitude of the applied field and φ the well-known orientation of the external magnetic field. In Eq. (5.37) we only consider the two-dimensional in-plane magnetized case, where we disregard the shape anisotropy contribution due to the magnetic thin film. In order to model the observed angle dependence, Eq. (5.37) is numerically minimized with respect to φ_m for each external magnetic field angle φ. For this purpose, we use an anisotropy constant $K_{c1} = -600\,\mathrm{J/m^3}$, which corresponds to the literature value of YIG at room temperature found in Ref. [204]. To simulate our angle dependent measurement, we replace the $\cos^2(\varphi)$ fitting function with a simulation of the form

$$V_{det}^{1\omega}(\varphi) = \Delta V_{det0}^{1\omega} \cos^2(\varphi_m(\varphi)), \tag{5.38}$$

where $\Delta V_{det0}^{1\omega}$ is the amplitude of the modulation. The argument of the $\cos^2()$ function in Eq. (5.38) is extracted from the Stoner-Wohlfarth-model and provides the magnetization angle φ_m as a function of the external magnetic field angle φ. Eq. (5.38) is plotted in Fig. 5.7**a** (red solid line) together with the respective data (black data points) and the simple $\cos^2(\varphi)$ fit (blue solid line). The simulation that includes the cubic anisotropy shows a much better agreement with the experimental data than the simple $\cos^2(\varphi)$ fit. This observation can be further solidified by plotting the residual $\mathrm{Res}(V_{det}^{1\omega})$ calculated by the difference between the data and the $\cos^2(\varphi)$-fit (blue data points) as well as the difference between the data and the simulation of Eq. (5.38) (red data points) in Fig. 5.7**b**. Moreover, we plot the difference between the simulation (Eq. (5.38)) and the $\cos^2(\varphi)$-fit as the green solid line. The residual of the fit to the data (blue points) shows a finite modulation and agrees reasonably well with the theoretical expectation shown by the green solid line. This modulation is expected for the appearance of a cubic anisotropy in our data, since this is obviously not included in this simple $\cos^2(\varphi)$-fit. In contrast, the difference of the simulation and the data (red points), shows a vanishing modulation. Hence, we conclude that our data fits well to our simulation, since the angular dependence of the magnon transport signal can be accurately modeled by introcuding a cubic anisotropy to the simulation with an anisotropy constant that corresponds to the literature value [204].

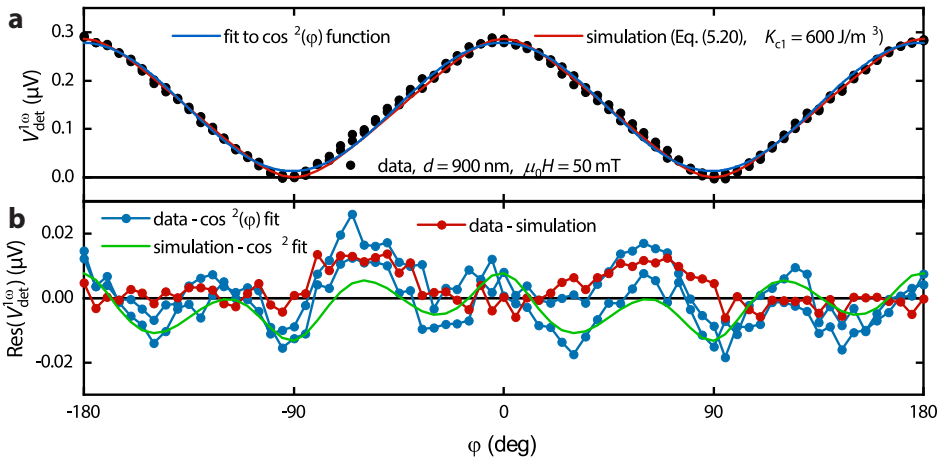

Fig. 5.7 – **a** Magnon transport signal $V_{\mathrm{det}}^{1\omega}$ for the device presented in the main text for a modulator current of $I_{\mathrm{mod}} = 0\,\mu\mathrm{A}$ (black data points taken from Fig. 5.8). The blue solid line represents a $\cos^2(\varphi)$-fit to the data, while the red solid line is a simulation based on Eq. (5.38). **b** Residual $\mathrm{Res}(V_{\mathrm{det}}^{1\omega})$ of the $\cos^2(\varphi)$ fit to the data shown in **a** (blue points with line). The difference between the simulation and the $\cos^2(\varphi)$-fit is shown as the solid green line, showing good agreement with the blue points. Additionally, the difference between the simulation and the data (red data points with line) is shown, where a mostly vanishing modulation is observed.

5.3 Spin Conductivity Control of Spin Hall Effect Induced Magnons

As discussed in Ch. 2.7, variations in the magnon density in MI/HM heterostructures can be excited both electrically via the SHE as well as thermally via Joule heating. This Section is focussed on the electrically excited magnons at the injector. They propagate from the injector to the detector, at which they are detected as the first harmonic voltage signal $V_{\mathrm{det}}^{1\omega}$. Here, the change of the magnon transport between injector and detector under the influence of the DC modulator current is investigated.

In a first step, we investigate the magnon propagation between injector and detector in the thin YIG layer for different modulator currents I_{mod}. To this end, we measure $V_{\mathrm{det}}^{1\omega}$ as a function of the magnetic field orientation φ (cf. Fig. 5.2**a**) with a fixed magnetic field strength of $\mu_0 H = 50\,\mathrm{mT}$. The results are shown in Fig. 5.8**a** and **b** for $I_{\mathrm{mod}} > 0$ and $I_{\mathrm{mod}} < 0$, respectively. In both panels, the black data points exhibit the characteristic ($\cos^2\varphi$) modulation expected for magnon transport between injector and detector when $I_{\mathrm{mod}} = 0$. This results from the variation of the magnon injection with φ, exhibiting maxima for $\boldsymbol{H}$ perpendicular to the direction of I_{inj} (appearing at $\varphi = -180°, 0°, 180°$) [8,9]. The rather triangular shape of the angle dependent measurement for $I_{\mathrm{mod}} = 0$ is due to the cubic magnetocrystalline anisotropy of the YIG film discussed in Ch. 5.2.6. The most striking observation, however, is the significant enhancement of the detector signal observed at $\varphi = \pm 180°$ in Fig. 5.8**a** when $I_{\mathrm{mod}} > 0$. This can be

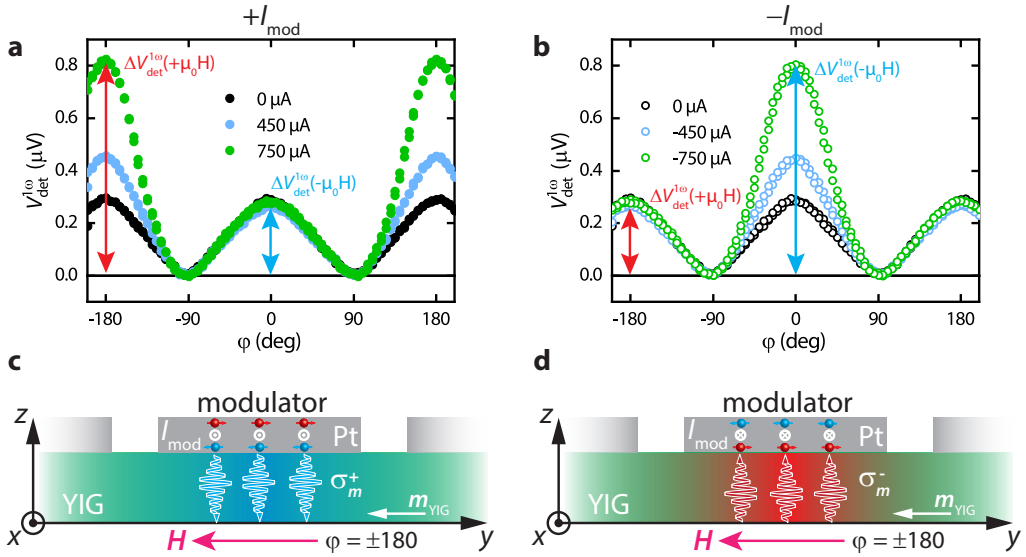

Fig. 5.8 – First harmonic detector signal $V_{\mathrm{det}}^{1\omega}$ plotted versus the rotation angle φ of the in-plane field at $\mu_0 H = 50\,\mathrm{mT}$ for **a** positive and **b** negative DC bias currents I_{mod} in the modulator. **a** The detector signal for $I_{\mathrm{mod}} > 0$ is significantly increased at $\varphi = \pm 180°$ and mostly unaffected at $\varphi = 0°$. **b** For $I_{\mathrm{mod}} < 0$, we observe a 180° shifted behavior, where the signal increase is evident at $\varphi = 0°$, while unchanged for $\varphi = \pm 180°$. **c** Schematic depiction of the device for $I_{\mathrm{mod}} > 0$ and $\varphi = \pm 180°$. Due to $\boldsymbol{s} \uparrow\Uparrow \boldsymbol{m}_{\mathrm{YIG}}$, the magnon density beneath the modulator is increased via both the SHE- and thermally-induced magnon injection, leading to an overall increased magnon density and related conductivity σ_{m}^{+}. **d** Same as **c** but with inverted current direction $I_{\mathrm{mod}} < 0$ and therefore $\boldsymbol{s} \uparrow\Downarrow \boldsymbol{m}_{\mathrm{YIG}}$. Consequently, a depletion of the magnon system due to the SHE is evident, resulting in a reduced magnon density and related conductivity σ_{m}^{-}. The depletion is counterbalanced by the thermal injection of magnons.

understood by considering Fig. 5.8**c** and Eq. (5.30): when the relative orientation between the spin polarization $\boldsymbol{s}$ at the interface and the magnetization direction $\boldsymbol{m}_{\mathrm{YIG}}$ is parallel, magnons accumulate underneath the modulator, resulting in an increased magnon density and associated conductivity σ_{m}^{+} and therefore a larger $V_{\mathrm{det}}^{1\omega}$. Figure 5.8**b** shows the measurement for the inverted DC current direction ($I_{\mathrm{mod}} < 0$). Here, we observe the expected 180° shifted case: an enhancement for $\varphi = 0°$ and no significant change for ±180°. As depicted in Fig. 5.8**d**, the reversed current direction results in the spin polarization $\boldsymbol{s}$ being antiparallel to $\boldsymbol{m}_{\mathrm{YIG}}$, therefore depleting the magnon system in the YIG. A decreased magnon density and associated conductivity σ_{m}^{-} is thus expected and should lead to a decreased magnon transport signal $V_{\mathrm{det}}^{1\omega}$. However, the expected depletion is counterbalanced by the thermally injected magnons present due to the Joule heating in the modulator strip, which increases the magnon density and therefore the magnon conductivity. Hence, only slight changes are observed for these configurations. All of the basic features observed in these measurements can be explained by the current induced magnon conductivity modulation based on magnon density modulation comprised in Eq. (5.30).

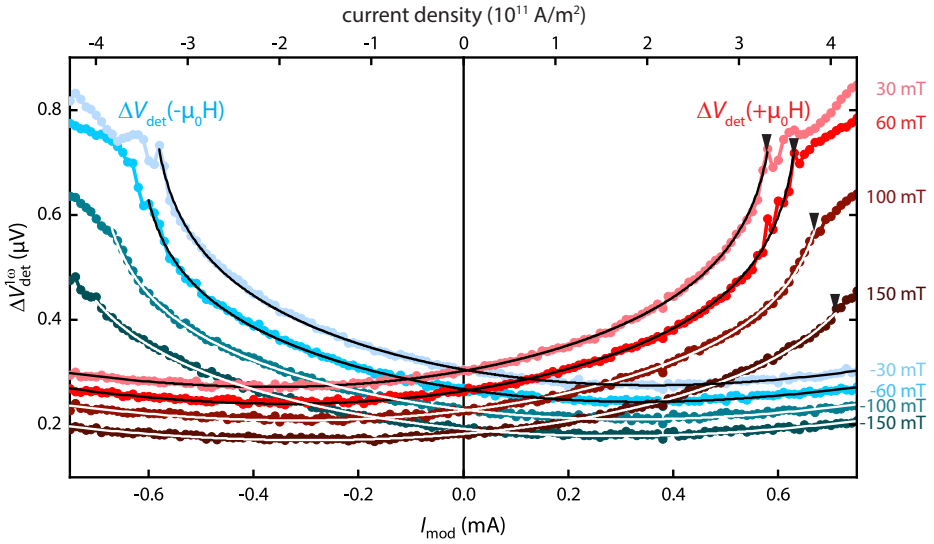

Fig. 5.9 – Extracted amplitudes $\Delta V_{\mathrm{det0}}^{1\omega}(+\mu_0 H)$ and $\Delta V_{\mathrm{det0}}^{1\omega}(-\mu_0 H)$ (as indicated in Fig. 5.8) of the magnon transport signal for different external magnetic fields plotted versus the DC current I_{mod} in the modulator. The transition into the damping compensation state for positive I_{mod} is indicated by black triangles (maximum slope of the curves). The transition shifts to larger DC currents with increasing external magnetic fields. The solid black and white lines are fits to Eq. (5.58) discussed in Ch. 5.3.4.

For a quantitative analysis of the data presented in Fig. 5.8, we extract the signal amplitudes $\Delta V_{\mathrm{det}}^{1\omega}(+\mu_0 H)$ and $\Delta V_{\mathrm{det}}^{1\omega}(-\mu_0 H)$ (indicated in Fig. 5.8**a**, **b**) as a function of I_{mod} for various magnetic field amplitudes $\mu_0 H$. The resulting dependence of the detector signals $\Delta V_{\mathrm{det}}^{1\omega}(+\mu_0 H)$ and $\Delta V_{\mathrm{det}}^{1\omega}(-\mu_0 H)$ as a function of the moduator current is shown in Fig. 5.9. Solid lines in Fig. 5.8**a** are fits to Eq. (5.58) and will be discussed in Ch. 5.3.4. Note that we define positive fields $+\mu_0 H$ to point along $-y$ and negative fields $-\mu_0 H$ to point along $+y$. In the following, we will separately discuss the low current bias regime for $|I_{\mathrm{mod}}| < 0.4\,\mathrm{mA}$ and the critical current regime for $|I_{\mathrm{mod}}| > 0.4\,\mathrm{mA}$.

5.3.1 Low Bias Current Regime

We start by focussing on the low current bias regime ($|I_{\mathrm{mod}}| < 0.4\,\mathrm{mA}$) of Fig. 5.9. Here, the $\Delta V_{\mathrm{det}}^{1\omega}(I_{\mathrm{mod}})$ curves can be modelled by a superposition of a linear and quadratic current dependence, accounting for the SHE- and thermally-induced magnons, respectively [172]. Since $\Delta V_{\mathrm{det}}^{1\omega}(I_{\mathrm{mod}}) \propto \sigma_{\mathrm{m}}(I_{\mathrm{mod}})$ as explained in Ch. 5.2.1, the total magnon conductivity including the (low bias) current-induced modulations can be expressed as

$$\sigma_{\mathrm{m}} = \sigma_{\mathrm{m}}^{0} + \Delta\sigma_{\mathrm{SHE}} I_{\mathrm{mod}} + \Delta\sigma_{\mathrm{th}} I_{\mathrm{mod}}^{2}, \tag{5.39}$$

where σ_{m}^{0} is the equilibrium magnon conductivity at zero modulation current, $\Delta\sigma_{\mathrm{SHE}}$ is the SHE-induced magnon conductivity change and $\Delta\sigma_{\mathrm{th}}$ represents the

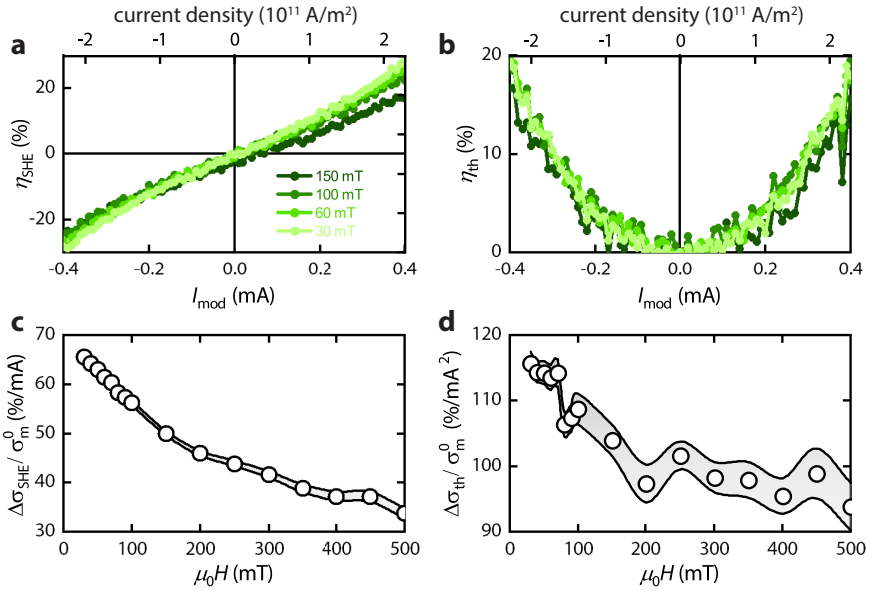

Fig. 5.10 – **a** Spin Hall effect induced relative modulation strength η_{SHE} calculated from the experimental data using Eq. (5.41a). **b** Thermally induced modulation η_{th} calculated using Eq. (5.41b). **c** Spin Hall effect induced efficiency $\Delta\sigma_{\mathrm{SHE}}/\sigma_{\mathrm{m}}^0$ in units of $\%\,\mathrm{mA}^{-1}$ as a function of the applied magnetic field. **d** Thermally induced efficiency $\Delta\sigma_{\mathrm{th}}/\sigma_{\mathrm{m}}^0$ in units of $\%\,\mathrm{mA}^{-2}$ as a function of the applied magnetic field.

thermally-induced magnon conductivity change as derived in Ch. 5.1.2. We point out once again that we assume the magnon conductivity change within the low bias regime to be entirely determined by a magnon density change as derived in Ch. 5.1.2. In this regime, the magnon relaxation time is considered to be constant.

The SHE-induced and thermally-induced contributions can be distinguished according to their symmetries: while the SHE contribution is odd, the thermal contribution is even under field reversal. Therefore, we extract the modulation amplitude due to the SHE-induced injection (thermal injection) by calculating the antisymmetric (symmetric) part of the voltage amplitudes as

$$\Delta V_{\mathrm{det}}^{\mathrm{SHE}} = [\Delta V_{\mathrm{det}}^{1\omega}(+\mu_0 H) - \Delta V_{\mathrm{det}}^{1\omega}(-\mu_0 H)]/2 \propto \Delta\sigma_{\mathrm{SHE}} I_{\mathrm{mod}} \tag{5.40a}$$

$$\Delta V_{\mathrm{det}}^{\mathrm{th}} = [\Delta V_{\mathrm{det}}^{1\omega}(+\mu_0 H) + \Delta V_{\mathrm{det}}^{1\omega}(-\mu_0 H)]/2 \propto \sigma_{\mathrm{m}}^0 + \Delta\sigma_{\mathrm{th}} I_{\mathrm{mod}}^2 \tag{5.40b}$$

and then normalize $\Delta V_{\mathrm{det}}^{\mathrm{SHE}}$ and $\Delta V_{\mathrm{det}}^{\mathrm{th}}$ according to

$$\eta_{\mathrm{SHE}} = \frac{\Delta V_{\mathrm{det}}^{\mathrm{SHE}}}{\Delta V_{\mathrm{det0}}^{1\omega}} = \frac{\Delta\sigma_{\mathrm{SHE}} I_{\mathrm{mod}}}{\sigma_{\mathrm{m}}^0} = \frac{\sigma_{\mathrm{m}}^{\mathrm{SHE}}}{\sigma_{\mathrm{m}}^0} \tag{5.41a}$$

$$\eta_{\mathrm{th}} = \frac{\Delta V_{\mathrm{det}}^{\mathrm{th}} - \Delta V_{\mathrm{det0}}^{1\omega}}{\Delta V_{\mathrm{det0}}^{1\omega}} = \frac{\Delta\sigma_{\mathrm{th}} I_{\mathrm{mod}}^2}{\sigma_{\mathrm{m}}^0} = \frac{\sigma_{\mathrm{m}}^{\mathrm{th}}}{\sigma_{\mathrm{m}}^0} \tag{5.41b}$$

with $\Delta V_{\mathrm{det0}}^{1\omega} = \Delta V_{\mathrm{det}}^{1\omega}(I_{\mathrm{mod}} = 0) \propto \sigma_{\mathrm{m}}^0$ the detector amplitude at zero DC modulation current. The relative modulation strength η_{SHE} (η_{th}) is then proportional to the ratio of the SHE (thermally) induced magnon conductivity $\sigma_{\mathrm{m}}^{\mathrm{SHE}} = \Delta\sigma_{\mathrm{SHE}} I_{\mathrm{mod}}$

($\sigma_m^{th} = \Delta\sigma_{th} I_{mod}^2$) and the magnon conductivity in thermal equilibrium σ_m^0 [172]. Figure 5.10**a** shows η_{SHE} as a function of the DC modulator current for the low bias regime ($|I_{mod}| \lesssim 0.4\,\mathrm{mA}$) and different magnetic field strengths. Clearly, the expected linear behaviour is evident [172]. We then investigate the field dependence of the modulation efficiency $\mathrm{d}\eta_{SHE}/\mathrm{d}I_{mod} = \Delta\sigma_{SHE}/\sigma_m^0$, which is evaluated as the slope of η_{SHE} by linearly fitting the data within the shown current range $|I_{mod}| < 0.4\,\mathrm{mA}$. The result is shown in Fig. 5.10**c**, where the magnetic field dependence of the efficiency is plotted in units of %/mA. The observed dependence is found to show a monotonous decrease and to be similar to the usual magnetic field dependence found for SHE induced magnon transport [166]. As predicted by simulations of the current-induced magnon density increase presented in Ref. [172], the modulation efficiency for 10 nm thin YIG films at $\mu_0 H = 50\,\mathrm{mT}$ is expected to revolve around $\sim 16\,\%/\mathrm{mA}$. Our YIG thin film in this study with $t_{YIG} = 13.4\,\mathrm{nm}$, however, shows a significantly larger efficiency of $\sim 60\,\%/\mathrm{mA}$ at $\mu_0 H = 50\,\mathrm{mT}$, which exceeds the prediction by a factor of ~ 4. Thus, our results show that thermal magnon based logic is even more efficient in very thin YIG films than theoretically expected. In Fig. 5.9**b**, the thermally induced relative modulation strength η_{th} is shown as a function of the DC modulator current. Here, the small current regime follows a quadratic dependence with the applied DC current, which is expected for the thermal injection of magnons. Similar to the modulation efficiency determined from the slope of η_{SHE}, we fit η_{th} with a quadratic current dependence and extract the coefficient corresponding to $(1/2)\,\mathrm{d}^2\eta_{th}/\mathrm{d}I_{mod}^2 = \Delta\sigma_{th}/\sigma_m^0$, which is shown in Fig. 5.9**d** in units of $\%/\mathrm{mA}^2$. Again, an overall decreasing trend of the modulation efficiency by thermal magnon injection is observed, corroborating the results found in Fig. 5.10**c** for the SHE-induced magnon injection. This result also agrees well with previous reports presenting the field dependence of thermally induced magnon transport [166].

5.3.2 Critical Current Regime

For currents $|I_{mod}| > 0.4\,\mathrm{mA}$, it is evident from Fig. 5.9 that the DC current modulation deviates significantly from the linear and quadratic behaviour verified for the low current bias regime. This manifests itself by a very large slope in the $\Delta V_{det}^{1\omega}(I_{mod})$ curves for $I_{mod} > 0.5\,\mathrm{mA}$ (marked by black triangles in Fig. 5.9 for positive I_{mod}). We have derived in Ch. 5.1.2 via very simplistic assumptions this non-linear, diverging behaviour of the magnon conductivity by assuming a diverging magnon lifetime τ_m in this regime. Although it is likely to be not perfectly valid to project the changes in the magnon density and magnon lifetime to the linear and non-linear regime separately, respectively (see last paragraph in Ch. 5.1.2), we follow this line of interpretation in the following. In order to study this critical behaviour in more detail, we isolate the modulation effects in

$\Delta V_{\mathrm{det}}^{1\omega}(I_{\mathrm{mod}})$ stemming from the non-linear and non-quadratic critical regime by calculating the critical detector amplitude

$$\Delta V_{\mathrm{det}}^{1\omega,\mathrm{crit}}(I_{\mathrm{mod}}) = \Delta V_{\mathrm{det}}^{1\omega}(I_{\mathrm{mod}}) - [\Delta R_{\mathrm{SHE}} I_{\mathrm{mod}} + \Delta R_{\mathrm{th}} I_{\mathrm{mod}}^2] \tag{5.42}$$

where $\Delta R_{\mathrm{SHE}} = (\Delta\sigma_{\mathrm{SHE}}/\sigma_{\mathrm{m}}^0)\,\Delta V_{\mathrm{det0}}^{1\omega}$ and $\Delta R_{\mathrm{th}} = (\Delta\sigma_{\mathrm{th}}/\sigma_{\mathrm{m}}^0)\,\Delta V_{\mathrm{det0}}^{1\omega}$ are the linear (SHE) and quadratic (thermal) coefficients characterizing the efficiencies of the modulation effects in the low current bias regime in terms of the detector voltage. A graphical representation of this signal correction is given in Fig. 5.11**a**. Here, representative detector signal amplitudes $\Delta V_{\mathrm{det}}^{1\omega}$ are shown for $\mu_0 H = \pm 60\,\mathrm{mT}$. The lightly colored solid lines correspond to the fitting function

$$\Delta V_{\mathrm{det}}^{1\omega}(I_{\mathrm{mod}}) = \Delta V_{\mathrm{det0}}^{1\omega} + \Delta R_{\mathrm{SHE}} I_{\mathrm{mod}} + \Delta R_{\mathrm{th}} I_{\mathrm{mod}}^2, \tag{5.43}$$

where the fit range is limited to the low current bias regime $|I_{\mathrm{mod}}| < 0.4\,\mathrm{mA}$ (grey shaded area in Fig. 5.11**a**). The fits are extrapolated to larger currents beyond $|0.4\,\mathrm{mA}|$. Evidently, the fits significantly deviate from the data for $|I_{\mathrm{mod}}| > 0.4\,\mathrm{mA}$. These deviations from the fits are calculated by Eq. (5.42) and plotted in Fig. 5.11**b**. For $I_{\mathrm{mod}} > 0.4\,\mathrm{mA}$, the critical detector signal $\Delta V_{\mathrm{det}}^{1\omega,\mathrm{crit}}$ reveals a smeared out step-function which mirrors the magnon conductivity enhancement due to the critical regime only. A saturation of the enhancement is evident for large (positive) currents. The origin of the strong enhancement can be attributed to the compensation of the magnetic damping (cf. Ch. 5.1) in the YIG film and will be discussed in detail in Ch. 5.3.3. In the negative current bias regime, $\Delta V_{\mathrm{det}}^{1\omega,\mathrm{crit}}$ also reveals an unexpected deviation from the fit for large currents. The origin of this deviation might be related to the thermal excitation of the optical magnon branch of YIG [111], which becomes considerably stronger occupied due to the current-induced temperature increase that we verified via thermometry measurements in Ch. 5.2.4. Due to the ferrimagnetic nature of YIG, this optical magnon branch features an inverted polarization/chirality of the corresponding magnon modes. Hence, a stronger occupation of the optical modes leads to a counteracting contribution to the magnon conductivity $\sigma_{\mathrm{m}} \propto n_{\mathrm{m}}^{\mathrm{ac}} - n_{\mathrm{m}}^{\mathrm{opt}}$, where $n_{\mathrm{m}}^{\mathrm{ac}}$ and $n_{\mathrm{m}}^{\mathrm{opt}}$ are the magnon densities of the acoustic and optical branches, respectively. A verification of this claim, however, requires further investigation and will not be investigated in more detail in this thesis.

As a next step, we will interpret the experimental data in terms of an equivalent spin resistor model, from which we can calculate an equivalent spin resistance of the YIG transport channel. In Fig. 5.11**c**, we adopted an equivalent spin resistor model for our device based on the model presented in Ref. [36]. Via the SHE, the spin chemical potential $\mu_{\mathrm{s}}^{\mathrm{inj}}$ is acting as the 'spin battery' at the injector. The transferred spin chemical potential $\mu_{\mathrm{s}}^{\mathrm{det}}$ is measured across the detector. The spin

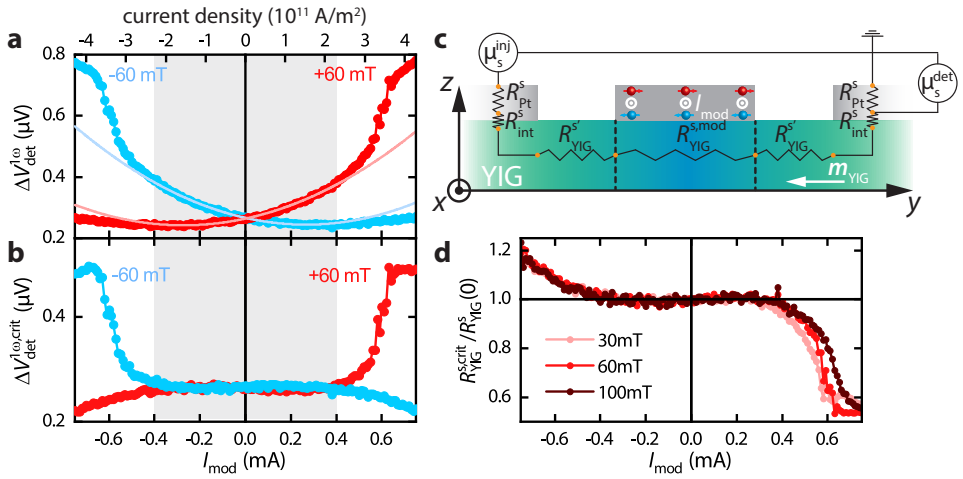

Fig. 5.11 – **a** First harmonic detector signal $V_{\mathrm{det}}^{1\omega}$ as a function of the modulator current I_{mod} for $\mu_0 H = \pm 60\,\mathrm{mT}$ taken from Fig. 5.9. The solid lines correspond to fits to Eq. (5.43). **b** Critical detector amplitude $\Delta V_{\mathrm{det}}^{1\omega,\mathrm{crit}}$ calculated via Eq. (5.42), reflecting the deviation of the fits to the data shown in panel **a**. **c** Equivalent spin resistor model of our device. **d** Critical spin resistance $R_{\mathrm{YIG}}^{\mathrm{s,crit}}$ normalized to the spin resistance $R_{\mathrm{YIG}}^{\mathrm{s}}(0)$ at zero modulator current I_{mod}.

transfer efficiency is then defined as $\eta_{\mathrm{s}} = \mu_{\mathrm{s}}^{\mathrm{det}}/\mu_{\mathrm{s}}^{\mathrm{inj}}$. Based on the spin resistor network shown in Fig. 5.11**c**, η_{s} can be expressed as

$$\eta_{\mathrm{s}} = \frac{R_{\mathrm{Pt}}^{\mathrm{s}}}{R_{\mathrm{YIG}}^{\mathrm{s}} + 2R_{\mathrm{int}}^{\mathrm{s}} + 2R_{\mathrm{Pt}}^{\mathrm{s}}}, \tag{5.44}$$

where the spin resistance of YIG is $R_{\mathrm{YIG}}^{\mathrm{s}} = 2R_{\mathrm{YIG}}^{\mathrm{s}'} + R_{\mathrm{YIG}}^{\mathrm{s,mod}}$ with $R_{\mathrm{YIG}}^{\mathrm{s}'}$ being the spin resistances outside the region beneath the modulator, while $R_{\mathrm{YIG}}^{\mathrm{s,mod}}$ represents the one within. Note that we assume $R_{\mathrm{YIG}}^{\mathrm{s,mod}}$ to be the only parameter in Eq. (5.44) that is dependent on the modulator current I_{mod}. Furthermore, $R_{\mathrm{Pt}}^{\mathrm{s}} = l_{\mathrm{s}}/(\sigma_{\mathrm{e}} A_{\mathrm{int}} \tanh(t_{\mathrm{Pt}}/l_{\mathrm{s}}))$ is the spin resistance of the Pt strip and $R_{\mathrm{int}}^{\mathrm{s}} = 1/(g_{\mathrm{s}} A_{\mathrm{int}})$ the interface spin resistance with g_{s} the interfacial spin conductance as introduced in Ch. 2.5. For the convenience of working with well-known electrical units, we have defined the spin conductance as $g_{\mathrm{s}} = \frac{e^2}{h} g$, such that g_{s} is given in units of $\mathrm{S\,m^{-2}}$. Using the theoretical expression of g from Eq. (2.38), it follows that $g_{\mathrm{s}} \approx 0.05 \frac{e^2}{h} g_{\mathrm{r}}^{\uparrow\downarrow}$ for an ambient temperature of $T = 280\,\mathrm{K}$ used in our experiment. Moreover, $A_{\mathrm{int}} = w l_{\mathrm{Pt}}$ is the area of the Pt interfacing the YIG film. The spin transfer efficiency η_{s} can also be deduced from the experiments and reads [36]

$$\eta_{\mathrm{s}} = \frac{t_{\mathrm{Pt}}}{l_{\mathrm{s}} \theta_{\mathrm{SH}}^2} \frac{\sqrt{2}\,\Delta V_{\mathrm{det}}^{1\omega}}{I_0 R_{\mathrm{det}}} \frac{(e^{t_{\mathrm{Pt}}/l_{\mathrm{s}}} + 1)(e^{2t_{\mathrm{Pt}}/l_{\mathrm{s}}} + 1)}{(e^{t_{\mathrm{Pt}}/l_{\mathrm{s}}} - 1)^3}, \tag{5.45}$$

with R_{det} being the resistance of the Pt detector strip[36]. Solving Eq. (5.44) for $R^{\mathrm{s}}_{\mathrm{YIG}}$ gives $R^{\mathrm{s}}_{\mathrm{YIG}} = \frac{R^{\mathrm{s}}_{\mathrm{Pt}}}{\eta_{\mathrm{s}}} - (2R^{\mathrm{s}}_{\mathrm{Pt}} + 2R^{\mathrm{s}}_{\mathrm{int}})$. For the final expression of $R^{\mathrm{s}}_{\mathrm{YIG}}$, we neglect the last two terms contained in brackets, leading to

$$R^{\mathrm{s}}_{\mathrm{YIG}} = \frac{R^{\mathrm{s}}_{\mathrm{Pt}}}{\eta_{\mathrm{s}}}. \tag{5.46}$$

This is a reasonable assumption when considering typical values for the measured voltage signals $\Delta V^{1\omega}_{\mathrm{det}} \sim 1\,\mu\mathrm{V}$ that enter η_{s} in Eq. (5.45), suggesting that $R^{\mathrm{s}}_{\mathrm{Pt}}/\eta_{\mathrm{s}}$ is typically two orders of magnitude larger than $(2R^{\mathrm{s}}_{\mathrm{Pt}} + 2R^{\mathrm{s}}_{\mathrm{int}})$. We now use the critical detector amplitude $\Delta V^{1\omega,\mathrm{crit}}_{\mathrm{det}}$ to calculate the critical spin resistance $R^{\mathrm{s,crit}}_{\mathrm{YIG}}$ of YIG via Eq. (5.46)[37]. Finally, we arrive at Fig. 5.11**d**, where $R^{\mathrm{s,crit}}_{\mathrm{YIG}}/R^{\mathrm{s}}_{\mathrm{YIG}}(0)$ is plotted versus I_{mod} with $R^{\mathrm{s}}_{\mathrm{YIG}}(0)$ being the spin resistance at $I_{\mathrm{mod}} = 0$ used for normalization. The results are shown for different (positive) external magnetic field magnitudes. Just like the critical detector signal $\Delta V^{1\omega,\mathrm{crit}}_{\mathrm{det}}$ shown in Fig. 5.11**b**, the $R^{\mathrm{s,crit}}_{\mathrm{YIG}}(I_{\mathrm{mod}})$ curves enable us to determine the impact on magnon transport stemming solely from non-linear and non-quadratic modulations in terms of the magnon spin resistance.

5.3.3 Damping Compensation and Magnon Bose-Einstein Condensation

Having introduced the spin resistance concept for our magnon transport device, we now analyze the magnon transport data with respect to the theories of SOT-induced damping compensation and magnon BEC formation discussed in Ch. 5.1.1. On the basis of these theoretical predictions, our physical picture of the magnon transport is condensed in Fig. 5.12**a** and **b**. For the sake of simplicity, we only consider magnon transport beneath the modulator and therefore disregard the magnon decay on either side of the modulator. When $I_{\mathrm{mod}} = 0$ (panel **a**), the magnon density $n^{\mathrm{inj}}_{\mathrm{m}}$ from the injector decays exponentially (orange solid line). For $I_{\mathrm{mod}} = I_{\mathrm{crit}}$ (panel **b**), the threshold current for the damping compensation is reached, the magnon lifetime diverges according to Eq. (5.32) and spin transport with an effectively vanishing magnon decay ensues [188]. This corresponds to a zero effective damping state and is illustrated by the large magnon accumulation beneath the modulator. Hence, the experimental expectation corresponds to a zero resistance transport of magnons beneath the modulator. We now test for this prediction in this and the succeeding Sections.

[36] In order to account for the full voltage signal, we introduced a factor of $\sqrt{2}$ to the voltage amplitudes $\Delta V^{1\omega}_{\mathrm{det}}$ in Eq. (5.45), since our lock-in detection unit outputs the root mean squared (RMS) signal and therefore is not representative for the actual signal.

[37] Strictly speaking, it is not valid to refer the critical enhancement to the spin resistance directly. This is because the correction of the voltage signals performed in Eq. (5.42) does not reflect a proper treatment of conductances, which usually have to be added reciprocally. The current analyisis still provides a suggestive visualization of the non-linear spin resistance behaviour. For a more rigorous analysis, we refer the reader to Ch. 5.3.4.

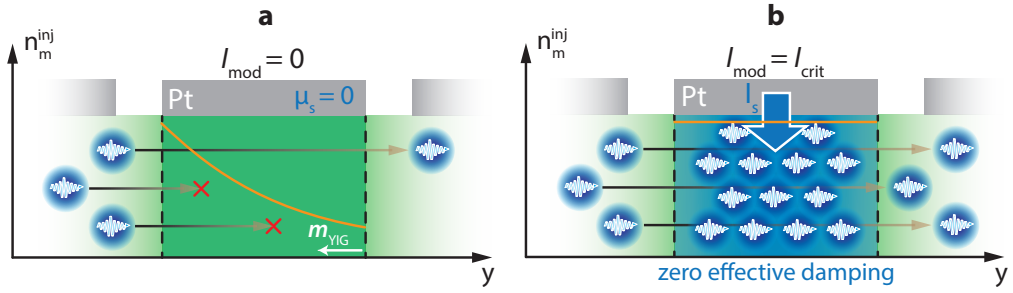

Fig. 5.12 – Illustrations of the magnon transport from injector to detector. We here only consider magnon transport directly below the modulator. **a** For $I_{mod} = 0$, magnons (blue wiggly arrows) generated by the injector diffuse from left to right. Magnon decay events, indicated by red crosses, result in a finite lifetime and a corresponding characteristic spin diffusion length depicted as an exponential decay of the injector magnon density n_m^{inj} (orange solid line). The modulator only statically affects the transport properties via magnon absorption. **b** For $I_{mod} = I_{crit}$, the modulator current is large enough to compensate the magnetic damping of the YIG, resulting in effectively vanishing magnon decay beneath the modulator. The damping compensation is illustrated by a large magnon accumulation beneath the modulator.

In Fig. 5.13**a** the critical spin resistance $R_{YIG}^{s,crit}$ is shown for the main device ($d = 900\,nm$, black data points) and a second device ($d = 700\,nm$, orange data points) for $\mu_0 H = 50\,mT$. In the positive bias regime, we define a characteristic onset current I_{on}, at which the magnon resistance $R_{YIG}^{s,crit}$ starts to drop rapidly by $0.13\,\Omega$ (black data points) and by $0.11\,\Omega$ (orange data points) and saturates at a finite value above the second characteristic current I_{crit}. Here, we define I_{on} as the current at which $R_{YIG}^{s,crit}$ drops by 10 % compared to the constant resistance below the critical regime for $I_{mod} < 0.4\,mA$. The critical current I_{crit} is taken at the current level where $R_{YIG}^{s,crit}$ starts saturating. This corresponds to the value of I_{mod} where the $\Delta V_{det}^{1\omega}(I_{mod})$ curves exhibit their maximum slope (see black triangles in Fig. 5.9). In order to validate the critical currents $I_{on/crit}$ extracted from our data, we plot them as a function of the applied magnetic field in Fig. 5.13**b** for the main device (black open and closed circles, respectively). Additionally, we plot I_{crit} for a second device with $d = 700\,nm$ (orange data points). Note that the critical spin resistance $R_{YIG}^{s,crit}$ (for the main device) is also shown for different magnetic fields in Fig. 5.11**d**. We first focus on the main device ($d = 900\,nm$, black data points): for I_{on} (I_{crit}), we observe a characteristic current around 0.45 mA (0.6 mA) for $\mu_0 H < 50\,mT$ and both critical currents increase with the applied magnetic field strength for $\mu_0 H > 50\,mT$. We now use Eqs. (5.14a) and (5.14b) to quantitatively compare the experimentally determined field dependence of I_{on} and I_{crit}, respectively, to their theoretical prediction. In Fig. 5.13**b**, the theoretical curves are shown for both I_{crit} (red line) and I_{on} (blue line), showing very good agreement with the experimental data. The values used for Eqs. (5.14a) and (5.14b) are summarized in Tab. 5.2. All of these values used for simulating our data have been determined experimentally. The characteristic parameters α_{eff} and α_{sp} entering Eqs. (5.12a) and (5.12b) are determined independently using the ferromagnetic

resonance experiments presented in Ch. 5.2.3. For a good quantitative agreement with our data, we used an inhomogenous broadening of $\mu_0 \delta H = 2.7\,\mathrm{mT}$, which is slightly larger than the experimentally determined value of 2.54 mT (cf. Tab. 5.1). Since, however, we had to use a different (but similar) YIG film for the FMR characterization (cf. 5.2.3), it is not surprising that the inhomogenous broadening is slightly different for the YIG film used for the magnon transport experiments[38]. Note, that the strong increase of the theory curve for small magnetic fields is due to the field dependent second term in Eq. (5.15). Hence, the effective damping α_{eff} diverges when the magnetic field approaches zero. The slight discrepancy between experimental data and theory for $\mu_0 H < 50\,\mathrm{mT}$ in Fig. 5.13**b** stems from the in-plane magnetocrystalline anisotropy (see Sec. 5.2.6), which could be included by substituting $H \to H + H_{\mathrm{ani}}$ in Eqs. (5.14b) and (5.15) (where H_{ani} denotes the cubic anisotropy field, see last paragraph in Ch. 5.1.1). To keep the number of parameters low, however, this is not included here. To test for reproducibility, we included the data for I_{crit} from a second device with $d = 700\,\mathrm{nm}$ (orange spheres), which is in quantitative agreement with the data for the main device with $d = 900\,\mathrm{nm}$.

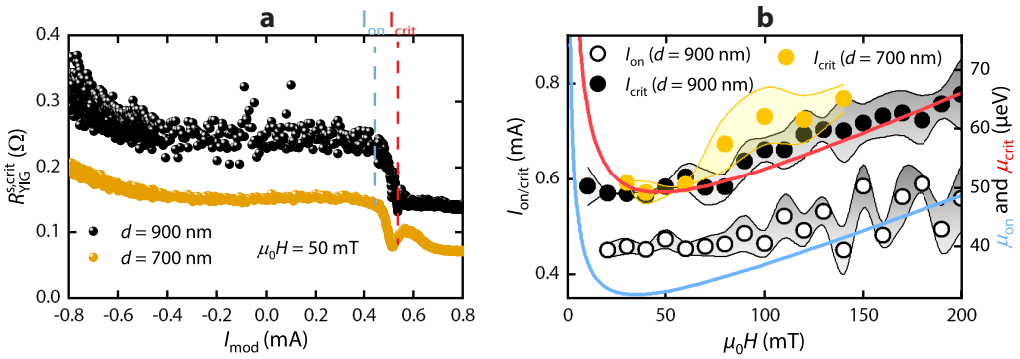

Fig. 5.13 – **a** Critical magnon spin resistance $R_{\mathrm{YIG}}^{\mathrm{s,crit}}$ of the YIG channel between injector and detector for the main device ($d = 900\,\mathrm{nm}$, black data points) and a second device ($d = 700\,\mathrm{nm}$, orange data points) for an external magnetic field of $\mu_0 H = 50\,\mathrm{mT}$. Note, that $R_{\mathrm{YIG}}^{\mathrm{s,crit}}$ is corrected for effects associated with (linear) SHE and (quadratic) thermal magnon injection effects. A very steep decrease of $R_{\mathrm{YIG}}^{\mathrm{s,crit}}$ for $I_{\mathrm{on}} < I_{\mathrm{mod}} < I_{\mathrm{crit}}$ is evident for both devices. **b** Critical currents $I_{\mathrm{on/crit}}$ versus applied magnetic field $\mu_0 H$. The right y-axis shows the critical chemical potentials $\mu_{\mathrm{on/crit}}$ from Eqs. (5.12a) and (5.12b) (solid blue and red lines, respectively).

The analysis demonstrates that our experimental results can be well rationalized by the SOT-induced compensation of the magnetic damping beneath the modulator strip, which we measure as a characteristic enhancement of the magnon conductivity between injector and detector. As derived in Ch. 5.1, the threshold

[38] We note that there can be significant differences in the damping properties between different YIG films, although they are nominally prepared with identical growth parameters.This also includes the spin pumping induced damping parameter α_{sp}, which is determined by the interface spin mixing conductance. In principle, it is therefore possible that the YIG film used for the magnon transport experiments has, in reality, a different combination of magnetic damping properties (α_{G}, M_{s} and δH) that account for the experimental data. We will see in Ch. 5.3.4 another approach for the determination of these parameters.

Device $d = 900\,\mathrm{nm}$	Symbol	Value	Unit
Pt strip thickness	t_{Pt}	3.5	nm
Pt strip width	w	500	nm
Pt spin diffusion length [54]	l_{s}	1.5	nm
Pt spin Hall angle [54]	θ_{SH}	0.11	
Pt conductivity	σ_{e}	1.74×10^{6}	$1/\Omega\mathrm{m}$
YIG thickness	t_{YIG}	13.4	nm
gyromagnetic ratio	γ	1.78×10^{11}	rad/Ts
YIG saturation magnetization	$\mu_0 M_{\mathrm{s}}$	140	mT
spin mixing conductance	$g_{\mathrm{r}}^{\uparrow\downarrow}$	1.02×10^{19}	$1/\mathrm{m}^2$
effective spin mixing conductance	$g_{\mathrm{eff}}^{\uparrow\downarrow}$	6.07×10^{18}	$1/\mathrm{m}^2$
Gilbert damping	α_{G}	2.17×10^{-3}	
spin pumping induced damping	α_{sp}	6.0×10^{-3}	
inhomogenous broadening	$\mu_0 \delta H$	2.7	mT

Tab. 5.2 – Values for the parameters entering Eq. (5.12a), (5.12b) and (5.13) used for the theory curves shown in Fig. 5.13**b**.

conditions calculated from the theories of both SHOs and DC pumped magnon BEC (and herein in particular the swasing threshold μ_{crit}) are identical, suggesting that the magnon system beneath the modulator undergoes a BEC transition as proposed by Bender *et al.* in Ref. [187]. According to Bender *et al.*, the threshold of the BEC is determined by the continuous condensation of magnons into the ground state (cf. Ch. 5.1), corresponding to a phase transition of second order. The observation of a smooth transition of $R_{\mathrm{YIG}}^{\mathrm{s,crit}}$ in Fig. 5.13**a** might be indicative of this second order phase transition, where magnons are condensing continuously into a steady state Bose-Einstein condensate. In the context of the spin resistance, this continuous magnon condensation from the thermal magnon cloud (representing the excited magnons above the ground state) into the ground state is reflected by a continuously diverging magnon lifetime τ_{m} within the non-linear regime (cf. Ch. 5.1.2 and Eq. (5.31)). Hence, the sudden spin resistance drop might be related to a sharp entropy drop in the magnon system since the condensed magnons carry no entropy [187]. This supports the claim of the observation of the theoretically predicted second-order phase transition (see also Ch. 7.1). The swasing threshold μ_{crit} is then associated with the full compensation of the intrinsic magnetic damping (i.e. $\tau_{\mathrm{m}} \to \infty$), which we have shown to be fully identical to the threshold condition of the SHO theory (cf. 5.1) and can thus be identified with an auto-oscillation of the magnetization. In a common sense, this auto-oscillation/swasing threshold might actually be referred to as a magnon BEC, since it corresponds to a macroscopic occupation of the lowest magnon energy state rather than the onset of condensation as defined in Ref. [187]. The difference between the BEC threshold and the swasing/damping compensation threshold originates from the fact that magnons represent excitations with a finite lifetime and hence correspond to a non-conserved quantity.

Even though the arguments stated above, together with the compelling agreement of our data with the theoretical prediction of the phase transition support the emergence of a magnon BEC, our experiment cannot unambiguously determine whether the magnon system does indeed undergo this phase transition. This is rooted in various reasons: although the critical currents fit well to the DC pumped magnon BEC theory, the threshold conditions are essentially given by the equality of the magnon relaxation and pumping rate and thus assume no coherence of the excited modes, which represents a necessary requirement for a BEC. Therefore, the magnon system in our experiment is likely to be described by multiple, rather independent auto-oscillations of the magnetization [181, 205, 206] beneath the modulator, which usually do not necessarily correspond to the lowest possible magnon energy state. Since we had no access to frequency sensitive measurements of the magnon system, we cannot check for this feature easily. However, in Ch. 5.5, we present micromagnetic simulations of the SOT-driven dynamics in the YIG film, which enables us to access the excited frequency spectrum from a numerical standpoint. The simulations suggest the formation of multiple spin wave bullets [184, 207] beneath the modulator with evanescent character.

5.3.4 Phenomenological Model for the Critical Magnon Conductivity Modulation

While the low bias regime investigated in Ch. 5.3.1 is properly described by a linear (SHE) and quadratic (thermal) modulation of the magnon conductivity due to a magnon density change as demonstrated in Eq. (5.30), this description clearly breaks down for larger currents (cf. Ch. 5.3.2). As discussed in the second part of Ch. 5.1.2, the divergence of the magnon lifetime τ_m due to the damping compensation might represent a more accurate description of this non-linear regime. A theoretical approach to derive this non-trivial magnon spin conductivity enhancement is proposed by S. Takei in Ref. [188]. Similar to Ref. [187] discussed in Ch. 5.1, the author S. Takei considers magnon BEC formation under the influence of a spin chemical potential μ_s in a MI/HM bilayer and also computes the magnon spin conductivity $\sigma_m^{mod} \propto 1/R_{YIG}^{s,mod}$ due to the SHE-induced spin chemical potential bias in a HM modulator attached to a magnetic material, identical to our YIG/Pt device structure. Its dependence on the modulator current was discussed in the context of Eq. (5.32), according to which the magnon conductivity beneath the modulator diverges as $\sigma_m \propto (\mu_{crit} - \mu_s)^{-1/2} \propto (1 - I_{mod}/I_{crit})^{-1/2}$ when $I_{mod} \to I_{crit}$ with the characteristic exponent of $-1/2$. We will include this theoretical prediction into our experimental modelling in the following.

For a complete description of the magnon conductivity present in the YIG transport channel, we make use of the equivalent spin resistor model introduced in Fig. 5.11**c**, according to which the total magnon conductivity can be written as

$$\sigma_m = \frac{\hbar}{2e^2}\frac{2d' + w_{mod}}{A_{YIG}}\left(2R^{s'}_{YIG} + R^{s,mod}_{YIG}(I_{mod})\right)^{-1}, \tag{5.47}$$

where $R^{s,mod}_{YIG}(I_{mod})$ refers to the I_{mod}-dependent resistance beneath the modulator. Furthermore, d' is the distance between the center of the injector (detector) and the left (right) edge of the modulator and $A_{YIG} = t_{YIG} l_{Pt}$ is the cross section of the YIG transport channel. The prefactor $(2d' + w_{mod})/A_{YIG}$ therefore accounts for the conversion into a geometry-independent conductivity rather than conductance. In order to express Eq. (5.47) exclusively in terms of conductivities, we first rewrite the YIG spin resistances R^{s}_{YIG} into spin resistivities ρ^{s}_{YIG} according to $R^{s'}_{YIG} = (d'/A_{YIG})\rho^{s0}_{YIG}$ and $R^{s,mod}_{YIG} = (w_{mod}/A_{YIG})\rho^{s}_{YIG}(I_{mod})$ with $\rho^{s0}_{YIG} = \rho^{s}_{YIG}(I_{mod} = 0)$. Using these relations, we can rewrite Eq. (5.47) as

$$\sigma_m = \frac{\hbar}{2e^2}\left(2\rho^{s'}_{YIG} + \rho^{s,mod}_{YIG}(I_{mod})\right)^{-1}, \tag{5.48}$$

where we defined the scaled spin resistivities

$$\rho^{s'}_{YIG} = \frac{d'}{2d' + w_{mod}}\rho^{s0}_{YIG}, \tag{5.49}$$

$$\rho^{s,mod}_{YIG}(I_{mod}) = \frac{w_{mod}}{2d' + w_{mod}}\rho^{s}_{YIG}(I_{mod}). \tag{5.50}$$

In order to switch to conductivities, we further define the corresponding scaled magnon conductivities

$$\sigma'_m = \frac{\hbar}{2e^2}\left(\rho^{s'}_{YIG}\right)^{-1}, \tag{5.51}$$

$$\sigma^{mod}_m(I_{mod}) = \frac{\hbar}{2e^2}\left(\rho^{s,mod}_{YIG}(I_{mod})\right)^{-1}. \tag{5.52}$$

Finally, we introduce the modulator current dependence for σ^{mod}_m by identifying it with Eq. (5.32) introduced in Ch. 5.1.2, while the magnon conductivity σ'_m to the left and right of the modulator is considered to be constant and thus unchanged by the modulator current. As a final result, we obtain

$$\sigma_m(I_{mod}) = \left\{2(\sigma'_m)^{-1} + \left[\sigma^{0,mod}_m\left(1 - \frac{I_{mod}}{I_{crit}}\right)^{-1/2} + \Delta\sigma_{th} I^2_{mod}\right]^{-1}\right\}^{-1}, \tag{5.53}$$

where we introduced the scaled equilibrium magnon conductivity beneath the modulator

$$\sigma_{\mathrm{m}}^{0,\mathrm{mod}} = \frac{2d' + w_{\mathrm{mod}}}{w_{\mathrm{mod}}}\,\sigma_{\mathrm{m}}^{0} \tag{5.54}$$

with σ_{m}^{0} the actual equilibrium magnon conductivity independent of the geometry[39]. When the resistivity left and right to the modulator $\rho_{\mathrm{YIG}}^{\mathrm{s}'} = 0$, Eq. (5.53) reduces to Eq. (5.32). As a sanity check, we can calculate the predictions of the model in the limiting cases of $I_{\mathrm{mod}} = 0$ and $I_{\mathrm{mod}} = I_{\mathrm{crit}}$. For a vanishing modulator current, we obtain the equilibrium magnon conductivity

$$\sigma_{\mathrm{m}}^{0} \equiv \sigma_{\mathrm{m}}(I_{\mathrm{mod}} = 0) = \left(2(\sigma_{\mathrm{m}}')^{-1} + (\sigma_{\mathrm{m}}^{0,\mathrm{mod}})^{-1}\right)^{-1} = \left(2\rho_{\mathrm{YIG}}^{\mathrm{s}'} + \rho_{\mathrm{YIG}}^{\mathrm{s,mod0}}\right)^{-1}, \tag{5.55}$$

where $\rho_{\mathrm{YIG}}^{\mathrm{s,mod0}} = \rho_{\mathrm{YIG}}^{\mathrm{s,mod}}(I_{\mathrm{mod}} = 0)$. At the critical current, we expect the critical magnon conductivity

$$\sigma_{\mathrm{m}}^{\mathrm{crit}} \equiv \sigma_{\mathrm{m}}(I_{\mathrm{mod}} = I_{\mathrm{crit}}) = \left(2(\sigma_{\mathrm{m}}')^{-1}\right)^{-1} = \left(2\rho_{\mathrm{YIG}}^{\mathrm{s}'}\right)^{-1}, \tag{5.56}$$

which suggests that the resistivity beneath the modulator vanishes at I_{crit}, i.e. $\rho_{\mathrm{YIG}}^{\mathrm{s,mod}}(I_{\mathrm{crit}}) = 0$. We further define the ratio

$$\eta_{\mathrm{crit}} = \frac{\sigma_{\mathrm{m}}'}{\sigma_{\mathrm{m}}^{0,\mathrm{mod}}} = \frac{w_{\mathrm{mod}}}{d'}, \tag{5.57}$$

where we used Eq. (5.51), (5.49), (5.54) and $(\rho_{\mathrm{YIG}}^{\mathrm{s0}})^{-1} = \sigma_{\mathrm{m}}^{0}$ to arrive at the final result. The ratio η_{crit} therefore depends exclusively on the device geometry, in particular on the ratio between modulated and unmodulated regions. For our main device with $d' = 650\,\mathrm{nm}$ and $w_{\mathrm{mod}} = 500\,\mathrm{nm}$, we expect $\eta_{\mathrm{crit}} \approx 0.77$. In our following experimental analysis, we will assume that the current induced changes of the magnon conductivity are restricted to the region right beneath the modulator, while the regions right and left of it are left unchanged. A deviation of the experimentally determined η_{crit} from the expected value of 0.77 then indicates the aforementioned assumptions to be invalid. We will see in the subsequent subsections that the phenomenological description of the magnon conductivity modulation given in Eq. (5.53) is able to reproduce the critical current regime very compellingly.

[39] Note that we assumed the same geometric scaling $(2d' + w_{\mathrm{mod}})/w_{\mathrm{mod}}$ shown in Eq. (5.54) to be also absorbed in the thermally induced magnon conductivity change $\Delta\sigma_{\mathrm{th}}$.

Angular Dependence

First, we study the angular dependence of the detector signals with respect to the model expressed in Eq. (5.53). Therefore, we rephrase Eq. (5.53) to account for the angle dependent detector voltage amplitudes $V_{\mathrm{det}}^{1\omega}(\varphi)$. Due to the symmetry of the SHE-induced magnon injection, being only active for a parallel alignment of magnetization direction $\boldsymbol{m}_{\mathrm{YIG}}$ and spin polarization $\boldsymbol{s}$ (cf. Ch. 2.4), its magnitude is proportional to $\sim I_{\mathrm{mod}}(-\cos(\varphi))$[40]. The thermal injection, on the other hand, does not scale with the angle φ of the magnetization orientation. We can thus include the angle dependence of the detector signals as

$$V_{\mathrm{det}}^{1\omega}(\varphi, I_{\mathrm{mod}}) = \cos^2(\varphi) \times \left\{ 2(\Delta V')^{-1} + \left[\Delta V_{\mathrm{mod}}^{0} \left(1 - \frac{I_{\mathrm{mod}}(-\cos(\varphi))}{I_{\mathrm{crit}}} \right)^{-1/2} + \Delta R_{\mathrm{th}} I_{\mathrm{mod}}^2 \right]^{-1} \right\}^{-1} \tag{5.58}$$

where the coefficients $\Delta V'$, $\Delta V_{\mathrm{mod}}^{0}$ and ΔR_{th} correspond to σ_{m}', $\sigma_{\mathrm{m}}^{0,\mathrm{mod}}$ and $\Delta\sigma_{\mathrm{th}}$ in Eq. (5.53), respectively, and simply act as proportionality factors to account for the conversion of the different terms into voltages. Furthermore, the first $\cos^2(\varphi)$ function accounts for the usual angle dependence resulting from the SHE-induced magnon transport between injector and detector (cf. Ch. 2.7). In order to account for the additional SHE symmetry at the modulator, we replaced $I_{\mathrm{mod}} \rightarrow I_{\mathrm{mod}}(-\cos(\varphi))$ in the term related to the SHE-induced magnon injection (i.e. the diverging term) of Eq. (5.53) [172, 188]. On the basis of Eq. (5.58), we can separate the different angle symmetries and thus write down a fitting equation for the angle dependence as

$$V_{\mathrm{det}}^{1\omega}(\varphi) = \frac{A\cos^2(\varphi) + B\cos^2(\varphi)\left(1 - \frac{I_{\mathrm{mod}}(-\cos(\varphi))}{I_{\mathrm{crit}}}\right)^{1/2}}{1 + C\left(1 - \frac{I_{\mathrm{mod}}(-\cos(\varphi))}{I_{\mathrm{crit}}}\right)^{1/2}}, \tag{5.59}$$

where $A = \Delta V'/2$, $B = (1/2)\,(\Delta V'/\Delta V_{\mathrm{mod}}^{0})\Delta R_{\mathrm{th}} I_{\mathrm{mod}}^2$, $C = (1/\Delta V_{\mathrm{mod}}^{0})(\Delta R_{\mathrm{th}} I_{\mathrm{mod}}^2 + \Delta V'/2)$ and I_{crit} are used as fit parameters. In Fig. 5.14, the angle dependent detector signals $V_{\mathrm{det}}^{1\omega}$ are plotted for different modulator currents, where panel **a** corresponds to $I_{\mathrm{mod}} > 0$ and panel **b** to $I_{\mathrm{mod}} < 0$. Since our phenomenological model in Eq. (5.53) is only valid up to $I_{\mathrm{mod}} = I_{\mathrm{crit}}$, we restrict the fitting via Eq. (5.59) to currents up to $I_{\mathrm{mod}} = 0.5\,\mathrm{mA} \lesssim I_{\mathrm{crit}}$. Furthermore, we fix the fit parameter I_{mod} to the corresponding value used in the respective data set. The fit results are shown as the solid lines in Fig. 5.14**a** and **b**. Evidently, we can excellently

[40] Positive (negative) magnetic fields are defined at $\varphi = \pm 180°$ ($\varphi = 0°$) (cf. Fig. 5.2**a**). Thus, magnons are injected (depleted) via the SHE when $H \cdot I_{\mathrm{mod}} > 0$ ($H \cdot I_{\mathrm{mod}} < 0$). In order to account for these conditions, the minus sign before the $\cos(\varphi)$-function is introduced such that for the injection (depletion) of magnons $I_{\mathrm{mod}}(-\cos(\varphi) > 0$ ($I_{\mathrm{mod}}(-\cos(\varphi)) < 0$).

reproduce the angle dependence with the phenomenological model presented in Eq. (5.59). In particular, it is able to reproduce the rather sharp spike observed for the large currents $I_{\mathrm{mod}} = \pm 0.5\,\mathrm{mA} \sim I_{\mathrm{crit}}$, which is due to the additional angle symmetry introduced in Eq. (5.59) near I_{crit}.

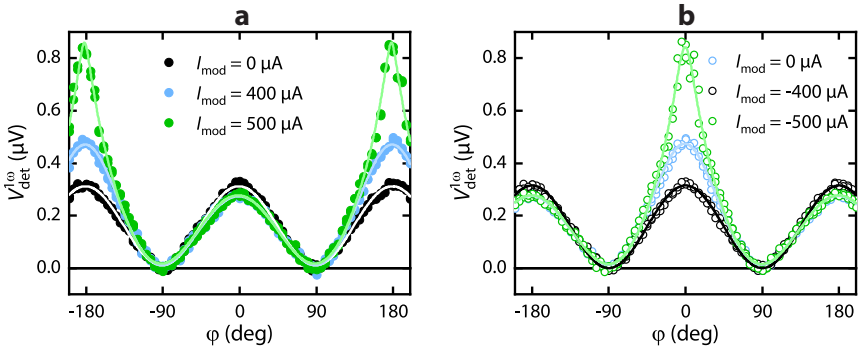

Fig. 5.14 – First harmonic detector signal $V_{\mathrm{det}}^{1\omega}$ plotted versus the rotation angle φ of the in-plane field at $\mu_0 H = 50\,\mathrm{mT}$ for **a** positive and **b** negative DC bias currents I_{mod} in the modulator, similar to Fig. 5.8. However, we restrict ourselves to the current regime $I_{\mathrm{mod}} \lesssim I_{\mathrm{crit}}$. **a** Magnon transport signal for $I_{\mathrm{mod}} > 0$. **b** Magnon transport signal for $I_{\mathrm{mod}} < 0$. Solid lines are fits to Eq. (5.59).

Eventually, we achieve an accurate phenomenological modelling of the experimentally observed angle dependence based on Eq. (5.53). Since the most prominent modulation of the angle dependence stems from the square root dependencies in Eq. (5.59), which is based on the SHE-induced injection of magnons [188], we can conclude that the electrically injected magnons via the SHE are exclusively responsible for the damping compensation (or BEC/swasing transition) in our experiment. By implication, this suggests that the thermally-induced magnons do not contribute to the damping compensation, but rather hinder the magnon system to reach damping compensation, which corroborates the theoretical prediction [187, 188]. We note that a temperature increase due to Joule heating leads to an increase of the interface spin conductance [36] and might therefore also reinforce the damping compensation by increasing the interface spin transparency. This, however, does still not account for the observed angle dependence as the temperature increase does not depend on φ.

Current Dependence

For the purpose of validating our model further, we fit Eq. (5.58) to the current dependence of $V_{\mathrm{det}}^{1\omega}$ shown in Fig. 5.9. To this end, we set $\varphi = \pm 180°$ for positive magnetic fields, while $\varphi = 0°$ for negative magnetic fields. In the fitting routine, we use $\Delta V'$, $\Delta V_{\mathrm{mod}}^{0}$, ΔR_{th} and I_{crit} as the free fitting parameters. We further restrict the fit range up to the point exhibiting the largest slope, which corresponds to the divergence of the square root term in Eq. (5.58). Beyond this point, the model is no longer valid. Evidently, we find an excellent agreement of our phenomenological model with the experimental data. To check for the predictions of the model, we

extract the fit parameter I_{crit} for each external magnetic field and plot the result in Fig. 5.15**a** as the blue open circles. For comparison, we also plot the critical currents that were extracted manually at the point of the maximum slope in Fig. 5.9 together with the corresponding simulation of Eq. (5.14b) discussed in Ch. 5.3.3 (black closed circles and red line, respectively). The critical currents extracted from our fitting function (Eq. (5.58)) show a very good agreement with those extracted manually, besides that the former exhibits a slightly larger slope. This most probably owes to the fact that the manual extraction becomes increasingly inaccurate at larger field values since the critical enhancement of the $V_{\mathrm{det}}^{1\omega}(I_{\mathrm{mod}})$ curves becomes increasingly smaller, making the manual extraction tedious. In order to check for the predictions of our model, we attempt to fit the blue data points in Fig. 5.15**a** with the expression for the critical threshold current given in Eq. (5.14b). Unlike implemented for the simulation of the red curve shown in Fig. 5.15**a**, where we determined the spin mixing conductance $g_{\mathrm{r}}^{\uparrow\downarrow}$ of our YIG film via FMR measurements of a comparable film (see Ch. 5.2.3), we here instead determine the spin mixing conductance directly via measuring the SMR at the modulator [54]. The corresponding relative SMR amplitude is determined to $\sim 4 \times 10^{-4}$. Using Eqs. (2.46) and (5.6) together with the values given in Tab. 5.2 results in an effective spin mixing conductance $g_{\mathrm{eff}}^{\uparrow\downarrow} = 1.72 \times 10^{18}\,\mathrm{m}^{-2}$, which is used to calculate the spin pumping induced damping parameter $\alpha_{\mathrm{sp}} = 1.75 \times 10^{-3}$. We use this parameter as a fixed value in the fit. Moreover, we include a finite cubic anisotropy field by substituting $H \to H + H_{\mathrm{ani}}$ in Eq. (5.14b) (cf. Ch. 5.1.1). The resulting fit is shown as the orange solid line in Fig. 5.15**a**, featuring the free fitting parameters $\mu_0 \delta H = 0.72\,\mathrm{mT} \pm 0.02\,\mathrm{mT}$, $\alpha_{\mathrm{G}} = (1.14 \pm 0.1) \times 10^{-3}$ and $\mu_0 H_{\mathrm{ani}} = 9.54\,\mathrm{mT} \pm 2.13\,\mathrm{mT}$. The values are also listed in Tab. 5.3 for convenience. The extracted values for α_{G} and $\mu_0 \delta H$ are in good agreement with typical values determined for thin YIG films grown at the Walther-Meißner-Institut. Comparing them to the ones determined via FMR in Ch. 5.2.3, a significant difference is apparent. Since, however, the FMR measurements have been conducted on a different YIG film, the discrepancy is not surprising. Upon comparing the cubic anisotropy field to the literature value given by $\mu_0 H_{\mathrm{ani}} = 2|K_{\mathrm{c1}}|/M_{\mathrm{s}} = 10.8\,\mathrm{mT}$ (with $|K_{\mathrm{c1}}| = -600\,\mathrm{J\,m^{-3}}$ corresponding to the room temperature value taken from Ref. [204]), we find very good agreement to the fitted value of H_{ani}. Eventually, we can conclude that the model based on the non-linear magnon conductivity modulation given in Eq. (5.53) is a very suitable tool for the extraction of the critical currents and is likely to provide better results than the manual extraction.

Apart from the critical currents, we can also extract the ratio η_{crit} defined in Eq. (5.57) via our fit parameters. Since the fit parameters are voltage quantities and thus proportional to the magnon conductances rather than conductivities, we have to include the geometrical features for the calculation of the respective magnon

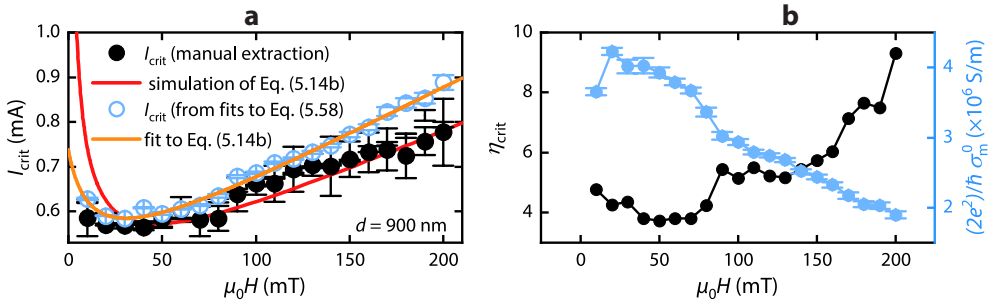

Fig. 5.15 – **a** Comparison of the critical currents I_{crit}, either (i) manually extracted by determining the maximum slope of the $\Delta V_{det}^{1\omega}$ (black closed data points taken from Fig. 5.13**b**) or (ii) by fitting Eq. (5.58) to the $\Delta V_{det}^{1\omega}(I_{mod})$ curves in Fig. 5.9 and extracting I_{crit} as a fitting parameter (blue open data points). The red line corresponds to the simulation of Eq. (5.14b) using the values from Tab. 5.2, while the orange solid line is a fit to Eq. (5.14b) to the blue data points. In the latter, we included a cubic anisotropy field H_{ani} to the fitting equation and determined the spin pumping induced damping parameter from SMR measurements at the modulator. We used α_G, δH and H_{ani} as free fit parameters. **b** Ratio η_{crit} as defined in Eq. (5.57) plotted as a function of the external magnetic field (black points, left vertical axis). The right blue axis and data points show the equilibrium magnon conductivity σ_m^0 calculated with Eq. (5.61).

conductivities according to $\sigma_m' \propto (d'/A_{YIG})\Delta V'$ and $\sigma_m^{0,mod} \propto (w_{mod}/A_{YIG})\Delta V_{mod}^0$. The ratio η_{crit} can then be determined from the expermimental quantities as

$$\eta_{crit} = \frac{d'}{w_{mod}} \frac{\Delta V'}{\Delta V_{mod}^0}. \tag{5.60}$$

Using the fit parameters from Eq. (5.58), the conductivity ratio η_{crit} is plotted as a function of the external magnetic field in Fig. 5.15**b** (black data points). While it shows a fairly constant behaviour for fields up to $\mu_0 H \approx 80\,\mathrm{mT}$, we observe a significant increase for larger magnetic fields, which is in contrast to our expectation of a constant value for η_{crit}. This unexpected behaviour probably owes to the fact that the model projects the majority of the field dependence to only one of the fit parameters, which is captured by $\Delta V_{mod}^0 \propto \sigma_m^{0,mod}$ in our case. The inclusion of the expected field dependence of the conductivities (as e.g. shown in Eq. (5.62) further below) into the model might resolve this issue, but is also likely to increase its complexity unnecessarily. In the following, we will therefore limit ourselves to the minimum value of η_{crit} around $\mu_0 H = 50\,\mathrm{mT}$. In contrast to the expected value of 0.77, we here find $\eta_{crit} \approx 4$. As discussed in the beginning of this Section, this suggests that the current induced conductivity modulation extends to a larger width than the mere modulator width w_{mod}. Adjusting the ratio d'/w_{mod} in Eq. (5.60) to achieve $\eta_{crit} = 0.77$ results in the effective values $d'_{eff} \approx 310\,\mathrm{nm}$ and $w_{mod}^{eff} \approx 1.18\,\mu\mathrm{m}$. This means that the magnon conductivity (resistivity) at the critical current diverges (vanishes) for a width of at least 1.18 µm. Comparing this value to the (experimental) modulator width of $w_{mod} = 540\,\mathrm{nm}$ (determined for the main device via AFM measurements presented in Ch. 5.2.2), indicates that the zero resistance state extends to a significantly larger area than

given by the modulator width. In particular, the zero resistance state exceeds the modulator width by roughly $\sim 320\,\mathrm{nm}$ on each side. Since the magnons exhibit a finite diffusion length of about $1\,\mu\mathrm{m}$ (see next Ch. 5.3.5), it is reasonable that the zero resistance region extends to larger values than naively suggested from w_{mod}.

After establishing the effective widths for the modulated ($w^{\mathrm{eff}}_{\mathrm{mod}}$) and unmodulated ($d'_{\mathrm{eff}}$) regions in our device, we can now extract the equilibrium magnon conductivity σ^0_{m} from our critical magnon conductivity model defined in Eq. (5.58). According to Eq. (5.54), we can express the equilibrium magnon conductivity as $\sigma^0_{\mathrm{m}} = [w^{\mathrm{eff}}_{\mathrm{mod}}/(2d'_{\mathrm{eff}} + w^{\mathrm{eff}}_{\mathrm{mod}})]\,\sigma^{0,\mathrm{mod}}_{\mathrm{m}}$. Furthermore, the scaled equilibrium magnon conductivity beneath the modulator scales with the corresponding fit parameters as $\sigma^{0,\mathrm{mod}}_{\mathrm{m}} \propto (w^{\mathrm{eff}}_{\mathrm{mod}}/A_{\mathrm{YIG}})\,\Delta V^0_{\mathrm{mod}}$. In order to convert the corresponding fit parameter $\Delta V^0_{\mathrm{mod}}$ from Eq. (5.58) (which is given in units of V) into the magnon conductivity $\sigma^{0,\mathrm{mod}}_{\mathrm{m}}$, we make use of Eq. (5.46), from which follows that

$$\sigma^0_{\mathrm{m}} = \frac{\hbar}{2e^2}\frac{w^{\mathrm{eff}}_{\mathrm{mod}}}{2d'_{\mathrm{eff}} + w^{\mathrm{eff}}_{\mathrm{mod}}}\left(\frac{w^{\mathrm{eff}}_{\mathrm{mod}}}{A_{\mathrm{YIG}}}\frac{\eta_{\mathrm{s}}(\Delta V^0_{\mathrm{mod}})}{R^{\mathrm{s}}_{\mathrm{Pt}}}\right). \tag{5.61}$$

The expression in brackets refers to the scaled equilibrium magnon conductivity $\sigma^{0,\mathrm{mod}}_{\mathrm{m}}$ and η_{s} is the spin transfer efficiency which is a linear function of $\Delta V^0_{\mathrm{mod}}$. The result of Eq. (5.61) is plotted as a function of the external magnetic field in Fig. 5.15**b** (blue data points). We find $(2e^2)/\hbar\,\sigma^0_{\mathrm{m}} \approx 4.2 \times 10^6\,\mathrm{S\,m^{-1}}$ for the maximum around $\mu_0 H = 20\,\mathrm{mT}$ and an overall monotonous decrease of the conductivity for larger magnetic fields. The initial increase observed for the first two data points is likely to be related to the initial magnetization saturation of the YIG. In theory, the field dependence of the magnon conductivity can be included when a finite magnon gap $\Delta = \hbar\gamma\mu_0 H$ is considered in the calculation of the magnon current density $\boldsymbol{j}_{\mathrm{m}}$ (see Eq. (2.52)), which was omitted in the derivation shown in the theory Chapter 2.7.2. When including a magnon gap in the dispersion according to $\epsilon_{\mathrm{m}}(\boldsymbol{k}) = J_{\mathrm{s}}k^2 + \Delta$, an approximate solution to Eq. (2.52) (from which the magnon conductivity is deduced) reads as

$$\sigma^0_{\mathrm{m}}(\Delta) \approx \frac{3}{\zeta(3/2)}\hbar\frac{n_{\mathrm{m}}\tau_{\mathrm{m}}}{m_{\mathrm{m}}}\,\mathrm{Li}_{5/2}\left(\mathrm{e}^{-\Delta/(k_{\mathrm{B}}T)}\right), \tag{5.62}$$

where $\mathrm{Li}_n(z)$ is the polylogarithmic function of order n. Since $\Delta \ll k_{\mathrm{B}}T$ in our case, Eq. (5.62) can be reasonably approximated up to first order, suggesting a linear decreasing behaviour of the magnon conductivity as a function of the external magnetic field H. Indeed, a linear behaviour fits well to the observed evolution in Fig. 5.15**b** and thus further validates our suggested model for the magnon conductivity modulation. More intuitively speaking, as the magnon gap increases with increasing magnetic field strength, low frequency magnons are depleted and are therefore diminishing the magnon conductivity due to the associated magnon density decrease. We note, that the predicted field dependence suggested by

Eq. (5.62) (for experimentally reasonable values regarding the magnon gap and temperature) predicts a significantly weaker dependence on the external field than what is experimentally observed. While the theory suggests a relative conductivity change (from 0 mT to 200 mT) of about $\sim$ 0.2 %, the experimentally observed decrease seen in Fig. 5.15**b** is much larger at about $\sim$ 54 %. This discrepancy was observed in multiple studies in recent literature [166, 208] and indicates the underrated importance of low frequency magnons for the SHE-induced magnon transport. Furthermore, additional field dependencies stemming from sources unrelated to the magnon conductivity itself, such as the spin conductance g at the injector or the spin Hall physics in Pt, have been disregarded here but are likely to affect the overall field dependence of our experimentally measured signals.

Overall, the analysis of the magnon conductivity/spin resistivity based on the theoretical prediction by S. Takei in Ref. [188] demonstrates a very compelling agreement between theory and experiment. It significantly enhances the precision of extracting critical currents from the magnon transport data and offers further insight into the physics of the critical magnon conductivity modulation. Moreover, the excellent agreement between theory and experiment might be regarded as a further indication for the formation of a DC pumped magnon BEC beneath the modulator. According to the micromagnetic simulations implemented in Ch. 5.5, however, it is unlikely that the supposed BEC can be interpreted as a spatially uniform magnetization precession beneath the modulator, though its spectral coherence near I_{crit} is large. As for now, it might therefore still be bold to claim that the magnon system is in a BEC state when the critical current is reached. Frequency sensitive measurements of the magnon system are therefore desirable.

5.3.5 Spatial Extension of the Damping Compensated Region

In the preceding Ch. 5.3.4, we have demonstrated excellent agreement between the experimental data and our phenomenological model based on the theoretical prediction of critical magnon conductivity enhancement derived in Ref. [188]. As predicted by our corresponding model shown in Eq. (5.53), the magnon conductivity at the critical current suggests a vanishing magnon resistivity beneath the modulator, which might be interpreted as spin superfluidity [209–213]. We therefore expect the YIG spin resistance to conform to $R^{\mathrm{s}}_{\mathrm{YIG}} = 2R^{\mathrm{s}'}_{\mathrm{YIG}} + R^{\mathrm{s,mod}}_{\mathrm{YIG}}$ for $I_{\mathrm{mod}} = 0$ and $R^{\mathrm{s}}_{\mathrm{YIG}} = 2R^{\mathrm{s}'}_{\mathrm{YIG}}$ for $I_{\mathrm{mod}} = I_{\mathrm{crit}}$, i.e. $R^{\mathrm{s,mod}}_{\mathrm{YIG}} \to 0$ (cf. Eq. (5.53)). In order to test this prediction, we perform measurements of $R^{\mathrm{s}}_{\mathrm{YIG}}$ as a function of the injector-detector separation d_{id}, both for the case of zero current modulation as well as for critical current modulation. The difference between the critical and equilibrium distance dependencies should then give insight into how large the modulated regime with supposedly zero resistance is.

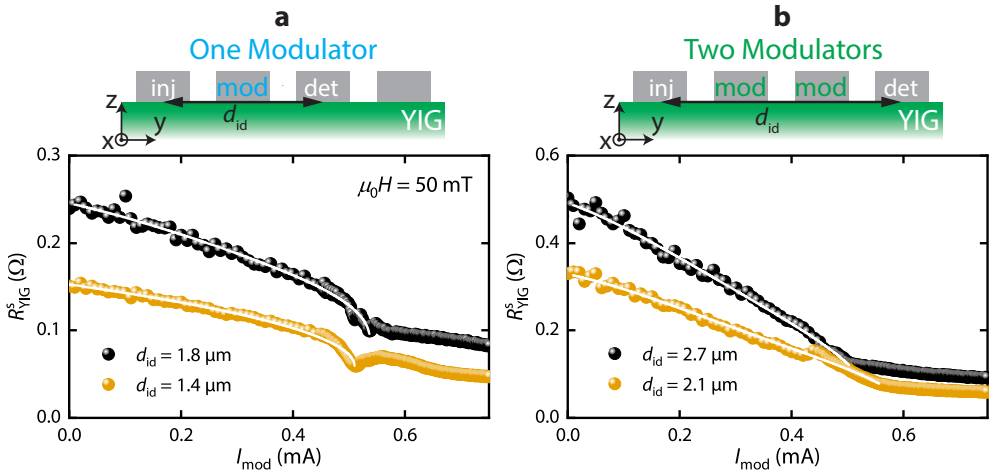

Fig. 5.16 – Calculated spin resistance R^s_{YIG} as a function of the modulator current I_{mod} for $\mu_0 H = 50\,\text{mT}$. The data shows the results for two different devices represented by black and orange data points. The corresponding injector-detector distance d_{id} is indicated. **a** R^s_{YIG} evaluated for the usual configuration depicted above the plot, where a single modulator is used. **b** R^s_{YIG} calculated based on measurements using two modulator strips employing the configuration depicted above the plot. White solid lines are fits to the inverse of the fitting function given in Eq. (5.58)

First and foremost, we calculate the total YIG spin resistance R^s_{YIG} as a function of I_{mod} from our first harmonic voltage signals $\Delta V^{1\omega}_{det}$ at the detector. To this end, we plug $\Delta V^{1\omega}_{det}$ into Eq. (5.45) and calculate the spin resistance R^s_{YIG} via Eq. (5.46). In Fig. 5.16**a**, we plot the result for the main device ($d = 900\,\text{nm}$) and a second device ($d = 700\,\text{nm}$) for an external magnetic field $\mu_0 H = 50\,\text{mT}$. The corresponding injector-detector separation d_{id} for the two devices is indicated in the figure. For the sake of completeness, we have fitted the data by the the inverse of our magnon conductivity model parameterized by the fitting function given in Eq. (5.58) (white solid lines). Beyond the critical regime, the curves exhibit another decreasing behaviour with reduced slope, which might be related to the continuing SHE- and thermally induced magnon injection in this regime. In order to test for a vanishing spin resistance beneath the modulators discussed above, we additionally measured the magnon transport under the influence of two modulators situated in between the injector and detector contact, as depicted in Fig. 5.16**b**. Here, the modulator current is simultaneously applied to both modulator strips, while the magnon transport is measured between injector and detector as usual. Qualitatively, a similar behaviour compared to the single modulator measurements shown in Fig. 5.16**a** is observed. We again fitted the inverse of our model to the data which is indicated by the white lines. Interestingly, a major difference in the fitting parameters arises for $\Delta V' \propto \sigma'_m$ upon comparing the two configurations. In fact, $\Delta V'$ is tens of orders of magnitude larger for the two modulator experiment as compared to the one with only a single modulator. Since σ'_m quantifies the conductivity next to the modulators (see equivalent spin resistor model in Fig. 5.11**c**), its value is supposed to be unchanged by the modulator current in an ideal case. The

suggested extremely large value extracted from the experiment, however, suggests that the corresponding spin resistivity $\rho^{s'}_{YIG} = (\sigma'_m)^{-1} \approx 0$. Consequently, the total spin resistivity ρ^{s}_{YIG} at the critical current I_{crit} is expected to completely vanish in the YIG transport channel. Under this assumption, the remaining resistance R^{s}_{YIG} in Fig. 5.16**b** for $I_{mod} > I_{crit}$ must be attributed to the interfacial spin resistances R^{s}_{int} and the electronic spin resistance R^{s}_{Pt} in the Pt layers. We will test for this conjecture via the distance dependent measurements in the following.

In Fig. 5.17**a** and **b**, R^{s}_{YIG} is plotted as a function of d_{id}. Here, the black data points correspond to the spin resistance for $I_{mod} = 0$. As introduced in Ch. 2.7.2, we expect an exponential increase of the spin resistance with increasing distance[41]. Therefore, we fit the data with an exponential function of the form

$$R^{s}_{YIG}(d_{id}) = R^{s}_{0}(I_{mod})\, e^{d_{id}/\lambda_m}, \tag{5.63}$$

where $R^{s}_{0}(I_{mod})$ is the spin resistance for $d_{id} = 0$ at the modulator current I_{mod} and λ_m is the magnon diffusion length. From the fit, which is shown as the black solid lines in Fig. 5.17**a** and **b**, we obtain $\lambda_m = 1.2\,\mu m$. Note, that we limited the fit range to $d_{id} \geq 1\,\mu m$ since the exponential behaviour breaks down for $d_{id} < \lambda_m$ to become algebraic (see Ch. 2.7.2). As a next step, we plot R^{s}_{YIG} for a modulator current of $I_{mod} = 0.6\,mA \geq I_{crit}$, where we expect zero resistance beneath the modulator. The result is shown as the blue open data points in Fig. 5.17**a**, exhibiting a clear resistance drop compared to the zero current modulation. The data is also fitted with Eq. (5.63), obtaining $\lambda_m = 1.1\,\mu m$, in reasonable agreement with the diffusion length obtained for the non-modulated case. Assuming $\lambda_m = 1.2\,\mu m$ for both functions, we can calculate the distance between the two exponential curves (as indicated in Fig. 5.17**a**), by equating the two exponentials according to

$$R^{s}_{0}(I_{crit}) e^{(d_{id}+\Delta d)/\lambda_m} \stackrel{!}{=} R^{s}_{0}(0) e^{d_{id}/\lambda_m}, \tag{5.64}$$

where Δd is the distance by which one of the curves has to be shifted in order to account for the observed resistance change. Solving for Δd results in

$$\Delta d = \lambda_m \ln\left(\frac{R^{s}_{0}(0)}{R^{s}_{0}(0.6\,mA)}\right), \tag{5.65}$$

where $R^{s}_{0}(I_{mod})$ is determined from the exponential fits. For the single modulator configuration depicted in Fig. 5.17**a**, we obtain $\Delta d_1 \approx 1.8\,\mu m$. Hence, we can account for the resistance drop by assuming zero resistance magnon transport within a transport length of $1.8\,\mu m$ when $I_{mod} = 0.6\,mA \geq I_{crit}$. As derived from our magnon conductivity model in Ch. 5.3.4, the effective region adopting zero resistance magnon transport in our main device was estimated to $w^{eff}_{mod} \approx 1.18\,\mu m$,

[41] Since the detector amplitude $\Delta V^{1\omega}_{det}$ is expected to decrease exponentially, the corresponding spin resistance $R^{s}_{YIG} \propto 1/\Delta V^{1\omega}_{det}$ therefore increases exponentially.

considerably smaller than the zero resistance transport length Δd_1 extracted here. This discrepancy might be related to the fact that we extracted a lower limit for η_{crit} (cf. Fig. 5.15) and therefore also a lower limit for $w_{\mathrm{mod}}^{\mathrm{eff}}$. Nonetheless, we can compare Δd_1 with the maximum spatial extension $\Delta d_1^{\mathrm{max}} = 2\lambda_{\mathrm{m}} + w_{\mathrm{mod}} \approx 2.7\,\mu\mathrm{m}$ of the zero resistance region, for which we considered the finite magnon diffusion length $\lambda_{\mathrm{m}} = 1.2\,\mu\mathrm{m}$ at both sides of the modulator and obviously the modulator width $w_{\mathrm{mod}} = 0.5\,\mu\mathrm{m}$. The modulation ratio $\Delta d_1 / \Delta d_1^{\mathrm{max}} \approx 0.66$, meaning that 66 % of the maximally possible extension of the magnon conductivity modulation adopts a zero resistance state.

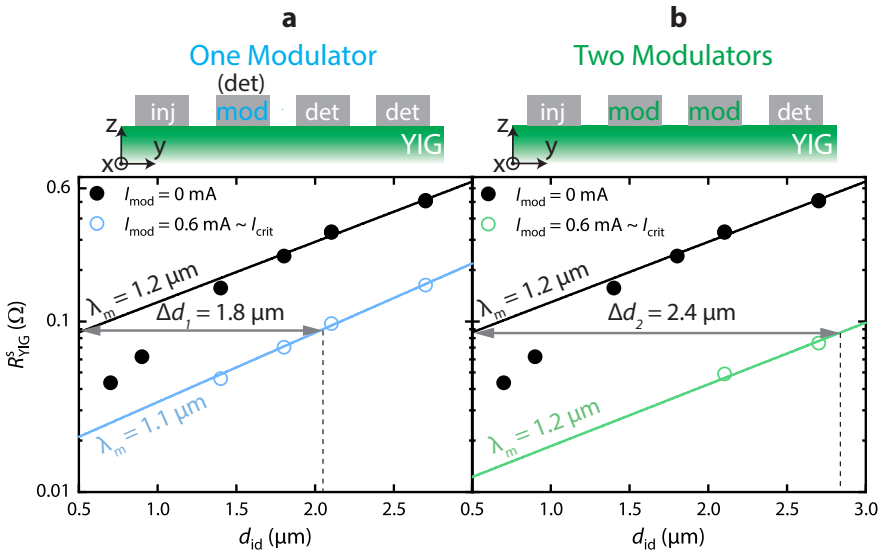

Fig. 5.17 – Magnon spin resistance $R_{\mathrm{YIG}}^{\mathrm{s}}$ as a function of the distance d_{id} between injector and detector. In both panels **a** and **b**, the black data points correspond to the distance dependence when no DC modulation current is applied. **a** Single modulator configuration: the blue data points show $R_{\mathrm{YIG}}^{\mathrm{s}}$ for $I_{\mathrm{mod}} = 0.6\,\mathrm{mA}$, employing the configuration with a single DC modulation strip as depicted above the plot. A remarkable decrease of $R_{\mathrm{YIG}}^{\mathrm{s}}$ compared to the zero current modulation is evident. Solid lines are fits to Eq. (5.63) for $d_{\mathrm{id}} \geq 1\,\mu\mathrm{m}$. The spin resistance decrease can be accounted for when we consider an approximately $\sim 1.8\,\mu\mathrm{m}$ long transport length with zero resistance. **b** Two modulator configuration: the green data points show the distance dependence for $I_{\mathrm{mod}} = 0.6\,\mathrm{mA}$ when two strips are simultaneously biased with the same DC modulator current as indicated above. Here, zero resistance magnon transport is found to occur over a distance of $\sim 2.4\,\mu\mathrm{m}$.

In a second experiment, we measure the distance dependent spin resistance $R_{\mathrm{YIG}}^{\mathrm{s}}$ for the configuration using two modulators, both of which are subject to the simultaneous application of the the modulator current I_{mod}. Similar to the single modulator configuration, we compare the distance dependence for $I_{\mathrm{mod}} = 0$ (black data points in Fig. 5.17**b**, same as in panel **a**) with the distance dependence when a current of $I_{\mathrm{mod}} = 0.6\,\mathrm{mA} \sim I_{\mathrm{crit}}$ is applied to both modulators at the same time (green open data points). Fitting Eq. (5.63) to both datasets, extracting the fit parameters and utilizing Eq. (5.65) results in a zero resistance transport distance of $\Delta d_2 \approx 2.4\,\mu\mathrm{m}$. Naively, we would have expected this length scale

to have doubled in size compared to the single modulator case. Instead, we only find $\Delta d_2 = 1.33\Delta d_1$. Since, however, the maximum extension of the zero resistance transport length in the two modulator configuration can be estimated to $\Delta d_2^{\mathrm{max}} = 2\lambda_{\mathrm{m}} + 2w_{\mathrm{mod}} + d_{\mathrm{e}} = 3.6\,\mu\mathrm{m}$, where $d_{\mathrm{e}} = 0.4\,\mu\mathrm{m}$ is the edge-to-edge distance between the two modulators for the main device (and thus represents an upper limit as it was the maximum d_{e} considered). This results in a modulation ratio of $\Delta d_2^{\mathrm{max}}/\Delta d_2 = 0.66$, which perfectly matches with the modulation ratio determined for the single modulator case. We therefore conclude that our distance dependent measurements give a decent estimate for the spatial extension of the damping compensated region with zero resistance magnon transport.

It is important to point out that the present analysis based on the magnon conductivity model (cf. Eq. (5.53)) implicitly makes the very crude assumption that there is a defined border between regions with a magnon conductivity being modulated by the DC current and regions that are not affected by it. Clearly, this is a direct consequence of the equivalent spin resistor network on which our magnon conductivity model is based on. In reality, however, the magnon conductivity modulation adopts a continuous change with increasing distance from the modulator, rather than having discrete values for certain regions. The extracted values for the zero resistance transport length Δd must therefore be considered as effective length scales and might not necessarily reflect the actual spatial extensions. It should also be noted that apart from the SHE-induced and thermal spin Seebeck induced magnon injection (and thus conductivity modulation), there might also be a considerable effect from the mere temperature rise in our sample, as quantified in Ch. 5.2.4. In principle, this leads to an additional magnon conductivity increase due to the thermal activation of magnons, for which we do not account here but might also influence our analysis of the spatial extension of the zero resistance state.

In conclusion, we have shown that the compensation of the magnetic damping via current induced injection of magnons is compatible with zero resistance magnon transport beneath the modulator. This zero resistance is interpreted by a diverging magnon lifetime τ_{m} and therefore results in lossless magnon transport. We want to point out that this feature by itself is not sufficient to verify the formation of a magnon BEC as proposed in Refs. [187, 188]. In particular, the coherence of the achieved state cannot be verified by the magnon transport measurements. Instead of a coherent BEC state with a macroscopic number of magnons in the ground state, the vanishing spin resistance beneath the modulator could, in principle, be also explained by the excitation of a broad frequency spectrum of magnons. This scenario, however, is rebutted by the critical magnon coductivity increase observed in our experiment, which is not compatible with a mere linear (or quadratic) increase of magnon density n_{m}. The ultimate question in this regard is, therefore, if the zero resistance transport can be verified over macroscopic distances. Previous experiments studied the propagation length of

coherently excited magnons under the influence of the critical SOT threshold for damping compensation and found a 10-fold increase of the propagation length in a YIG/Pt device [181]. The authors argue that the expected divergence of the propagation length (i.e. vanishing of spin resistance) at the ciritcal current is counteracted by effects associated with the current-induced heating in the Pt strip leading to a decrease of the effective magnetization. From an experimental point of view, it is therefore unlikely to achieve actual zero resistance transport over macroscopic distances. Note, that the effects of the current-induced heating on the magnetization are also discussed in conjunction with the micromagnetic simulations presented in Ch. 5.5.

5.4 Spin Conductivity Control of Thermally Induced Magnons

Besides the electrical AC injection of magnons via the SHE, Joule heating in the injector also locally affects the magnon distribution via a spin Seebeck torque (quantified by the interfacial spin Seebeck coefficient S introduced in Ch. 2.5). Consequently, a finite magnon chemical potential distribution is generated via the thermal excitation process, resulting in the diffusion and transport of thermally induced magnons [8, 36]. In this Section, their transport properties under the influence of the DC modulator current is investigated and quantified by the second harmonic voltage signal $V_{\mathrm{det}}^{2\omega}$ at the detector via lock in detection (cf. Ch. 3.4.2).

5.4.1 Angular Dependence

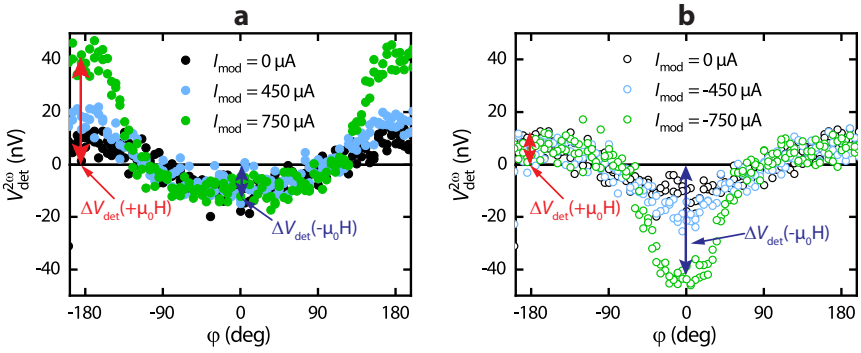

Fig. 5.18 – Magnetic field orientation φ dependent second harmonic signal $V_{\mathrm{det}}^{2\omega}$ at the detector for **a** positive and **b** negative DC currents in the modulator with an externally applied magnetic field of $\mu_0 H = 50\,\mathrm{mT}$.

Similar to Ch. 5.3, we start with the angular dependent signal modulation of the raw voltage signals $V_{\mathrm{det}}^{2\omega}$. This is shown for both positive and negative modulator currents I_{mod} in Fig. 5.18**a** and **b** for $\mu_0 H = 50\,\mathrm{mT}$, respectively. For $I_{\mathrm{mod}} = 0$, the signals show a $\cos(\varphi)$ type of modulation (cf. Ch. 2.7.1), typical for thermally-induced magnon transport [8, 123]. As expected, we find significant

enhancements of the magnon transport signals for finite modulator currents I_{mod}. For $I_{\mathrm{mod}} > 0$ (panel **a**), the transport signal is substantially increased when $\varphi = \pm 180°$, while for $I_{\mathrm{mod}} < 0$ it is enhanced when $\varphi = 0°$ (panel **b**). This perfectly agrees with the angle dependence of the first harmonic transport signals investigated in Fig. 5.8.

5.4.2 Current Dependence and Extraction of Critical Currents

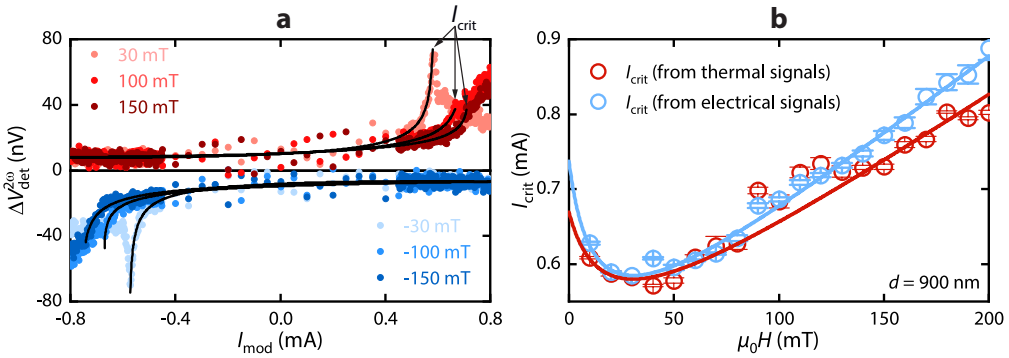

Fig. 5.19 – **a** Second harmonic voltage amplitudes $\Delta V_{\mathrm{det}}^{2\omega}$ as a function of I_{mod} for both positive (red data points) and negative (blue data points) external magnetic fields. Red data points correspond to the field direction along $\varphi = \pm 180°$, while blue data points correspond to $\varphi = 0°$. Solid black lines are fits to Eq. (5.58). **b** Comparison of the critcal currents determined from the SHE-induced (electrical) and thermal signals via fitting Eq. (5.58) to the first harmonic amplitudes $\Delta V_{\mathrm{det}}^{1\omega}(I_{\mathrm{mod}})$ shown in Fig. 5.9 as well as to the second harmonic signals $V_{\mathrm{det}}^{2\omega}(I_{\mathrm{mod}})$ shown in panel **a**, respectively. Solid lines are fits to Eq. (5.14b), where we included a cubic anisotropy field H_{ani} and assumed a fixed value for α_{sp} determined from SMR measurements at the modulator.

Subsequently, we investigate the amplitudes $\Delta V_{\mathrm{det}}^{2\omega}$ (indicated in Fig. 5.18) as a function of the applied modulator current I_{mod} in Fig. 5.19**a** for both positive (red data points) and negative (blue data points) field orientations, respectively. In the low bias regime ($|I_{\mathrm{mod}}| < 0.4\,\mathrm{mA}$), the qualitative behaviour of the curves exhibit a rather flat structure, considerably different from the SHE-induced transport signature shown in Fig. 5.9. On the one hand, this might suggests that the SHE- and thermally-induced magnon conductivity change is quantitatively different for the transport/diffusion of thermally-induced magnons than for SHE-induced magnons from the injector, which might be in accordance with the findings from Ref. [214]. On the other hand, a considerable contribution from bulk magnon transport driven by the Joule heating induced temperature gradient is very likely to influence the behaviour of the thermal signals. An attempt to interpret the data with this additional complexity in mind is given in Ch. 7.1. For this Section, this peculiarity is however not taken into account and we therefore retain the assumption that the I_{mod}-dependence of $\Delta V_{\mathrm{det}}^{2\omega}$ is exclusively proportional to σ_{m}. In any case, the signals in the critical current regime ($|I_{\mathrm{mod}}| > 0.4\,\mathrm{mA}$) exhibit a very steep increase, reminiscent of the critical magnon conductivity enhancement observed for the first harmonic signals in Fig 5.9. As just indicated, we assume the

transport of the thermally induced magnons to be dominantly driven by a gradient in the magnon chemical potential μ_m (cf. Ch. 5.2.1). Thus, we naively expect that a magnon conductivity change introduced via the current at the modulator has a similar impact on the thermal signals as compared to the observations regarding the electrical signals. We can test for this expectation by fitting the $\Delta V_{det}^{2\omega}(I_{mod})$ curves with our phenomenological model presented in Eq. (5.58). Similar to the procedure implemented for the first harmonic signals, the fitting range is restricted up to the point exhibiting the largest slope. The result is shown as the black solid lines in Fig. 5.19**a**. Remarkably, we observe an excellent agreement between the model and the experimental data. Extracting the critical current I_{crit} from the fits and plotting them against the external magnetic field results in Fig. 5.19**b** (red open circles). For comparison, we also plot the critical currents extracted from fitting Eq. (5.58) to the electrical signals shown in Fig. 5.15**a** (blue open circles, same as in Fig. 5.15). A very good agreement between both datasets is observed. Furthermore, the solid lines represent fits to Eq. (5.14b), the fit parameters of which are summarized in Tab. 5.3. Both sets of parameters result in reasonable values for the damping properties as well as anisotropy fields. We therefore conclude that both electrically as well as thermally driven magnon transport is suitable to observe the critical magnon conductivity enhancement in our experiments, indicating the validity of our assumption that the thermally induced magnons are dominated by the magnon chemical potential.

We want to point out that it might still be beneficial to interpret the modulation of the second harmonic signal from a different perspective. To this end, we lift the assumption that the thermal second harmonic signal at the detector is exclusively determined by the magnon conductivity σ_m and the associated magnon chemical potential profile μ_m, but take into account that also temperature gradient-driven magnon currents characterized by the bulk spin Seebeck coefficient L have a significant contribution (cf. Ch. 2.7.2), in accordance with previous studies [124]. It has been further shown both theoretically [109, 127, 215] and also experimentally [124, 216] that the bulk spin Seebeck coefficient L exhibits a strong correlation to the magnon heat conductivity κ_m, which is also immediately clear when we consider our derivation of L and κ_m in Eqs. (2.56) and (2.57). This strongly suggests that the second harmonic signal offers access to the behaviour of κ_m when the magnon system undergoes the supposed BEC phase transition. Indications for this claim might be present in the second harmonic signal modulations when interpreting the data from the perspective of temperature gradient driven currents. For details of these considerations, we refer the reader to Ch. 7.1.

Fit results of Eq. (5.14b) in Fig. 5.19**b**	Symbol	Value	Unit
Electrical signals			
Gilbert damping	α_G	$(1.14 \pm 0.1) \times 10^{-3}$	
inhomogenous broadening	$\mu_0 \delta H$	0.72 ± 0.02	mT
cubic anisotropy field	$\mu_0 H_{ani}$	9.54 ± 2.13	mT
Thermal signals			
Gilbert damping	α_G	$(0.73 \pm 0.09) \times 10^{-3}$	
inhomogenous broadening	$\mu_0 \delta H$	0.79 ± 0.03	mT
cubic anisotropy field	$\mu_0 H_{ani}$	15.2 ± 3.7	mT

Tab. 5.3 – Values for the free fitting parameters entering Eq. (5.14b) extracted from the fits to the field dependent critical current data shown in Fig. 5.19**b**.

5.5 Micromagnetic Simulations

Inspired by the micromagnetic approach put forward in Ref. [217], we study the spin current injection via the SHE in the modulator into the YIG layer in a numerical fashion. To this end, we use the micromagnetic simulation code *MuMax3* [185]. In particular, this allows for the investigation of the time-dependent magnetization dynamics in the YIG layer exposed to large spin currents and thus enables us to access the frequency spectrum of the spin current driven magnetization dynamics, which we could not investigate experimentally.

Within the micromagnetic simulation code, our magnetic thin film is divided into cubic cells of size 5 nm × 5 nm × 13.4 nm, where the latter corresponds to the thickness of our YIG film. The total lateral area under consideration is 2560 nm × 2560 nm. Each of the cells hosts a magnetic moment that interacts with its neighbours via the exchange and dipolar coupling. The magnetization dynamics are captured by the Landau-Lifshitz-Gilbert (LLG) equation [92]. Finite temperature is accounted for in the simulation by a fluctuating thermal magnetic field [185] added to the LLG. The YIG film is exposed to an in-plane external magnetic field of $\mu_0 H = 50$ mT. To simulate our experimental configuration, we use the experimentally determined magnetic properties of YIG at room temperature (~ 295 K), in particular the saturation magnetization $\mu_0 M_s(T = 295\,\mathrm{K}) = 140$ mT (cf. Ch. 5.2.3) and the exchange constant $A_{ex}(T = 295\,\mathrm{K}) = 3.7$ pJ taken from Ref. [218]. The magnetic damping of the YIG film is considered via the field- and magnetization-dependent effective damping α_{eff} introduced in Eq. (5.15), which takes into account the additional damping contribution due to sample inhomogeneities. An increased damping $\alpha_{eff} + \alpha_{sp}$ due to spin pumping is assumed in the region beneath the Pt spin current injector (i.e. the modulator). The spin current injection via a $t_{Pt} = 3.5$ nm thick and $w = 500$ nm wide Pt strip is considered by the addition of the Slonczewski torque term to the LLG [90]. The spin Hall physics is incorporated by assuming an interface spin current transparency of $\mathcal{T} = 0.33$ between Pt and YIG and a spin Hall angle of $\theta_{SH} = 0.11$, both of which

are multiplied to the charge curent density $j_{\mathrm{mod}} = I_{\mathrm{mod}}/(t_{\mathrm{Pt}}w)$. All the used values correspond to the experimentally determined values given in Tab. 5.2.

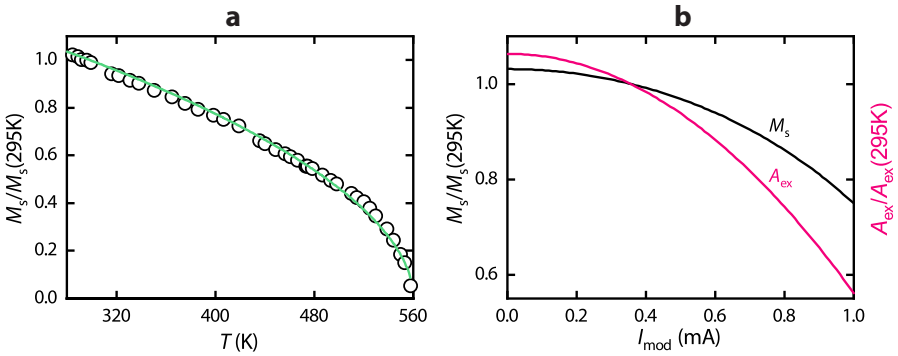

Fig. 5.20 – a Temperature dependence of the YIG saturation magnetization M_s taken from Ref. [219] normalized to its magnitude at $T = 295\,\mathrm{K}$. The green solid line is a fit to Eq. (5.66). **b** Modulator current dependence of the normalized YIG magnetization $M_s/M_s(295\,\mathrm{K})$ (black line) and exchange constant $A_{ex}/A_{ex}(295\,\mathrm{K})$ (magenta line) constructed via the parabolic $T(I_{\mathrm{mod}})$ curve of the modulator electrode given in Fig. 5.5**b** and the $M_s(T)$ function presented in Eq. (5.66).

As discussed in Ch. 5.2.4, our device experiences a significant temperature increase due to the large modulator currents. We therefore adjust the temperature of the simulations accordingly[42]. In general, both M_s and A_{ex} also exhibit a considerable decrease with increasing temperatures. We therefore expect M_s and A_{ex} to be a function of I_{mod} in our experiment. In order to take this into account for the simulation, we use the temperature dependence of the magnetization of YIG from Ref. [219]. We map this to our case upon normalizing the data to its room temperature value ($T = 295\,\mathrm{K}$), which is shown in Fig. 5.20**a**. The green solid line corresponds to a fit to the general phenomenological expectation for the temperature dependent magnetization according to

$$\frac{M_s(T)}{M_s(295\,\mathrm{K})} = \frac{M_s^0}{M_s(295\,\mathrm{K})}\left(1-\left(\frac{T}{T_C}\right)^n\right)^m, \tag{5.66}$$

where M_s^0 is the saturation magnetization at 0 K, T_C is the Curie temperature of YIG and n, m are exponents characterizing the temperature dependence. The fit yields $M_s^0/M_s(295\,\mathrm{K}) \approx 1.45$, $T_C \approx 560.4\,\mathrm{K}$, $n \approx 1.1$ and $m \approx 0.53$. From Fig. 5.5**b**, we extract the current dependence of the temperature in the modulator strip by fitting a parabolic function to the data and plug the resulting $T(I_{\mathrm{mod}})$ function into Eq. (5.66). As a result, we constructed a current dependence of the (normalized) magnetization which is shown in Fig. 5.20**b** as the black solid line. Additionally, we assume $A_{ex}(T) \propto M_s(T)^2$ as expected from mean-field theory [217, 220, 221]. The corresponding normalized exchange constant is also plotted as a function of

[42] We here assume a spatially homogeneous temperature distribution, which is reasonable for our investigation, since we limit our analysis to the magnetization dynamics beneath the modulator. As shown in Ref. [217], a more accurate temperature distribution has no considerable influence on the observed dynamics.

I_{mod} in Fig. 5.20**b** as the magenta colored line. We note, that the effective damping α_{eff} considered for our simulation also becomes a temperature/current dependent quantity since the temperature/current dependency of the YIG magnetization enters in Eq. (5.15). Hence, for each current magnitude, the simulation adjusts the corresponding values for the ambient temperature, magnetization, exchange constant and damping in each cell.

Figure 5.21**a** illustrates the simulated experimental configuration and coordinate system, the geometry of which is based on the actual device investigated in the preceding Sections. The lateral area depicts a snapshot of the normalized magnetic vector field $\boldsymbol{m}(x, y, z)$ indicated by black arrows. Their direction is additionally indicated by the color scheme defined in Fig. 5.21**b**. The noisy background stems from a the thermal fluctuating field incorporated in the simulation to account for finite temperature. A Pt strip electrode with a width $w = 500\,\mathrm{nm}$ is simulated by defining a region of width w into which the spin current is injected. It therefore represents the modulator in the simulation. Following Ref. [217], absorbing boundary conditions (ABC) are applied to the edges in y-direction, while periodic boundary conditions (PBC) are assumed at the boundaries along x. This entails a simulation of an infinitely long Pt electrode, which is reasonable considering the actual length $l_{\mathrm{Pt}} = 162\,\mu\mathrm{m}$ of the modulator in our experiments. Panels **c**-**h** show snapshots of the magnetic vector field for different modulator currents $I_{\mathrm{mod}} \geq I_{\mathrm{crit}}$ as indicated in the pictures. While the magnetic vector field does not show any clearly visible dynamic response for $I_{\mathrm{mod}} = 0.5\,\mathrm{mA} < I_{\mathrm{crit}}$ in **a**, larger values $I_{\mathrm{mod}} \gtrsim 0.57\,\mathrm{mA} \approx I_{\mathrm{crit}}$ give rise to the appearance of the first vsible spin wave dynamics (**c**). The localized, circular shaped spot featuring large amplitude magnetization dynamics is generally referred to as a spin-wave bullet mode [207, 217]. Their density beneath the spin current exposed region increases rapidly with increasing current as evident from panels **c**-**f**. For even larger currents (panel **g**, **h**), the magnetization dynamics enters a chaotic regime, which is, however, not investigated in our experiments where $I_{\mathrm{mod}} \leq 0.8\,\mathrm{mA}$.

Quantitatively, we can extract the critical current from the simulations by studying the deviation of $\boldsymbol{m}(x, y, z)$ beneath the modulator from its equilibrium direction along y. We thus study the m_y component of the magnetic vector field in the following. In the inset of Fig. 5.22, the complete temporal evolution of $m_{\mathrm{y}}^{\mathrm{mod}} = \langle m_y \rangle_{\mathrm{mod}}$ averaged across the modulator area is plotted up to $t = 100\,\mathrm{ns}$ for different I_{mod}. It becomes immediately clear that the deviation becomes large for currents $I_{\mathrm{mod}} > 0.57\,\mathrm{mA}$. We can quantify this deviation by calculating its time average $\langle m_{\mathrm{y}}^{\mathrm{mod}} \rangle_{\Delta t} = 1/\Delta t \int_{t_{\mathrm{i}}}^{t_{\mathrm{f}}} m_{\mathrm{y}}^{\mathrm{mod}}(t)\mathrm{d}t$ with the initial time t_{i}, the final time t_{f} and the corresponding time interval $\Delta t = t_{\mathrm{f}} - t_{\mathrm{i}}$. We choose $t_{\mathrm{i}} = 50\,\mathrm{ns}$ and either $t_{\mathrm{f}} = 100\,\mathrm{ns}$ or $t_{\mathrm{f}} = 150\,\mathrm{ns}$[43]. This calculation corresponds to the arithmetic average of $m_{\mathrm{y}}^{\mathrm{mod}}$ for $t > 50\,\mathrm{ns}$, after which dynamic equilibrium is mostly achieved. In

[43] Whether $t_{\mathrm{f}} = 100\,\mathrm{ns}$ or $t_{\mathrm{f}} = 150\,\mathrm{ns}$ simply depends upon the length of the simulation run, which was different for some of the simulations.

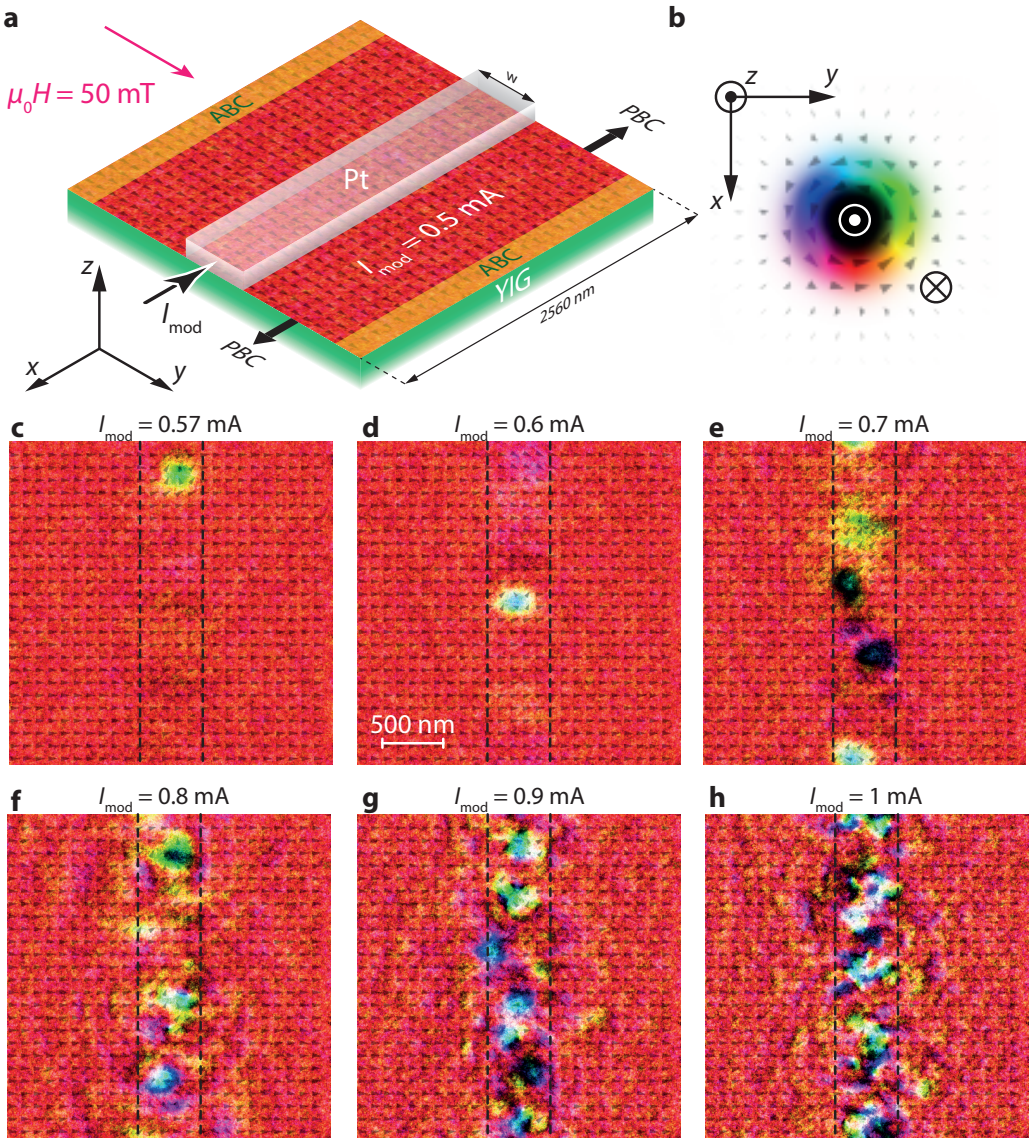

Fig. 5.21 – **a** Depiction of the experimental configuration used in the simulation based on the actual YIG/Pt sample layout. The lateral area shows a snapshot of the color coded map of the normalized magnetic vector field $\boldsymbol{m}(x, y, z)$ under the influence of a current $I_{\text{mod}} = 0.5\,\text{mA} < I_{\text{crit}}$ in the Pt strip. Absorbing boundary conditions (ABC) were applied to the edges along y, while periodic boundary conditions (PBC) are assumed on the edges along x. The film is exposed to an in-plane magnetic field of $\mu_0 H = 50\,\text{mT}$ oriented along the y-axis. **b** Definition of the coordinate system and the relation between the color scheme and the direction of the magnetization indicated by black arrows. **c**, **d**, **e**, **f**, **g**, **h** Snapshots of $\boldsymbol{m}(x, y, z)$ for different modulator currents $I_{\text{mod}} \geq I_{\text{crit}}$. In the simulation, the threshold for damping compensation/swasing (Eq. (5.14b)) corresponds to the formation of spin wave bullet modes beneath the Pt strip (**c**). Increasing currents show a rapidly increasing density of bullet modes (**e**, **f**). Even larger currents lead to a chaotic regime (**g**, **h**) [217].

analogy to Ref. [217], we investigate this time averaged deviation in terms of an order parameter defined as

$$\psi = \frac{1 - \langle m_{\text{y}}^{\text{mod}} \rangle_{\Delta t}}{2}. \tag{5.67}$$

In this definition, $\psi = 0$ is equivalent to a perfect alignment along the equilibrium direction y, while $\psi = 1$ corresponds to a fully switched state along $-y$. ψ is plotted as a function of I_{mod} in Fig. 5.22 as black spheres. Evidently, ψ has a mostly constant behaviour for $I_{\mathrm{mod}} \lesssim 0.57\,\mathrm{mA}$, and a very sharp, threshold-like increase for $I_{\mathrm{mod}} \gtrsim 0.57\,\mathrm{mA}$. The orange data points corresponds to the order parameter calculated when only Joule heating is considered, but zero spin current injection is applied. The shaded region therefore constitutes the thermal agitation of the order parameter and acts as the baseline for the black data points. To compare with our experiments, we plot the normalized critical voltage signal $\Delta V_{\mathrm{det}}^{1\omega,\mathrm{crit}} / \Delta V_{\mathrm{det0}}^{1\omega}$ (which is corrected for linear and quadratic contributions, cf. Eq. (5.42)) in Fig. 5.22 (green data points, referring to the right y-axis). The vertical dashed line in the Figure indicates $I_{\mathrm{crit}} \approx 0.57\,\mathrm{mA}$ and corresponds to the extracted value of I_{crit} from the experiments presented in the precedent Sections. This value perfectly matches with the threshold observed for the order parameter ψ. As a result, the critical current extracted from our experiments can be identified with the onset of the nucleation of the transient spin-wave bullet modes, for which the magnetic damping is locally compensated. Their rapid increase in density observed in Fig. 5.21**c** to **d** results in the sharp increase of the magnon conductivity and therefore the detector signal observed in our experiments. The experimental data regarding $\Delta V_{\mathrm{det}}^{1\omega,\mathrm{crit}}$ shown in Fig. 5.22 also exhibits non-monotonous, erratic jumps. While the origin of these features is not entirely clear, it is conspicuous that the simulation of the order parameter also exhibits an irregular behaviour in a very similar current range compared to the experimental transport data. Since these features vanish for larger external magnetic fields, the field might have a stabilizing effect on the nucleation of the bullets, leading to a smoother increase in their density. Overall, there is a striking relation between the order parameter ψ and our experimental data, indicating the validity of our claims.

In addition to the deviation from the equilibrium direction defined via ψ, we can further investigate the temporal evolution of the dynamic components of the magnetic vector field $\boldsymbol{m}(x, y, z)$, allowing for a spectral analysis of the excited spin dynamics beneath the modulator. In particular, the transverse components m_x and m_z of the y-magnetized magnetic film are characteristic for the dynamic part of the magnetization. We therefore analyze the temporal evolution of $m_x^{\mathrm{mod}} = \langle m_x \rangle_{\mathrm{mod}}$ averaged across the modulator area. In Fig. 5.23**a**, m_x^{mod} is plotted as a function of time for a time interval of 10 ns. Clearly, a strong increase in the amplitude of the waveforms is observed when we cross the critical current $I_{\mathrm{crit}} \approx 0.57\,\mathrm{mA}$ (extracted from the fits to Eq. (5.58) shown in Fig. 5.15), indicative of the threshold behaviour and formation of large amplitude spin wave bullets as discussed before. In a next step, we perform fast Fourier transformations (FFT) to the time-dependent transverse magnetization $\hat{m}_x^{\mathrm{mod}}(f) = \mathrm{FFT}(m_x^{\mathrm{mod}}(t))$. We then plot the magnitude $\sqrt{\mathrm{Re}(\hat{m}_x^{\mathrm{mod}}(f))^2 + \mathrm{Im}(\hat{m}_x^{\mathrm{mod}}(f))^2}$ of the FFT which results in the spectra shown in Fig. 5.23**b**. The FFT is performed for $t > 50\,\mathrm{ns}$, ensuing that we only capture the

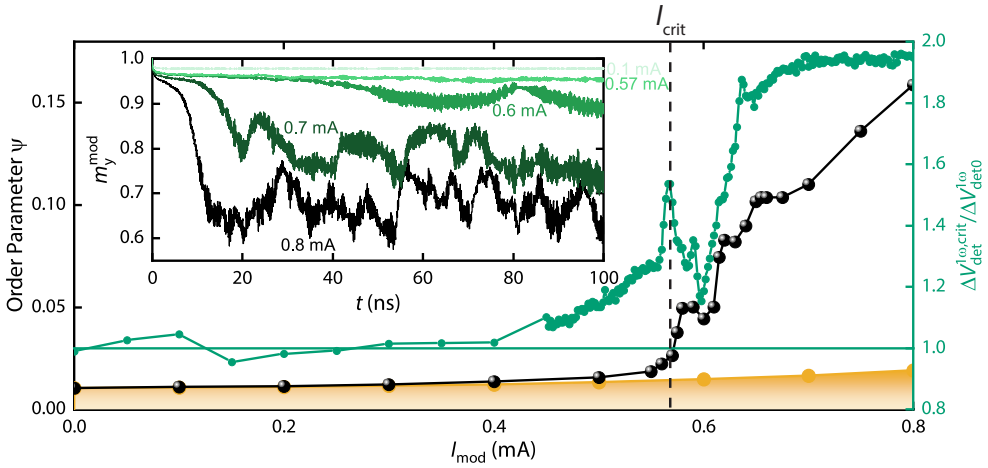

Fig. 5.22 – Order parameter ψ defined in Eq. (5.67) plotted versus I_{mod} (black spheres). The orange points and the shaded region beneath corresponds to the magnitude of ψ when only Joule heating with zero spin current injection is considered, i.e. due to thermal agitation only. The inset shows the temporal evolution of the normalized magnetization $m_{\mathrm{y}}^{\mathrm{mod}}$ averaged over the modulator region for different currents I_{mod}.

dynamics of the steady state. The spectra are shown for different currents in the modulator. While the critical regime $I_{\mathrm{mod}} \gtrsim I_{\mathrm{crit}}$ is depicted in the main graph, the inset represents spectra for $I_{\mathrm{mod}} < I_{\mathrm{crit}}$. Furthermore, the red vertical dashed line in both graphs indicates the (in-plane) FMR frequency $f_0 \approx 2.7\,\mathrm{GHz}$ calculated via Eq. (5.10) using $\mu_0 M_{\mathrm{s}}(T = 295\,\mathrm{K}) = 140\,\mathrm{mT}$ and $\mu_0 H = 50\,\mathrm{mT}$. The low bias regime in the inset depicts a small increase of the spectrum's overall magnitude. A small, but noticable increase in this regime is observed at frequencies slightly below the FMR frequency f_0[44]. Overall, no significantly large change in the spectrum can be observed for $I_{\mathrm{mod}} < I_{\mathrm{crit}}$.

Increasing the current to 0.55 mA results in a drastic increase of the magnitude of the spectrum, as shown via the black line in the main graph of Fig. 5.23**b**. A strong peak with a considerably lower frequency than f_0 is observed. This peak further increases in magnitude and decreases in frequency when the current reaches a value slightly above the critical value at 0.575 mA (dark green spectrum). The strong amplitude and the current-induced decrease of the peak frequency of the excited modes is typical for spin-wave bullet dynamics [207, 217]. Further increasing the current to 0.7 mA shifts the main peak of the spectrum to even lower frequencies, but also its magnitude is decreasing. Additionally, the spectrum becomes broadened at these large currents considerably above I_{crit}, indicating that the excess energy from the spin current injection is distributed over the lower frequency spectrum. This broadening becomes even more prominent for currents

[44] We note that in the calculation of the FMR frequency f_0 it is not considered that the current-induced temperature increases, leading to a reduced magnetization (cf. 5.20**b**) and therefore a reduced f_0. Thus, the observed increase slightly below f_0 is pefectly reasonable.

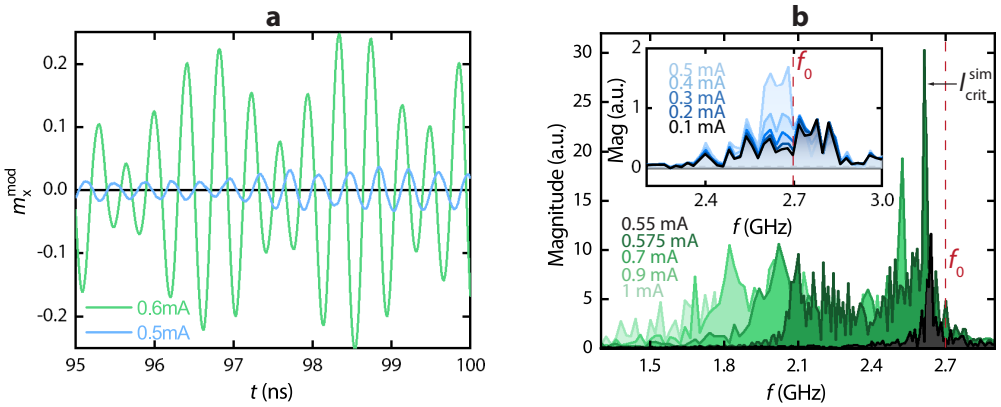

Fig. 5.23 – **a** Part of the temporal evolution of the normalized magnetization m_x^{mod} averaged over the modulator region for $I_{mod} = 0.5\,mA < I_{crit}$ (blue line) and $I_{mod} = 0.6\,mA > I_{crit}$ (green line). **b** Fourier spectra of the $m_x^{mod}(t)$ dynamics plotted for different modulator currents $I_{mod} \gtrsim I_{crit}$ as indicated. The inset shows the spectra obtained for $I_{mod} \lesssim I_{crit}$. $f_0 \approx 2.7\,GHz$ corresponds to the fundamental (in-plane) FMR frequency at $\sim 295\,K$.

$I_{mod} = 0.9\,mA$ and $I_{mod} = 1\,mA$, where no strong single peak feature can be recognized anymore.

The evolution of the frequency spectrum under the influence of large spin current injection suggests that the critical current $I_{crit} \approx 0.57\,mA$ determined from our experiments can be reasonably identified with the maximum peak in the frequency spectrum found for $I_{crit}^{sim} = 0.575\,mA$ from the simulations (Fig. 5.23**b**). At I_{crit}^{sim}, we find the largest peak amongst the whole evolution of the current-induced magnetization dynamics. A narrow peak in the spectrum corresponds to a large magnon occupation of a single energy state. This is synonymous to the statement that the spin current induced magnetization dynamics features the largest coherence at the critical current I_{crit}^{sim}. Theory predicts that the strong magnon conductivity enhancement observed in our experiments can be ascribed to the condensation of magnons into a single energy state [188]. Our simulations do indeed indicate this strong correlation between the magnon conductivity enhancement and the spectral distribution/coherence of the magnon modes, since we find $I_{crit} \approx I_{crit}^{sim}$. Moreover, experimental reports investigating the influence of coherent magnon generation via microwave techniques on the behaviour of the magnon conductivity indicate a similar behaviour, i.e. a magnon conductivity enhancement when the magnon occupation becomes strongly excited in a narrow low frequency band near the minimum [208]. Large currents beyond 0.7 mA, on the other hand, show weak coherence in the simulations, i.e. a broadened spectrum. Correspondingly, the data shows only weak magnon conductivity modulation in this regime (cf. Fig. 5.22). Recent experimental results on spin Hall oscillators with perpendicular magnetic anisotropy (PMA) also show a clear increase in the coherence of the oscillations, making the investigation of magnetic insulators with PMA an interesting direction for future research of current-induced magnon BEC [222].

In conclusion, our micromagnetic approach offers exciting insights into the relation between the spin current induced magnetization dynamics and our magnon conductivity measurements. The simulations suggest the formation of spin wave bullets at the critical current with a rapidly increasing density when the current is further increased. Moreover, we could identify a strong correlation between the coherence of the excited magnon modes and the behaviour of the magnon conductivity, suggesting that the largest modifications of the latter can be identified with strong coherence of modes, while the excitation of a broad frequency spectrum has a negligible effect on the magnon conductivity.

5.6 Summary and Conclusion

In this Chapter, we have investigated the magnon conductivity modulation via the injection of spin current in a three-terminal YIG/Pt device. While the magnon conductivity measurement in YIG is implemented upon driving SHE-induced magnon transport between a Pt spin injector and detector, we simultaneously tune the magnon density via the additional spin current injection in a third Pt modulator electrode placed in between. The modulator current dependence of this magnon conductivity was then investigated in great detail. For the sake of clarity, we have introduced a low bias current regime and a critical current regime that we separately studied.

Within the low current bias regime, we could qualitatively reproduce the results of previous reports [172]. In addition, we found a largely improved modulation efficiency of $\sim 60\,\%/\mathrm{mA}$ within this regime, exceeding the expected value evaluated by simulations of the magnon chemical potential beneath the modulator by a factor of four [172].

Rich physics have been observed within the critical current regime, where the magnon conductivity modulation exhibits a very large non-linear increase. This non-linearity was linked to the physics of both spin-Hall oscillators as well as to more recent theories studying charge current induced magnon Bose-Einstein condensation. Interestingly, we could show that the threshold conditions of the two theories are fully identical, since both are defined by the compensation of the magnetic damping via the current induced antidamping spin torque at a magnet/metal interface. In our experiments, this threshold could be identified with the critical current I_{crit} at which the magnon conductivity exhibits a very large slope followed by a kink towards a flatter increase. For intuitive reasons, we have progressed by isolating the critical behaviour of the magnon conductivity from the well-known linear effects. Rewriting this critical magnon conductivity in terms of an associated critical YIG spin resistance led to a continuous, but rapid decrease of the spin resistance at the critical current. This decrease was argued to reflect the associated entropy drop of the magnon system entering a magnon BEC regime, indicative of the supposed second-order phase transition.

We could demonstrate that the field dependence of the critical current fits well to the theoretical prediction from Ref. [187], which was discussed in detail in Ch. 5.1. A second threshold at $I_{on} < I_{crit}$, which is defined as the onset of a continuous condensation of magnons, was also extracted from the data and good agreement to its theoretical prediction given in Ref. [187] was found either. Based on another theoretical prediction calculating the critical magnon conductivity enhancement of a magnetic material near the transition into a charge current induced magnon BEC [188], we were able to introduce a phenomenological model for the current dependent magnon conductivity modulation, reproducing the data well up to the critical current I_{crit}. The validity of the model has been further tested by extracting its parameters from fits to the experimental data and comparing them to our magnon transport device, offering reliable results. Moreover, our model could be utilized to estimate the effective region modulated by the charge current. An experimental test of the theoretical claim of zero spin resistance beneath the modulator has been implemented by distance dependent measurements, which indeed indicates the supposed loss-free transport of magnons over a distance significantly larger than the width of the modulator electrode. Due to the lack of experiments verifying zero resistance transport over macroscopic distances, a final verification of this claim could not be provided.

Similar investigations have been conducted with regards to the transport of magnons excited by thermal spin current injection due to the Joule heating in the injector. Our phenomenological model of the non-linear magnon conductivity modulation based on the theory presented in Ref. [188] reveals a compelling agreement with the thermally-induced magnon transport data. The extraction of the corresponding critical currents exhibits perfect agreement with those extracted for the electrically induced signals.

While we had no direct experimental access to the frequency spectrum of the excited magnon modes, we instead studied the confined spin current injection into the YIG layer via micromagnetic simulations using the open source code *MuMax3*. The simulations revealed the onset of a nucleation of spin wave bullet modes at the critical current I_{crit}. A rapid increase in their density when increasing the current beyond I_{crit} was observed, which eventually led to a chaotic regime for the largest currents investigated. The frequency spectrum attained via the temporal evolution of the dynamic magnetization components unveiled that the largest coherence of the excited modes directly correspond to I_{crit}. For larger currents, the frequency spectrum is broadened. We argued that the strong modifications in the measured magnon conductivity are correlated with the coherence of the excited modes. This claim is corroborated by theoretical calculations that predict large magnon conductivity via condensation of magnons into a single energy state [188].

During the course of this Chapter, we repeatedly addressed the question whether the magnon system enters a BEC state and if the magnon transport can

be considered as spin superfluid. Regarding the magnon BEC transition, we have found multiple arguments in favor of this claim, but we unfortunately miss an unambiguous verification. As pointed out by E. B. Sonin in Ref. [209], however, the exact prerequisites for a magnon system to prove itself as a BEC are not unambiguous in literature. In any case, the feature of coherence represents one of the necessary requirements for BEC that are uncontroversial. Our micromagnetic simulations indicate no distinct spatial coherence of the magnetization dynamics beneath the modulator electrode. The spectral coherence, on the other hand, was found to be large for a narrow range of currents around I_{crit}. Achieving both spatial and spectral coherence might therefore be an issue of the geometrical features of the device [223]. Tuning the spatial boundary conditions in an appropriate manner is potentially sufficient to achieve this goal. Besides these issues, we still could verify various theoretical predictions regarding current induced magnon BEC in our experiment. With regards to spin superfluidity, it is rather unlikely that such dissipationless transport ensues in our device. Even if spatial and spectral coherence is achieved, the formation of a magnon BEC does *not* necessarily lead to superfluidity [209] as sometimes assumed [224]. Moreover, while the effective magnon relaxation time might indeed diverge as damping compensation is achieved, this does of course not entail a scatter-free transport of magnons since e.g. magnon-magnon interactions are still present.

At the end of the day, the more important question might not lie in the unambiguous realization and verification of achieving magnon BEC (which is of academic nature anyway), but rather if the features of the concepts observed in our experiment can be beneficial towards devices and applications. In this regard, we think that the experiment shows great potential for the implementation of pure magnon-based control units. It thus lays the foundation for future experiments ranging from zero resistance magnon transport to efficient non-linear spin current manipulation.

6 Spin Transport Effects in Antiferromagnetic α-Fe_2O_3/Pt Heterostructures

The exchange interaction is the quintessence of magnetic ordering phenomena. Depending on the crystal structure, the quantum indistinguishability of electrons together with the Coulomb repulsion of the electronic wavefunctions in a material indirectly decides on the symmetry of their corresponding spin wave functions. Remarkably, numerous crystalline materials forming naturally on earth feature an antiparallel spin orientation of neighbouring electron spins due to this exchange mechanism, resulting in a special type of magnetic ordering called antiferromagnetism. Antiferromagnets generally feature strong exchange energies resulting in high frequency spin dynamics in the THz-range [32, 225–228] leading to ultrafast response times [229, 230]. While they are perfectly ordered in their interior, they do not exhibit any exterior magnetic stray field like their ferromagnetic counterparts. In his 1970 Nobel Prize speech, Louis Néel therefore described antiferromagnetic materials as 'interesting but useless', since it was believed that only strong magnetic fields are capable of manipulating these materials due to their vanishing magnetic stray field. This view has drastically changed in recent years, since when antiferromagnets have been shown to be efficiently manipulated by the application of electric currents and the associated spin torque effects [74, 225]. Insulating antiferromagnets, on the other hand, can be exposed to spin-orbit torque by attaching them to heavy metal layers and employing the spin Hall effect [117, 150]. Hence, the transport of antiferromagnetic magnon excitations could be implemented, which is difficult to achieve by means of microwave techniques due to their aforementioned high frequency spin dynamics [228].

Spin and information transport via magnons in magnetic insulators offers distinct advantages [8, 12, 117, 162, 231–236]. While ferromagnetic magnons carry spin in only one direction determined by the orientation of the magnetization, antiferromagnetic magnons come in pairs with opposite spins or Néel order precession chiralities. The latter can combine to form zero-spin excitations corresponding to linearly polarized oscillations of the Néel order [237, 238]. In general, the pairs of antiferromagnetic magnons and their superpositions can be described via a pseudospin [121, 239–241] in a manner similar to the actual spin of an electron. The corresponding mathematical analogy has also been invoked in predicting emergent spin-orbit coupling effects with AFI magnons [121, 241, 242], including topological states [241, 243–246]. Within some arbitrarily chosen convention, one particular spatial component of such a pseudospin corresponds to the measurable magnon

spin, while the two transverse components characterize the mode ellipticity and correspond to zero-spin excitations. The formal equivalence between electron spin and antiferromagnetic magnon pseudospin has been predicted to result in a range of phenomena that are completely analogous in electronic systems and antiferromagnetic insulators [121, 239–242, 247, 248]. The experimental realizations of these theoretical predictions promise to lift antiferromagnetic magnonics to a new level of functionalities.

In the experiments presented in this Chapter, we realize antiferromagnetic magnon transport by spin current injection via the SHE in a Pt injector attached to the antiferromagnetic insulator α-Fe_2O_3 (hematite). Consequently, an excess of spin-up magnons is produced [51, 117, 213], which can be considered as a non-equilibrium pseudospin density along the injected spin polarization $\boldsymbol{s}$. The diffusive pseudospin transport is then measured at a second Pt detector (cf. Ch. 2.7). Due to the presence of an easy-plane anisotropy and Dzyaloshinskii-Moriya interaction (DMI) in our films, spin-up and -down magnons are coherently coupled and therefore no longer eigenexcitations [32, 241]. Instead, the eigenexcitations of the coupled systems are determined by the direction of the so-called pseudofield, which, in turn, is characterized by the coherent mode coupling strength and thus by the magnitude and direction of the DMI and anisotropy energies. As a result, the injected pseudospin density along $\boldsymbol{s}$ precesses around the the transversely-oriented pseudofield with time while the magnons diffuse away from the injector. Its precession frequency Ω is determined by the anisotropy and a combination of the DMI field and canting-induced net magnetic moment. We control the latter by an external magnetic field and hereby obtain a handle on Ω. The resulting spin signal at the detector oscillates as a function of the external magnetic field due to a coherent interconversion of spin 1 to spin 0 excitations (and vice versa) due to the precessing pseudospin density. This observation manifests the first realization of the magnonic analogue of the electronic Hanle effect [249–251] and the Datta-Das transistor [252], unlocking the high potential of antiferromagnetic magnonics towards the realization of rich electronics-inspired phenomena.

We further investigate the thermally induced magnon transport due to Joule heating in our α-Fe_2O_3/Pt devices. Here, the two antiferromagnetic magnon modes of hematite are simultaneously excited at the injector. Our data reveals that the transported spin is determined by the net magnetization rather than the direction of the Néel vector [117], significantly different from the electrically induced magnon transport [13]. We argue that the $\boldsymbol{k}$-vector averaged energy splitting between the antiferromagnetic magnon modes is small and that the magnon spin along the Néel order is therefore negligible [32]. A finite spin along the net magnetization direction, however, persists due to the canted magnetizations. In addition to the thermal magnon transport effect, a considerable lateral temperature gradient generated across the width of the Pt detector drives a pure spin current into

the hematite by means of the spin Nernst effect (SNE) [55]. This interfacial spin current also drives a charge current in the metal which appears as a transverse magnetothermopower (i.e. voltage signal) in our electrical open circuit conditions. The emerging angle symmetry of the thermal voltage signal reveals that the direction of the Néel order $\boldsymbol{n}$ represents the relevant boundary condition for the absorption or reflection of the incoming spin current. Our results demonstrate that the use of an antiferromagnetic order vector as the boundary condition for the SNE in Pt enables a much improved differentiation from spin Seebeck related effects that are proportional to the net magnetization. Most importantly, our temperature dependent results of the magnetothermopower signal are in perfect agreement with the theoretical prediction of the temperature dependent spin Nernst angle of Pt, thus verifying its complete suppression at low temperatures.

This Chapter is organized as follows: in Ch. 6.1 we present the theoretical foundations of the pseudospin concept, which represents an extremely convenient way to describe antiferromagnetic magnon excitations and their transport. Chapter 6.2 introduces our sample geometry for magnon transport measurements in α-Fe_2O_3 and corresponding preliminary measurements for pre-characterization purposes of the sample. We progress with the presentation of the key results in Ch. 6.3.1, where we use the pseudospin concept to rationalize our experimental data and demonstrate the first antiferromagnetic magnon analogue of the electronic Hanle effect. Finally, we investigate the thermal effects arising due to the Joule heating in our device, featuring both thermally induced magnon transport and the transverse spin Nernst magnetothermopower effect. A summary and conclusion is given in Ch. 6.5.

Throughout this Chapter, we extensively reuse text and figures published in T. Wimmer, A. Kamra, J. Gückelhorn, M. Opel, S. Geprägs, R. Gross, H. Huebl, M. Althammer, *Observation of Antiferromagnetic Magnon Pseudospin Dynamics and the Hanle Effect*, Physical Review Letters **125**, 247204 (2020) as well as A. Kamra, T. Wimmer, H. Huebl, M. Althammer, *Antiferromagnetic magnon pseudospin: Dynamics and diffusive transport*, Physical Review B **102**, 174445 (2020).

6.1 Theoretical Concepts

The theoretical framework employed for the description of the antiferromagnetic magnon transport is presented in this Section. In particular, we start with the introduction of the concept of pseudospin in Ch. 6.1.1, which conveys an extremely useful way to describe antiferromagnetic magnon excitations and their eigenstates under the influence of arbitrary magnetic interactions on top of the underlying exchange mechanism. Moreover, the relation between pseudospin and the classical antiferromagnetic Néel vector dynamics is given therein. In Ch. 6.1.2, the temporal dynamics of pseudospin and its consequences on diffusive transport for the pseudospin density is introduced. Particularly, we here analyze

the one-dimensional solution of the pseudospin diffusion equation. We note that the theoretical framework outlined here only considers the most important results of the detailed theory published in Ref. [10].

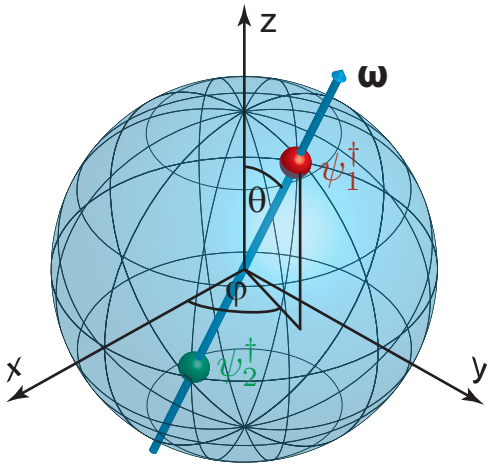

Fig. 6.1 – Depiction of a Bloch sphere together with the pseudofield vector $\boldsymbol{\omega}$. The red and green spheres indicate the intersections of $\boldsymbol{\omega}$ with the Bloch sphere and represent the corresponding eigenmodes $\psi_1^\dagger$ and $\psi_2^\dagger$. The transformation describing $\psi_1^\dagger$ and $\psi_2^\dagger$ in terms of the spin-up and -down eigenmodes is given in Eq. (6.5).

6.1.1 Antiferromagnetic Magnons and Pseudospin Concept

Generally, antiferromagnetic excitations feature two degenerate magnon modes[45] typically denotes as α- and β-modes [32]. These two modes represent the spin-up (spin $+1$) and spin-down (spin -1) excitations along the Néel vector and can be viewed as its right- and left-circular precession chiralities in the classical picture (we here set $\hbar = 1$). Due to the large exchange energy considerably dominating over all other magnetic interactions in typical antiferromagnets, the α- and β-modes constitute our natural basis. Thus, we consider the hamiltonian of two coherently coupled, antiferromagnetic spin-up and -down magnon modes characterized by the (uncoupled) frequencies ω_α and ω_β [10]:

$$\begin{aligned}\hat{H} &= \omega_\alpha \hat{\alpha}^\dagger \hat{\alpha} + \omega_\beta \hat{\beta}^\dagger \hat{\beta} + \frac{\Omega}{2}\hat{\alpha}\hat{\beta}^\dagger + \frac{\Omega^*}{2}\hat{\alpha}^\dagger \hat{\beta} \\ &= \begin{pmatrix} \hat{\alpha}^\dagger & \hat{\beta}^\dagger \end{pmatrix} \begin{pmatrix} \omega_\alpha & \Omega^*/2 \\ \Omega/2 & \omega_\beta \end{pmatrix} \begin{pmatrix} \hat{\alpha} \\ \hat{\beta} \end{pmatrix} \\ &= \underline{\hat{\alpha}}^\dagger \underline{H}_{\text{in}} \underline{\hat{\alpha}},\end{aligned} \tag{6.1}$$

where we set $\hbar = 1$ and α, β indicate the spin-up and -down magnon modes forming our basis. Operators and matrices/vectors are indicated with an overhead

[45] Note that the degeneracy of the two modes is only valid for collinear antiferromagnets.

hat and underline, respectively. Ω denotes the coherent coupling rate of the modes. To diagonalize the hamiltonian $\underline{H}_{\text{in}}$ in Eq. (6.1), we write

$$\hat{H} = \begin{pmatrix} \hat{\psi}_1^\dagger & \hat{\psi}_2^\dagger \end{pmatrix} \begin{pmatrix} \omega_1 & 0 \\ 0 & \omega_2 \end{pmatrix} \begin{pmatrix} \hat{\psi}_1 \\ \hat{\psi}_2 \end{pmatrix} = \underline{\hat{\psi}}^\dagger \underline{H}_{\text{diag}} \underline{\hat{\psi}}, \tag{6.2}$$

where $\omega_{1,2}$ and $\hat{\psi}_{1,2}$ are the eigenvalues and eigenstates, respectively, of the corresponding eigenvalue equation for $\underline{H}_{\text{in}}$. Solving the eigenvalue problem allows for the transformation $\underline{H}_{\text{diag}} = \underline{P}^\dagger \underline{H}_{\text{in}} \underline{P}$, where the associated (unitary) transformation matrix $\underline{P}$ becomes

$$\underline{P} = \begin{pmatrix} \cos\left(\frac{\theta_1}{2}\right) & e^{i\varphi_2} \sin\left(\frac{\theta_2}{2}\right) \\ e^{i\varphi_1} \sin\left(\frac{\theta_1}{2}\right) & \cos\left(\frac{\theta_2}{2}\right) \end{pmatrix}, \tag{6.3}$$

which is written in terms of the Bloch sphere representation with $\theta_{1,2}$ and $\varphi_{1,2}$ parametrizing the two eigenvectors on the Bloch sphere. Due to $\underline{P}$ being a unitary matrix with $\underline{P}^\dagger = \underline{P}^{-1}$, it follows that $\theta_2 = \pi - \theta_1$ and $\varphi_2 = \pi + \varphi_1$. This enables a representation of the two eigenvectors on the Bloch sphere as two antiparallel vectors. Hence we can further simplify $\underline{P}$ to [10]

$$\underline{P} = \begin{pmatrix} \cos\left(\frac{\theta}{2}\right) & -e^{-i\varphi} \sin\left(\frac{\theta}{2}\right) \\ e^{i\varphi} \sin\left(\frac{\theta}{2}\right) & \cos\left(\frac{\theta}{2}\right) \end{pmatrix}, \tag{6.4}$$

where the subscript 1 has been dropped. The eigenmodes written in terms of the natural basis spanned by $\hat{\alpha}^\dagger$ and $\hat{\beta}^\dagger$ then become

$$\begin{pmatrix} \hat{\psi}_1^\dagger & \hat{\psi}_2^\dagger \end{pmatrix} = \begin{pmatrix} \hat{\alpha}^\dagger & \hat{\beta}^\dagger \end{pmatrix} \begin{pmatrix} \cos\left(\frac{\theta}{2}\right) & -e^{-i\varphi} \sin\left(\frac{\theta}{2}\right) \\ e^{i\varphi} \sin\left(\frac{\theta}{2}\right) & \cos\left(\frac{\theta}{2}\right) \end{pmatrix}. \tag{6.5}$$

A schematic depiction of a Bloch sphere and the two associated states $\hat{\psi}_1^\dagger$ (red sphere) and $\hat{\psi}_2^\dagger$ (green sphere) for arbitrary (θ, φ) is given in Fig. 6.1. We note that the eigenvectors on the Bloch sphere are given in the space of creation operators. This is different from the typical use of a Bloch sphere, which represents wavefunctions, rather than operators, of a two-level system [10]. The representation might therefore rather be considered as a Poincaré sphere, which is usually used for mapping of the polarization states of light [253].

We now introduce the pseudospin operator $\hat{\boldsymbol{L}} = \hat{L}_x \hat{\boldsymbol{x}} + \hat{L}_y \hat{\boldsymbol{y}} + \hat{L}_z \hat{\boldsymbol{z}}$:

$$\hat{L}_x = \frac{1}{2}(\underline{\hat{\alpha}}^\dagger \underline{\sigma}_x \underline{\hat{\alpha}}) = \frac{1}{2}(\hat{\alpha}\hat{\beta}^\dagger + \hat{\alpha}^\dagger \hat{\beta}), \tag{6.6a}$$

$$\hat{L}_y = \frac{1}{2}(\underline{\hat{\alpha}}^\dagger \underline{\sigma}_y \underline{\hat{\alpha}}) = \frac{i}{2}(\hat{\alpha}\hat{\beta}^\dagger - \hat{\alpha}^\dagger \hat{\beta}), \tag{6.6b}$$

$$\hat{L}_z = \frac{1}{2}(\underline{\hat{\alpha}}^\dagger \underline{\sigma}_z \underline{\hat{\alpha}}) = \frac{1}{2}(\hat{\alpha}^\dagger \hat{\alpha} - \hat{\beta}^\dagger \hat{\beta}), \tag{6.6c}$$

where $\underline{\sigma}_{x,y,z}$ are the Pauli matrices. Using $\hat{\boldsymbol{L}}$, we can rewrite the hamiltonian in Eq. (6.1) as

$$\hat{H} = 2\omega_0 \hat{L}_0 - \boldsymbol{\omega} \cdot \hat{\boldsymbol{L}}, \tag{6.7}$$

where $\hat{L}_0 = \frac{1}{2}(\hat{\underline{a}}^\dagger \underline{\sigma}_0 \hat{\underline{a}}) = \frac{1}{2}(\hat{\alpha}^\dagger \hat{\alpha} + \hat{\beta}^\dagger \hat{\beta})$ with $\underline{\sigma}_0$ the 2×2 identity matrix. Furthermore, ω_0 and the components of $\boldsymbol{\omega}$ are given by [10]

$$\omega_0 = \frac{\omega_\alpha + \omega_\beta}{2}, \tag{6.8a}$$

$$\omega_z = -(\omega_\alpha - \omega_\beta), \tag{6.8b}$$

$$\omega_x + i\omega_y = -\Omega. \tag{6.8c}$$

The quantity $\boldsymbol{\omega}$ is referred to as the pseudofield, the properties of which are such that the eigenmodes on the Bloch sphere are collinear with $\boldsymbol{\omega}$ [10]. Thus, the eigenmodes of the antiferromagnetic excitations are given by the direction of the pseudofield vector, which is, in turn, given by the difference of the uncoupled frequencies of the α- and β-modes (Eq. (6.8b)) as well as the mode coupling Ω (Eq. (6.8c)).

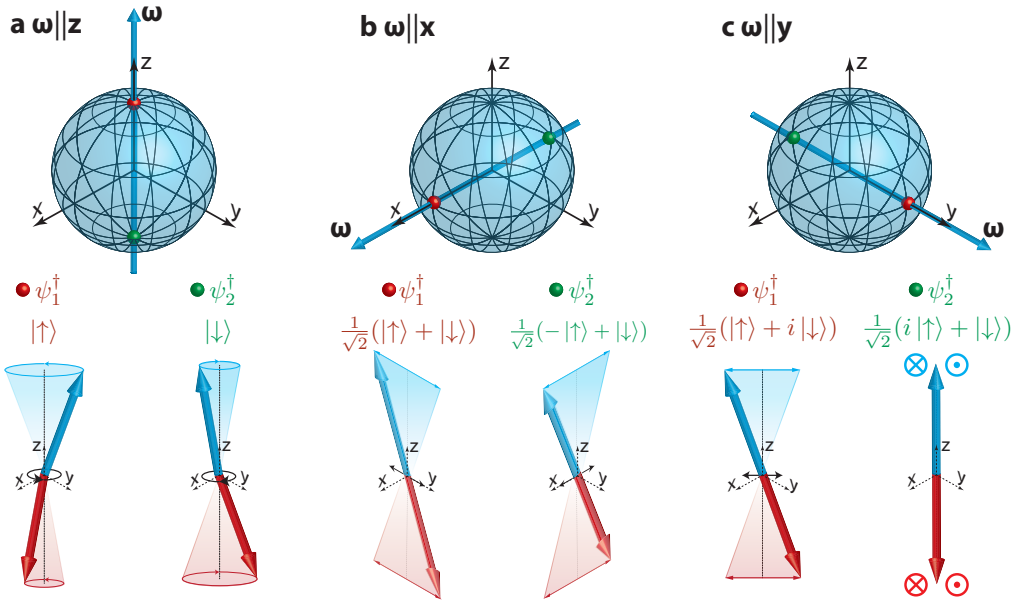

Fig. 6.2 – Relation between the Bloch sphere representation of the eigenmodes (red and green spheres) and the corresponding Néel vector dynamics for $\boldsymbol{\omega} \parallel \hat{\boldsymbol{z}}$ (**a**), $\boldsymbol{\omega} \parallel \hat{\boldsymbol{x}}$ (**b**) and $\boldsymbol{\omega} \parallel \hat{\boldsymbol{y}}$ (**c**). In addition, the superpositions of the spin-up ($|\uparrow\rangle$) and -down ($|\downarrow\rangle$) basis states are given for each eigenmode.

In general, the pseudofield is dependent on the details of the magnetic interactions present in the antiferromagnet [10, 13]. The knowledge of the pseudofield allows for a convenient description of the eigenmodes for arbitrary antiferromagnets. For the three orthogonal directions of the pseudofield, the relation between the eigenmodes and their corresponding Néel vector dynamics in Landau-Lifshitz

description is depicted in Fig. 6.2**a**, **b** and **c**: for $\boldsymbol{\omega} \parallel \hat{\boldsymbol{z}}$ (**a**), the eigenmodes are equal to the spin-up and -down magnon modes referring to circular precessions of the sublattice magnetizations. When $\boldsymbol{\omega} \parallel \hat{\boldsymbol{x}}$ (**b**), linear oscillations of the Néel vector corresponding to zero spin excitations form the eigenmodes, which are given by linear superpositions of the underlying spin-up and -down basis states. As suggested by the orthogonality of the two eigenmodes, the linear oscillation planes are perpendicular to each other. For the case when $\boldsymbol{\omega} \parallel \hat{\boldsymbol{y}}$ (**c**), linear oscillations in planes 45° tilted with respect to the eigenmodes for $\boldsymbol{\omega} \parallel \hat{\boldsymbol{x}}$ deploy.

6.1.2 Pseudospin Dynamics and Diffusive Transport

According to Ref. [10], the expectation value of the pseudospin operator (divided by the sample volume V) is

$$\boldsymbol{L} \equiv \langle \hat{\boldsymbol{L}} \rangle = \frac{1}{2V} \left(- \left. \frac{\partial N(\epsilon)}{\partial \epsilon} \right|_{\epsilon=\omega_0} \right) (\boldsymbol{\omega} + \boldsymbol{\mu}_\mathrm{s}) = \boldsymbol{L}_0 + \frac{1}{2V} \left(- \left. \frac{\partial N(\epsilon)}{\partial \epsilon} \right|_{\epsilon=\omega_0} \right) \boldsymbol{\mu}_\mathrm{s}, \quad (6.9)$$

which we refer to as the pseudospin density. Here, $\boldsymbol{L}_0 \propto \boldsymbol{\omega}$ is the equilibrium contribution to $\boldsymbol{L}$ and $N(\epsilon) = \left(\exp\left(\frac{\epsilon}{k_\mathrm{B} T} \right) - 1 \right)^{-1}$ is the Bose-Einstein distribution function with k_B the Boltzmann constant, T the temperature and ϵ the single magnon energy. Furthermore, we introduced the pseudospin chemical potential [10]

$$\boldsymbol{\mu}_\mathrm{s} = (\mu_1 - \mu_2)(\sin(\theta)\cos(\varphi)\hat{\boldsymbol{x}} + \sin(\theta)\sin(\varphi)\hat{\boldsymbol{y}} + \cos(\theta)\hat{\boldsymbol{z}}), \quad (6.10)$$

where $\mu_{1,2}$ are the magnon spin chemical potentials of the respective eigenmodes [254]. Different to the usually scalar-valued magnon chemical potential defined for ferromagnetic systems, the pseudospin chemical potential constitutes a vectorial quantity, thereby accounting for the eigenmode information via (θ, φ). While the pseudofield $\boldsymbol{\omega}$ accounts for the equilibrium density due to an energy/occupation imbalance between the eigenmodes (cf. (6.8b)), the pseudospin chemical potential $\boldsymbol{\mu}_\mathrm{s}$ is caused by a finite chemical potential difference between the modes and thus accounts for non-equilibrium effects. Note, that only the z-component of $\boldsymbol{\mu}_\mathrm{s}$ constitutes a finite (measurable) magnon spin, since the transverse components refer to zero spin modes. For the diffusive transport of pseudospin, obviously only the non-equilibrium part given by $\boldsymbol{\mu}_\mathrm{s}$ has to be considered. Before we investigate the diffusive transport, however, we study the temporal evolution of the pseudospin density $\boldsymbol{L}$. We thus obtain

$$\frac{\mathrm{d}\boldsymbol{\mu}_\mathrm{s}}{\mathrm{d}t} = \boldsymbol{\mu}_\mathrm{s} \times \boldsymbol{\omega}, \quad (6.11)$$

which follows from the Heisenberg equation of motion for the pseudospin operator $\hat{\boldsymbol{L}}$ [10] and employing Eq. (6.9) therafter. Equation (6.11) describes a precession of $\boldsymbol{\mu}_\mathrm{s}$ around the fictitious pseudofield $\boldsymbol{\omega}$.

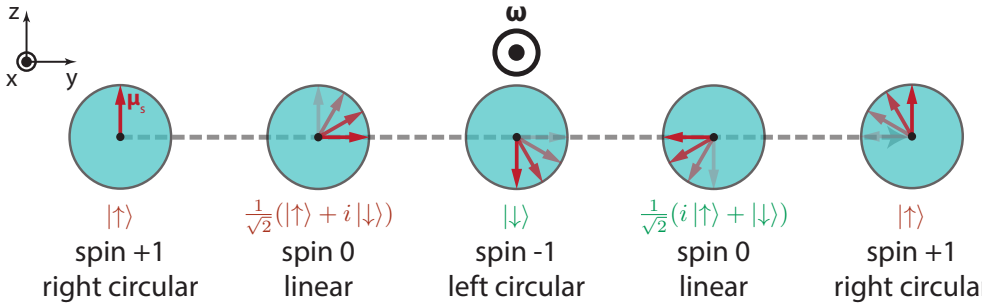

Fig. 6.3 – Precession of the pseudospin chemical potential $\boldsymbol{\mu}_\mathrm{s}$ around the fictitious pseudofield $\boldsymbol{\omega}$. Each direction of $\boldsymbol{\mu}_\mathrm{s}$ is related to the eigenmode given via the superposition of the quantum basis states.

For the sake of an intuitive approach towards Eq. (6.11), we consider an initial pseudospin chemical potential $\boldsymbol{\mu}_\mathrm{s} = \mu_\mathrm{s}\hat{\boldsymbol{z}}$ along z and a pseudofield $\boldsymbol{\omega} = \omega\hat{\boldsymbol{x}}$ pointing along the x-direction. Since $\boldsymbol{\mu}_\mathrm{s}$ is not collinear with $\boldsymbol{\omega}$, the non-equilibrium spin accumulation is not comprised of eigenmodes of the system and therefore starts to precess around $\boldsymbol{\omega}$. In the classical Landau-Lifshitz picture, the Néel vector dynamics change from right circular to linear to left cicular to linear and back to right circular. The precession of $\boldsymbol{\mu}_\mathrm{s}$, together with the corresponding quantum superposition states, is depicted in Fig. 6.3. We observe an oscillation of the actual magnon spin density, i.e. the z-component of $\boldsymbol{\mu}_\mathrm{s}$. In a realistic scenario, dephasing and decoherence processes additionally lead to a reduction of $\boldsymbol{\mu}_\mathrm{s}$ and a gradual alignment with the pseudofield $\boldsymbol{\omega}$, which eventually leads the pseudospin chemical potential $\boldsymbol{\mu}_\mathrm{s}$ to feature the actual eigenmodes of the system.

As to describe diffusive transport of pseudospin [249, 255], we introduce the averaged pseudospin density

$$\boldsymbol{\mathcal{S}} \equiv \sum_{\boldsymbol{k}} \frac{1}{2V} \left(- \left. \frac{\partial N(\epsilon)}{\partial \epsilon} \right|_{\epsilon=\omega_{0\boldsymbol{k}}} \right) (\boldsymbol{\omega}_{\boldsymbol{k}} + \boldsymbol{\mu}_\mathrm{s}) = \chi(\boldsymbol{\omega} + \boldsymbol{\mu}_\mathrm{s}), \tag{6.12}$$

which takes into account the contribution from all excited wavevectors $\boldsymbol{k}$ [10]. We have introduced the effective susceptibility and average pseudofield as

$$\chi \equiv \int \frac{\mathrm{d}^3k}{(2\pi)^3} \frac{1}{2} \left(- \left. \frac{\partial N(\epsilon)}{\partial \epsilon} \right|_{\epsilon=\omega_{0\boldsymbol{k}}} \right), \tag{6.13}$$

$$\boldsymbol{\omega} = \langle \boldsymbol{\omega}_{\boldsymbol{k}} \rangle_\mathrm{BZ} \equiv \frac{\int \frac{\mathrm{d}^3k}{(2\pi)^3} \boldsymbol{\omega}_{\boldsymbol{k}} \frac{1}{2} \left(- \left. \frac{\partial N(\epsilon)}{\partial \epsilon} \right|_{\epsilon=\omega_{0\boldsymbol{k}}} \right)}{\int \frac{\mathrm{d}^3k}{(2\pi)^3} \frac{1}{2} \left(- \left. \frac{\partial N(\epsilon)}{\partial \epsilon} \right|_{\epsilon=\omega_{0\boldsymbol{k}}} \right)}, \tag{6.14}$$

where $\omega_{0\boldsymbol{k}}$ denotes the dispersion of the uncoupled magnon energy. Eventually, we can write down the general diffusion equation of the pseudospin density $\boldsymbol{\mathcal{S}}$ including the pseudospin dynamics

$$\frac{\partial \boldsymbol{\mathcal{S}}}{\partial t} = D\nabla^2 \boldsymbol{\mathcal{S}} - \frac{\boldsymbol{\mathcal{S}} - \boldsymbol{\mathcal{S}}_0}{\tau_\mathrm{s}} + \boldsymbol{\mathcal{S}} \times \boldsymbol{\omega}, \tag{6.15}$$

where $\boldsymbol{\mathcal{S}}_0$ is the equilibrium spin density and τ_s is the spin relaxation time (assumed to be isotropic). Furthermore, we use the $\boldsymbol{k}$-dependent spin diffusion constant $D_\mathbf{k} = \frac{1}{3}\tau v_{\boldsymbol{k}}^2 = \frac{1}{3}\tau(\boldsymbol{\nabla}\omega_{0\boldsymbol{k}})^2$ with τ the average scattering time and $\boldsymbol{v}_{\boldsymbol{k}} = \boldsymbol{\nabla}\omega_{0\boldsymbol{k}}$ the group velocity of each magnon mode. The average diffusion constant is then defined as

$$D = \langle D_{\boldsymbol{k}} \rangle_\mathrm{BZ} = \frac{\int \frac{\mathrm{d}^3k}{(2\pi)^3} \frac{1}{3}\tau(\boldsymbol{\nabla}\omega_{0\boldsymbol{k}})^2 \frac{1}{2} \left(- \left. \frac{\partial N(\epsilon)}{\partial \epsilon} \right|_{\epsilon=\omega_{0\boldsymbol{k}}} \right)}{\int \frac{\mathrm{d}^3k}{(2\pi)^3} \frac{1}{2} \left(- \left. \frac{\partial N(\epsilon)}{\partial \epsilon} \right|_{\epsilon=\omega_{0\boldsymbol{k}}} \right)}. \tag{6.16}$$

Substituting Eq. (6.12) into Eq. (6.15) results in the diffusion equation for $\boldsymbol{\mu}_\mathrm{s}$:

$$\frac{\partial \boldsymbol{\mu}_\mathrm{s}}{\partial t} = D\nabla^2 \boldsymbol{\mu}_\mathrm{s} - \frac{\boldsymbol{\mu}_\mathrm{s}}{\tau_\mathrm{s}} + \boldsymbol{\mu}_\mathrm{s} \times \boldsymbol{\omega}. \tag{6.17}$$

We emphasize once more, that only the z-component of $\boldsymbol{\mu}_\mathrm{s}$ corresponds to the measurable and finite magnon spin. Equation (6.17) represents one of the central results of this theory. When we consider $\boldsymbol{\mu}_\mathrm{s} \parallel \boldsymbol{\omega}$, the last term in Eq. (6.17) is zero and it reduces to the well-known spin/magnon diffusion equation introduced in Ch. 2.7.2. For $\boldsymbol{\mu}_\mathrm{s} \perp \boldsymbol{\omega}$, the non-equilibrium pseudospin chemical potential does not correspond to the eigenmodes of the system and starts to precess around $\boldsymbol{\omega}$ (in addition to the conventional diffusion). We can further define the diffusive pseudospin current density as

$$\underline{\boldsymbol{j}}_\mathrm{s} = -D\boldsymbol{\nabla} \otimes \boldsymbol{\mathcal{S}} = -D\chi\boldsymbol{\nabla} \otimes \boldsymbol{\mu}_\mathrm{s}, \tag{6.18}$$

with $\underline{\boldsymbol{j}}_\mathrm{s}$ being a tensorial quantity involving the direction of the current flow as well as its pseudospin direction. This is analogous to the introduction of the spin current density in Ch. 2.3.1, Eq. (2.16).

In the following, we will discuss the one-dimensional solution of the diffusion equation given in Eq. (6.17). We therefore consider diffusion along the z-direction and further assume the following boundary conditions

$$-D\chi \left. \frac{\partial \mu_{\mathrm{s}z}}{\partial z} \right|_{z=0} = j_{\mathrm{s}0}, \tag{6.19}$$

$$\left. \frac{\partial \mu_{\mathrm{s}x,\mathrm{s}y}}{\partial z} \right|_{z=0} = 0, \tag{6.20}$$

which assumes a magnonic spin current density j_{s0} at $z = 0$ and explicitly zero spin current with regards to the x- and y-component of $\boldsymbol{\mu}_s$. This particularly implies that only spin-up and -down magnons can be injected into the antiferromagnet. This is justified by the perturbative treatment of the mode coupling: when a z-polarized spin current density is injected into the antiferromagnet from an external source, a localized spin of size $+1$ or -1 is excited therein. On a very short time scale proportional to the inverse of the exchange energy, the spin is delocalized thereby becoming a respective spin-up or -down magnon mode. On a much larger time scale proportional to the inverse of the mode coupling frequency, the delocalized spin-up or -down magnon modes recognize that they are not eigenmodes of the system and therefore start to precess according to the diffusion equation (6.17).

Having worked out the appropriate boundary conditions given in Eqs. (6.19) and (6.20), we further assume $\boldsymbol{\omega} = \omega_y \hat{\boldsymbol{y}} + \omega_z \hat{\boldsymbol{z}}$ for the pseudofield. As discussed in Ch. 6.1.1, this corresponds to an antiferromagnet hosting spin excitations with magnitudes between 0 and 1, corresponding to the general case of an elliptical Néel vector precession. Finally, we solve the pseudospin diffusion equation (6.17) in steady state by claiming $\partial \boldsymbol{\mu}_s / \partial t = 0$. After some algebra, we arrive at

$$\mu_{sz}(z) = \mu_{osc}(z) + \mu_{dec}(z), \tag{6.21}$$

$$\mu_{osc}(z) = \frac{\omega_y^2}{\omega_y^2 + \omega_z^2} \frac{\lambda_s j_{s0}}{D\chi(a^2 + b^2)} e^{-az/\lambda_s} \left[a \cos\left(\frac{bz}{\lambda_s}\right) - b \sin\left(\frac{bz}{\lambda_s}\right) \right], \tag{6.22}$$

$$\mu_{dec}(z) = \frac{\omega_z^2}{\omega_y^2 + \omega_z^2} \frac{\lambda_s j_{s0}}{D\chi} e^{-z/\lambda_s}, \tag{6.23}$$

where $\lambda_s = \sqrt{D\tau_s}$ is the magnon (pseudo)spin diffusion length and we have further defined

$$a \equiv \frac{1}{\sqrt{2}} \sqrt{1 + \sqrt{1 + \beta^2}}, \tag{6.24}$$

$$b \equiv \frac{1}{\sqrt{2}} \sqrt{-1 + \sqrt{1 + \beta^2}}, \tag{6.25}$$

$$\beta^2 \equiv \tau_s^2 (\omega_y^2 + \omega_z^2). \tag{6.26}$$

As evident from Eqs. (6.21)-(6.23), the solution of the measurable magnon spin chemical potential $\mu_{sz}(z)$ is composed of a decaying ($\mu_{dec}(z)$) and an onscillating ($\mu_{osc}(z)$) contribution. The decaying part may be understood as the fractional circular polarization content given by the prefactor $[\omega_z^2/(\omega_y^2 + \omega_z^2)]$. It therefore constitutes the part of the injected spin that does not precess around the pseudofield $\boldsymbol{\omega}$, as it is already aligned with it. The oscillating contribution, on the contrary, represents the transverse components of the injected modes given by the fraction $[\omega_y^2/(\omega_y^2 + \omega_z^2)]$, which precesses around the pseudofield with a frequency of $\sqrt{\omega_y^2 + \omega_z^2}$. Equations (6.21)-(6.26) are the key result of this theory and are

capable to rationalize our magnon transport measurements outlined in Ch. 6.3.1. Although our magnon based description of an ordered AFI is, strictly speaking, a low temperature approximation, it has been found to work well even at high temperatures [256, 257].

The methodology developed in this theory is expected to find applications in understanding magnonic spin transport in a broad range of AFIs. Due to its validity for any coherently coupled bosonic modes, it may also trigger the development of spin-dynamics-inspired physical insights for, among others, coupled optomechanical [258] and optomagnonic systems [238, 259, 260].

6.2 Sample Layout and Measurement Technique

In this Section, we introduce the experimental details of our magnon transport experiments, including the sample layout of the α-Fe_2O_3/Pt heterostructures and the used measurement technique.

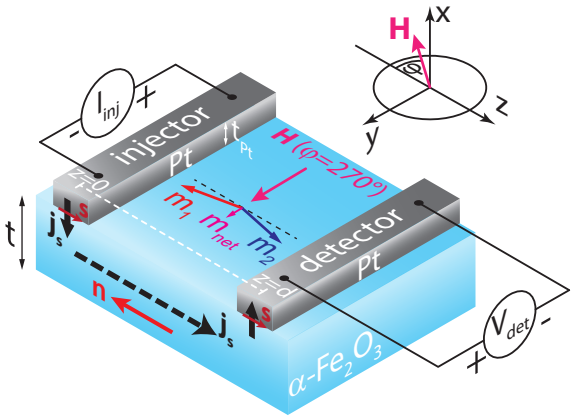

Fig. 6.4 – Sketch of the device geometry, the electrical wiring and the coordinate system. The canting of the magnetic sublattices $\boldsymbol{m}_1$ and $\boldsymbol{m}_2$, the corresponding net magnetization $\boldsymbol{m}_{\text{net}}$ as well as the Néel order parameter $\boldsymbol{n}$ are illustrated. Upon applying a charge current I_{inj} to the injector, a spin current j_s with spin polarization $\boldsymbol{s}$ is generated via the SHE and injected into the hematite (α-Fe_2O_3) with thickness t. At the same time, Joule heating in the injector leads to a thermal generation of magnons. For both processes, the emerging antiferromagnetic magnon current is detected via the inverse SHE-induced current at the detector by measuring the voltage drop V_{det}. The electrical and thermal signals are separated by the current reversal method described in Ch. 3.4.1.

For our magnon transport experiments, we use the antiferromagnetic insulator (AFI) hematite (α-Fe_2O_3) introduced in Ch. 3.1.2. The $t = 15\,\text{nm}$ thick, single crystalline (0001)-oriented thin film was grown via pulsed laser deposition at the Walther-Meißner-Institut on a (0001)-oriented sapphire (Al_2O_3) substrate using a substrate temperature of 320 °C, an oxygen pressure of 25 µbar, a laser fluence at the target of $2.5\,\text{J/cm}^2$ and a repetition rate of 2 Hz. A schematic of the sample structure is shown in Fig. 6.4. The film is characterized by an easy y-z-plane anisotropy and an out-of-plane DMI vector. The thin hematite layer features an easy-plane phase over the entire temperature range and therefore lacks the

Morin transition [145] (see Ch. 3.1.2). The equilibrium Néel vector $\boldsymbol{n}$ and the sublattice magnetizations $\boldsymbol{m}_{1,2}$ thus lie in the y-z-plane with a small canting angle between $\boldsymbol{m}_1$ and $\boldsymbol{m}_2$. An applied magnetic field along $\hat{\boldsymbol{y}}$ orients the Néel vector along $-\hat{\boldsymbol{z}}$. The magnitude of the external magnetic field $\mu_0 H$ further controls the canting angle and the net induced magnetization $\boldsymbol{m}_{\text{net}} = \boldsymbol{m}_1 + \boldsymbol{m}_2$, both bearing a constant DMI-induced offset and a variable contribution linear in $\mu_0 H$. For the injection and detection of magnons in the hematite, platinum (Pt) electrodes with a thickness of 5 nm were deposited via DC magnetron sputtering and patterned into strips of lengths $l = 162\,\mu\text{m}$ (injector) and $l = 148\,\mu\text{m}$ (detector) via electron beam lithography. Subsequently, an Al layer of 50 nm is deposited on the film by DC sputtering and patterned into leads for the Pt strips to contact the device electrically (see Ch. 3.2 for details on the fabrication process). Each of the structures studied in this thesis have a constant detector width of $w_{\text{det}} = 500\,\text{nm}$ and edge-to-edge distances of either $d_{\text{edge}} = 200\,\text{nm}$ or $d_{\text{edge}} = 400\,\text{nm}$. The injector widths vary from $w_{\text{inj}} = 200\,\text{nm}$ to $w_{\text{inj}} = 800\,\text{nm}$. We therefore use the center-to-center distance between the strips to obtain the effective transport length d (see Fig. 6.4). DC current densities in the order of $2 \times 10^{11}\,\text{A}\,\text{m}^{-2}$ are fed through the injector strips with a Keithley 2400 current source. To detect the magnon spin signal, we measure the voltage signals V_{det} at the detectors using a Keithley 2182 nanovoltmeter. We separate the electrical (thermal) signals $V_{\text{det}}^{\text{el}}$ ($V_{\text{det}}^{\text{th}}$) stemming from the SHE-based magnon injection (thermal magnon injection) using the current reversal method described in Ch. 3.4.1. We perform angle dependent measurements of V_{det} by rotating the external magnetic field H in the plane of the sample by an angle φ (see Fig. 6.4)

6.3 Electrically Induced Magnon Transport

This Section is focussed on the SHE-induced magnon transport in the hematite layer. As introduced in Ch. 6.2, a z-polarized electron spin accumulation is generated at the injector of the Pt/α-Fe_2O_3 interface, leading to a z-polarized, diffusive magnon spin and pseudospin current in the hematite (cf. Fig. 6.4). For the emerging electrical detector signals we define the normalized magnon spin signal $R_{\text{det}}^{\text{el}} = (V_{\text{det}}^{\text{el}}/I_{\text{inj}}) \cdot (A_{\text{inj}}/A_{\text{det}})$, where A_{inj} and A_{det} are the interface areas at the injector and detector, respectively. This allows us to compare between different device geometries and injector currents I_{inj} [11].

6.3.1 Antiferromagnetic Magnon Hanle Effect and Pseudospin Dynamics

In order to quantitatively model the pseudospin transport signal, we employ the one-dimensional solution for μ_{sz} (given in Eqs. (6.21)-(6.23)) derived from the pseudospin diffusion equation in Ch. 6.1.2. Since we study the magnon transport in a hematite layer as thin as 15 nm, a one-dimensional treatment of the magnon pseudospin diffusion is justified. According to our theory of antiferromagnetic magnon diffusion [10] outlined in Ch. 6.1, the direction of the pseudofield $\boldsymbol{\omega}$ determines the eigenmodes of the AFI. Hence, the knowledge of the components of $\boldsymbol{\omega}$ for the description of the diffusive magnon transport is required. We recall that $\omega_z = -(\omega_\alpha - \omega_\beta)$ is determined by an imbalance between the energies of the spin-up and -down magnon modes (see Ch. 6.1.1) and is therefore given by the energy splitting of the respective magnon dispersions, which correspond to the natural circularly polarized basis states. Although the mode frequencies ω_α and ω_β are generally non-degenerate for a canted antiferromagnet like ours [32], we assume $\omega_z \approx 0$. This assumption is justified since the diffusive transport is governed by thermal magnons with large $\boldsymbol{k}$-vectors [36]. For large $\boldsymbol{k}$, the energy splitting between the modes is negligible [32]. The transverse components ω_x and ω_y, on the contrary, are determined by the mode coupling Ω (cf. Eqs. (6.8c)) and therefore characterize the coherent effect [121, 237, 238] of spin-nonconserving, emergent spin-orbit [241, 242] interactions that couple the natural spin-up and -down magnon modes to form superposition states therof. Note, that for finite ω_z and a vanishing mode coupling $\Omega = 0$ (i.e. $\omega_x = \omega_y = 0$), the one-dimensional diffusion equation μ_{sz} reduces to the magnon spin transport equation for easy-axis collinear AFIs [116, 261] and is therefore governed by the decaying contribution, i.e. $\mu_{sz}(z) = \mu_{dec}(z)$ (cf. Eq. (6.23)). In our hematite film, however, easy-plane anisotropy and canting-mediated non-collinearity break the rotational symmetry about the Néel order and coherently couple the opposite spin magnon modes leading to $\omega_x = 0$ but $\omega_y \neq 0$. Hence, we expect $|\Omega| = |\omega_y|$ from Eq. (6.8c). As shown in Ref. [13], the resulting ($\boldsymbol{k}$-vector averaged) coupling Ω due to these anisotropic magnetic interactions is given by

$$\hbar\Omega = \hbar\omega_{an} - \mu_0 H_{DMI} m_{net} = \hbar\tilde{\omega}_{an} - \mu_0 \tilde{m} H, \tag{6.27}$$

where we drop the assumption that $\hbar = 1$ to reconvert into SI units. Here, $\hbar\tilde{\omega}_{an}$ is the reduced anisotropy energy, H_{DMI} is the effective DMI field and $\tilde{m}$ is an equivalent magnetic moment that parametrizes the DMI strength [142]. The latter allows for elucidating the linear $\mu_0 H$-dependence of the non-collinearity-mediated contribution to Ω[46]. Assuming that the total net magnetic moment of

[46] In general, Ω is expected to bear a constant contribution from anisotropy and a canting-mediated contribution that depends on the applied field $\mu_0 H$. These will differ for different materials and crystal structures, and Ω *vs.* $\mu_0 H$ may thus be considered as a Taylor expansion.

our film can be expressed as $m_{\mathrm{net}} = m_{\mathrm{net0}} + \chi_{\perp} H$ with $\chi_{\perp}$ the susceptibilty of easy-plane hematite and m_{net0} the net magnetic moment at zero external magnetic field due to the DMI, it follows from Eq. (6.27) that $\tilde{m} = \chi_{\perp} H_{\mathrm{DMI}} = m_{\mathrm{net0}}$ and $\hbar\tilde{\omega}_{\mathrm{an}} = \hbar\omega_{\mathrm{an}} - \mu_0 m_{\mathrm{net0}} H_{\mathrm{DMI}}$. The two terms in Eq. (6.27) represent the energy contributions of the spin non-conserving magnetic interactions in our material, represented by the easy-plane anisotropy and the DMI. Due to $\omega_y \neq 0$ (i.e. $\Omega \neq 0$), we expect a finite contribution from the oscillating term $\mu_{\mathrm{osc}}(z)$ defined in Eq. (6.22), which we can control with the external magnetic field according to Eq. (6.27). The resulting measurable z-component of the pseudospin chemical potential then becomes

$$\mu_{\mathrm{sz}}(z) = \frac{j_{\mathrm{s0}}\lambda_s}{D\chi(a^2+b^2)} \mathrm{e}^{-az/\lambda_{\mathrm{s}}} \left(a\cos\frac{bz}{\lambda_{\mathrm{s}}} - b\sin\frac{bz}{\lambda_{\mathrm{s}}} \right), \tag{6.28}$$

which describes the magnon spin density at a distance z from the injector. It is proportional to the magnon spin signal amplitude $\Delta R_{\mathrm{det}}^{\mathrm{el}}$ measured by the detector electrode at $z = d$. Together, Eqs. (6.27) and (6.28) describe a field-controllable precession of the pseudospin chemical potential in the x-z plane and describe the key phenomenon reported here, forming the basis for analyzing our experimental data.

In Fig. 6.5**a**, the relation between the pseudospin chemical potential $\boldsymbol{\mu}_{\mathrm{s}}$ and its corresponding Néel vector dynamics is illustrated for four different directions of $\boldsymbol{\mu}_{\mathrm{s}}$ in that plane (see also Ch. 6.1.1). According to Eq. (6.28), the pseudospin chemical potential transport as a function of the external magnetic field H is expected to behave as depicted in Fig. 6.5**b**-**c**: at the compensation field H_{c}, the anisotropy and the DMI contributions just cancel, resulting in $\Omega = 0$. The pseudospin potential, in this case, propagates through the AFI without any precession (**b**). In contrast, for the field H_0, the pseudospin of the magnons arriving at the detector electrode points orthogonal to the z-axis (**c**). This corresponds to a linearly polarized pseudospin configuration with zero magnon spin density and thus a vanishing magnon spin signal at the detector. For H_{inv}, the magnon pseudospin and actual spin densities have reversed directions while propagating from injector to detector (**d**). This situation corresponds to a negative magnon spin signal in the detector.

In Fig. 6.5**e**, measurements of $\Delta R_{\mathrm{det}}^{\mathrm{el}}$ as a function of the in-plane magnetic field $\mu_0 H$ applied along the length of the Pt strips ($\varphi = 270°$) are shown. Theoretical curves (white solid lines) are plotted together with experimental data (black and blue data points) for two devices featuring different electrode spacings d. The theory curves have been fitted to the data based upon Eq. (6.28), particularly with

$$\Delta R_{\mathrm{det}}^{\mathrm{el}} = R_0 + R_{\mathrm{osc}} \frac{\lambda_s}{D(a^2+b^2)} \mathrm{e}^{-az/\lambda_{\mathrm{s}}} \left(a\cos\frac{bz}{\lambda_{\mathrm{s}}} - b\sin\frac{bz}{\lambda_{\mathrm{s}}} \right), \tag{6.29}$$

where $R_{\mathrm{osc}} = C_{\mathrm{osc}}\, j_{\mathrm{s0}}/\chi$ with C_{osc} a constant factor accounting for the conversion between magnon chemical potential and the magnon spin signal $\Delta R_{\mathrm{det}}^{\mathrm{el}}$ at the

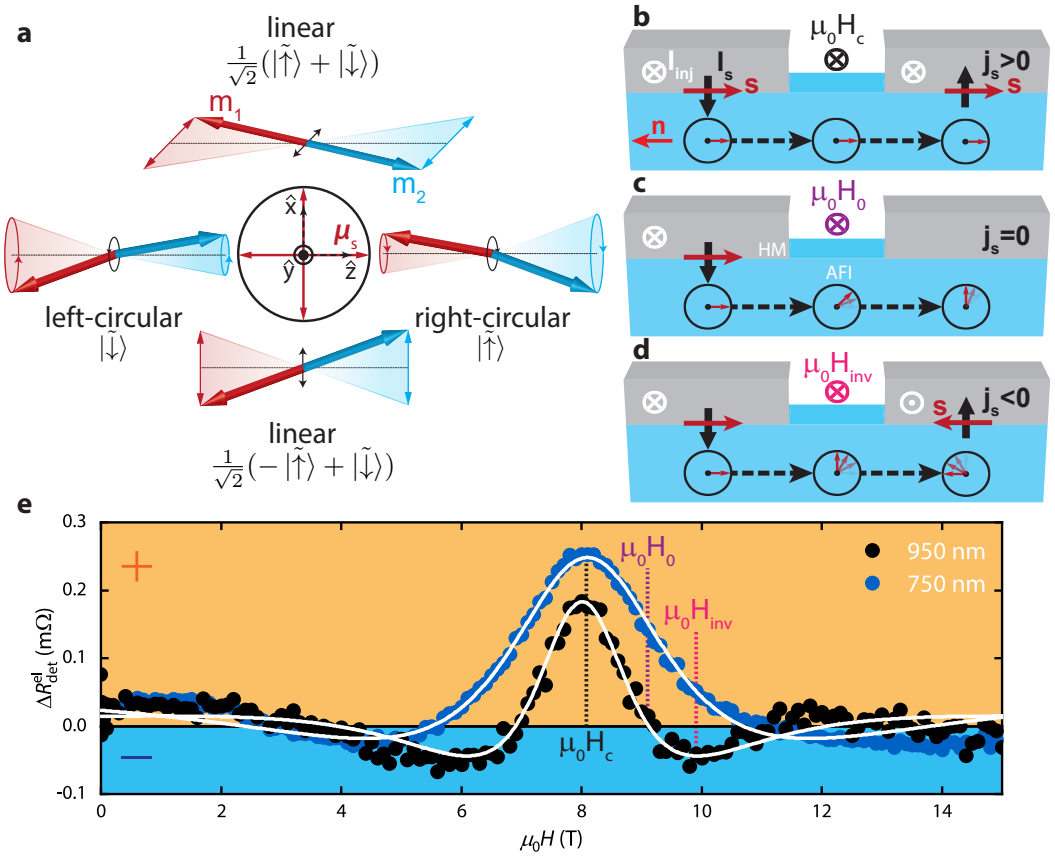

Fig. 6.5 – **a** Pseudospin chemical potential $\boldsymbol{\mu}_s$ description of magnonic excitations obtained by linear superpositions of spin-up and -down antiferromagnetic magnons that correspond to right- and left-circular precessions of the Néel vector $\boldsymbol{n}$, respectively. A pseudospin collinear with the z-axis corresponds to spin-up or -down magnons carrying spin ± 1. As the pseudospin rotates away from the z-axis, the precession of the Néel vector becomes increasingly elliptical merging into a linear oscillation for $\boldsymbol{\mu}_s \parallel \hat{\boldsymbol{x}}$, corresponding to zero-spin excitations. The z-component of pseudospin is measured via μ_{sz} and determines the actual magnonic spin probed in our measurements. **b**, **c** and **d** Magnonic spin along $\hat{\boldsymbol{z}} \parallel \boldsymbol{n}$ is injected and detected by the left and right heavy metal (HM) electrodes, respectively, deposited on an antiferromagnetic insulator (AFI). The pseudospin precesses with a frequency controlled by the applied magnetic field while diffusing from the injector to the detector. As a result, positive (**b**), zero (**c**), or negative (**d**) magnon spin is detected giving rise to an analogous behavior of the measured spin signal between the two electrodes as shown in **e**. The white curves depict the theoretical model fit (Eq. (6.29)) to the experimental data shown via black and blue circles for devices with an injector-detector distance of $d = 950\,\text{nm}$ and $d = 750\,\text{nm}$, respectively, at $T = 200\,\text{K}$.

detector. Furthermore, we introduce R_0 to account for a finite offset signal observed in our data. For the fitting routine, we choose the free parameters to be R_0, R_{osc}, D, τ_s and $\tilde{\omega}_{\text{an}}$. We further treat $\tilde{m} = m_{\text{net0}}$ as a fixed parameter in the fit using the bulk value $m_{\text{net0}} = 2.1 \times 10^{-25}\,\text{A m}^2$ taken from Ref. [262].

Evidently, the fits show a compelling agreement with our experimental data. Consistent with our model, we see a pronounced peak in the positive magnon spin signal regime for both devices. This peak corresponds to the compensation field $\mu_0 H_c$ for which $\Omega = 0$. Due to the vanishing pseudospin precession frequency at

$\mu_0 H_c$, the peak position is independent of the electrode spacing d. For increasing field strength, the spin signal decreases until it approaches zero signal at $\mu_0 H_0$, corresponding to a 90° rotation of the pseudospin vector, i.e. a linear polarization of the propagating magnon modes carrying zero spin. A sign inversion of the spin signal is evident when the field is further increased to $\mu_0 H_{\mathrm{inv}}$, corresponding to a full 180° rotation of the pseudospin vector $\boldsymbol{\mathcal{S}}$ and therefore an inversion of the magnon mode chirality/spin (cf. Fig. 6.5**a**). Since both $\mu_0 H_0$ and $\mu_0 H_{\mathrm{inv}}$ correspond to a finite precession frequency Ω, their values are expected to vary with the spacing d between the injector and detector electrodes, in agreement with our experimental data in Fig. 6.5**e**. As evident, the same behaviour is observed for decreasing field strength $\mu_0 H < \mu_0 H_c$, corresponding to a pseudospin precession in the opposite sense. We note, that the finite offset R_0 used in the fit equation (6.29), which is not contained in Eq. (6.28), can be motivated by the decaying contribution μ_{dec} that is non-zero for $\omega_z > 0$. Therefore, R_0 can be rationalized by a finite circular polarization content of the eigenmodes, leading to a non-precessing pseudospin contribution along z. According to Eq. (6.8b), the finite circular polarization parametrized by ω_z is induced by a non-degeneracy, i.e. splitting of the two magnon eigenmodes, which is indeed expected for our film [151, 263]. We nonetheless assumed $\omega_z = 0$ in Eq. (6.28), since the full description via Eqs. (6.21)-(6.23) does not yield satisfactory fit results. Hence, the circular polarization content of the magnon spin diffusion is treated as a constant offset R_0 in our model.

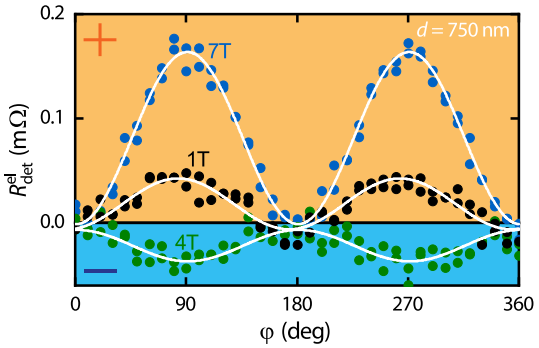

Fig. 6.6 – Angle dependent magnon spin signals $R_{\mathrm{det}}^{\mathrm{el}}$ for electrically excited magnons measured at the detector for $T = 200\,\mathrm{K}$ with a center-to-center distance of $d = 750\,\mathrm{nm}$. The white solid lines are fits to a $\sin^2(\varphi)$-type function.

Subsequently, we measure the magnon spin signal $R_{\mathrm{det}}^{\mathrm{el}}$ at the detector as a function of the external magnetic field orientation φ within the y-z-plane as illustrated in Fig. 6.4. The result is shown in Fig. 6.6 for a center-to-center strip distance of $d = 750\,\mathrm{nm}$. The data exhibit a 180°-symmetric modulation consistent with the SHE-mediated spin injection and detection of magnons [8, 9] (see also Ch. 2.7.1). Hence, the angle dependence can be fitted with a simple $\Delta R_{\mathrm{det}}^{\mathrm{el}} \sin^2(\varphi)$ function, where $\Delta R_{\mathrm{det}}^{\mathrm{el}}$ represents the amplitude of the electrical magnon spin signal. The signal modulation is shifted by $\sim 90°$ compared to similar measurements on

ferrimagnetic materials [8, 9, 198]. This is due to the fact that the electrical magnon excitation is only active when $\boldsymbol{\mu}_\mathbf{s} \parallel \mathbf{n}$, i.e. for $\mathbf{H} \perp \mathbf{n}$ in our experiments. Thus, we can confirm that the excited magnons in our experiments originate from the antiferromagnetic Néel order, consistent with previous experiments in AFIs [117]. Most importantly, we indeed observe two sign inversions of $R_{\mathrm{det}}^{\mathrm{el}}$ in the investigated field range. While a positive signal is measured for $\mu_0 H = 1\,\mathrm{T}$ and 7 T, a negative signal ensues at 4 T. These measurements are further evidence for the rotation of the pseudospin vector via the coherent coupling Ω between the antiferromagnetic magnon modes described in the spin diffusion equation (6.17).

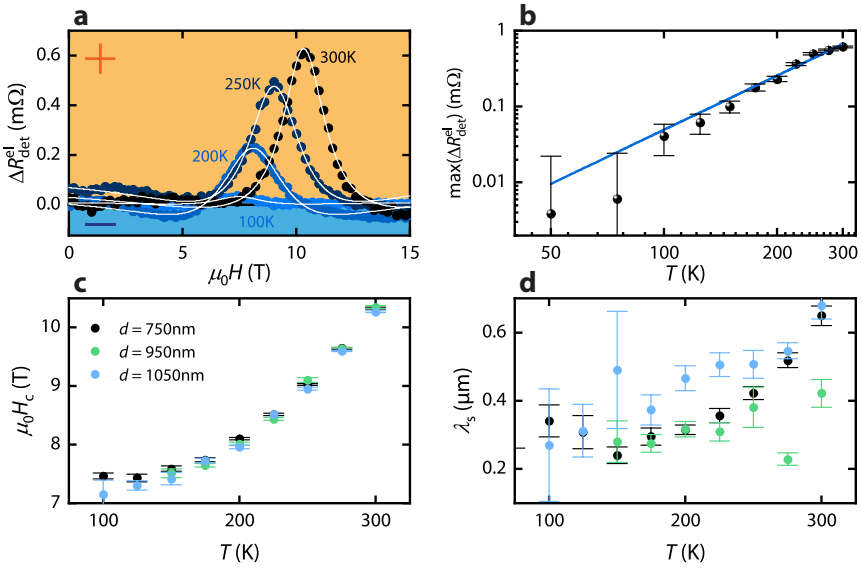

Fig. 6.7 – **a** Electrically excited magnon spin signals $\Delta R_{\mathrm{det}}^{\mathrm{el}}$ for a structure with strip distance $d = 750\,\mathrm{nm}$ plotted as a function of magnetic field for different temperatures. Light colored solid lines are fits to Eq. (6.29). **b** Temperature dependence of the maximum signal $\max(\Delta R_{\mathrm{det}}^{\mathrm{el}})$ extracted at the compensation field $\mu_0 H_c$ for each temperature from panel **a**. The solid blue line is a fit to a power law dependence, suggesting $\Delta R_{\mathrm{det}}^{\mathrm{el}} \propto T^{2.36}$. **c** Compensation field $\mu_0 H_c$ versus temperature extracted from experiments with devices of varying d. The temperature dependence of $\mu_0 H_c$ follows the temperature trend of the easy-plane anisotropy of hematite. **d** Spin diffusion length λ_s as a function of temperature extracted from experimental data from different devices with varying d. Obviously, λ_s increases with increasing temperature for all investigated structures.

Last but not least, we extract the magnon transport parameters from our data using the diffusive spin transport model given in Eq. (6.29). To this end, we carried out temperature-dependent measurements of the field-dependent magnon spin signals $\Delta R_{\mathrm{det}}^{\mathrm{el}}$, which are shown in Fig. 6.7**a**. Here, light colored solid lines correspond to fits to Eq. (6.29). For all investigated temperatures and devices with varying d, we obain excellent agreement between our experiments and the theoretical model, strongly supporting the validity of our theory. As evident from Fig. 6.7**a**, we observe a decrease of the peak amplitude at $\mu_0 H_c$ with decreasing temperature, which is expected from the electrically excited magnon transport

effect [9, 171, 264, 265]. We extract the maximum signal amplitudes $\max(\Delta R_{\mathrm{det}}^{\mathrm{el}})$, evaluated at the compensation field $\mu_0 H_{\mathrm{c}}$, for each temperature and plot the result in Fig. 6.7**b**. Fitting the data with a simple power law dependence of the form $\Delta R_{\mathrm{det},0}^{\mathrm{el}} T^n$, we find $n = 2.36$ (blue solid line in Fig. 6.7**b**). This agrees reasonably well with theoretical results that predict a temperature dependence of $\propto T^2$ for the electron spin to magnon conversion at a HM/AFI interface [264], verifying that the transport is indeed due to pure magnon currents. The slight discrepancy between theory and our data most probably stems from addtional temperature dependencies due to the transport of the magnons, which is not included in the spin to magnon interface conversion parameter of Ref. [264]. In addition to the temperature induced decrease of the magnon transport, we find a clear decrease of the compensation field with decreasing temperature in Fig. 6.7**a**. For a quantitative treatment of this behaviour, we extract $\mu_0 H_{\mathrm{c}}$ for each temperature from the fits (via $\tilde{\omega}_{\mathrm{an}}$) and plot its temperature dependence in Fig. 6.7**c**. For each structure, we observe a constant behaviour in the temperature range from 100 K to 150 K. A significant increase is evident for larger temperatures up to 300 K. As evident from Eq. (6.27), the compensation field can be expressed as $\mu_0 H_{\mathrm{c}} = \hbar \tilde{\omega}_{\mathrm{an}} (\tilde{m})^{-1}$. Therefore, $\mu_0 H_{\mathrm{c}}$ directly corresponds to the normalized anisotropy energy $\tilde{\omega}_{\mathrm{an}}$ of the hematite. We thus expect that $\mu_0 H_{\mathrm{c}}$ follows the temperature dependence of the easy-plane anisotropy. This is supported by previous measurements of the temperature dependence of the anisotropy energy in hematite, which qualitatively agree with the temperature dependence of $\mu_0 H_{\mathrm{c}}$ [146]. Hence, our results support the assumption that the coupling strength Ω defined in Eq. (6.27) is related to the easy-plane anisotropy in hematite. Finally, we calculate the magnon diffusion length λ_{s} using the extracted diffusion constant D and the spin relaxation time τ_{s} from our fits. The obtained temperature dependence of λ_{s} is shown in Fig. 6.7**d**. Overall, we find an increase of λ_{s} with increasing temperature for all studied injector-detector distances d. At room temperature, we extract $\lambda_s \approx 0.5\,\mu\mathrm{m}$, which is in perfect agreement with recent reports measuring the spin diffusion length in the easy-plane phase of hematite thin films using distance-dependent measurements [151, 263].

As a key result of this subection, we have experimentally demonstrated the coherent control of spin currents and magnon pseudospin dynamics in antiferromagnetic insulators. This opens new avenues for antiferromagnetic magnonic applications such as spin based transistors or field-controlled switchable devices. Moreover, our experimental exploitation of the magnonic equivalent of a spin-1/2 electron system provides the first crucial step towards various pseudospin-based concepts such as an unconventional non-Abelian computing scheme [240].

6.3.2 Crosstalk Between Injector and Detector

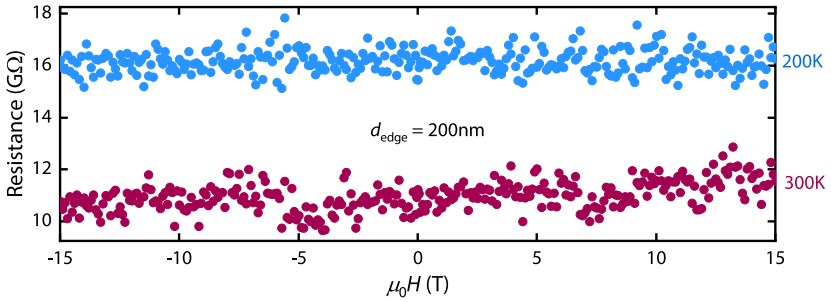

Fig. 6.8 – Resistance as a function of magnetic field (applied along the length of the Pt electrodes) measured between an injector and detector electrode with an edge-to-edge distance $d_{\mathrm{edge}} = 200\,\mathrm{nm}$ for two different temperatures $T = 300\,\mathrm{K}$ and $T = 200\,\mathrm{K}$.

To verify that the electrical magnon transport between the Pt injector and detector is mediated by magnon excitations, we have to exclude an electrical crosstalk across the supposedly insulating hematite film. For that reason, we check for the insulating nature of the hematite thin film by applying a constant voltage of $V_{\mathrm{cross}} = 5\,\mathrm{V}$ between the injector and detector electrode and measure the corresponding current I_{cross}. In Fig. 6.8, the resistance is calculated as $V_{\mathrm{cross}}/I_{\mathrm{cross}}$ and is plotted as a function of the external magnetic field applied along the length of the Pt electrodes for two different temperatures. We here apply the field along the length of the Pt strips to mimic the measurement configuration implemented for the case of finite magnon transport between injector and detector, see Ch. 6.3.1. The measured device exhibits an edge-to-edge distance of $d_{\mathrm{edge}} = 200\,\mathrm{nm}$. As evident from the data, we observe a highly insulating resistance with a minimum value of $\sim 10\,\mathrm{G\Omega}$ at the highest measured temperature of $T = 300\,\mathrm{K}$. As expected, the resistance even increases to $\sim 16\,\mathrm{G\Omega}$ when lowering the temperature to $T = 200\,\mathrm{K}$. Due to the good insulating behaviour of our hematite, we can exclude any spurious contribution to the electrical magnon transport signal observed in Ch. 6.3.1, as e.g. an antiferromagnetic anisotropic magnetoresistance from the hematite itself.

6.3.3 Current-Voltage Characteristics

We further verify the expected linearity of the electrical magnon transport signals as a function of the injector current I_{inj}. For this purpose, we apply a field corresponding to the compensation field $\mu_0 H_{\mathrm{c}}$ along the length of the Pt electrodes to ensure the maximum signal. As discussed in Ch. 6.3.1, the compensation field $\mu_0 H_{\mathrm{c}}$ ensues the maximum signal response at the detector and is therefore used to study the current dependence. The measurement of the detector voltage $V_{\mathrm{det}}^{\mathrm{el}}$ as a function of the current density $J_{\mathrm{inj}} = I_{\mathrm{inj}}/(t_{\mathrm{Pt}} w_{\mathrm{inj}})$ in the injector is shown in Fig. 6.9**a** for two different injector-detector distances d at a temperature $T = 200\,\mathrm{K}$. The same measurement is repeated at a temperature $T = 300\,\mathrm{K}$ and shown in

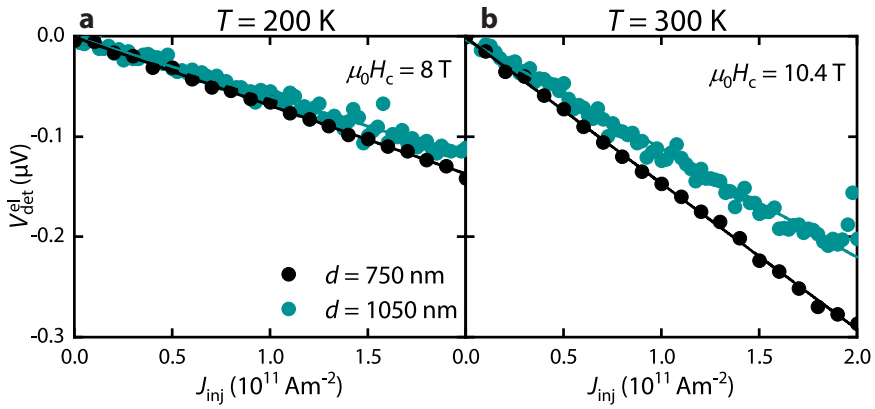

Fig. 6.9 – **a** Current-voltage characteristics measured for $T = 200\,\mathrm{K}$ at the corresponding compensation field $\mu_0 H_c = 8\,\mathrm{T}$ applied along the length of the Pt electrodes. **b** Current-voltage characteristic measured for $T = 300\,\mathrm{K}$ at the corresponding compensation field $\mu_0 H_c = 10.4\,\mathrm{T}$. Both panels show the data for two different devices with $d = 750\,\mathrm{nm}$ and $d = 1050\,\mathrm{nm}$. Solid lines are linear fits to the data.

Fig. 6.9**b**. Each device shows a clear linear behaviour as a function of the injector current, as expected from the magnon transport effect [8, 117]. The solid lines represent linear fits to the data.

6.4 Thermally Induced Magnon Transport and Transverse Spin Nernst Magnetothermopower

In the following, the thermal contribution $V_{\mathrm{det}}^{\mathrm{th}}$ of the detector signals is investigated. As a consequence of the local heating at the injector, two thermally-induced effects contributing to the detector signal $V_{\mathrm{det}}^{\mathrm{th}}$ are present. First, as depicted in Fig. 6.10**a**, the thermal injection of the antiferromagnetic magnon modes leads to a locally excited non-equilibrium magnon distribution that diffuses throughout the antiferromagnet. These magnons are excited via the current induced spin Seebeck effect at the injector (governed by the spin Seebeck coefficient S introduced in Ch. 2.5) and their transport is expected to be driven by the non-uniform magnon chemical potential distribution. Temperature gradient induced spin currents can be disregarded for the thermally excited magnon transport [36]. This thermal magnon transport (TMT) in hematite has already been previously reported in Ref. [117] and has also been investigated in other antiferromagnets [266]. Since the thermal activation of the magnon system is not spin-selective (unlike the injection of spin current via the SHE [13, 117]), both antiferromagnetic magnon modes with opposite chirality (i.e. spin polarization) are simultaneously excited (see the blue and red wiggly arrows in Fig. 6.10**a**). The transported spin is therefore given by a superposition of these two excitations. Since the frequencies of the two modes are generally non-degenerate for a canted antiferromagnetic state [32], we expect spin transport contributions from both the Néel vector $\boldsymbol{n}$ as well as

the net magnetization $\boldsymbol{m}_{\text{net}}$ in the hematite. As reported in Ref. [117] as well as supported by our data, however, the contribution from $\boldsymbol{n}$ to the TMT turns out to be negligible for the typical length scales investigated. We can justify this observation by considering that the magnon transport at hand is dominated by thermal magnons with large $\boldsymbol{k}$. As shown in Ref. [32], the energy splitting of the two magnon modes in a canted antiferromagnetic configuration becomes negligible for large $\boldsymbol{k}$-vectors, thus considerably decreasing the remaining finite magnon spin along $\boldsymbol{n}$. We can therefore assume the TMT to be exclusively proportional to the net magnetization $\boldsymbol{m}_{\text{net}}$ [117]. At the detector, the diffusing magnon accumulation is converted into a charge current via the ISHE. Due to the symmetry of the ISHE, the angle dependence of the corresponding detector signal $V_{\text{det}}^{\text{th}}$ is expected to be proportional to a $\sin(\varphi)$ function [117].

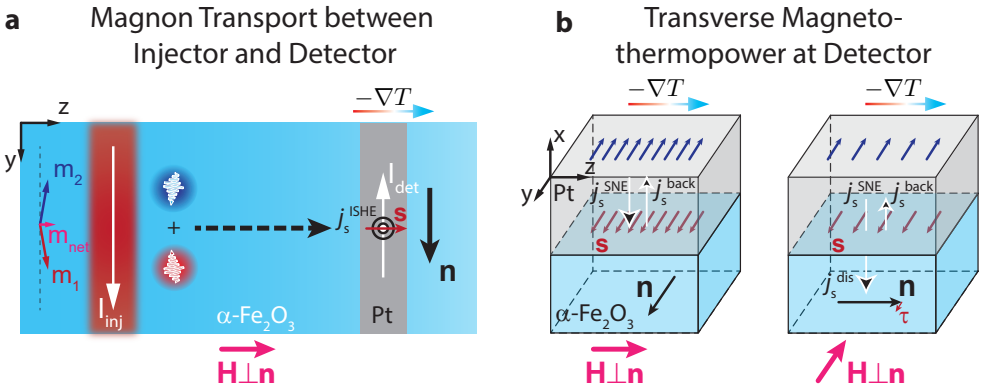

Fig. 6.10 – a Joule heating induces a thermal injection of the two antiferromagnetic magnon modes (blue and red wiggly arrows). The effective magnetic moment is given by their superposition and is dominantly proportional to the canted net magnetization $\boldsymbol{m}_{\text{net}}$. The lateral diffusion of the magnons is electrically detected at the Pt detector via the spin current density $j_{\text{s}}^{\text{ISHE}}$ injected into the Pt detector and converted to a charge current I_{det} via the inverse SHE. **b** Sketch of an α-Fe_2O_3/Pt bilayer. In open circuit conditions, the temperature gradient along z generates a spin accumulation along $\boldsymbol{s}$ at the α-Fe_2O_3/Pt interface with $\boldsymbol{s} \perp -\nabla T$. Depending on the relative orientation of $\boldsymbol{s}$ and $\boldsymbol{n}$, the spin accumulation at the interface is either unaffected by the hematite (for $\boldsymbol{s} \parallel \boldsymbol{n}$, left hand side) or partially dissipated via a spin current $j_{\text{s}}^{\text{dis}}$ in the hematite (for $\boldsymbol{s} \perp \boldsymbol{n}$, right hand side).

The second effect refers to the lateral temperature gradient that emerges across the width of the Pt detector electrode, as indicated in Fig. 6.10**a**. A schematic depiction of the temperature-gradient driven physics at the detector interfacing with the α-Fe_2O_3 is shown in Fig. 6.10**b**. Due to the spin Nernst effect (SNE) [55], the thermal gradient $-\nabla T$ along the z-direction is converted into a pure spin current density $\boldsymbol{j}_{\text{s}}^{\text{SNE}} = \hbar/(2e)\theta_{\text{SN}}\boldsymbol{j}_{\text{c}}^{\text{th}} \times \boldsymbol{s}$ (cf. Eq. (2.26)). Here, $\boldsymbol{j}_{\text{c}}^{\text{th}} = -\sigma_{\text{e}} S_{\text{e}} \nabla T$ is the temperature gradient-driven charge current along z with S_{e} the conventional Seebeck coefficient. As a consequence of the negative spin Nernst angle $\theta_{\text{SN}} < 0$ [55] as well as the negative Seebeck coefficient S_{e} in Pt [267, 268], a spin current density along the $-x$-direction with a spin polarization $\boldsymbol{s}$ oriented along the y-direction is injected into the hematite. In open circuit conditions, neither charge

nor spin currents can flow in the Pt. The temperature gradient $-\nabla T$ therefore leads to the generation of an electrochemical and spin-chemical potential (i.e. spin accumulation) counteracting the conventional Seebeck current j_c^{th} and spin Nernst current j_s^{SNE} via the emerging diffusive charge/spin currents. The spin current backflow in the Pt is indicated in the Figure as j_s^{back}. In steady state, a spin accumulation μ_s with spin polarization $\boldsymbol{s}$ along y builds up at the top and bottom interface of the Pt. Its relative orientation to the Néel vector $\boldsymbol{n}$ then determines the relevant boundary condition: for $\boldsymbol{n} \parallel \boldsymbol{s}$ (left panel in Fig. 6.10**b**), the spin accumulation cannot dissipate in the hematite. If $\boldsymbol{s} \nparallel \boldsymbol{n}$ (right panel in Fig. 6.10**b**), a spin transfer torque $\boldsymbol{\tau}$ can be exerted on $\boldsymbol{n}$ [269], leading to a finite spin current j_s^{dis} dissipating in the hematite and a reduction of the spin accumulation μ_s in the Pt layer. While j_s^{dis} decays within the antiferromagnetic hematite, the counterflowing spin current j_s^{back} is converted back to a charge current via the inverse SHE. In open circuit conditions, an electric field across the x-y-plane of the Pt arises, the direction of which depends upon the relative orientation of $\boldsymbol{n}$ to $\boldsymbol{s}$[47]. In our experimental configuration, we measure the transverse contribution of this effect, which we identify as the transverse spin Nernst magnetothermopower (TSNM). Based on the change of the boundary condition of the SNE-induced spin accumulation at the interface with the orientation of the applied magnetic field, its conversion to a voltage signal is expected to follow an angle dependence proportional to $\sin(2\varphi)$. For $\boldsymbol{n} \parallel \boldsymbol{s}$ (i.e. $\varphi = \pi/2, 3\pi/2$), the SNE-induced spin accumulation is unaffected by the magnetic order $\boldsymbol{n}$ in the hematite. Since we measure the transverse voltage drop along the length (y-direction) of the Pt detector, the maximum voltage signal is expected for $\varphi = \pi/2 \pm \pi/4, 3\pi/2 \pm \pi/4$ (the maxima/minima of the TSNM are therefore shifted by $\pi/4 = 45°$ compared to a longitudinal measurement [55]). Hence, we expect $V_{det}^{th} \propto \sin(\varphi)\cos(\varphi) \propto \sin(2\varphi)$.

In order to represent the superposition of both the TMT and TSNM, the total angle dependence of the thermal detector signal V_{det}^{th} is expressed as

$$V_{det}^{th}(\varphi) = V_0 + \Delta V_{det}^{TMT} \sin\varphi + \Delta V_{det}^{TSNM} \sin 2\varphi, \tag{6.30}$$

where V_0 is a constant offset voltage due to conventional thermal voltages independent of φ, V_{det}^{TMT} is the amplitude of the TMT in the hematite and V_{det}^{TSNM} represents the amplitude of the TSNM. Typical angle dependent measurements of V_{det}^{th} at the detector are shown in Fig. 6.11**a** for various external magnetic field strengths. Here, the solid lines are fits to Eq. (6.30). Clearly, we find an excellent agreement of the fit with the experimental data, validating the presence of the thermal effects discussed in Fig. 6.10**a** and **b**. In order to separate the TSNM from

[47] The spin polarization $\boldsymbol{s}$ of the counteracting spin current j_s^{back} is determined by the direction of the Néel vector $\boldsymbol{n}$. This can be viewed as a reflection of the incident spin $\boldsymbol{s}$ of the SNE-induced spin current when interacting with $\boldsymbol{n}$: the transmitted part is given by the transverse component of $\boldsymbol{s}$ with respect to the quantization axis along $\boldsymbol{n}$ (thereby exerting a torque on $\boldsymbol{n}$), while the reflected part is given by the parallel component.

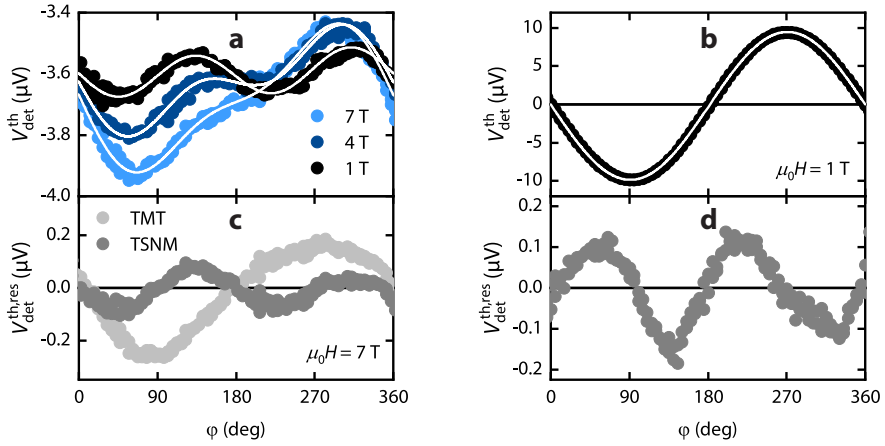

Fig. 6.11 – **a** Detector signal $V_{\mathrm{det}}^{\mathrm{th}}$ as a function of magnetic field orientation φ for different external magnetic field strengths, where a superposition of both the TMT and TSNM signal is observed. The data is shown for a device with heater-detector distance $d = 750\,\mathrm{nm}$ at $T = 200\,\mathrm{K}$. Solid lines are fits to Eq. (6.30). **b** Detector signal $V_{\mathrm{det}}^{\mathrm{th}}$ measured on a similar device fabricated on the ferrimagnetic insulator YIG (with thickness $t_{\mathrm{YIG}} = 2\,\mu\mathrm{m}$) for $d = 2.1\,\mu\mathrm{m}$ at $T = 220\,\mathrm{K}$ and $\mu_0 H = 1\,\mathrm{T}$. The white solid line is a fit to a $\sin(\varphi)$-type function. **c** Residual signals $V_{\mathrm{det}}^{\mathrm{th,res}}$ extracted from panel **a** using the different angular symmetries of the TMT (light gray points) and TSNM (dark gray points) for $\mu_0 H = 7\,\mathrm{T}$. **d** Residual signal $V_{\mathrm{det}}^{\mathrm{th,res}}$ of the fit to the data shown in panel **b**, exhibiting the TSNM in YIG. A 90° phase shift is observed compared to the TSNM in hematite.

TMT, we extract the 180°-symmetric and 360°-symmetric signals stemming from the TSNM and TMT, respectively, by separately fitting the total signals shown in Fig. 6.11**a** by a $\sin(\varphi)$-type and $\sin(2\varphi)$-type function. We then plot the residuals of the fits in Fig. 6.11**c**, which we denote as $V_{\mathrm{det}}^{\mathrm{th,res}}$ (here shown for $\mu_0 H = 7\,\mathrm{T}$). As expected, the 360°-symmetric modulation due to the TMT (light gray points) shows a minimum (maximum) signal for $\varphi = 90°$ ($\varphi = 270°$), where the net magnetization points perpendicular to the Pt detector. The 180°-symmetric signal due to the TSNM (dark gray points) shows the expected $\sin(2\varphi)$ modulation. In order to experimentally demonstrate whether the TSNM is determined by the interaction of the spin polarization $\boldsymbol{s}$ with the Néel vector $\boldsymbol{n}$ or the net magnetization $\boldsymbol{m}_{\mathrm{net}}$, we compare the results presented for hematite (Figs. 6.11**a** and **c**) with a reference sample using the ferrimagnetic insulator yttrium iron garnet (YIG). Similar Pt nanostrips have been prepared on the YIG film. As shown in Fig. 6.11**b**, the thermal detector signal measured on the YIG sample shows a clear $\sin(\varphi)$-type modulation due to the TMT in YIG [8], which is fitted to the data as the white solid line. In Fig. 6.11**d**, the residual of this fit is shown, demonstrating a clear $\sin(2\varphi)$ signature indicating the TSNM in YIG/Pt [55]. Most interestingly, however, we observe a 90° phase shift of the TSNM signal in YIG as compared to the TSNM signal measured in the hematite shown in Fig. 6.11**c**. Since we have $\boldsymbol{H} \perp \boldsymbol{n}$ in hematite and $\boldsymbol{H} \parallel \boldsymbol{m}_{\mathrm{YIG}}$ in YIG (with $\boldsymbol{m}_{\mathrm{YIG}}$ the YIG magnetization vector), we infer that the TSNM in the antiferromagnetic insulator hematite is

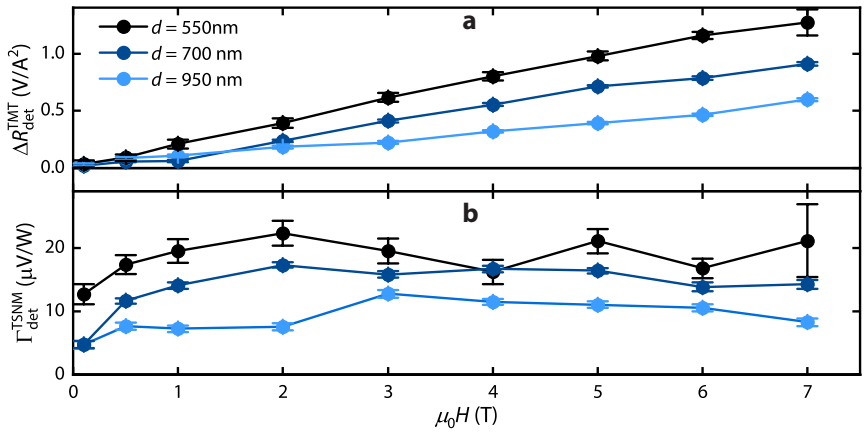

Fig. 6.12 – Signal amplitudes of the TMT **a** and TSNE **b** extracted from the fits to the experimental data shown in Fig. 6.11**a** via Eq. (6.30). **a** TMT signal amplitude $\Delta R_{\mathrm{det}}^{\mathrm{TMT}}$ plotted as a function of the external magnetic field for different distances d. Each of the devices shows a linearly increasing TMT for increasing field strength. **b** TSNM signal $\Gamma_{\mathrm{det}}^{\mathrm{TSNE}}$ as a function magnetic field, showing an increase of the signal at low field strength and a saturation above $\sim 2\,\mathrm{T}$.

indeed determined by the Néel order $\boldsymbol{n}$ rather than the net magnetization $\boldsymbol{m}_{\mathrm{net}}$. This is consistent with the SMR effect in antiferromagnetic insulators [270, 271]. The comparison between the thermal detector signals in YIG/Pt and α-Fe_2O_3/Pt highlights a further crucial difference: due to the much larger net magnetization $\boldsymbol{m}_{\mathrm{YIG}}$ as compared to the field-induced net magnetization $\boldsymbol{m}_{\mathrm{net}}$ of hematite, the TMT is blatantly dominant in YIG (cf. Fig. 6.11**b**). The Néel vector and the small net magnetization of hematite due to canted sublattice magnetizations, on the contrary, allow for an unambiguous, easily accessible differentiation of the TSNM and TMT, respectively.

In the next step, we extract the signal amplitudes $\Delta V_{\mathrm{det}}^{\mathrm{TMT}}$ and $\Delta V_{\mathrm{det}}^{\mathrm{TSNM}}$ from the fits to the angle dependent signals shown in Fig. 6.11**a**. In order to compare the TMT signals between different heater geometries and heater currents I_{inj}, we define the normalized signal amplitudes $\Delta R_{\mathrm{det}}^{\mathrm{TMT}} = (\Delta V_{\mathrm{det}}^{\mathrm{TMT}} / I_{\mathrm{inj}}^2) \cdot (A_{\mathrm{inj}} / A_{\mathrm{det}})$, where A_{inj} and A_{det} account for the injector and detector areas interfacing the hematite film [11]. Regarding the TSNM signals, we normalize the voltage signals to the heater power $P_{\mathrm{heat}} = R_{\mathrm{inj}} I_{\mathrm{inj}}^2$ and define $\Gamma_{\mathrm{det}}^{\mathrm{TSNM}} = \Delta V_{\mathrm{det}}^{\mathrm{TSNM}} / P_{\mathrm{heat}}$ with R_{inj} the resistance of the injector. The evolution of these amplitudes with the external magnetic field for different distances d is shown in Fig. 6.12**a** and **b** for $\Delta R_{\mathrm{det}}^{\mathrm{TMT}}$ and $\Gamma_{\mathrm{det}}^{\mathrm{TSNM}}$, respectively. The TMT signal linearly increases with temperature as the external field $\mu_0 H$ increases. This is consistent with the picture given in Fig. 6.10**a**, since the magnitude m_{net} of the net magnetization is expected to linearly increase as a function of $\mu_0 H$ as $m_{\mathrm{net}} \sim \chi_\perp H$ (with $\chi_\perp$ the magnetic susceptibility

of hematite in the easy plane phase)[48]. The field dependence of the TSNM signal in Fig. 6.12**b** indicates an increase for small fields and a saturation above $\sim 2\,\mathrm{T}$. The observed saturation of the signal is expected for the TSNM since it follows the SMR amplitude in $Pt/\alpha Fe_2O_3$ [270–272], which is also determined by the relative orientation of $\boldsymbol{n}$ and $\boldsymbol{s}$. Since the hematite shows a complex phase separation into three domain families below the monodomanization field H_{MD} (cf. Ch.3.1.2), we expect the full amplitude of the TSNM contribution $\Gamma_{\mathrm{det}}^{\mathrm{TSNM}}$ only above $H_{\mathrm{MD}} \approx 3\,\mathrm{T}$, which corresponds to the value extracted from SMR measurements [271]. This agrees reasonably well with the saturation behaviour of the TSNM observed in Fig. 6.12**b**[49]. Both the detector signals corresponding to the TMT and TSNM also show a clear decrease of the signal with increasing distance d from the injector/heater. For the TMT, this is due to the diffusive decay of the thermally excited magnon distribution over distance [8, 117]. The decreasing TSNM, on the other hand, stems from the decrease of the temperature gradient across the detector width, which is expected to be lower when increasing the distance to the heater source.

Finally, we study the temperature dependence of the TMT and TSNM signals $\Delta R_{\mathrm{det}}^{\mathrm{TMT}}$ and $\Gamma_{\mathrm{det}}^{\mathrm{TSNM}}$, respectively. Figure 6.13**a** shows the temperature dependent TMT signals for $\mu_0 H = 7\,\mathrm{T}$. A significant increase is evident at temperatures below 50 K. Above 50 K, an increase up to $\sim$ 150 K with a subsequent slight decrease up to 300 K is observed, hence showing a peak-like dependence. Besides the rather strong enhancement at low T, the temperature dependence above 50 K resembles the one reported for the local SSE in YIG [273]. Here, the observed peak-like T-dependence is rationalized via the magnon diffusion length and the thermal occupation of magnons, both of which have monotonous, but counteracting temperature dependencies according to Ref. [273]. Consequently, a peak-like T-dependence can be argued. The rather inconspicuous peak observed in our data can also be explained on the basis of these arguments: since our film is only 15 nm thin, the magnon diffusion length has a minor impact across the thickness of the film since $\lambda_{\mathrm{s}} > t$ always holds. This leads to the fact that the temperature dependence is dominated by the thermal magnon occupation [273], effectively making the total T-dependence flatter. We note, that the comparison of our TMT data to the local SSE measurements in YIG [273] is only reasonable to a limited extent, since the lateral diffusion of magnons also plays a significant role in our

[48] It should be pointed out that the field dependence of the thermally induced magnon transport in antiferromagnets is not straightforward to derive in general. In particular, for an accurate description one must take into account the field dependence of the magnon dispersion relation, which in turn is determined by the magnetic properties of the antiferromagnet [266].

[49] Note that there is a significant difference between the monodomainization fields determined from SQUID magnetometry ($\mu_0 H_{\mathrm{MD}} \approx 700\,\mathrm{mT}$, see Ch. 3.1.2) and from SMR measurements ($\mu_0 H_{\mathrm{MD}} \approx 3\,\mathrm{T}$ [271]). This discrepancy most likely stems from the fact that the SMR is dominantly sensitive to the surface magnetic moments of the hematite rather than the bulk magnetic properties sensed by the SQUID magnetometer. Therefore, surface pinning effects due to rough interfaces can significantly enhance the saturation field observed in the magnetotransport measurements as compared to the SQUID measurements.

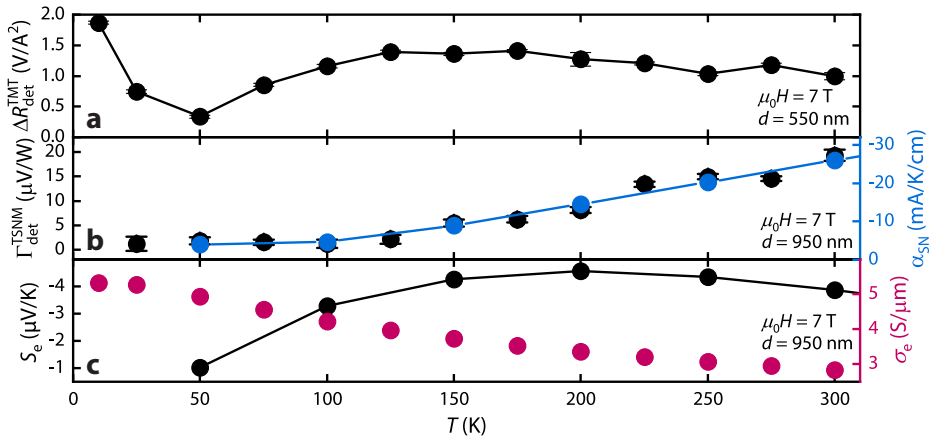

Fig. 6.13 – Normalized TMT and TSNM signal amplitudes ΔR_{det}^{TMT} (**a**) and Γ_{det}^{TSNM} (**b**) extracted from the fits to Eq. (6.30) plotted as a function of temperature for $\mu_0 H = 7$ T. The $\Delta R_{det}^{TMT}(T)$ data are shown for a device with $d = 550$ nm in panel **a**. A significant increase for temperatures below 50 K is observed. For $T > 50$ K, the signal increases up to ~ 150 K and subsequently decreases up to 300 K. The Γ_{det}^{TMT}(T) signals are shown for a device with $d = 950$ nm in panel **b**. Blue data points correspond to the theoretical calculation of the spin Nernst conductivity α_{SN}. A monotonous decrease of Γ_{det}^{TMT} is observed for decreasing temperature and a complete suppression is observed below ~ 100 K, in perfect agreement with the theoretically predicted α_{SN}. **c** Theoretical calculation of the temperature dependence of the conventional (longitudinal) Seebeck coefficient S_e of Pt (black points) and experimentally determined conductivity σ_e of the Pt injector for the $d = 950$ nm device (purple points).

device structure, rather than only the thickness of the magnetic film. A detailed investigation of the temperature dependence of the TMT signals is, however, not provided here. The low temperature enhancement below 50 K is a feature that is resilient also in local current-driven SSE measurements in YIG/Pt bilayers [274]. While the origin of this feature is not clear yet, it is unique to the current-driven SSE and might be related to the resistance behaviour of Pt at low temperatures.

The temperature dependence of the TSNM signal amplitudes is shown in Fig. 6.13**b**. In the investigated temperature range from 300 K down to 25 K, we observe a monotonous decrease of the signal with decreasing temperature. For $T \lesssim 100$ K, the signal completely vanishes below the noise limit. Due to the conversion of the thermally driven charge current density j_c^{th} into the spin current density j_s^{SNE} via the SNE (Fig. 6.10**a**), and the back-conversion of the reflected part of the spin current into the experimentally measured charge current/voltage via the SHE, both the spin Nernst angle θ_{SN} as well as the spin Hall angle θ_{SH} are involved in the process. The relevant scaling parameters to consider for the TSNM are therefore $\Delta V_{det}^{TSNM} \propto S_e g_r^{\uparrow\downarrow} l_s \theta_{SH} \theta_{SN}$ [55], where S_e is the longitudinal Seebeck coefficient of Pt, $g_r^{\uparrow\downarrow}$ the real part of the spin mixing interface conductance, l_s the spin diffusion length of Pt and θ_{SN} as well as θ_{SH} the spin Nernst and spin Hall angle of Pt, respectively. The parameters $g_r^{\uparrow\downarrow}$, l_s as well as θ_{SH} can be reasonably treated as only weakly temperature dependent [275, 276]. We are

thus left with the temperature dependence of both S_e and θ_{SN} of Pt. Based on the theoretical description of the SNE in Pt in Ref. [55], we plot the temperature dependent spin Nernst conductivity $\alpha_{SN} = -\theta_{SN}\sigma_e S_e$ (with σ_e the longitudinal electrical conductivity of Pt) together with our experimental data in Fig. 6.13**b** (blue data points). Evidently, the agreement between theory and experiment is excellent, strongly corroborating a decrease of α_{SN} with decreasing temperature. In order to determine whether S_e or θ_{SN} causes the vanishing TSNM signal, we plot the theoretically calculated S_e as a function of temperature in Fig. 6.13**c** (black points with line). Obviously, it shows a finite magnitude even for $T \leq 100\,\mathrm{K}$, excluding it as the source of the vanishing TSNM signal. This is also supported by experimental quantifications of S_e in bulk Pt [267] as well as thin films [268][50]. Considering that $\theta_{SN} = S^s_{trans}/S_e$ (with S^s_{trans} the transverse Seebeck coefficient [59]), it follows that S^s_{trans} must approach zero at low temperatures, in accordance with theory [59–61]. The low temperature suppression of S^s_{trans} is based on the dominance of extrinsic contributions (i.e. impurity scattering [46, 48]) to the spin Nernst conductivity in Pt. Indeed, the Pt conductivity σ_e in our sample changes from 300 K to 10 K by about $\sim 45\,\%$ (see Fig. 6.13**c**, purple points), hence exhibiting a finite, non-diverging conductivity at low temperatures corroborating the dominance of impurity scattering. The theoretical description of the spin Nernst effect in Pt [55] suggests a decrease of θ_{SN} between 300 K and 200 K by a factor of ~ 2, which is supported by our TSNM data shown in Fig. 6.13. Taking all these considerations together, the vanishing TSNM for $T \lesssim 100\,\mathrm{K}$ can be interpreted as a decrease of θ_{SN} towards zero[51], an observation which has eluded an experimental observation thus far.

In conclusion, we have investigated the TMT and TSNM in a α-Fe_2O_3/Pt device. For the TMT, we found that the signal is proportional to the field-induced net magnetization of the canted hematite sublattices. Its temperature dependence further revealed a strong resemblence with previous reports of the local SSE in YIG/Pt structures [273]. The excellent agreement of the spin Nernst theory calculations with our TSNM data suggests a vanishing spin Nernst angle of Pt at low temperatures and the dominance of extrinsic contributions to the SNE. We demonstrate that the spin Nernst effect is sensitive to the direction of the Néel vector of the antiferromagnet, thus representing a suitable platform to discern the TSNM and TMT. Our results shed light on the interaction of purely thermally

[50] Although the Seebeck coefficient for bulk Pt exhibits a sign change at $T \approx 170\,\mathrm{K}$ [267], measurements of Pt thin films in the $\sim 100\,\mathrm{nm}$ thickness range show a clear increase of the zero crossing temperature, inferring that we have no zero crossing of the Seebeck coefficient for our 5 nm thick Pt electrodes. This claim is supported by the temperature dependence of our TSNM signals, which do not show any indication of a sign change.

[51] We note that a quantitative evaluation of the temperature dependence of θ_{SN} is tedious, as it requires the quantification of the temperature gradient present at the detector electrode (which by itself is a temperature dependent quantity) as well as a rigorous experimental evaluation of the temperature dependent Seebeck coefficient S_e of thin film Pt.

driven spin currents with antiferromagnets and therefore provide key insights into the physics of pure spin current based magnetothermal effects in AFI/Pt bilayers.

6.5 Summary and Conclusion

Various spin transport related effects in the antiferromagnetic insulator hematite (α-Fe_2O_3) have been investigated in this Chapter. Upon injecting magnon spin via both the SHE as well as by thermal spin Seebeck torque in a Pt electrode attached to the antiferromagnet, the emerging magnon spin chemical potential was measured at a second Pt detector electrode for electrically and thermally induced effects separately.

Inspired by the Bloch sphere description of a spin-1/2 two-level system, we started to introduce the concept of the antiferromagnetic pseudospin. Here, antiferromagnetic magnon modes are described by two antiparallel vectors on a Bloch sphere. Within this pseudospin framework, the magnon eigenmodes of an antiferromagnet are determined by the pseudofield, which, in turn, is given by the energy contributions of the magnetic interactions at play. Most importantly, each interaction that breaks the rotational symmetry of the antiferromagnetic Néel order couples the natural (circularly polarized) spin-up and -down eigenmodes, hence allowing for an interconversion between oppositely polarized spin states. An externally excited pseudospin density generally precesses around the direction of the pseudofield, thereby transmuting between circularly and linearly polarized magnon modes.

In our electrically induced magnon transport measurements, we could experimentally demonstrate the precession of an externally induced antiferromagnetic pseudospin density in hematite. Due to the easy-plane anisotropy and DMI-induced canting of the sublattice magnetizations, the rotational symmetry about the Néel order is broken and the spin-up and -down magnon modes are coherently coupled, leading to the emergence of a precessional motion of the excited pseudospin density. The canting of the sublattices can be tuned by the application of an external magnetic field, which therefore alters the coupling of the modes and enables an easily accessible handle on the pseudospin precession frequency. The emerging field dependence of the pseudospin chemical potential (measured by the Pt detector) exhibits an oscillation between positive and negative spin signals and can be quantitatively explained by the 1D-solution of the pseudospin diffusion equation that incorporates its precessional motion. This observation and its compelling agreement with the antiferromagnetic pseudospin theory manifests the first realization of pseudospin dynamics and the antiferromagnetic magnon Hanle effect. The magnon Hanle data allows for the extraction of the magnon spin diffusion length, which was estimated to be around 0.5 µm at room temperature.

The thermally induced contribution to the detector signal revealed two distinct effects. The first contribution referred to the thermally induced magnon transport

effect, which was found to be proportional to the net magnetization $\boldsymbol{m}_{\mathrm{net}}$ of the canted hematite sublattice magnetizations rather than its Néel vector. The magnetic field dependence fits well to the expected linear response of $\boldsymbol{m}_{\mathrm{net}}$ to the external field. Furthermore, its temperature dependence could be understood on the basis of previous reports of the SSE in YIG/Pt [273]. We identified a second contribution to the thermal signal as the transverse spin Nernst magnetothermopower, which arises due to the generation of a lateral temperature gradient across the width of the Pt detector electrode. This represents the first observation of the interaction of a spin Nernst induced spin current with an antiferromagnetic Néel order, revealing that the latter represents the relevant boundary condition for the spin current. This feature, together with the small canted net magnetization of hematite allows for an unambiguous, easily accessible differentiation of the spin Nernst- and magnon transport-related effects, the latter of which is proportional to the net magnetization. Most importantly, the temperature dependence of the effect demonstrates a vanishing spin Nernst angle θ_{SN} with decreasing temperature, in perfect agreement with the theoretical calculation of the spin Nernst conductivity α_{SN} [55, 60, 61].

Outlook

7

The novel concepts for the control and manipulation of magnon transport presented in the previous Chapters have provoked new experiments and ideas for future work. Some of these ideas and preliminary experiments are presented within the scope of this Chapter, representing an outlook towards the next steps in this subject.

7.1 Thermodynamic Interpretation of the Spin Current Induced Critical Magnon Conductivity Modulation

In the following Section, we outline an interesting idea for an alternative approach towards the interpretation of the second harmonic magnon transport signal modulations $\Delta V_{\mathrm{det}}^{2\omega}(I_{\mathrm{mod}})$ discussed in Ch. 5.4.2. To this end, we recall the driving forces for the magnon spin and heat currents in a magnetic insulator (cf. Eq. (2.54))

$$\boldsymbol{j}_{\mathrm{m}} = -\sigma_{\mathrm{m}} \nabla \mu_{\mathrm{m}} - \hbar \frac{L}{T_{\mathrm{p}}} \nabla T_{\mathrm{m}}, \tag{7.1}$$

$$\boldsymbol{j}_{\mathrm{h}} = -L \nabla \mu_{\mathrm{m}} - \kappa_{\mathrm{m}} \nabla T_{\mathrm{m}}, \tag{7.2}$$

where L denotes the bulk spin Seebeck coefficient and κ_{m} the magnon heat conductivity [127, 215, 216], both of which have been rigorously derived in Ch. 2.7.2 within linear response. We here consider a small but finite difference between the phonon (base) temperature T_{p} and the magnon temperature T_{m}. In principle, both magnon spin and magnon heat currents are capable of inducing an inverse SHE signal at the detector interface. While the magnon spin currents at the interface are converted via the spin conductance g, a finite heat current generates a temperature difference δT between the magnon and electron system at the detector interface, which permits an interfacial spin current via the spin Seebeck coefficient S (cf. Ch. 2.5). The magnon chemical potential μ_{m} as well as the magnon temperature T_{m} are affected by the injector current in a linear and quadratic fashion according to

$$\mu_{\mathrm{m}} = \mu_{\mathrm{m}}^{\mathrm{SHE}}[I_{\mathrm{inj}}] + \mu_{\mathrm{m}}^{\mathrm{SSE}}[I_{\mathrm{inj}}^2], \tag{7.3}$$

$$T_{\mathrm{m}} = T_{\mathrm{p}}[I_{\mathrm{inj}}^2] + \delta T_{\mathrm{J}}[I_{\mathrm{inj}}^2] + \delta T_{\mathrm{SPE}}[I_{\mathrm{inj}}], \tag{7.4}$$

where μ_m^{SHE} and μ_m^{SSE} are the magnon chemical potentials induced via the SHE and SSE, respectively (see also Ch. 5.1.2), T_p is the phonon base temperature, δT_J is the Joule heating-induced temperature change of the magnon system with respect to T_p and δT_{SPE} is the temperature change induced by the spin Peltier effect (i.e. a temperature change caused by the SHE-induced spin current)[52] [200]. Each of these quantities is either a linear or quadratic function of the applied injector current I_{inj} as indicated in the square brackets. In the experiment, we can discern effects proportional to even and odd powers in the low frequency AC injector current I_{inj} whilst measuring the first and second harmonic voltage signal at the detector. By substituting Eqs. (7.3) and (7.4) into Eqs. (7.1) and (7.2) and further separate contributions linear and quadratic in I_{inj}, the first harmonic magnon spin and heat currents are

$$j_m^{1\omega} = -\sigma_m \nabla \mu_m^{SHE} - \hbar \frac{L}{T_p} \nabla \delta T_{SPE}, \tag{7.5}$$

$$j_h^{1\omega} = -L \nabla \mu_m^{SHE} - \kappa_m \nabla \delta T_{SPE}, \tag{7.6}$$

while the second harmonic currents become

$$j_m^{2\omega} = -\sigma_m \nabla \mu_m^{SSE} - \hbar \frac{L}{T_p} \nabla (T_p + \delta T_J), \tag{7.7}$$

$$j_h^{2\omega} = -L \nabla \mu_m^{SSE} - \kappa_m \nabla (T_p + \delta T_J). \tag{7.8}$$

In this very general description, we expect both first and second harmonic voltage signals to be proportional to all of the transport coefficients σ_m, L and κ_m. Considering our typical experimental setting and appropriate length scales, however, we can simplify the expected signal contributions drastically. First of all, the magnon-phonon relaxation length was shown to be extremely small, viz. in the nanometer regime [36, 125, 200]. For the typical length scales of a few μm considered in our transport devices, the magnon temperature T_m therefore quickly equilibrates with the phonon temperature T_p. Thus, $T_m = T_p$ represents a reasonable assumption and according to Eq. (7.4) leads to $\delta T_J = \delta T_{SPE} = 0$. Furthermore, while the heat currents j_h can potentially be a source of a spin Seebeck-induced detector signal due to the temperature profile as mentioned above, it was shown that for the typical length scales considered in our magnon transport devices such effects are negligible [124][53]. It is thus safe to assume no contribution from the magnon

[52] The individual terms in Eqs. (7.3) and (7.4) can be derived from the magnon spin and heat diffusion equations by applying proper boundary conditions at the Pt/YIG interface. In particular, the SHE-induced spin current and Joule heating induced heat current have to be taken into account.

[53] Considering our lateral transport structure, we expect the AC temperature gradient from the injector current to be dominantly transversely oriented to the detector interface, especially for large injector-detector distances in the μm-regime. This configuration is reminiscent of the transverse SSE experiments supposedly observed and explained in Refs. [101, 277, 278]. However, its existence has long been controversial. Indeed, careful experiments have shown a complete absence of the transverse SSE [279] and we can thus safely neglect any contributions from it.

heat currents $\boldsymbol{j}_\mathrm{h}$. With these simplifications and disregarding heat currents, the equations above reduce to

$$\boldsymbol{j}_\mathrm{m}^{1\omega} = -\sigma_\mathrm{m} \nabla \mu_\mathrm{m}^\mathrm{SHE}, \tag{7.9}$$

$$\boldsymbol{j}_\mathrm{m}^{2\omega} = -\sigma_\mathrm{m} \nabla \mu_\mathrm{m}^\mathrm{SSE} - \hbar \frac{L}{T_\mathrm{p}} \nabla T_\mathrm{p}. \tag{7.10}$$

Finally, we expect

$$\Delta V_\mathrm{det}^{1\omega} \propto \sigma_\mathrm{m}, \tag{7.11}$$

$$\Delta V_\mathrm{det}^{2\omega} \propto \sigma_\mathrm{m} + L \tag{7.12}$$

for the first and second harmonic voltage signals. As suspected from experiments [36], the first harmonic signal can reasonably be assumed as a direct measure of the magnon conductivity σ_m [12, 172, 280]. The second harmonic signal $\Delta V_\mathrm{det}^{2\omega}$, on the other hand, must be considered as a superposition of σ_m and L. Although a contribution from L has been disregarded in our analysis of the thermal signals in Ch. 5.4, the modulator current dependent data $\Delta V_\mathrm{det}^{2\omega}(I_\mathrm{mod})$ should be investigated with this peculiarity in mind, especially since the thermally-induced magnon transport signals were indeed shown to have a significant contribution from the magnon current driven by the temperature gradient and should therefore scale with the bulk spin Seebeck coefficient L [124]. It has been further shown both theoretically [109, 127, 215] and also experimentally [124, 216] that the bulk spin Seebeck coefficient L exhibits a strong correlation to the magnon heat conductivity κ_m. Next to σ_m, the second harmonic signal $\Delta V_\mathrm{det}^{2\omega}(I_\mathrm{mod})$ might therefore also be considered as a measure of the magnon heat conductivity κ_m. This is also strongly corroborated by the microscopic expressions for L and κ_m derived in Ch. 2.7.2, viz. Eqs. (2.56) and (2.57). Disregarding numerical prefactors, we here find $\kappa_\mathrm{m} = k_\mathrm{B} L$, meaning that they only differ by the Boltzmann constant. It should be pointed out that for the sake of a more accurate modelling, one might keep the contribution from δT_J, i.e. the temperature change of the the magnon system with respect to the phonons. This is because the difference between T_m and T_p is expected to be considerably larger right at the interface to the detector [125] and might therefore not be disregarded in general. In any case, independent of taking into account δT_J, the second harmonic signal is still expected to be given by a superposition of σ_m and $\kappa_\mathrm{m} = k_\mathrm{B} L$.

We now analyze our data with the above considerations in mind and explicitly concentrate on the behaviour of the signals around the critical regime. To this end, we plot the second harmonic signals $\Delta V_\mathrm{det}^{2\omega}(I_\mathrm{mod})$ around the critical current in Fig. 7.1**a** and **b** for positive and negative magnetic fields, respectively. We further restrict the analysis to the low field regime for which $\mu_0 H \leq 50\,\mathrm{mT}$. For each of the curves, we observe a pronounced peak feature at I_crit. This peak is resilient for

magnetic fields $|\mu_0 H| \leq 50\,\mathrm{mT}$ but vanishes for larger field values[54]. The shape of this peak feature is reminiscent of the so-called 'lambda-point' in the context of the physics of superfluids. This 'λ'-shaped curve is usually obtained from measuring the specific heat of a Bose-gas (e.g. of ^{4}He [281]) undergoing a second-order superfluid phase transition, i.e. BEC transition. Considering this strong similarity, we now argue exclusively in terms of the magnon heat conductivity κ_m and exclude the modulation of magnon conductivity σ_m for now. As argued above, this particularly means that we now consider the transport of a magnon spin current driven by the temperature gradient ∇T_p rather than by the gradient $\nabla \mu_\mathrm{m}$. Consequently, the second harmonic voltage amplitudes shall be ultimately viewed as a measure of the magnon heat capacity C_m. This specifically assumes a linear relation according to $\kappa_\mathrm{m} \propto C_\mathrm{m}$, hence $\Delta V_\mathrm{det}^{2\omega}(I_\mathrm{mod}) \propto C_\mathrm{m}$. In the superfluid phase transition of a conventional Bose-gas, the specific heat is discontinuous (recall the 'λ'-shape disussed above) and therefore characterizes it as a second-order phase transition. As observed, the thermally driven magnon transport signal $\Delta V_\mathrm{det}^{2\omega}(I_\mathrm{mod})$ in our experiment is thus expected to strongly increase at the critical point. This raises the question whether the 'λ' signature in our data can be considered as a validation for a magnon BEC transition featuring spin superfluidity as discussed in Ch. 5.3.3 and beyond.

To tackle this question, we return to Fig. 7.1**a** and **b**. In general, the theoretical framework of phase transitions provides a mathematical tool for their characterization via so-called critical exponents [282][55]. For this purpose, we introduce the reduced current $\iota = 1 - I_\mathrm{mod}/I_\mathrm{crit}$ (in analogy to the reduced temperature used for temperature driven phase transitions). The heat capacity (at constant pressure) C_p near a superfluid/BEC phase transition is then expected to behave according to

$$C_\mathrm{p} \sim \begin{cases} D\iota^{-\alpha} & \iota \geq 0 \\ D'(-\iota)^{-\alpha'} & \iota \leq 0 \end{cases}, \tag{7.13}$$

where D and D' are proportionality factors used for fitting. α and α' are the respective critical exponents defined for the disordered phase ($I_\mathrm{mod} < I_\mathrm{crit}$, outside of BEC state) and ordered phase ($I_\mathrm{mod} > I_\mathrm{crit}$, within the BEC state). Equation (7.13) is fitted to the critical regime of the $\Delta V_\mathrm{det}^{2\omega}$ curves, i.e. the 'λ'-shaped curves in Fig. 7.1**a** and **b** (grey lines). Decent agreement is observed for the fits to the experimental data. This indicates the validity of the proposed thermodynamic analysis. We recall that this analysis is only valid under the assumption that the

[54] We neglect the data for $\mu_0 H = -50\,\mathrm{mT}$ and $\mu_0 H = 10\,\mathrm{mT}$ in Fig. 7.1**a** and **b**, respectively, since no characterictic peak in the critical regime could be observed. The reason for the asymmetry between the negative and positive fields is most likely due to trapped flux in our superconducting magnet generating the field. This introduces a finite offset in the field values which is not taken into account in the data.

[55] Strictly speaking, the concept of critical exponents only applies for equilibrium systems. Since we consider our system in steady state and can mostly treat it as a quasi-equilibrium [187], we can justify the analysis in spite of this intricacy.

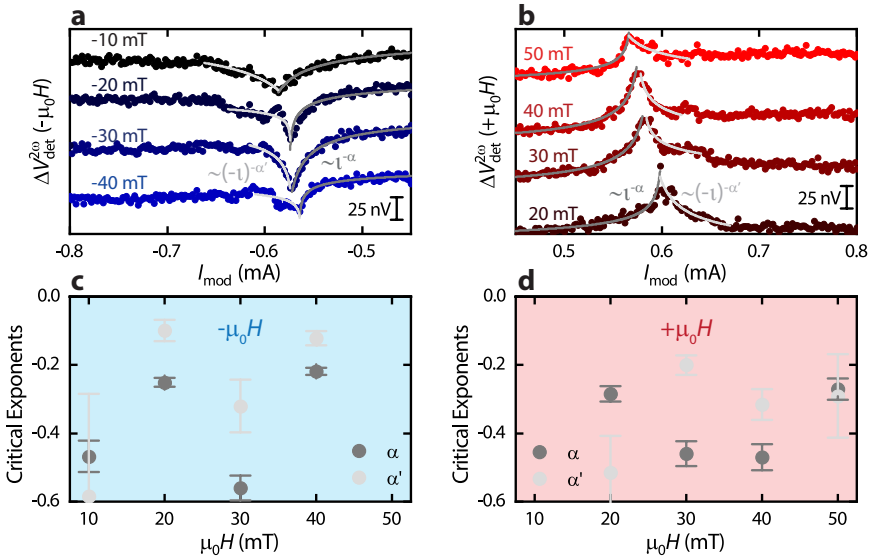

Fig. 7.1 – a (**b**) Second harmonic voltage amplitudes $\Delta V^{2\omega}_{\mathrm{det}}$ for the negative (positive) field and current regime. Both panels are restricted to fields $|\mu_0 H| \leq 50\,\mathrm{mT}$ and currents $|I_{\mathrm{mod}}| > 0.4\,\mathrm{mA}$. For clarity, the datasets for each field have an arbitrary offset applied to them. Green solid lines correspond to fits to Eq. (7.13). **c**, **d** Critical exponents α and α' defined in Eq. (7.13) plotted versus externally applied field. The exponents are extracted from both the negative (**c**) and positive (**d**) field regime. Both exponents fall in the range $0.1 \leq \alpha, \alpha' \leq 0.5$.

second harmonic signals represent an appropriate measure of the (magnon) heat capacity in our experiment. The distinctive 'λ'-shape vanishes for fields above 50 mT, which might be indicative of the suppression of the BEC state when the external field exceeds the anisotropy field [283]. From a qualtitative perspective, the data agrees well with the theoretical prediction. In favor of a quantitative approach, we extract the critical exponents α and α' from the fits, which are plotted as a function of the applied field in Fig. 7.1**c** and **d** for negative and positive field bias, respectively. Overall, we observe exponents within the range $0.1 \leq \alpha, \alpha' \leq 0.5$ for both field biases. Due to the rather small signal amplitudes observed for the second harmonic voltages, the fits feature considerable errors and the resulting spread of the exponents is large. Thus, no convincing statement about their quantitative relation to typical critical exponents measured for superfluid phase transitions can be given [284–288]. This is also likely to be rooted in the fact that we deal with a strongly driven, non-equilibrium system, for which the analysis via critical exponents might not be perfectly valid. It is therefore not obvious how and if the critical exponents extracted for the superfluid transitions of conventional Bose-gases compare to the critical exponents one should expect for a current-induced magnon spin superfluid transition. In this context, a more recent work suggests that the spin Seebeck effect measured at the interface of a normal metal/magnetic insulator heterostructure should decrease when entering the magnon BEC/spin

superfluid phase [283]. A direct measure of the heat conductivity of the system via the 3ω-method could also give a better understanding of the thermal YIG properties under spin current injection [289, 290]. Future investigations should test for these predictions as they might be able to unravel the question whether the magnon transport in the spin current induced damping compensated region can be considered as superfluid and ultimately classify the magnon system under these condtions as a BEC.

We might also extend our thermodynamic interpretation to the first harmonic signals, where we observe a rapid (i.e. with a large slope), but continuous transition of the associated magnon conductivity/resistance (see Ch. 5.3.3 and Fig. 5.13**a**). As introduced in Ch. 5.1.2, the magnon conductivity beneath the modulator can be expressed as in Eq. (5.32), which we restate here for convenience

$$\sigma_\mathrm{m} = \sigma_\mathrm{m}^0 \left(1 - \frac{I_\mathrm{dc}}{I_\mathrm{crit}}\right)^{-1/2} + \Delta\sigma_\mathrm{th} I_\mathrm{dc}^2. \tag{7.14}$$

For small modulator currents $I_\mathrm{mod} \ll I_\mathrm{crit}$, the first term in Eq. (7.14) can be approximated up to first order according to $\sigma_\mathrm{m}^0 \left(1 - \frac{I_\mathrm{dc}}{I_\mathrm{crit}}\right)^{-1/2} \approx \sigma_\mathrm{m}^0 \left(1 + I_\mathrm{mod}/(2I_\mathrm{crit})\right)$. In this limit, the magnon conductivity modulation is equivalent to the magnon density induced conductivity modulation derived in Ch. 5.1.2 (Eq. (5.30)). As also pointed out in Ch. 5.1.2, the conductivity modulation for large modulator currents I_mod is more suitable to be described in terms of the magnon lifetime, which diverges as the current approaches I_crit. In the language of magnon BEC, this diverging magnon lifetime is induced by the continuous condensation of magnons [187, 188] into the ground state. A macroscopic condensation of magnons is reached when $I_\mathrm{mod} \sim I_\mathrm{crit}$ referring to the compensation of the magnetic damping. As shown in Ref. [187], the condensed magnons carry no entropy, meaning that the transition observed in the first harmonic signals might be considered as an indication of the entropy drop of the system. A continous change of the entropy of a system with a large slope is characteristic of a second-order phase transition, in agreement with the theoretical expectation for current-induced magnon BEC transitions [187]. For that reason, it immediately follows that the associated heat capacity of the system, essentially being the first derivative of the entropy with respect to (in this case) current, has to display a discontinuity, as indicated by the 'λ'-shaped curves observed for the second harmonic voltage amplitudes. Of course, this again assumes that the second harmonic signal is significantly influenced by the heat conductivity/capacity properties of the magnon system. A rigorous verification of these claims would strongly indicate the experimental proof of a second-order phase transition due to a current-induced magnon BEC transition. As demonstrated in Ch. 5.5 via micromagnetic simulations, the system indeed adopts a rather coherent state for $I_\mathrm{mod} \approx I_\mathrm{crit}$, which is a necessary requirement for the label BEC. For slightly larger currents $I_\mathrm{mod} \geq I_\mathrm{crit}$, however, the spatial ho-

mogeneity as well as spectral coherence of the magnetization dynamics is strongly diminished, making the supposed BEC state rather instable.

7.2 Magnon Transport Modulation Beyond the Critical Current Regime

In recent measurements conducted at the WMI, we have increased the modulator current to values far beyond the regime investigated in Ch. 5. To this end, we prepared a sample very similar to the one considered in Ch. 5, consisting of the bilayer structure YIG(13)/Pt(5) (numbers in brackets denote the layer thickness in nm). The magnon conductivity modulation for such large currents is shown as the normalized first (second) harmonic detector voltage $\Delta V_{\mathrm{det}}^{1\omega}/\Delta V_{\mathrm{det0}}^{1\omega}$ ($\Delta V_{\mathrm{det}}^{2\omega}/\Delta V_{\mathrm{det0}}^{2\omega}$) as a function of I_{mod} in Fig. 7.2**a** (**c**). First of all, the critical behaviour is reproduced in the first and second harmonic signals and manifests itself as a kink in the curves (as indicated by the grey dashed arrows in Fig. 7.2**a** and **c**). It further obeys the field- and current-symmetry dictated by the SHE- and thermally-induced magnon injection in the Pt modulator and injector. When going beyond this critical regime, however, the behaviour of the first and second harmonic signal becomes very different. While the first harmonic experiences a rapid drop in signal for both field and current directions until leveling out at zero transport signal, the second harmonic shows distinct peak features strongly related to the rapidly vanishing signal in the first harmonic (indicated by black dashed lines). The peaks appear for both current directions and same current magnitude, but are larger when the field-current configuration corresponds to the SHE-induced magnon injection rather than depletion. With regards to the supposed phase transition in the magnon system at the critical current that we discussed in the previous Section, we can argue very similarly for these features: taking the thermometry measurements presented in Ch. 5.2.4 as a guide, it is very likely that the temperature for these large currents exceeds the Curie temperature $T_{\mathrm{C}} \approx 560\,\mathrm{K}$ of YIG [291]. Hence, we expect the YIG beneath the modulator to enter the paramagnetic state, thereby blocking the magnon transport from the injector and explaining the vanishing transport signal in the first harmonic. Under the assumption that the second harmonic signal can again be regarded as a measure of the magnonic heat capacity, the peaks might be identified with traces of the heat capacity reflecting the second order magnetic phase transition at T_{C}. The peaks being larger for the SHE-induced injection regime might be explained by the additonal magnon excitations therein, hence leading to a larger magnon heat capacity change at the transition.

To corroborate these claims, we have recently measured the magnon transport in YIG between two Pt strips modulated by an Iridium (Ir) modulator strip placed in between (conducted by Emir Karadža at the WMI [292]). The Ir is characterized by a large resistance and much lower spin Hall efficiency as compared to the

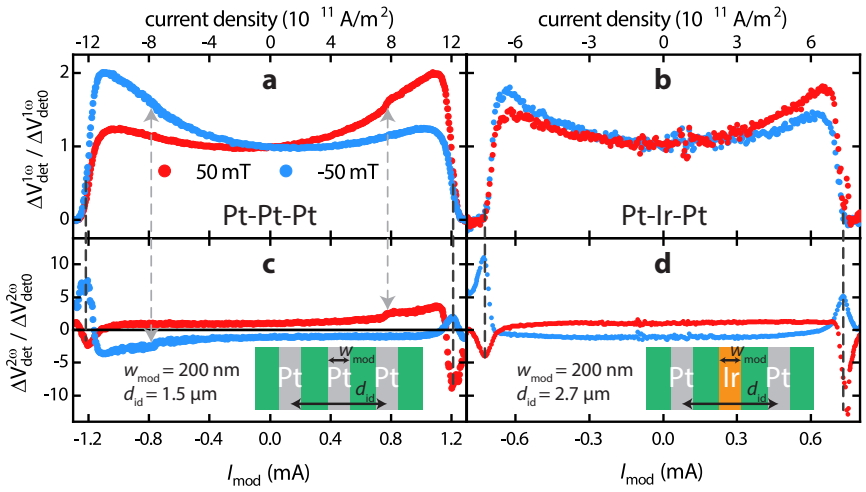

Fig. 7.2 – Normalized first (**a**, **b**) and second (**c**, **d**) harmonic signals $\Delta V_{\mathrm{det}}^{1\omega}/\Delta V_{\mathrm{det0}}^{1\omega}$ and $\Delta V_{\mathrm{det}}^{2\omega}/\Delta V_{\mathrm{det0}}^{2\omega}$, respectively, for a device with Pt modulator (**a**, **c**) and Ir modulator (**b**, **d**).

Pt modulation [292]. In this way, we increase the thermal contribution to the modulation significantly and switch off the SHE-induced magnon-related phase transition at the critical current. In Fig. 7.2**b** and **d**, respectively, the normalized first and second harmonic signals $\Delta V_{\mathrm{det}}^{1\omega}/\Delta V_{\mathrm{det0}}^{1\omega}$ and $\Delta V_{\mathrm{det}}^{2\omega}/\Delta V_{\mathrm{det0}}^{2\omega}$ are shown for a sample with a 5 nm thick Ir modulator (capped with 1.5 nm Ta to prevent oxidation) and Pt injector/detector with the same thickness. The YIG film for this sample was 20 nm thick. As evident from the first and second harmonic signal in Fig. 7.2**b** and **d**, the asymmetry of the curves with respect to the external field direction is very small, indicating the low SHE efficiency of the Ir modulation. Indeed, a critical current regime can neither be observed in the first nor second harmonic signal. We thus conclude that the SHE in Ir is too small to induce a damping compensation/BEC transition of the magnon system. For large currents, however, the behaviour of both signals becomes essentially equivalent to the case for Pt considered before. This experiment therefore convincingly verifies two conjectures: (i) the magnon damping compensation can only be induced via electrical magnon injection and cannnot be achieved via a thermal spin Seebeck torque [187, 291] (as already discussed in Ch. 5) and (ii) the large current transition related to the vanishing magnon transport signal in the first harmonic is (most likely) of pure thermal origin. Similar to the case for the Pt modulation, the Ir modulation does also show asymmetric peaks for positive and negative current polarities that switch positions under field reversal. This also corroborates the yet finite SHE efficiency in Ir.

7.3 Magnon Transport Modulation via Coherent Microwave Excitation of Spin Waves

Our experiments discussed in Chapter 5 showed that the non-linear excitation of spin waves via the SHE significantly affects the magnon conductivity σ_m. The physics of this magnon transport modulation is rich and our micromagnetic simulations (cf. Ch. 5.5) indicate that the magnon conductivity is mostly affected when the magnetization dynamics beneath the modulator exhibits large coherence. This observation raises the question whether a coherent excitation of the magnetization via a frequency-selective microwave setup results in similar modulation of the magnon transport. A first attempt towards answering this question from our group at the WMI has been put forward within the Supplemental Information of our paper in Ref. [12] (T. Wimmer, M. Althammer, L. Liensberger, N. Vlietstra, S. Geprägs, M. Weiler, R. Gross, H. Huebl, *Spin Transport in a Magnetic Insulator with Zero Effective Damping*, Physical Review Letters **123**, 257201 (2019)). A more thorough investigation has also been put forward by another group which focussed on studying the microwave control of magnon transport in Ref. [208]. Independent of each other, both works have shown that the modulation of magnon transport via microwaves is much more complicated than via the SHE-induced spin current injection. Surprisingly, they both seem to have revealed a very significant drop in the magnon transport signal when the microwave frequency is in resonance with the magnetization precession [12, 208]. For off-resonant conditions slightly above the ferromagnetic resonance (FMR) of the YIG film, however, a comparably smaller but still significant enhancement of the signal was observed [208].

In our very recent experiments, we have addressed the microwave-induced modulation of magnon transport in a more elaborate and systematic manner. The corresponding setup and sample geometry is illustrated in Fig. 7.3**a**. Here, we have prepared two 5 nm-thick Pt strips together with an antenna electrode composed of a Ru(8)/Cu(75)/Ta(3) layered structure[56] placed in between the Pt electrodes (numbers in brackets denote the layer thickness in nm). The three electrode structure is patterned on a 23 nm-thick YIG film grown via pulsed laser deposition at the WMI, very similar to the one studied in Ch. 5. The widths of each electrode (Pt and antenna) is 500 nm, while the center-to-center distance between the Pt strips is 1.5 µm. The magnon transport is realized by injecting a low-frequency ($f = \omega/(2\pi) \approx 7$ Hz) charge current $I_{inj} = I_0 \sin(\omega t)$ with $I_0 = 200$ µA to the left Pt electrode (injector) and measuring the first and second harmonic

[56] The reason for this comparably complicated Ru/Cu/Ta trilayer antenna is explained as follows: the YIG/Ru interface was empirically shown to have very little to vanishing impact on the magnon transport between the two Pt strips. Other materials such as Al, on the other hand, have been observed to completely suppress magnon transport (at least in very thin YIG), possibly due to Al diffusion into YIG. The subsequent Cu layer is thick and is used as the main current-carrying part of the antenna, mostly due to its good electrical conductivity. The final Ta layer acts as a capping for the Cu to prevent oxidation of the latter.

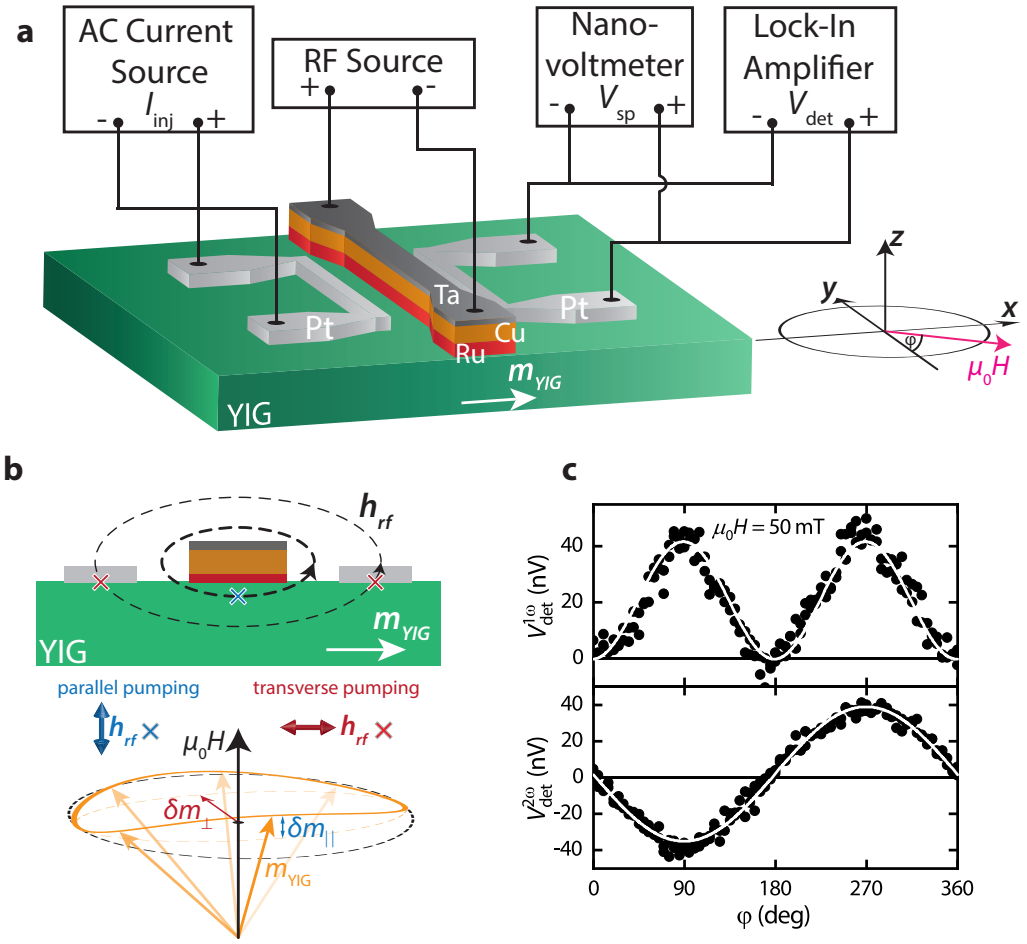

Fig. 7.3 – **a** Schematic illustration of the sample structure, coordinate system and the measurement setup. Magnon transport in a thin YIG film is measured between the left and right Pt electrodes utilized as spin injector and detector, respectively, via low frequency lock-in detection. Simultaneously, the third electrode composed of a Ru/Cu/Ta trilayer is subjected to a RF source and thereby employed as a microwave antenna. **b** Side view of the sample, together with a qualitative depiction of the RF magnetic field driven by the microwave antenna. For the depicted case of an in-plane magnetized YIG film oriented perpendicular to the electrodes, the RF magnetic field can couple to either the transverse (red cross) or longitudinal (blue cross) oscillation of the magnetization - corresponding to either transverse or parallel pumping. A depiction of the transverse and longitudinal dynamic components of an elliptically precessing magnetization vector are shown in the lower panel. **c** Angle dependent magnon transport measurements of the first harmonic (upper panel) and second harmonic (lower panel) voltage signals without microwave application at the antenna.

voltage signal via lock-in detection at the right Pt electrode (detector) (cf. Ch. 3.4.2). Simultaneously, a RF-microwave source is connnected to the antenna in the center used to coherently drive the magnetization in YIG. The lock-in detection at the detector is used to (i) distinguish between SHE- and thermally-induced magnon transport from the injector and (ii) to exclude any microwave-induced crosstalk effects via electromagnetic coupling between the antenna and the detector. In addition to this magnon transport measurement, we simultaneously record the DC voltage at the detector which corresponds to the microwave-induced DC spin

pumping signal [77, 94, 98, 293, 294]. In this particular geometry, we have to be aware of different excitations mechanisms with respect to the relative orientation of the YIG magnetization and the RF magnetic field $\boldsymbol{h}_{\mathrm{rf}}$ of the antenna. A side view of the qualitative spatial distribution of the RF magnetic field induced by the antenna is depicted in Fig. 7.3**b**. In order to enable magnon transport, the magnetization is fixed perpendicular to the electrodes. Hence, the RF magnetic field points mostly perpendicular to the YIG magnetization ($\boldsymbol{h}_{\mathrm{rf}} \perp \boldsymbol{m}_{\mathrm{YIG}}$) beneath the injector/detector, while mostly parallel right beneath the antenna ($\boldsymbol{h}_{\mathrm{rf}} \parallel \boldsymbol{m}_{\mathrm{YIG}}$). In principle, both configurations enable the excitation of magnetization dynamics. The transverse geometry ($\boldsymbol{h}_{\mathrm{rf}} \perp \boldsymbol{m}_{\mathrm{YIG}}$) represents the more common configuration which is typically used in various types of FMR experiments. Here, the RF field couples to the transverse component $\delta m_{\perp}$ of the precessing magnetization (cf. Fig. 7.3**b**). Accordingly, the excitation of spin waves is active for resonant conditions of precession frequency and RF frequency. Magnetization dynamics excited in this configuration is referred to as *transverse pumping*. In contrast, for the parallel configuration ($\boldsymbol{h}_{\mathrm{rf}} \parallel \boldsymbol{m}_{\mathrm{YIG}}$), the RF field couples to the change of the longitudinal magnetization $\delta m_{\parallel}$. The longitudinal change $\delta m_{\parallel}$ is only non-zero for a finite ellipticity of the magnetization precession [295] (cf. Fig. 7.3**b**). Due to its shape anisotropy/demagnetizing field, a considerable ellipticity is, however, expected for our in-plane magnetized YIG thin film. Accordingly, the excitation of magnetization dynamics is active at twice the FMR frequency. This excitation scheme is known as *parallel pumping*. The absorption of microwave power is linear for the transverse pumping effect (at low powers), while the parallel pumping scheme refers to a high power level effect and thus exhibits a threshold-like behaviour with respect to the microwave absorption [296]. Ultimately, we expect both excitation schemes to be active in our configuration.

For a pre-characterization of the magnon transport, we measure the external magnetic field angle φ dependent voltage modulation at the detector without microwave excitation at the antenna. The corresponding first and second harmonic voltage signal $V_{\mathrm{det}}^{1\omega}$ and $V_{\mathrm{det}}^{2\omega}$, respectively, are shown in Fig. 7.3**c** for an externally applied magnetic field $\mu_0 H = 50\,\mathrm{mT}$. As expected, we observe the 180°-symmetric (360°-symmetric) modulation for the first (second) harmonic signal[57]. We can thus verify both SHE- and thermally-induced magnon transport in our sample. The white solid lines correspond to fits to a $\cos^2(\varphi)$ (first harmonic) and $\cos(\varphi)$ (second harmonic) function.

We now turn to the experiments using a finite microwave signal at the antenna. Within the scope of this outlook, we focus on a single RF pump frequency of $f_{\mathrm{p}} = 14\,\mathrm{GHz}$ and investigate our results for various RF power levels. First and foremost, we study the DC spin pumping signal V_{sp} at the detector of our sample,

[57] We note that the signals are relatively small when compared to typical signal magnitudes observed in Ch. 5 for a similar YIG film. This might be related to a comparably lower interface transparency for this particular sample.

which is shown in Fig. 7.4**a**. For the lowest power level $P_{\mathrm{rf}} = 0\,\mathrm{dBm}$ considered here, we find the expected Lorentzian-shaped spectrum behaviour of the spin pumping peak around the resonance field (black line with lowest peak signal). Due to this clear low-power signal and the fact that the resonance field corresponds to the RF pump frequency f_{p}, we conclude that the spin pumping signal stems from the transverse pumping effect. This observation also fits to the fact that the RF field of the antenna is mostly perpendicular to the magnetization beneath the detector (cf. Fig. 7.3**b**). For any power $P_{\mathrm{rf}} \geq 5\,\mathrm{dBm}$ shown in Fig. 7.4**a**, the Lorentzian shape is significantly distorted, signaling a non-linear behaviour of the magnetization dynamics. This becomes increasingly clear for the largest power levels, where the resonance field corresponding to the peak maximum is significantly shifted to larger field values. The corresponding frequency blue-shift of the magnetization precession can be induced by (i) the non-linear dynamics itself (which results in the resonance frequency becoming pump power dependent) as well as (ii) microwave-induced resonant heating of the YIG (thus lowering the saturation magnetization of YIG) [297, 298]. In addition to the frequency shift, the curves have a significantly distorted lineshape [297, 299]. This deformation manifests itself as an elongated shoulder on the left side (lower bias field side) of the resonance field, as well as a flattened tail extending towards larger fields on the right side (cf. Fig. 7.4**a**). As shown in Refs. [297, 299], this type of spectral deformation of the spin pumping signal lineshape can neither be fully described by (i) the microwave-induced opening of the magnetization precession cone nor by (ii) the resonant microwave heating. The authors of the cited references thus conclude that the deformation is caused by an additional excitation of non-coherent spin waves with finite wavevectors. Within the scope of this outlook, however, we refrain from a rigorous analysis of the corresponding power-dependent resonance field/frequency shift, spin pumping amplitudes etc., which are to be evaluated for a proper verification of the above claims.

In a next step, we study the first and second harmonic voltage signals $V_{\mathrm{det}}^{1\omega}$ and $V_{\mathrm{det}}^{2\omega}$ induced by the AC current at the injector. The corresponding measurements as a function of magnetic field oriented along x are shown around the resonance field in Fig. 7.4**b**. Rather drastic and complex modulations of the magnon transport signal for both electrical and thermal magnon excitation seem to be present in the lineshapes. In order to gain a better understanding of these complex shapes, we attempt to correlate these complex signals with the spin pumping results discussed before. Hence, we plot the normalized signals of all three detector signals, i.e. spin pumping $V_{\mathrm{sp}}/\Delta V_{\mathrm{sp}}$, first harmonic $V_{\mathrm{det}}^{1\omega}/\Delta V_{\mathrm{det}}^{1\omega}$ and second harmonic $V_{\mathrm{det}}^{2\omega}/\Delta V_{\mathrm{det}}^{2\omega}$, together in Fig. 7.4**c** (ΔV_{sp}, $\Delta V_{\mathrm{det}}^{1\omega}$ and $\Delta V_{\mathrm{det}}^{2\omega}$ correspond to the maximum modulation amplitudes observed in the lineshapes and are used for normalization). A closer look at the relation between the lineshapes reveals that the first harmonic signals exhibit a conspicuous correlation to the first derivative of the spin pumping signal with respect to the external field, whereas the second harmonic shows a

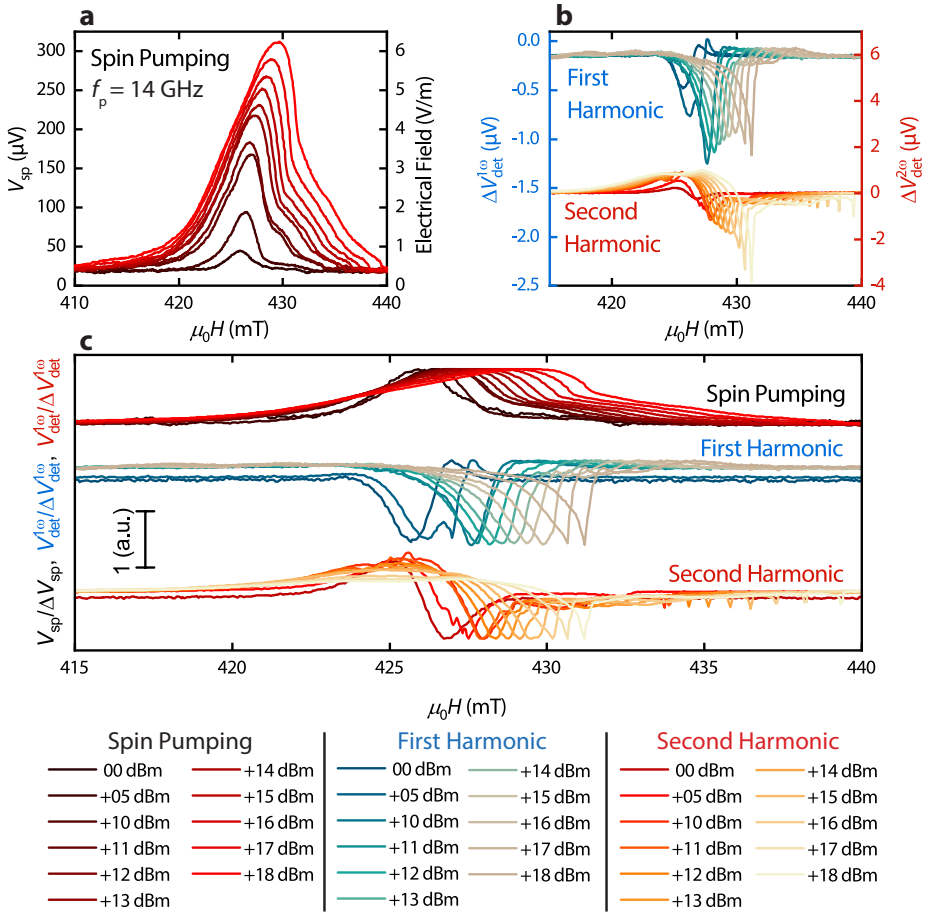

Fig. 7.4 – **a** DC spin pumping signal V_{sp} as a function of external magnetic field recorded at the detector for various RF power levels. **b** First and second harmonic detector voltage $V^{1\omega}_{det}$ and $V^{2\omega}_{det}$, respectively, as a function of magnetic field for various RF power levels. **c** Overview plot to compare DC spin pumping as well as the first and second harmonic magnon transport signals at the detector. Each of the curves is normalized to its absolute maximum signal amplitude.

correspondence to its second derivative. Taking the numerical first and second derivative of V_{sp} makes this correlation strikingly clear, especially for the sharp peak features observed for the transport signals. A visualization of this correlation is, however, omitted here. Nonetheless, this immediately raises the question whether the magnon transport signals picked up via the lock-in detection scheme might be superimposed by a large signal contribution stemming from the spin pumping physics, rather than magnon transport. Indeed, such a measurement artifact could be reasonable in our measurement setup. A possible source of this artifact might be related to the Oersted field generated by the AC modulated injector current $I_{inj} = I_0 \sin(\omega t)$ with $f = \omega/(2\pi) \approx 7\,\mathrm{Hz}$. In the present configuration, the current-induced Oersted field points parallel/antiparallel to the YIG magnetization $\boldsymbol{m}_{YIG}$ beneath the injector. The total field applied in our sample might therefore be composed of a static bias field with a slight modulation according to $H(t) = H_{ext} + h_{ac} \sin(\omega t)$, where h_{ac} is the magnitude of the Oersted

field and depends linearly on the injector current I_{inj}. We further consider the field dependent spin pumping voltage in the most general sense as

$$V_{\mathrm{sp}}(H(t)) = V_{\mathrm{sp}}^{0} f(H(t)) = V_{\mathrm{sp}}^{0} \left(f(H_{\mathrm{r}}) + \left.\frac{\partial f}{\partial H}\right|_{H_{\mathrm{r}}} H(t) + \frac{1}{2} \left.\frac{\partial^2 f}{\partial H^2}\right|_{H_{\mathrm{r}}} H(t)^2 + \mathcal{O}(H(t)^3) \right), \tag{7.15}$$

where V_{sp}^{0} denotes the peak amplitude of the spin pumping voltage and $f(H)$ corresponds to the mathematical relation capturing the field dependence of the spin pumping lineshape. In the simplest case, $f(H)$ takes the form of a Lorentzian function. We here assumed a Taylor expansion around the resonance field H_{r} up to second order and denote the derivatives of $f(H)$ as $f' = \left.\frac{\partial f}{\partial H}\right|_{H_{\mathrm{r}}}$ and $f'' = \left.\frac{\partial^2 f}{\partial H^2}\right|_{H_{\mathrm{r}}}$. Recalling the lock-in signal generation discussed in Ch. 3.4.2, we expect for the n^{th}-harmonic:

$$V_{\mathrm{X}}^{n\omega} = \frac{\sqrt{2}}{T} \int_{t}^{t+T} \sin(n\omega t') V_{\mathrm{sp}}(H(t'))\, \mathrm{d}t' \tag{7.16}$$

$$V_{\mathrm{Y}}^{n\omega} = \frac{\sqrt{2}}{T} \int_{t}^{t+T} \cos(n\omega t') V_{\mathrm{sp}}(H(t'))\, \mathrm{d}t', \tag{7.17}$$

where the subscripts X and Y denote the two quadratures of the signal phase shifted by 90°. Performing the calculation for the first two harmonics ($n = 1, 2$) by substituting Eq. (7.15) into Eqs. (7.16) and (7.17), we obtain

$$V_{\mathrm{X}}^{1\omega} = \frac{1}{\sqrt{2}} V_{\mathrm{sp}}^{0} h_{\mathrm{ac}} (f' + f'' H_{\mathrm{ext}}) \qquad V_{\mathrm{Y}}^{1\omega} = 0 \tag{7.18}$$

$$V_{\mathrm{X}}^{2\omega} = 0 \qquad V_{\mathrm{Y}}^{2\omega} = -\frac{1}{2\sqrt{2}} V_{\mathrm{sp}}^{0} h_{\mathrm{ac}}^{2} f''. \tag{7.19}$$

As suspected from the data, we indeed see that the first harmonic signal due to the field modulation is proportional to the first derivative of the spin pumping signal given by f', while the second harmonic is related to f''. Additionally, the first harmonic is also proportional to f'' due to the finite static bias magnetic field H_{ext}. Considering the expected magnon transport signal due to current-induced magnon injection discussed in Ch. 3.4.2, the total detector signal is expected to be composed of $V_{\mathrm{det}}^{1\omega} = \frac{1}{\sqrt{2}}(I_1 R_1 + V_{\mathrm{sp}}^{0} h_{\mathrm{ac}}(f' + f'' H_{\mathrm{ext}}))$ and $V_{\mathrm{det}}^{2\omega} = \frac{1}{2\sqrt{2}}(I_1^2 R_2 - V_{\mathrm{sp}}^{0} h_{\mathrm{ac}}^{2} f'')$[58]. In principle, it should be possible to extract the pure signal related to the magnon transport modulation by correcting $V_{\mathrm{det}}^{1\omega}$ and $V_{\mathrm{det}}^{2\omega}$ for any contributions related to the spin pumping signal. In practice, however, this requires a very accurate determination of the field modulation h_{ac} via the Oersted field, which in turn affects the magnitude of the lock-in detected signals. According to the Karlqvist equations [300], the Oersted field of a current-carrying sheet similar to our thin

[58] In Ch. 3.4.2, we additionally assume a finite phase factor ϕ for the detector current, which we have set to $\phi = 0$ in this discussion.

Pt injector can be estimated, it is however unclear how the non-homogenous field distribution beneath the detector affects the magnitude. In order to accurately distinguish between the different contributions involved in the detector signals, alternative measurement approaches should be conducted in future experiments. A DC method as implemented in Ref. [280] could replace the AC lock-in detection and therefoe suppress the current-induced field modulation. Furthermore, the above conjectures could be easily tested by conducting the same experiment at low temperatures, where the magnon transport is expected to be completely suppressed [9, 171], while the spin pumping-induced signals should persist. Hence, such an experiment might offer another way to distinguish between the different contributions while maintaining the experimental measurement strategy.

7.4 Electric Field Control of Antiferromagnetic Magnon Pseudospin Transport

In Chapter 6, we have shown the first observation of antiferromagnetic magnon pseudospin dynamics in the form of the antiferromagnetic magnon Hanle effect [10, 13]. We could show the coherent control of the antiferromagnetic magnon transport by the application of an external magnetic field. For practical applications in modern information technology, however, the required fields are far too large to be feasible in practical circumstances. Moreover, controlling the transport via electric fields rather than magnetic fields would represent a far superior method with respect to real-world applications. In Fig. 7.5**a**, one possible way to manipulate the pseudospin transport via electric field is presented. Here, a normal metal (NM) electrode is placed in between two Pt strips on an AFI attached to a back electrode. In such an arrangement, the application of a voltage V_g between the NM and the back electrode generates an electric field across the AFI in between the transport channel enclosed by the Pt electrodes. As proposed in Ref. [239], this electric field modulates the effective DMI strength in the AFI. Enabling to tune the DMI in the AFI offers a very efficient way to control the magnon transport properties, since it is (next to the external field) the main contributor to the pseudospin precession frequency discussed in the context of the AFI hematite in Ch. 6. The main challenge to succeed in this might be the growth of an AFI with sufficient quality directly onto a metallic electrode. In this regard, a more simple approach would be to deposit the metallic back electrode not in direct contact to the AFI, but rather beneath the substrate carrying the AFI hence ensuring its crystal quality. A major drawback with this approach, however, might be that the required voltages for a reasonable electric field magnitude are extraordinary high to allow for a significant control of the transport properties.

Another idea for voltage-controlled magnon transport in AFIs is illustrated in Fig. 7.5**b**. The presented sample structure is equivalent to Fig. 7.5**a** except for

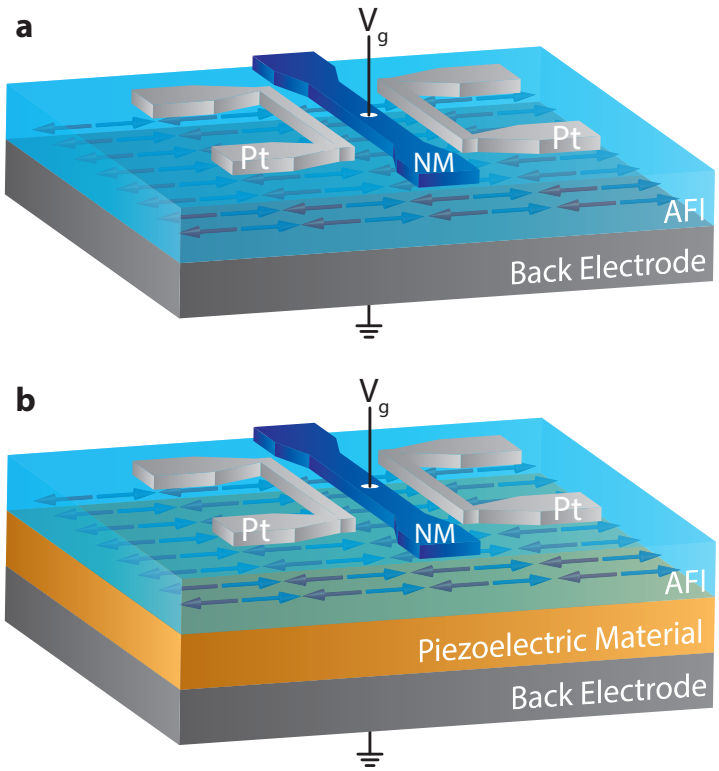

Fig. 7.5 – Proposals for sample structures enabling the electric field control of antiferromagnetic magnon pseudospin transport in an AFI/Pt heterostructure. **a** An additional NM electrode placed in between the Pt strips, together with a back electrode below the AFI film enables the local application of an electric field across the AFI. Such electric field may allow for the control of the DMI strength in the AFI according to Ref. [34]. **b** Similar structure as in panel **a**, but extended by a piezoelectric material placed in between the AFI and the back electrode. The application of an electric field between the NM and the back electrode leads to a deformation of the piezoelectric substrate and thus a sizable strain in the AFI. This arrangement might thus allow for an optimized and enhanced control of the magnon transport properties in the AFI via its magnetoelastic coupling.

an additional piezoelectric layer in between the AFI and the back electrode. In this arrangement, the application of the voltage V_g leads to the deformation of the piezoelectric material. Consequently, strain is induced in the adjacent AFI. A finite magnetoelastic coupling in the AFI can thus considerably change the magnetic properties of the AFI. This approach is particularly interesting with respect to the rich domain formation observed in thin hematite films recently [150]. It was shown that the domain walls lead to enhanced spin wave scattering and therefore suppress magnon transport. A sizable strain in the AFI might, however, lead to a significant reduction of domains and perhaps even allow for the formation of a single domain state due to the introduction of a strain-induced magnetic easy axis.

Review

8

The subject of this dissertation was to elaborate and investigate novel approaches for the control and manipulation of magnon spin currents in magnetic insulators. These magnonic currents have been excited exclusively in a non-coherent fashion via DC currents in metallic electrodes, implying the participation of a broad spectral range of spin waves in the transport. In contrast to coherently excited spin waves in the gigahertz regime, our magnon transport device therefore features a strong influence of short wavelength magnons at thermal energies. These short wavelength feature makes it well suited to be described in the particle picture similar to the well-known diffusive electron transport[59], in contrast to coherent types of transport typically described in the wave picture. In particular, the broad spectral distribution of magnons participating in the transport implies a comparably small mean free path, thus legitimizing a diffusive treatment of the magnon transport similarly to the elctron case [8, 36]. This similarity to the conventional electron transport actually enables a broad range of electron-inspired physics in the magnonics business [12, 13, 172]. The most crucial difference, however, lies in the fundamental nature of magnons compared to electrons. While the latter belong to the particle class of fermions and represents a conserved quantity, the former correspond to a non-conserved bosonic quasiparticle. This complicates the straightforward implementation of magnonic devices significantly. To overcome this issue is at the core of the present work. In particular, we give special attention to the excitation of magnon spin currents and their efficient manipulation. Multiple approaches to tackle these challenges have been put forward herein, the main messages of which we will recapitulate Chapter by Chapter in the following.

The influence of the ferromagnetic metal alloy $Co_{25}Fe_{75}$ (CoFe) employed as a spin injector deposited on YIG was investigated in Chapter 4 [11]. The general features of ferromagnetic spin injection could be replicated when compared to an earlier work presented in Ref. [65]. Different to the observations in Ref. [65], however, our ferromagnetic CoFe has shown a negligible contribution from the pure spin Hall effect and rather exhibited only the anomalous spin Hall effect related to its magnetization [63]. As a main result, we determined the anomalous spin Hall angle of CoFe employing a multiterminal spin injection/detection device that included both paramagnetic Pt and ferromagnetic CoFe as spin injectors/detectors. This renders our magnon transport experiments as a suitable tool for the determination of the spin Hall physics in ferromagnets, which otherwise is rather

[59] Of course, electrons in a solid state environment have to be described as Bloch-waves. However, due to their typically very short wavelength at the Fermi energy (similar to magnons at thermal energies), the treatment of electrons as particles is justified.

difficult due to superimposed magnetoresistance effects such as the anisotropic magnetoresistance. We additionally observed a yet unclear feature referring to a significant asymmetry of the magnon transport signals under magnetization reversal of both CoFe and YIG when using CoFe as either injector or detector. While we could not yet give an answer to this feature, it promises an interesting starting point for future investigations in this direction.

Chapter 5 covered the modulation of magnon conductivity in YIG via the implementation of a transistor-like three-terminal magnon transport device based on Ref. [172]. The application of a DC current to a Pt modulator electrode enclosed by a Pt injector and detector revealed that the magnon conductivity in ultra-thin YIG can be tuned very efficiently [12], actually far better than expected from simulations [172]. In this regard, our main result was the spin current induced excitation of non-linear magnetization dynamics beneath the modulator, which has been detected by a drastic non-linear change of the associated magnon conductivity [12]. We extensively discussed this result in the context of spin current induced magnetic damping compensation as well as the related phenomenon of magnon Bose-Einstein condensation (BEC). While we could undoubtedly confirm the damping compensation, the verification of a magnon BEC has eluded an unambiguous answer. Still, we could demonstrate various features indicating the formation of a magnon BEC proposed in theory [187, 188], among them the quantitative account for the non-linear magnon conductivity behaviour [188] or magnon BEC threshold conditions for the applied DC current [187]. Our micromagnetic simulations suggested a large spectral coherence of the magnetization dynamics near damping compensation, corroborating the possibility of BEC formation. The lack of spatial coherence of the magnetization dynamics, however, does not support this conclusion since it constitutes a necessary feature of a magnon BEC. In general, our experiments demonstrated the great potential that lies in the spin current induced magnon conductivity modulation for the implementation of magnon-based information technology.

Last but not least, we have demonstrated the first observation of the antiferromagnetic magnon Hanle effect by measuring the spin transport between two Pt strips deposited on the antiferromagnetic insulator (AFI) hematite in Chapter 6 [13]. This novel effect was substantiated by a theoretical framework introducing the antiferromagnetic magnon pseudospin as a powerful tool to describe antiferromagnetic magnon excitations and their dynamics [10]. The main result of these experiments constitutes the observation of an oscillating magnon transport signal between positive and negative values as a function of the external magnetic field. This enables a simple control over the magnitude and sign of the magnon transport signal. The oscillation could be interpreted as a consequence of the pseudospin precession frequency, which determines how quickly antiferromagnetic magnon

excitations transmute between circular and linear polarization states. The cause of this transmutation could be attributed to a finite coupling between the spin-up and -down basis states of the AFI, the source of which has been revealed to be the intrinsic Dzyaloshinskii-Moriya interaction of hematite, its magnetic easy plane anisotropy and the external field-induced canting of the magnetic sublattices. Our observation of the magnonic analog of the conventional electronic Hanle effect, together with its pseudospin description constitutes an important step towards novel electron-inspired magnonics for future investigations.

Interestingly, we observed no pseudospin dynamics in the thermal magnon transport data of hematite. We attributed this to the thermal excitation process, which is not spin-selective and therefore proportional to the field-induced net magnetization [117]. As a consequence of a lateral temperature gradient generated across the detector width, we observed the transverse spin Nernst magnetothermopower (TSNM) [55]. In particular, the AFI enables a simpler detection of this effect, since it is far less overshadowed by the thermal magnon transport signal. Two main results have been encountered with respect to the TSNM: (i) the TSNM is sensitive to the Néel vector of the AFI and (ii) a vanishing signal modulation was observed at low temperatures, which we compellingly explained by a vanishing spin Nernst angle at low temperatures. The latter could be verified by a theoretical calculation of the temperature dependence of the spin Nernst conductivity being in perfect agreement with the measured results.

The results presented in this thesis fall rather neatly into the overarching theme of *Control and Manipulation of Magnonic Spin Currents in Magnetic Insulators*, the dedicated title of this work. While we think that our experimental results and interpretations in this subject have answered many of the associated questions, we are also glad that it has provoked new issues and ideas. We therefore hope that the future research in this field will benefit from the results presented herein.

List of Publications

- J. Gückelhorn, T. Wimmer, M. Müller, S. Geprägs, H. Huebl, R. Gross, M. Althammer, *Magnon transport in YIG/Pt nanostructures with reduced effective magnetization*, In preparation (2021).
- T. Wimmer, J. Gueckelhorn, M. Opel, S. Geprägs, R. Gross, H. Huebl, M. Althammer, *Analysis of Critical Behaviour and Electrical Annealing of Spin Current-Controlled Magnon Transistor Devices*, In preparation (2021).
- T. Wimmer, R. Schlitz, S. Geprägs, H. Huebl, R. Gross, S.T.B. Goennenwein, M. Althammer, *Electrical background signals between ferromagnetic metal electrodes deposited on a nonmagnetic substrate*, In preparation (2021).
- T. Wimmer, J. Gückelhorn, S. Wimmer, S. Mankovsky, H. Ebert, M. Opel, S. Geprägs, R. Gross, H. Huebl, M. Althammer, *Low Temperature Suppression of the Spin Nernst Angle in Pt*, arXiv:2103.12697, submitted to Physical Review Letters (2021).
- T. Wimmer, A. Kamra, J. Gückelhorn, M. Opel, S. Geprägs, R. Gross, H. Huebl, M. Althammer, *Observation of Antiferromagnetic Magnon Pseudospin Dynamics and the Hanle Effect*, Physical Review Letters **125**, 247204 (2020).
- A. Kamra, T. Wimmer, H. Huebl, M. Althammer, *Antiferromagnetic magnon pseudospin: Dynamics and diffusive transport*, Physical Review B **102**, 174445 (2020).
- J. Gückelhorn, T. Wimmer, S. Geprägs, H. Huebl, R. Gross, M. Althammer, *Quantitative comparison of magnon transport experiments in three-terminal YIG/Pt nanostructures acquired via dc and ac detection techniques*, Applied Physics Letters **117**, 182401 (2020).
- T. Wimmer, M. Althammer, L. Liensberger, N. Vlietstra, S. Geprägs, M. Weiler, R. Gross, H. Huebl, *Spin Transport in a Magnetic Insulator with Zero Effective Damping*, Physical Review Letters **123**, 257201 (2019).
- M. Althammer, A.V. Singh, T. Wimmer, Z. Galazka, H. Huebl, M. Opel, R. Gross, A. Gupta, *Role of interface quality for the spin Hall magnetoresistance in nickel ferrite thin films with bulk-like magnetic properties*, Applied Physics Letters **115**, 092403 (2019).

- T. Wimmer, B. Coester, S. Geprägs, R. Gross, S.T.B. Goennenwein, H. Huebl, M. Althammer, *Anomalous spin Hall angle of a metallic ferromagnet determined by a multiterminal spin injection/detection device*, Applied Physics Letters **115**, 092404 (2019).
- K. Ganzhorn, T. Wimmer, J. Barker, G.E.W. Bauer, Z. Qiu, E. Saitoh, N. Vlietstra, S. Geprägs, R. Gross, H. Huebl, S.T.B. Goennenwein, *Non-local magnon transport in the compensated ferrimagnet GdIG*, arXiv:1705.02871 (2017).
- K. Ganzhorn, T. Wimmer, J. Cramer, R. Schlitz, S. Geprägs, G. Jakob, R. Gross, H. Huebl, M. Kläui, S.T.B. Goennenwein, *Temperature dependence of the non-local spin Seebeck effect in YIG/Pt nanostructures*, AIP Advances **7**, 085102 (2017).
- K. Ganzhorn, S. Klingler, T. Wimmer, S. Geprägs, R. Gross, H. Huebl, S.T.B. Goennenwein, *Magnon-based logic in a multi-terminal YIG/Pt nanostructure*, Applied Physics Letters **109**, 022405 (2016).

Bibliography

[1] C. Hitchens, *God Is Not Great: How Religion Poisons Everything*, Twelve, Hachette Book Group USA, 237 Park Avenue, New York, NY 10169 (2007).

[2] Wikipedia, *Hitchen's razor — Wikipedia, The Free Encyclopedia* (2020).

[3] C. Sagan, A. Druyan, S. Soter, A. Malone, D. Kennard, G. Haines-Stiles, G. Andorfer, R. McCain, *Encyclopedia Galactica* (1980).

[4] G.E. Moore, *Cramming more components onto integrated circuits, Reprinted from Electronics, volume 38, number 8, April 19, 1965, pp.114 ff.*, IEEE Solid-State Circuits Society Newsletter **11**, 33 (2006).

[5] M.M. Waldrop, *The chips are down for Moore's law*, Nature **530**, 144 (2016).

[6] V.V. Kruglyak, S.O. Demokritov, D. Grundler, *Magnonics*, Journal of Physics D: Applied Physics **43**, 264001 (2010).

[7] V. Cherepanov, I. Kolokolov, V. L'vov, *The Saga of YIG: Spectra, Thermodynamics, Interaction and Relaxation of Magnons in a Complex Magnet*, Physics reports, North-Holland (1993).

[8] L.J. Cornelissen, J. Liu, R.A. Duine, J.B. Youssef, B.J. van Wees, *Long-distance transport of magnon spin information in a magnetic insulator at room temperature*, Nature Physics **11**, 1022 (2015).

[9] S.T.B. Goennenwein, R. Schlitz, M. Pernpeintner, K. Ganzhorn, M. Althammer, R. Gross, H. Huebl, *Non-local magnetoresistance in YIG/Pt nanostructures*, Applied Physics Letters **107**, 172405 (2015).

[10] A. Kamra, T. Wimmer, H. Huebl, M. Althammer, *Antiferromagnetic magnon pseudospin: Dynamics and diffusive transport*, Physical Review B **102**, 174445 (2020).

[11] T. Wimmer, B. Coester, S. Geprägs, R. Gross, S.T.B. Goennenwein, H. Huebl, M. Althammer, *Anomalous spin Hall angle of a metallic ferromagnet determined by a multiterminal spin injection/detection device*, Applied Physics Letters **115**, 092404 (2019).

[12] T. Wimmer, M. Althammer, L. Liensberger, N. Vlietstra, S. Geprägs, M. Weiler, R. Gross, H. Huebl, *Spin Transport in a Magnetic Insulator with Zero Effective Damping*, Physical Review Letters **123**, 257201 (2019).

[13] T. Wimmer, A. Kamra, J. Gückelhorn, M. Opel, S. Geprägs, R. Gross, H. Huebl, M. Althammer, *Observation of Antiferromagnetic Magnon Pseudospin Dynamics and the Hanle Effect*, Physical Review Letters **125**, 247204 (2020).

[14] W. Gerlach, O. Stern, *Das magnetische Moment des Silberatoms*, Zeitschrift für Physik **9**, 353 (1922).

[15] W. Gerlach, O. Stern, *Der experimentelle Nachweis der Richtungsquantelung im Magnetfeld*, Zeitschrift für Physik **9**, 349 (1922).

[16] E. Fermi, *Sulla quantizzazione del gas perfetto monoatomico*, Rendiconti Lincei (in Italian) **3**, 145 (1926).

[17] P. Dirac, *On the theory of quantum mechanics*, Proceedings of the Royal Society of London. Series A, Containing Papers of a Mathematical and Physical Character **112**, 661 (1926).

[18] S. Bose, *Plancks Gesetz und Lichtquantenhypothese*, Zeitschrift für Physik **26**, 178 (1924).

[19] A. Einstein, *Quantentheorie des einatomigen idealen Gases. Zweite Abhandlung*, in *Albert Einstein: Akademie-Vorträge*, 245–257, Wiley-VCH Verlag GmbH & Co. KGaA (2006).

[20] P. Ehrenfest, *Ersetzung der Hypothese vom unmechanischen Zwang durch eine Forderung bezüglich des inneren Verhaltens jedes einzelnen Elektrons*, Die Naturwissenschaften **13**, 953 (1925).

[21] W. Pauli, *Zur Quantenmechanik des magnetischen Elektrons*, Zeitschrift für Physik **43**, 601 (1927).

[22] J.J. Sakurai, J. Napolitano, *Modern Quantum Mechanics*, Cambridge University Press, 2. Ed. (2017).

[23] H. Rauch, A. Zeilinger, G. Badurek, A. Wilfing, W. Bauspiess, U. Bonse, *Verification of coherent spinor rotation of fermions*, Physics Letters A **54**, 425 (1975).

[24] S.A. Werner, R. Colella, A.W. Overhauser, C.F. Eagen, *Observation of the Phase Shift of a Neutron Due to Precession in a Magnetic Field*, Physical Review Letters **35**, 1053 (1975).

[25] J.D. Jackson, R.F. Fox, *Classical Electrodynamics, 3rd ed.*, American Journal of Physics **67**, 841 (1999).

[26] R. Gross, A. Marx, *Festkörperphysik*, Oldenbourg Wissenschaftsverlag (2012).

[27] T. Gilbert, *A phenomenological theory of damping in ferromagnetic materials*, IEEE Transactions on Magnetics **40**, 3443 (2004).

[28] L. Flacke, L. Liensberger, M. Althammer, H. Huebl, S. Geprägs, K. Schultheiss, A. Buzdakov, T. Hula, H. Schultheiss, E.R.J. Edwards, H.T. Nembach, J.M. Shaw, R. Gross, M. Weiler, *High spin-wave propagation length consistent with low damping in a metallic ferromagnet*, Applied Physics Letters **115**, 122402 (2019).

[29] T. Holstein, H. Primakoff, *Field Dependence of the Intrinsic Domain Magnetization of a Ferromagnet*, Physical Review **58**, 1098 (1940).

[30] B.A. Kalinikos, M.P. Kostylev, N.V. Kozhus, A.N. Slavin, *The dipole-exchange spin wave spectrum for anisotropic ferromagnetic films with mixed exchange boundary conditions*, Journal of Physics: Condensed Matter **2**, 9861 (1990).

[31] M.L. Néel, *Propriétés magnétiques des ferrites; ferrimagnétisme et antiferromagnétisme*, Annales de Physique **12**, 137 (1948).

[32] S.M. Rezende, A. Azevedo, R.L. Rodríguez-Suárez, *Introduction to antiferromagnetic magnons*, Journal of Applied Physics **126**, 151101 (2019).

[33] Y.T. Chen, S. Takahashi, H. Nakayama, M. Althammer, S.T.B. Goennenwein, E. Saitoh, G.E.W. Bauer, *Theory of spin Hall magnetoresistance*, Physical Review B **87**, 144411 (2013).

[34] Y.T. Chen, S. Takahashi, H. Nakayama, M. Althammer, S.T.B. Goennenwein, E. Saitoh, G.E.W. Bauer, *Theory of spin Hall magnetoresistance (SMR) and related phenomena*, Journal Physics: Condensed Matter **28**, 103004 (2016).

[35] P.C. van Son, H. van Kempen, P. Wyder, *Boundary Resistance of the Ferromagnetic-Nonferromagnetic Metal Interface*, Physical Review Letters **58**, 2271 (1987).

[36] L.J. Cornelissen, K.J.H. Peters, G.E.W. Bauer, R.A. Duine, B.J. van Wees, *Magnon spin transport driven by the magnon chemical potential in a magnetic insulator*, Physical Review B **94**, 014412 (2016).

[37] L.P. Kadanoff, P.C. Martin, *Hydrodynamic equations and correlation functions*, Annals of Physics **24**, 419 (1963).

[38] H.S. Bennett, P.C. Martin, *Spin Diffusion in the Heisenberg Paramagnet*, Physical Review **138**, A608 (1965).

[39] I.J. Lowe, S. Gade, *Density-Matrix Derivation of the Spin-Diffusion Equation*, Physical Review **156**, 817 (1967).

[40] M.A. Khasawneh, C. Klose, W.P. Pratt, N.O. Birge, *Spin-memory loss at Co/Ru interfaces*, Physical Review B **84**, 014425 (2011).

[41] H. Jiao, G.E.W. Bauer, *Spin Backflow and ac Voltage Generation by Spin Pumping and the Inverse Spin Hall Effect*, Physical Review Letters **110**, 217602 (2013).

[42] M.I. D'Yakonov, V.I. Perel', *Possibility of Orienting Electron Spins with Current*, Soviet Journal of Experimental and Theoretical Physics Letters **13**, 657 (1971).

[43] J.E. Hirsch, *Spin Hall Effect*, Physical Review Letters **83**, 1834 (1999).

[44] A. Hoffmann, *Spin Hall Effects in Metals*, IEEE Transactions on Magnetics **49**, 5172 (2013).

[45] M.V. Berry, *Quantal Phase Factors Accompanying Adiabatic Changes*, Proceedings of the Royal Society of London. A. Mathematical and Physical Sciences **392**, 45 (1984).

[46] J. Smit, *The spontaneous hall effect in ferromagnetics I*, Physica **21**, 877 (1955).

[47] J. Smit, *The spontaneous hall effect in ferromagnetics II*, Physica **24**, 39 (1958).

[48] L. Berger, *Side-Jump Mechanism for the Hall Effect of Ferromagnets*, Physical Review B **2**, 4559 (1970).

[49] M. Schreier, G.E.W. Bauer, V.I. Vasyuchka, J. Flipse, K. ichi Uchida, J. Lotze, V. Lauer, A.V. Chumak, A.A. Serga, S. Daimon, T. Kikkawa, E. Saitoh, B.J. van Wees, B. Hillebrands, R. Gross, S.T.B. Goennenwein, *Sign of inverse spin Hall voltages generated by ferromagnetic resonance and temperature gradients in yttrium iron garnet platinum bilayers*, Journal of Physics D: Applied Physics **48**, 025001 (2015).

[50] Y.K. Kato, R.C. Myers, A.C. Gossard, D.D. Awschalom, *Observation of the Spin Hall Effect in Semiconductors*, Science **306**, 1910 (2004).

[51] J. Sinova, S.O. Valenzuela, J. Wunderlich, C. Back, T. Jungwirth, *Spin Hall effects*, Reviews of Modern Physics **87**, 1213 (2015).

[52] N.H.D. Khang, Y. Ueda, P.N. Hai, *A conductive topological insulator with large spin Hall effect for ultralow power spin–orbit torque switching*, Nature Materials **17**, 808 (2018).

[53] B. Zhao, D. Khokhriakov, Y. Zhang, H. Fu, B. Karpiak, A.M. Hoque, X. Xu, Y. Jiang, B. Yan, S.P. Dash, *Observation of charge to spin conversion in Weyl semimetal WTe_2 at room temperature*, Physical Review Research **2**, 013286 (2020).

[54] M. Althammer, S. Meyer, H. Nakayama, M. Schreier, S. Altmannshofer, M. Weiler, H. Huebl, S. Geprägs, M. Opel, R. Gross, D. Meier, C. Klewe, T. Kuschel, J.M. Schmalhorst, G. Reiss, L. Shen, A. Gupta, Y.T. Chen, G.E.W. Bauer, E. Saitoh, S.T.B. Goennenwein, *Quantitative study of the spin Hall magnetoresistance in ferromagnetic insulator/normal metal hybrids*, Physical Review B **87**, 224401 (2013).

[55] S. Meyer, Y.T. Chen, S. Wimmer, M. Althammer, T. Wimmer, R. Schlitz, S. Geprägs, H. Huebl, D. Ködderitzsch, H. Ebert, G.E.W. Bauer, R. Gross, S.T.B. Goennenwein, *Observation of the spin Nernst effect*, Nature Materials **16**, 977 (2017).

[56] P. Sheng, Y. Sakuraba, Y.C. Lau, S. Takahashi, S. Mitani, M. Hayashi, *The spin Nernst effect in tungsten*, Science Advances **3**, e1701503 (2017).

[57] D.J. Kim, C.Y. Jeon, J.G. Choi, J.W. Lee, S. Surabhi, J.R. Jeong, K.J. Lee, B.G. Park, *Observation of transverse spin Nernst magnetoresistance induced by thermal spin current in ferromagnet/non-magnet bilayers*, Nature Communications **8**, 2041 (2017).

[58] A. Bose, S. Bhuktare, H. Singh, S. Dutta, V.G. Achanta, A.A. Tulapurkar, *Direct detection of spin Nernst effect in platinum*, Applied Physics Letters **112**, 162401 (2018).

[59] K. Tauber, M. Gradhand, D.V. Fedorov, I. Mertig, *Extrinsic Spin Nernst Effect from First Principles*, Physical Review Letters **109**, 026601 (2012).

[60] S. Wimmer, D. Ködderitzsch, K. Chadova, H. Ebert, *First-principles linear response description of the spin Nernst effect*, Physical Review B **88**, 201108 (2013).

[61] V. Popescu, P. Kratzer, P. Entel, C. Heiliger, M. Czerner, K. Tauber, F. Töpler, C. Herschbach, D.V. Fedorov, M. Gradhand, I. Mertig, R. Kováčik, P. Mavropoulos, D. Wortmann, S. Blügel, F. Freimuth, Y. Mokrousov, S. Wimmer, D. Ködderitzsch, M. Seemann, K. Chadova, H. Ebert, *Spin caloric transport from density-functional theory*, Journal of Physics D: Applied Physics **52**, 073001 (2018).

[62] D. Ralph, M. Stiles, *Spin transfer torques*, Journal of Magnetism and Magnetic Materials **320**, 1190 (2008).

[63] V.P. Amin, J. Li, M.D. Stiles, P.M. Haney, *Intrinsic spin currents in ferromagnets*, Physical Review B **99**, 220405 (2019).

[64] A. Davidson, V.P. Amin, W.S. Aljuaid, P.M. Haney, X. Fan, *Perspectives of electrically generated spin currents in ferromagnetic materials*, Physics Letters A **384**, 126228 (2020).

[65] K.S. Das, W.Y. Schoemaker, B.J. van Wees, I.J. Vera-Marun, *Spin injection and detection via the anomalous spin Hall effect of a ferromagnetic metal*, Physical Review B **96** (2017).

[66] K.S. Das, J. Liu, B.J. van Wees, I.J. Vera-Marun, *Efficient Injection and Detection of Out-of-Plane Spins via the Anomalous Spin Hall Effect in Permalloy Nanowires*, Nano Letters **18**, 5633 (2018).

[67] K.S. Das, F. Feringa, M. Middelkamp, B.J. van Wees, I.J. Vera-Marun, *Modulation of magnon spin transport in a magnetic gate transistor*, Physical Review B **101**, 054436 (2020).

[68] C. Safranski, E.A. Montoya, I.N. Krivorotov, *Spin–orbit torque driven by a planar Hall current*, Nature Nanotechnology **14**, 27 (2018).

[69] C. Safranski, J.Z. Sun, J.W. Xu, A.D. Kent, *Planar Hall Driven Torque in a Ferromagnet/Nonmagnet/Ferromagnet System*, Physical Review Letters **124**, 197204 (2020).

[70] D. rer. nat. Matthias Althammer, *Pure Spin Currents In Magnetic Insulators*, Habilitation, Technische Universität München (2020).

[71] M. Kimata, H. Chen, K. Kondou, S. Sugimoto, P.K. Muduli, M. Ikhlas, Y. Omori, T. Tomita, A.H. MacDonald, S. Nakatsuji, Y. Otani, *Magnetic and magnetic inverse spin Hall effects in a non-collinear antiferromagnet*, Nature **565**, 627 (2019).

[72] T.C. Chuang, D. Qu, S.Y. Huang, S.F. Lee, *Magnetization-dependent spin Hall effect in a perpendicular magnetized film*, Physical Review Research **2**, 032053 (2020).

[73] A. Mook, R.R. Neumann, A. Johansson, J. Henk, I. Mertig, *Origin of the magnetic spin Hall effect: Spin current vorticity in the Fermi sea*, Physical Review Research **2**, 023065 (2020).

[74] A. Manchon, J. Železný, I. Miron, T. Jungwirth, J. Sinova, A. Thiaville, K. Garello, P. Gambardella, *Current-induced spin-orbit torques in ferromagnetic and antiferromagnetic systems*, Reviews of Modern Physics **91**, 035004 (2019).

[75] A. Brataas, Y.V. Nazarov, G.E.W. Bauer, *Finite-Element Theory of Transport in Ferromagnet˜Normal Metal Systems*, Physical Review Letters **84**, 2481 (2000).

[76] Y. Tserkovnyak, A. Brataas, G.E.W. Bauer, *Enhanced Gilbert Damping in Thin Ferromagnetic Films*, Physical Review Letters **88**, 117601 (2002).

[77] Y. Tserkovnyak, A. Brataas, G.E.W. Bauer, *Spin pumping and magnetization dynamics in metallic multilayers*, Physical Review B **66**, 224403 (2002).

[78] B.J. van Wees, H. van Houten, C.W.J. Beenakker, J.G. Williamson, L.P. Kouwenhoven, D. van der Marel, C.T. Foxon, *Quantized conductance of point contacts in a two-dimensional electron gas*, Physical Review Letters **60**, 848 (1988).

[79] M. Büttiker, *Four-Terminal Phase-Coherent Conductance*, Physical Review Letters **57**, 1761 (1986).

[80] M. Johnson, R.H. Silsbee, *Interfacial charge-spin coupling: Injection and detection of spin magnetization in metals*, Physical Review Letters **55**, 1790 (1985).

[81] M. Johnson, R.H. Silsbee, *Coupling of electronic charge and spin at a ferromagnetic-paramagnetic metal interface*, Physical Review B **37**, 5312 (1988).

[82] X. Jia, K. Liu, K. Xia, G.E.W. Bauer, *Spin transfer torque on magnetic insulators*, EPL (Europhysics Letters) **96**, 17005 (2011).

[83] S. Maekawa, S. Valenzuela, E. Saitoh, T. Kimura, *Spin Current*, Oxford science publications, OUP Oxford (2012).

[84] X. Waintal, E.B. Myers, P.W. Brouwer, D.C. Ralph, *Role of spin-dependent interface scattering in generating current-induced torques in magnetic multilayers*, Physical Review B **62**, 12317 (2000).

[85] P.M. Haney, H.W. Lee, K.J. Lee, A. Manchon, M.D. Stiles, *Current induced torques and interfacial spin-orbit coupling: Semiclassical modeling*, Physical Review B **87**, 174411 (2013).

[86] M. Weiler, M. Althammer, M. Schreier, J. Lotze, M. Pernpeintner, S. Meyer, H. Huebl, R. Gross, A. Kamra, J. Xiao, Y.T. Chen, H. Jiao, G.E.W. Bauer, S.T.B. Goennenwein, *Experimental Test of the Spin Mixing Interface Conductivity Concept*, Physical Review Letters **111**, 176601 (2013).

[87] L. Liu, Y. Li, Y. Liu, T. Feng, J. Xu, X.R. Wang, D. Wu, P. Gao, J. Li, *Interfacial modulation of spin pumping in YIG/Pt*, Physical Review B **102**, 014411 (2020).

[88] S.A. Bender, Y. Tserkovnyak, *Interfacial spin and heat transfer between metals and magnetic insulators*, Physical Review B **91**, 140402 (2015).

[89] J.C. Slonczewski, *Conductance and exchange coupling of two ferromagnets separated by a tunneling barrier*, Physical Review B **39**, 6995 (1989).

[90] J. Slonczewski, *Current-driven excitation of magnetic multilayers*, Journal of Magnetism and Magnetic Materials **159**, L1 (1996).

[91] L. Berger, *Emission of spin waves by a magnetic multilayer traversed by a current*, Physical Review B **54**, 9353 (1996).

[92] L. LANDAU, E. LIFSHITZ, *On the theory of the dispersion of magnetic permeability in ferromagnetic bodies*, in *Perspectives in Theoretical Physics*, 51–65, Elsevier (1992).

[93] Y. Tserkovnyak, A. Brataas, G.E.W. Bauer, B.I. Halperin, *Nonlocal magnetization dynamics in ferromagnetic heterostructures*, Review of Modern Physics **77**, 1375 (2005).

[94] M.V. Costache, M. Sladkov, S.M. Watts, C.H. van der Wal, B.J. van Wees, *Electrical Detection of Spin Pumping due to the Precessing Magnetization of a Single Ferromagnet*, Physical Review Letters **97**, 216603 (2006).

[95] O. Mosendz, J.E. Pearson, F.Y. Fradin, G.E.W. Bauer, S.D. Bader, A. Hoffmann, *Quantifying Spin Hall Angles from Spin Pumping: Experiments and Theory*, Physical Review Letters **104**, 046601 (2010).

[96] K. Ando, S. Takahashi, J. Ieda, Y. Kajiwara, H. Nakayama, T. Yoshino, K. Harii, Y. Fujikawa, M. Matsuo, S. Maekawa, E. Saitoh, *Inverse spin-Hall effect induced by spin pumping in metallic system*, Journal of Applied Physics **109**, 103913 (2011).

[97] B. Heinrich, C. Burrowes, E. Montoya, B. Kardasz, E. Girt, Y.Y. Song, Y. Sun, M. Wu, *Spin Pumping at the Magnetic Insulator (YIG)/Normal Metal (Au) Interfaces*, Physical Review Letters **107**, 066604 (2011).

[98] C. Hahn, G. de Loubens, M. Viret, O. Klein, V.V. Naletov, J. Ben Youssef, *Detection of Microwave Spin Pumping Using the Inverse Spin Hall Effect*, Physical Review Letters **111**, 217204 (2013).

[99] M. Schreier, *Spin Tranfer Torque Mediated Magnetization Dynamics*, PhD thesis, Technische Universität München (2016).

[100] J. Xiao, G.E.W. Bauer, K.c. Uchida, E. Saitoh, S. Maekawa, *Theory of magnon-driven spin Seebeck effect*, Physical Review B **81**, 214418 (2010).

[101] K. Uchida, J. Xiao, H. Adachi, J. Ohe, S. Takahashi, J. Ieda, T. Ota, Y. Kajiwara, H. Umezawa, H. Kawai, G.E.W. Bauer, S. Maekawa, E. Saitoh, *Spin Seebeck insulator*, Nature Materials **9**, 894 (2010).

[102] H. Nakayama, M. Althammer, Y.T. Chen, K. Uchida, Y. Kajiwara, D. Kikuchi, T. Ohtani, S. Geprägs, M. Opel, S. Takahashi, R. Gross, G.E.W. Bauer, S.T.B. Goennenwein, E. Saitoh, *Spin Hall Magnetoresistance Induced by a Nonequilibrium Proximity Effect*, Physical Review Letters **110**, 206601 (2013).

[103] X.G. Wang, Z.W. Zhou, Y.Z. Nie, Q.L. Xia, G.H. Guo, *Self-consistent study of local and nonlocal magnetoresistance in a YIG/Pt bilayer*, Physical Review B **97**, 094401 (2018).

[104] N. Vlietstra, J. Shan, V. Castel, B.J. van Wees, J. Ben Youssef, *Spin-Hall magnetoresistance in platinum on yttrium iron garnet: Dependence on platinum thickness and in-plane/out-of-plane magnetization*, Physical Review B **87**, 184421 (2013).

[105] S. Meyer, R. Schlitz, S. Geprägs, M. Opel, H. Huebl, R. Gross, S.T.B. Goennenwein, *Anomalous Hall effect in YIG|Pt bilayers*, Applied Physics Letters **106**, 132402 (2015).

[106] J.M. Gomez-Perez, X.P. Zhang, F. Calavalle, M. Ilyn, C. González-Orellana, M. Gobbi, C. Rogero, A. Chuvilin, V.N. Golovach, L.E. Hueso, F.S. Bergeret, F. Casanova, *Strong Interfacial Exchange Field in a Heavy Metal/Ferromagnetic Insulator System Determined by Spin Hall Magnetoresistance*, Nano Letters **20**, 6815 (2020).

[107] K.W. Kim, *Spin transparency for the interface of an ultrathin magnet within the spin dephasing length*, Physical Review B **99**, 224415 (2019).

[108] M.D. Stiles, A. Zangwill, *Anatomy of spin-transfer torque*, Physical Review B **66**, 014407 (2002).

[109] S.S.L. Zhang, S. Zhang, *Magnon Mediated Electric Current Drag Across a Ferromagnetic Insulator Layer*, Physical Review Letters **109**, 096603 (2012).

[110] S.S.L. Zhang, S. Zhang, *Spin convertance at magnetic interfaces*, Physical Review B **86**, 214424 (2012).

[111] J. Barker, G.E. Bauer, *Thermal Spin Dynamics of Yttrium Iron Garnet*, Physical Review Letters **117** (2016).

[112] S. Geprags, A. Kehlberger, F.D. Coletta, Z. Qiu, E.J. Guo, T. Schulz, C. Mix, S. Meyer, A. Kamra, M. Althammer, H. Huebl, G. Jakob, Y. Ohnuma, H. Adachi, J. Barker, S. Maekawa, G.E.W. Bauer, E. Saitoh, R. Gross, S.T.B. Goennenwein, M. Klaui, *Origin of the spin Seebeck effect in compensated ferrimagnets*, Nature Communications **7**, (2016).

[113] J. Cramer, E.J. Guo, S. Geprägs, A. Kehlberger, Y.P. Ivanov, K. Ganzhorn, F.D. Coletta, M. Althammer, H. Huebl, R. Gross, J. Kosel, M. Kläui, S.T.B. Goennenwein, *Magnon Mode Selective Spin Transport in Compensated Ferrimagnets*, Nano Letters **17**, 3334 (2017).

[114] Y. Ohnuma, H. Adachi, E. Saitoh, S. Maekawa, *Spin Seebeck effect in antiferromagnets and compensated ferrimagnets*, Physical Review B **87**, 014423 (2013).

[115] C. Kim, S. Lee, H.G. Kim, J.H. Park, K.W. Moon, J.Y. Park, J.M. Yuk, K.J. Lee, B.G. Park, S.K. Kim, K.J. Kim, C. Hwang, *Distinct handedness of spin wave*

across the compensation temperatures of ferrimagnets, Nature Materials **19**, 980 (2020).

[116] K. Shen, *Pure spin current in antiferromagnetic insulators*, Physical Review B **100**, 094423 (2019).

[117] R. Lebrun, A. Ross, S.A. Bender, A. Qaiumzadeh, L. Baldrati, J. Cramer, A. Brataas, R.A. Duine, M. Kläui, *Tunable long-distance spin transport in a crystalline antiferromagnetic iron oxide*, Nature **561**, 222 (2018).

[118] S.M. Wu, W. Zhang, A. KC, P. Borisov, J.E. Pearson, J.S. Jiang, D. Lederman, A. Hoffmann, A. Bhattacharya, *Antiferromagnetic Spin Seebeck Effect*, Physical Review Letters **116**, 097204 (2016).

[119] I. Dzyaloshinsky, *A thermodynamic theory of "weak" ferromagnetism of antiferromagnetics*, Journal of Physics and Chemistry of Solids **4**, 241 (1958).

[120] T. Moriya, *Anisotropic Superexchange Interaction and Weak Ferromagnetism*, Physical Review **120**, 91 (1960).

[121] K. Shen, *Magnon Spin Relaxation and Spin Hall Effect Due to the Dipolar Interaction in Antiferromagnetic Insulators*, Physical Review Letters **124**, 077201 (2020).

[122] K.S. Olsson, K. An, G.A. Fiete, J. Zhou, L. Shi, X. Li, *Pure Spin Current and Magnon Chemical Potential in a Nonequilibrium Magnetic Insulator*, Physical Review X **10**, 021029 (2020).

[123] K. Ganzhorn, T. Wimmer, J. Cramer, R. Schlitz, S. Geprägs, G. Jakob, R. Gross, H. Huebl, M. Kläui, S.T.B. Goennenwein, *Temperature dependence of the nonlocal spin Seebeck effect in YIG/Pt nanostructures*, AIP Advances **7**, 085102 (2017).

[124] J. Shan, L.J. Cornelissen, N. Vlietstra, J. Ben Youssef, T. Kuschel, R.A. Duine, B.J. van Wees, *Influence of yttrium iron garnet thickness and heater opacity on the nonlocal transport of electrically and thermally excited magnons*, Physical Review B **94**, 174437 (2016).

[125] M. Schreier, A. Kamra, M. Weiler, J. Xiao, G.E.W. Bauer, R. Gross, S.T.B. Goennenwein, *Magnon, phonon, and electron temperature profiles and the spin Seebeck effect in magnetic insulator/normal metal hybrid structures*, Physical Review B **88**, 094410 (2013).

[126] T.H. Boyer, *The force on a magnetic dipole*, American Journal of Physics **56**, 688 (1988).

[127] S.M. Rezende, R.L. Rodríguez-Suárez, R.O. Cunha, A.R. Rodrigues, F.L.A. Machado, G.A. Fonseca Guerra, J.C. Lopez Ortiz, A. Azevedo, *Magnon spin-current theory for the longitudinal spin-Seebeck effect*, Physical Review B **89**, 014416 (2014).

[128] P. Drude, *Zur Elektronentheorie der Metalle*, Annalen der Physik **306**, 566 (1900).

[129] P. Drude, *Zur Elektronentheorie der Metalle; II. Teil. Galvanomagnetische und thermomagnetische Effecte*, Annalen der Physik **308**, 369 (1900).

[130] S. Geller, M. Gilleo, *The crystal structure and ferrimagnetism of yttrium-iron garnet, Y3Fe2(FeO4)3*, Journal of Physics and Chemistry of Solids **3**, 30 (1957).

[131] M.A. Gilleo, S. Geller, *Magnetic and Crystallographic Properties of Substituted Yttrium-Iron Garnet,* $3Y_2O_3 \cdot xM_2O_3 \cdot (5-x)Fe_2O_3$, Physical Review **110**, 73 (1958).

[132] C. Suchomski, *Strukturelle, optische und magnetische Eigenschaften von Nanokristallinen Metalloxid-Dünnfilmen mit mesoporöser Morphologie*, PhD thesis, Justus-Liebig-Universität Giessen (2012).

[133] G.F. Dionne, *Magnetic Oxides*, Springer US, 1. Ed. (2009).

[134] N. Miura, I. Oguro, S. Chikazumi, *Computer Simulation of Temperature and Field Dependences of Sublattice Magnetizations and Spin-Flip Transition in Gallium-Substituted Yttrium Iron Garnet*, Journal of the Physical Society of Japan **45**, 1534 (1978).

[135] P. Hansen, G. Winkler, K. Enke, *Landolt-Börnstein Group III: Condensed Matter (Part A: Garnets and Perovskites)*, Vol. 12A, Springer-Verlag (1978).

[136] H. Maier-Flaig, S. Klingler, C. Dubs, O. Surzhenko, R. Gross, M. Weiler, H. Huebl, S.T.B. Goennenwein, *Temperature-dependent magnetic damping of yttrium iron garnet spheres*, Physical Review B **95**, 214423 (2017).

[137] C. Dubs, O. Surzhenko, R. Linke, A. Danilewsky, U. Brückner, J. Dellith, *Sub-micrometer yttrium iron garnet LPE films with low ferromagnetic resonance losses*, Journal of Physics D: Applied Physics **50**, 204005 (2017).

[138] S. Klingler, H. Maier-Flaig, C. Dubs, O. Surzhenko, R. Gross, H. Huebl, S.T.B. Goennenwein, M. Weiler, *Gilbert damping of magnetostatic modes in a yttrium iron garnet sphere*, Applied Physics Letters **110**, 092409 (2017).

[139] M. Haertinger, C.H. Back, J. Lotze, M. Weiler, S. Geprägs, H. Huebl, S.T.B. Goennenwein, G. Woltersdorf, *Spin pumping in YIG/Pt bilayers as a function of layer thickness*, Physical Review B **92**, 054437 (2015).

[140] O. d'Allivy Kelly, A. Anane, R. Bernard, J.B. Youssef, C. Hahn, A.H. Molpeceres, C. Carrétéro, E. Jacquet, C. Deranlot, P. Bortolotti, R. Lebourgeois, J.C. Mage, G. de Loubens, O. Klein, V. Cros, A. Fert, *Inverse spin Hall effect in nanometer-thick yttrium iron garnet/Pt system*, Applied Physics Letters **103**, 082408 (2013).

[141] A.V. Chumak, A.A. Serga, M.B. Jungfleisch, R. Neb, D.A. Bozhko, V.S. Tiberkevich, B. Hillebrands, *Direct detection of magnon spin transport by the inverse spin Hall effect*, Applied Physics Letters **100**, 082405 (2012).

[142] A.H. Morrish, *Canted Antiferromagnetism: Hematite*, WORLD SCIENTIFIC (1995).

[143] E.J. Samuelsen, G. Shirane, *Inelastic neutron scattering investigation of spin waves and magnetic interactions in α-Fe2O3*, physica status solidi (b) **42**, 241 (1970).

[144] R.A. Alikhanov, Ž. Dimitrijević, S. Kraśnicki, H. Rżany, J. Todorović, A. Wanic, *Investigation of Magnon Dispersion Relation in α-Fe2O3- Additional Data*, physica status solidi (b) **41**, K103 (1970).

[145] F.J. Morin, *Magnetic Susceptibility of αFe_2O_3 and αFe_2O_3 with Added Titanium*, Physical Review **78**, 819 (1950).

[146] P.J. Besser, A.H. Morrish, C.W. Searle, *Magnetocrystalline Anisotropy of Pure and Doped Hematite*, Physical Review **153**, 632 (1967).

[147] R. Nathans, S.J. Pickart, H.A. Alperin, P.J. Brown, *Polarized-Neutron Study of Hematite*, Physical Review **136**, A1641 (1964).

[148] J.C. Marmeggi, D. Hohlwein, E.F. Bertaut, *Magnetic neutron laue diffraction study of the domain distribution in α-Fe2O3*, Physica Status Solidi (a) **39**, 57 (1977).

[149] J.A. Eaton, A.H. Morrish, *Magnetic Domains in Hematite At and Above the Morin Transition*, Journal of Applied Physics **40**, 3180 (1969).

[150] A. Ross, R. Lebrun, O. Gomonay, D.A. Grave, A. Kay, L. Baldrati, S. Becker, A. Qaiumzadeh, C. Ulloa, G. Jakob, F. Kronast, J. Sinova, R. Duine, A. Brataas, A. Rothschild, M. Kläui, *Propagation Length of Antiferromagnetic Magnons Governed by Domain Configurations*, Nano Letters **20**, 306 (2020).

[151] J. Han, P. Zhang, Z. Bi, Y. Fan, T.S. Safi, J. Xiang, J. Finley, L. Fu, R. Cheng, L. Liu, *Birefringence-like spin transport via linearly polarized antiferromagnetic magnons*, Nature Nanotechnology (2020).

[152] D. Tian, Y. Li, D. Qu, S.Y. Huang, X. Jin, C.L. Chien, *Manipulation of pure spin current in ferromagnetic metals independent of magnetization*, Physical Review B **94**, 020403 (2016).

[153] T. McGuire, R. Potter, *Anisotropic magnetoresistance in ferromagnetic 3d alloys*, IEEE Transactions on Magnetics **11**, 1018 (1975).

[154] T. Kimura, Y. Otani, T. Sato, S. Takahashi, S. Maekawa, *Room-Temperature Reversible Spin Hall Effect*, Physical Review Letters **98**, 156601 (2007).

[155] J. Sinova, S.O. Valenzuela, J. Wunderlich, C.H. Back, T. Jungwirth, *Spin Hall effects*, Review of Modern Physics **87**, 1213 (2015).

[156] A. Hamadeh, O. d'Allivy Kelly, C. Hahn, H. Meley, R. Bernard, A.H. Molpeceres, V.V. Naletov, M. Viret, A. Anane, V. Cros, S.O. Demokritov, J.L. Prieto, M. Muñoz, G. de Loubens, O. Klein, *Full Control of the Spin-Wave Damping in a Magnetic Insulator Using Spin-Orbit Torque*, Physical Review Letters **113**, 197203 (2014).

[157] N. Nagaosa, J. Sinova, S. Onoda, A.H. MacDonald, N.P. Ong, *Anomalous Hall effect*, Review of Modern Physics **82**, 1539 (2010).

[158] H. Wang, C. Du, P.C. Hammel, F. Yang, *Spin current and inverse spin Hall effect in ferromagnetic metals probed by Y3Fe5O12-based spin pumping*, Applied Physics Letters **104**, 202405 (2014).

[159] T. Taniguchi, J. Grollier, M. Stiles, *Spin-Transfer Torques Generated by the Anomalous Hall Effect and Anisotropic Magnetoresistance*, Physical Review Applied **3** (2015).

[160] V.P. Amin, J. Zemen, M.D. Stiles, *Interface-Generated Spin Currents*, Physical Review Letters **121**, 136805 (2018).

[161] K. Ganzhorn, S. Klingler, T. Wimmer, S. Geprägs, R. Gross, H. Huebl, S.T.B. Goennenwein, *Magnon-based logic in a multi-terminal YIG/Pt nanostructure*, Applied Physics Letters **109**, 022405 (2016).

[162] M. Althammer, *Pure spin currents in magnetically ordered insulator/normal metal heterostructures*, Journal of Physics D: Applied Physics **51**, 313001 (2018).

[163] J.D. Gibbons, D. MacNeill, R.A. Buhrman, D.C. Ralph, *Reorientable Spin Direction for Spin Current Produced by the Anomalous Hall Effect*, Physical Review Applied **9** (2018).

[164] S. Iihama, T. Taniguchi, K. Yakushiji, A. Fukushima, Y. Shiota, S. Tsunegi, R. Hiramatsu, S. Yuasa, Y. Suzuki, H. Kubota, *Spin-transfer torque induced by the spin anomalous Hall effect*, Nature Electronics **1**, 120 (2018).

[165] M.A.W. Schoen, D. Thonig, M.L. Schneider, T.J. Silva, H.T. Nembach, O. Eriksson, O. Karis, J.M. Shaw, *Ultra-low magnetic damping of a metallic ferromagnet*, Nature Physics **12**, 839 (2016).

[166] L.J. Cornelissen, B.J. van Wees, *Magnetic field dependence of the magnon spin diffusion length in the magnetic insulator yttrium iron garnet*, Physical Review B **93**, 020403 (2016).

[167] W. Zhang, M.B. Jungfleisch, W. Jiang, Y. Liu, J.E. Pearson, S.G.E.t. Velthuis, A. Hoffmann, F. Freimuth, Y. Mokrousov, *Reduced spin-Hall effects from magnetic proximity*, Physical Review B **91**, 115316 (2015).

[168] S. Geprägs, S. Meyer, S. Altmannshofer, M. Opel, F. Wilhelm, A. Rogalev, R. Gross, S.T.B. Goennenwein, *Investigation of induced Pt magnetic polarization in Pt/$Y_3Fe_5O_{12}$ bilayers*, Applied Physics Letters **101**, 262407 (2012).

[169] T. Kikkawa, M. Suzuki, J. Okabayashi, K.i. Uchida, D. Kikuchi, Z. Qiu, E. Saitoh, *Detection of induced paramagnetic moments in Pt on $Y_3Fe_5O_{12}$ via x-ray magnetic circular dichroism*, Physical Review B **95**, 214416 (2017).

[170] Y. Omori, E. Sagasta, Y. Niimi, M. Gradhand, L.E. Hueso, F. Casanova, Y. Otani, *Relation between spin Hall effect and anomalous Hall effect in 3d ferromagnetic metals*, Physical Review B **99**, 014403 (2019).

[171] L.J. Cornelissen, J. Shan, B.J. van Wees, *Temperature dependence of the magnon spin diffusion length and magnon spin conductivity in the magnetic insulator yttrium iron garnet*, Physical Review B **94**, 180402 (2016).

[172] L.J. Cornelissen, J. Liu, B.J. van Wees, R.A. Duine, *Spin-Current-Controlled Modulation of the Magnon Spin Conductance in a Three-Terminal Magnon Transistor*, Physical Review Letters **120**, 097702 (2018).

[173] G. Zahnd, L. Vila, V.T. Pham, M. Cosset-Cheneau, W. Lim, A. Brenac, P. Laczkowski, A. Marty, J.P. Attané, *Spin diffusion length and polarization of ferromagnetic metals measured by the spin-absorption technique in lateral spin valves*, Physical Review B **98**, 174414 (2018).

[174] E.C. Stoner, E.P. Wohlfarth, *A Mechanism of Magnetic Hysteresis in Heterogeneous Alloys*, Philosophical Transactions of the Royal Society A: Mathematical, Physical and Engineering Sciences **240**, 599 (1948).

[175] B.F. Miao, S.Y. Huang, D. Qu, C.L. Chien, *Inverse Spin Hall Effect in a Ferromagnetic Metal*, Physical Review Letters **111** (2013).

[176] J. Ahopelto, G. Ardila, L. Baldi, F. Balestra, D. Belot, G. Fagas, S.D. Gendt, D. Demarchi, M. Fernandez-Bolaños, D. Holden, A. Ionescu, G. Meneghesso, A. Mocuta, M. Pfeffer, R. Popp, E. Sangiorgi, C.S. Torres, *NanoElectronics*

roadmap for Europe: From nanodevices and innovative materials to system integration, Solid-State Electronics **155**, 7 (2019).

[177] R. Jansen, *Silicon spintronics*, Nature Materials **11**, 400 (2012).

[178] A. Hoffmann, *Pure spin-currents*, physica status solidi (c) **4**, 4236 (2007).

[179] M. Coll, J. Fontcuberta, M. Althammer, M. Bibes, H. Boschker, A. Calleja, G. Cheng, M. Cuoco, R. Dittmann, B. Dkhil, I.E. Baggari, M. Fanciulli, I. Fina, E. Fortunato, C. Frontera, S. Fujita, V. Garcia, S. Goennenwein, C.G. Granqvist, J. Grollier, R. Gross, A. Hagfeldt, G. Herranz, K. Hono, E. Houwman, M. Huijben, A. Kalaboukhov, D. Keeble, G. Koster, L. Kourkoutis, J. Levy, M. Lira-Cantu, J. MacManus-Driscoll, J. Mannhart, R. Martins, S. Menzel, T. Mikolajick, M. Napari, M. Nguyen, G. Niklasson, C. Paillard, S. Panigrahi, G. Rijnders, F. Sánchez, P. Sanchis, S. Sanna, D. Schlom, U. Schroeder, K. Shen, A. Siemon, M. Spreitzer, H. Sukegawa, R. Tamayo, J. van den Brink, N. Pryds, F.M. Granozio, *Towards Oxide Electronics: a Roadmap*, Applied Surface Science **482**, 1 (2019).

[180] M. Collet, X. de Milly, O. d'Allivy Kelly, V.V. Naletov, R. Bernard, P. Bortolotti, J.B. Youssef, V.E. Demidov, S.O. Demokritov, J.L. Prieto, M. Muñoz, V. Cros, A. Anane, G. de Loubens, O. Klein, *Generation of coherent spin-wave modes in yttrium iron garnet microdiscs by spin–orbit torque*, Nature Communications **7**, 10377 (2016).

[181] M. Evelt, V.E. Demidov, V. Bessonov, S.O. Demokritov, J.L. Prieto, M. Muñoz, J.B. Youssef, V.V. Naletov, G. de Loubens, O. Klein, M. Collet, K. Garcia-Hernandez, P. Bortolotti, V. Cros, A. Anane, *High-efficiency control of spin-wave propagation in ultra-thin yttrium iron garnet by the spin-orbit torque*, Applied Physics Letters **108**, 172406 (2016).

[182] M. Evelt, L. Soumah, A.B. Rinkevich, S.O. Demokritov, A. Anane, V. Cros, J. BenYoussef, G. de Loubens, O. Klein, P. Bortolotti, V.E. Demidov, *Emission of Coherent Propagating Magnons by Insulator-Based Spin-Orbit-Torque Oscillators*, Physical Review Applied **10**, 041002 (2018).

[183] M. Tsoi, A.G.M. Jansen, J. Bass, W.C. Chiang, M. Seck, V. Tsoi, P. Wyder, *Excitation of a Magnetic Multilayer by an Electric Current*, Physical Review Letters **80**, 4281 (1998).

[184] V.E. Demidov, S. Urazhdin, H. Ulrichs, V. Tiberkevich, A. Slavin, D. Baither, G. Schmitz, S.O. Demokritov, *Magnetic nano-oscillator driven by pure spin current*, Nature Materials **11**, 1028 (2012).

[185] A. Vansteenkiste, J. Leliaert, M. Dvornik, M. Helsen, F. Garcia-Sanchez, B.V. Waeyenberge, *The design and verification of MuMax3*, AIP Advances **4**, 107133 (2014).

[186] S.A. Bender, R.A. Duine, Y. Tserkovnyak, *Electronic Pumping of Quasiequilibrium Bose-Einstein-Condensed Magnons*, Physical Review Letters **108**, 246601 (2012).

[187] S.A. Bender, R.A. Duine, A. Brataas, Y. Tserkovnyak, *Dynamic phase diagram of dc-pumped magnon condensates*, Physical Review B **90**, 094409 (2014).

[188] S. Takei, *Spin transport in an electrically driven magnon gas near Bose-Einstein condensation: Hartree-Fock-Keldysh theory*, Physical Review B **100**, 134440 (2019).

[189] B. Hillebrands, A. Thiaville (Eds.), *Spin Dynamics in Confined Magnetic Structures III*, Springer Berlin Heidelberg (2006).

[190] D.D. Stancil, A. Prabhakar, *Spin Waves*, Springer US (2009).

[191] W. Zhang, W. Han, X. Jiang, S.H. Yang, S.S.P. Parkin, *Role of transparency of platinum–ferromagnet interfaces in determining the intrinsic magnitude of the spin Hall effect*, Nature Physics **11**, 496 (2015).

[192] M. Zwierzycki, Y. Tserkovnyak, P.J. Kelly, A. Brataas, G.E.W. Bauer, *First-principles study of magnetization relaxation enhancement and spin transfer in thin magnetic films*, Physical Review B **71**, 064420 (2005).

[193] E. Barati, M. Cinal, D.M. Edwards, A. Umerski, *Gilbert damping in magnetic layered systems*, Physical Review B **90**, 014420 (2014).

[194] C. Kittel, *On the Theory of Ferromagnetic Resonance Absorption*, Physical Review **73**, 155 (1948).

[195] P. Krivosik, N. Mo, S. Kalarickal, C.E. Patton, *Hamiltonian formalism for two magnon scattering microwave relaxation: Theory and applications*, Journal of Applied Physics **101**, 083901 (2007).

[196] M. Schreier, N. Roschewsky, E. Dobler, S. Meyer, H. Huebl, R. Gross, S.T.B. Goennenwein, *Current heating induced spin Seebeck effect*, Applied Physics Letters **103**, 242404 (2013).

[197] N. Thiery, A. Draveny, V.V. Naletov, L. Vila, J.P. Attané, C. Beigné, G. de Loubens, M. Viret, N. Beaulieu, J. Ben Youssef, V.E. Demidov, S.O. Demokritov, A.N. Slavin, V.S. Tiberkevich, A. Anane, P. Bortolotti, V. Cros, O. Klein, *Nonlinear spin conductance of yttrium iron garnet thin films driven by large spin-orbit torque*, Physical Review B **97**, 060409 (2018).

[198] J. Shan, P. Bougiatioti, L. Liang, G. Reiss, T. Kuschel, B.J. van Wees, *Nonlocal magnon spin transport in NiFe2O4 thin films*, Applied Physics Letters **110**, 132406 (2017).

[199] J. Li, Y. Xu, M. Aldosary, C. Tang, Z. Lin, S. Zhang, R. Lake, J. Shi, *Observation of magnon-mediated current drag in Pt/yttrium iron garnet/Pt(Ta) trilayers*, Nature Communications **7**, 10858 (2016).

[200] J. Flipse, F.K. Dejene, D. Wagenaar, G.E.W. Bauer, J.B. Youssef, B.J. van Wees, *Observation of the Spin Peltier Effect for Magnetic Insulators*, Physical Review Letters **113**, 027601 (2014).

[201] H. Wang, C. Du, P.C. Hammel, F. Yang, *Comparative determination of Y3Fe5O12/Pt interfacial spin mixing conductance by spin-Hall magnetoresistance and spin pumping*, Applied Physics Letters **110**, 062402 (2017).

[202] N. Thiery, V.V. Naletov, L. Vila, A. Marty, A. Brenac, J.F. Jacquot, G. de Loubens, M. Viret, A. Anane, V. Cros, J. Ben Youssef, N. Beaulieu, V.E. Demidov, B. Divinskiy, S.O. Demokritov, O. Klein, *Electrical properties of epitaxial yttrium iron garnet ultrathin films at high temperatures*, Physical Review B **97**, 064422 (2018).

[203] K. ichi Uchida, H. Adachi, T. Ota, H. Nakayama, S. Maekawa, E. Saitoh, *Observation of longitudinal spin-Seebeck effect in magnetic insulators*, Applied Physics Letters **97**, 172505 (2010).

[204] H.H. Landault, R. Boernstein, *Part A: Garnets and Perovskites*, Springer-Verlag (1978).

[205] V.E. Demidov, S. Urazhdin, E.R.J. Edwards, M.D. Stiles, R.D. McMichael, S.O. Demokritov, *Control of Magnetic Fluctuations by Spin Current*, Physical Review Letters **107**, 107204 (2011).

[206] Z. Duan, A. Smith, L. Yang, B. Youngblood, J. Lindner, V.E. Demidov, S.O. Demokritov, I.N. Krivorotov, *Nanowire spin torque oscillator driven by spin orbit torques*, Nature Communications **5** (2014).

[207] A. Slavin, V. Tiberkevich, *Spin Wave Mode Excited by Spin-Polarized Current in a Magnetic Nanocontact is a Standing Self-Localized Wave Bullet*, Physical Review Letters **95**, 237201 (2005).

[208] J. Liu, F. Feringa, B. Flebus, L.J. Cornelissen, J.C. Leutenantsmeyer, R.A. Duine, B.J. van Wees, *Microwave control of thermal-magnon spin transport*, Physical Review B **99**, 054420 (2019).

[209] E. Sonin, *Spin currents and spin superfluidity*, Advances in Physics **59**, 181 (2010).

[210] D.A. Bozhko, A.A. Serga, P. Clausen, V.I. Vasyuchka, F. Heussner, G.A. Melkov, A. Pomyalov, V.S. L'vov, B. Hillebrands, *Supercurrent in a room-temperature Bose–Einstein magnon condensate*, Nature Physics **12**, 1057 (2016).

[211] H. Skarsvåg, C. Holmqvist, A. Brataas, *Spin Superfluidity and Long-Range Transport in Thin-Film Ferromagnets*, Physical Review Letters **115**, 237201 (2015).

[212] A. Qaiumzadeh, H. Skarsvåg, C. Holmqvist, A. Brataas, *Spin Superfluidity in Biaxial Antiferromagnetic Insulators*, Physical Review Letters **118**, 137201 (2017).

[213] S. Takei, Y. Tserkovnyak, *Superfluid Spin Transport Through Easy-Plane Ferromagnetic Insulators*, Physical Review Letters **112**, 227201 (2014).

[214] J.M. Gomez-Perez, S. Vélez, L.E. Hueso, F. Casanova, *Differences in the magnon diffusion length for electrically and thermally driven magnon currents in* $Y_3Fe_5O_{12}$, Physical Review B **101**, 184420 (2020).

[215] S. Rezende, R. Rodríguez-Suárez, R. Cunha, J. López Ortiz, A. Azevedo, *Bulk magnon spin current theory for the longitudinal spin Seebeck effect*, Journal of Magnetism and Magnetic Materials **400**, 171 (2016).

[216] A. Akopyan, N. Prasai, B.A. Trump, G.G. Marcus, T.M. McQueen, J.L. Cohn, *Spin Seebeck effect in* Cu_2OSeO_3*: Test of bulk magnon spin current theory*, Physical Review B **101**, 100407 (2020).

[217] H. Ulrichs, *From chaotic spin dynamics to noncollinear spin textures in YIG nanofilms by spin-current injection*, Physical Review B **102**, 174428 (2020).

[218] S. Klingler, A.V. Chumak, T. Mewes, B. Khodadadi, C. Mewes, C. Dubs, O. Surzhenko, B. Hillebrands, A. Conca, *Measurements of the exchange stiffness of YIG films using broadband ferromagnetic resonance techniques*, Journal of Physics D: Applied Physics **48**, 015001 (2014).

[219] E.E. Anderson, *Molecular Field Model and the Magnetization of YIG*, Physical Review **134**, A1581 (1964).

[220] U. Atxitia, D. Hinzke, O. Chubykalo-Fesenko, U. Nowak, H. Kachkachi, O.N. Mryasov, R.F. Evans, R.W. Chantrell, *Multiscale modeling of magnetic materials: Temperature dependence of the exchange stiffness*, Physical Review B **82**, 134440 (2010).

[221] P. Nieves, O. Chubykalo-Fesenko, *Modeling of Ultrafast Heat- and Field-Assisted Magnetization Dynamics in FePt*, Physical Review Applied **5**, 014006 (2016).

[222] B. Divinskiy, S. Urazhdin, S.O. Demokritov, V.E. Demidov, *Controlled nonlinear magnetic damping in spin-Hall nano-devices*, Nature Communications **10** (2019).

[223] M. Mohseni, A. Qaiumzadeh, A.A. Serga, A. Brataas, B. Hillebrands, P. Pirro, *Bose–Einstein condensation of nonequilibrium magnons in confined systems*, New Journal of Physics **22**, 083080 (2020).

[224] Y.M. Bunkov, G.E. Volovik, *Magnon BEC and Spin Superfluidity: a 3He primer*, arXiv:0904.3889 (2009).

[225] T. Jungwirth, X. Marti, P. Wadley, J. Wunderlich, *Antiferromagnetic spintronics*, Nature Nanotechnology **11**, 231 (2016).

[226] V. Baltz, A. Manchon, M. Tsoi, T. Moriyama, T. Ono, Y. Tserkovnyak, *Antiferromagnetic spintronics*, Reviews of Modern Physics **90**, 015005 (2018).

[227] J. Li, C.B. Wilson, R. Cheng, M. Lohmann, M. Kavand, W. Yuan, M. Aldosary, N. Agladze, P. Wei, M.S. Sherwin, J. Shi, *Spin current from sub-terahertz-generated antiferromagnetic magnons*, Nature **578**, 70 (2020).

[228] P. Vaidya, S.A. Morley, J. van Tol, Y. Liu, R. Cheng, A. Brataas, D. Lederman, E. del Barco, *Subterahertz spin pumping from an insulating antiferromagnet*, Science **368**, 160 (2020).

[229] P. Němec, M. Fiebig, T. Kampfrath, A.V. Kimel, *Antiferromagnetic opto-spintronics*, Nature Physics **14**, 229 (2018).

[230] K. Olejník, T. Seifert, Z. Kašpar, V. Novák, P. Wadley, R.P. Campion, M. Baumgartner, P. Gambardella, P. Němec, J. Wunderlich, J. Sinova, P. Kužel, M. Müller, T. Kampfrath, T. Jungwirth, *Terahertz electrical writing speed in an antiferromagnetic memory*, Science Advances **4**, eaar3566 (2018).

[231] G.E.W. Bauer, E. Saitoh, B.J. van Wees, *Spin caloritronics*, Nature Materials **11**, 391 (2012).

[232] A.V. Chumak, V.I. Vasyuchka, A.A. Serga, B. Hillebrands, *Magnon spintronics*, Nature Physics **11**, 453 (2015).

[233] K. Nakata, P. Simon, D. Loss, *Spin currents and magnon dynamics in insulating magnets*, Journal of Physics D: Applied Physics **50**, 114004 (2017).

[234] W. Yuan, Q. Zhu, T. Su, Y. Yao, W. Xing, Y. Chen, Y. Ma, X. Lin, J. Shi, R. Shindou, X.C. Xie, W. Han, *Experimental signatures of spin superfluid ground state in canted antiferromagnet Cr2O3 via nonlocal spin transport*, Science Advances **4**, eaat1098 (2018).

[235] D. Hou, Z. Qiu, E. Saitoh, *Spin transport in antiferromagnetic insulators: progress and challenges*, NPG Asia Materials **11**, 35 (2019).

[236] A. Kamra, E. Thingstad, G. Rastelli, R.A. Duine, A. Brataas, W. Belzig, A. Sudbø, *Antiferromagnetic magnons as highly squeezed Fock states underlying quantum correlations*, Physical Review B **100**, 174407 (2019).

[237] A. Kamra, U. Agrawal, W. Belzig, *Noninteger-spin magnonic excitations in untextured magnets*, Physical Review B **96**, 020411 (2017).

[238] L. Liensberger, A. Kamra, H. Maier-Flaig, S. Geprägs, A. Erb, S.T.B. Goennenwein, R. Gross, W. Belzig, H. Huebl, M. Weiler, *Exchange-Enhanced Ultrastrong Magnon-Magnon Coupling in a Compensated Ferrimagnet*, Physical Review Letters **123**, 117204 (2019).

[239] R. Cheng, M.W. Daniels, J.G. Zhu, D. Xiao, *Antiferromagnetic Spin Wave Field-Effect Transistor*, Scientific Reports **6**, 24223 (2016).

[240] M.W. Daniels, R. Cheng, W. Yu, J. Xiao, D. Xiao, *Nonabelian magnonics in antiferromagnets*, Physical Review B **98**, 134450 (2018).

[241] M. Kawano, C. Hotta, *Thermal Hall effect and topological edge states in a square-lattice antiferromagnet*, Physical Review B **99**, 054422 (2019).

[242] M. Kawano, Y. Onose, C. Hotta, *Designing Rashba–Dresselhaus effect in magnetic insulators*, Communications Physics **2**, 27 (2019).

[243] A. Mook, J. Henk, I. Mertig, *Edge states in topological magnon insulators*, Physical Review B **90**, 024412 (2014).

[244] M.Z. Hasan, C.L. Kane, *Colloquium: Topological insulators*, Reviews of Modern Physics **82**, 3045 (2010).

[245] J. Liu, L. Wang, K. Shen, *Dipolar spin waves in uniaxial easy-axis antiferromagnets: A natural topological nodal-line semimetal*, Physical Review Research **2**, 023282 (2020).

[246] Y. Tokura, K. Yasuda, A. Tsukazaki, *Magnetic topological insulators*, Nature Reviews Physics **1**, 126 (2019).

[247] R. Cheng, S. Okamoto, D. Xiao, *Spin Nernst Effect of Magnons in Collinear Antiferromagnets*, Physical Review Letters **117**, 217202 (2016).

[248] V.A. Zyuzin, A.A. Kovalev, *Magnon Spin Nernst Effect in Antiferromagnets*, Physical Review Letters **117**, 217203 (2016).

[249] J. Fabian, A. Matos-Abiague, C. Ertler, P. Stano, I. Zutic, *Semiconductor Spintronics*, Acta Physica Slovaca **57**, 565 (2007).

[250] J.M. Kikkawa, D.D. Awschalom, *Lateral drag of spin coherence in gallium arsenide*, Nature **397**, 139 (1999).

[251] F.J. Jedema, H.B. Heersche, A.T. Filip, J.J.A. Baselmans, B.J. van Wees, *Electrical detection of spin precession in a metallic mesoscopic spin valve*, Nature **416**, 713 (2002).

[252] S. Datta, B. Das, *Electronic analog of the electro-optic modulator*, Applied Physics Letters **56**, 665 (1990).

[253] J.A. Jones, A.J. D'Addario, B.L. Rojec, G. Milione, E.J. Galvez, *The Poincaré-sphere approach to polarization: Formalism and new labs with Poincaré beams*, American Journal of Physics **84**, 822 (2016).

[254] B. Flebus, *Chemical potential of an antiferromagnetic magnon gas*, Physical Review B **100**, 064410 (2019).

[255] M. Wu, J. Jiang, M. Weng, *Spin dynamics in semiconductors*, Physics Reports **493**, 61 (2010).

[256] F. Keffer, R. Loudon, *Simple Physical Theory of Spin Wave Interactions*, Journal of Applied Physics **32**, S2 (1961).

[257] M. Bloch, *Magnon Renormalization in Ferromagnets Near the Curie Point*, Physical Review Letters **9**, 286 (1962).

[258] M. Aspelmeyer, T.J. Kippenberg, F. Marquardt, *Cavity optomechanics*, Review of Modern Physics **86**, 1391 (2014).

[259] D. MacNeill, J.T. Hou, D.R. Klein, P. Zhang, P. Jarillo-Herrero, L. Liu, *Gigahertz Frequency Antiferromagnetic Resonance and Strong Magnon-Magnon Coupling in the Layered Crystal* $CrCl_3$, Physical Review Letters **123**, 047204 (2019).

[260] H. Huebl, C.W. Zollitsch, J. Lotze, F. Hocke, M. Greifenstein, A. Marx, R. Gross, S.T.B. Goennenwein, *High Cooperativity in Coupled Microwave Resonator Ferrimagnetic Insulator Hybrids*, Physical Review Letters **111**, 127003 (2013).

[261] R.E. Troncoso, S.A. Bender, A. Brataas, R.A. Duine, *Spin transport in thick insulating antiferromagnetic films*, Physical Review B **101**, 054404 (2020).

[262] R.A. Lefever, *1.1.2 Hematite alpha-Fe2O3 and hematite with substitutions*, in *Landolt-Börnstein - Group III Condensed Matter*, 8–16, Springer-Verlag.

[263] R. Lebrun, A. Ross, O. Gomonay, V. Baltz, U. Ebels, A.L. Barra, A. Qaiumzadeh, A. Brataas, J. Sinova, M. Kläui, *Long-distance spin-transport across the Morin phase transition up to room temperature in ultra-low damping single crystals of the antiferromagnet α-Fe2O3*, Nature Communications **11** (2020).

[264] K. Chen, W. Lin, C.L. Chien, S. Zhang, *Temperature dependence of angular momentum transport across interfaces*, Physical Review B **94**, 054413 (2016).

[265] J. Fontcuberta, H.B. Vasili, J. Gàzquez, F. Casanova, *On the Role of Interfaces on Spin Transport in Magnetic Insulator/Normal Metal Heterostructures*, Advanced Materials Interfaces **6**, 1900475 (2019).

[266] G.R. Hoogeboom, B.J. van Wees, *Nonlocal spin Seebeck effect in the bulk easy-plane antiferromagnet NiO*, Physical Review B **102**, 214415 (2020).

[267] J.P. Moore, R.S. Graves, *Absolute Seebeck coefficient of platinum from 80 to 340 K and the thermal and electrical conductivities of lead from 80 to 400 K*, Journal of Applied Physics **44**, 1174 (1973).

[268] M. Kockert, R. Mitdank, A. Zykov, S. Kowarik, S.F. Fischer, *Absolute Seebeck coefficient of thin platinum films*, Journal of Applied Physics **126**, 105106 (2019).

[269] R. Cheng, M.W. Daniels, J.G. Zhu, D. Xiao, *Ultrafast switching of antiferromagnets via spin-transfer torque*, Physical Review B **91**, 064423 (2015).

[270] J. Fischer, O. Gomonay, R. Schlitz, K. Ganzhorn, N. Vlietstra, M. Althammer, H. Huebl, M. Opel, R. Gross, S.T.B. Goennenwein, S. Geprägs, *Spin Hall magnetoresistance in antiferromagnet/heavy-metal heterostructures*, Physical Review B **97**, 014417 (2018).

[271] J. Fischer, M. Althammer, N. Vlietstra, H. Huebl, S.T. Goennenwein, R. Gross, S. Geprägs, M. Opel, *Large Spin Hall Magnetoresistance in Antiferromagnetic $\alpha-Fe_2O_3$/Pt Heterostructures*, Physical Review Applied **13**, 014019 (2020).

[272] S. Geprägs, M. Opel, J. Fischer, O. Gomonay, P. Schwenke, M. Althammer, H. Huebl, R. Gross, *Spin Hall magnetoresistance in antiferromagnetic insulators*, Journal of Applied Physics **127**, 243902 (2020).

[273] E.J. Guo, J. Cramer, A. Kehlberger, C.A. Ferguson, D.A. MacLaren, G. Jakob, M. Kläui, *Influence of Thickness and Interface on the Low-Temperature Enhancement of the Spin Seebeck Effect in YIG Films*, Physical Review X **6**, 031012 (2016).

[274] N. Roschewsky, *Spin Effect Experiments*, Master's thesis, Technische Universität München (2014).

[275] S. Meyer, M. Althammer, S. Geprägs, M. Opel, R. Gross, S.T.B. Goennenwein, *Temperature dependent spin transport properties of platinum inferred from spin Hall magnetoresistance measurements*, Applied Physics Letters **104**, 242411 (2014).

[276] K.S. Das, F.K. Dejene, B.J. van Wees, I.J. Vera-Marun, *Temperature dependence of the effective spin-mixing conductance probed with lateral non-local spin valves*, Applied Physics Letters **114**, 072405 (2019).

[277] K. Uchida, S. Takahashi, K. Harii, J. Ieda, W. Koshibae, K. Ando, S. Maekawa, E. Saitoh, *Observation of the spin Seebeck effect*, Nature **455**, 778 (2008).

[278] H. Adachi, K. ichi Uchida, E. Saitoh, S. Maekawa, *Theory of the spin Seebeck effect*, Reports on Progress in Physics **76**, 036501 (2013).

[279] D. Meier, D. Reinhardt, M. van Straaten, C. Klewe, M. Althammer, M. Schreier, S.T.B. Goennenwein, A. Gupta, M. Schmid, C.H. Back, J.M. Schmalhorst, T. Kuschel, G. Reiss, *Longitudinal spin Seebeck effect contribution in transverse spin Seebeck effect experiments in Pt/YIG and Pt/NFO*, Nature Communications **6** (2015).

[280] J. Gückelhorn, T. Wimmer, S. Geprägs, H. Huebl, R. Gross, M. Althammer, *Quantitative comparison of magnon transport experiments in three-terminal YIG/Pt nanostructures acquired via dc and ac detection techniques*, Applied Physics Letters **117**, 182401 (2020).

[281] J.F. Allen, A.D. Miesener, *Flow Phenomena in Liquid Helium II*, Nature **142**, 643 (1938).

[282] L.D. Landau, E. Lifshitz, , Butterworth-Heinemann (1980).

[283] B. Flebus, S.A. Bender, Y. Tserkovnyak, R.A. Duine, *Two-Fluid Theory for Spin Superfluidity in Magnetic Insulators*, Physical Review Letters **116**, 117201 (2016).

[284] C. Edwards, J.A. Lipa, M.J. Buckingham, *Specific Heat of Xenon Near the Critical Point*, Physical Review Letters **20**, 496 (1968).

[285] J.M.H. Levelt Sengers.

[286] G. Ahlers, *Heat Capacity at Constant Pressure near the Superfluid Transition in* He^4, Physical Review Letters **23**, 464 (1969).

[287] K.H. Mueller, G. Ahlers, F. Pobell, *Thermal expansion coefficient, scaling, and universality near the superfluid transition of* ^{4}He *under pressure*, Physical Review B **14**, 2096 (1976).

[288] J.A. Lipa, D.R. Swanson, J.A. Nissen, T.C.P. Chui, U.E. Israelsson, *Heat Capacity and Thermal Relaxation of Bulk Helium very near the Lambda Point*, Physical Review Letters **76**, 944 (1996).

[289] D.G. Cahill, R.O. Pohl, *Thermal conductivity of amorphous solids above the plateau*, Physical Review B **35**, 4067 (1987).

[290] D.G. Cahill, M. Katiyar, J.R. Abelson, *Thermal conductivity of a-Si:H thin films*, Physical Review B **50**, 6077 (1994).

[291] J. Liu, X.Y. Wei, G.E.W. Bauer, J.B. Youssef, B.J. van Wees, *Electrically induced strong modulation of magnon transport in ultrathin magnetic insulator films*, Physical Review B **103**, 214425 (2021).

[292] E. Karadza, *Modulation of Magnon Spin Transport in Yttrium Iron Garnet via Metallic Electrodes with Varying Spin Hall Angles*, Master thesis, Technische Universität München (2021).

[293] F.D. Czeschka, L. Dreher, M.S. Brandt, M. Weiler, M. Althammer, I.M. Imort, G. Reiss, A. Thomas, W. Schoch, W. Limmer, H. Huebl, R. Gross, S.T.B. Goennenwein, *Scaling Behavior of the Spin Pumping Effect in Ferromagnet-Platinum Bilayers*, Physical Review Letters **107**, 046601 (2011).

[294] C.H. Du, H.L. Wang, Y. Pu, T.L. Meyer, P.M. Woodward, F.Y. Yang, P.C. Hammel, *Probing the Spin Pumping Mechanism: Exchange Coupling with Exponential Decay in $Y_3Fe_5O_{12}$Barrier/Pt Heterostructures*, Physical Review Letters **111**, 247202 (2013).

[295] T. Brächer, P. Pirro, B. Hillebrands, *Parallel pumping for magnon spintronics: Amplification and manipulation of magnon spin currents on the micron-scale*, Physics Reports **699**, 1 (2017).

[296] M. Sparks, *Ferromagnetic-relaxation Theory*, McGraw-Hill advanced physics monograph series, McGraw-Hill (1964).

[297] J. Lustikova, Y. Shiomi, Y. Handa, E. Saitoh, *Spectral shape deformation in inverse spin Hall voltage in Y3Fe5O12|Pt bilayers at high microwave power levels*, Journal of Applied Physics **117**, 073901 (2015).

[298] H.G. Bauer, P. Majchrak, T. Kachel, C.H. Back, G. Woltersdorf, *Nonlinear spin-wave excitations at low magnetic bias fields*, Nature Communications **6** (2015).

[299] R. Iguchil, K. Ando, T. An, E. Saitoh, T. Sato, *Evaluation of Nonlinear Effect in High Power Spin Pumping in Polycrystalline Bi-Substituted Yttrium Iron Garnet (Bi:YIG)/Pt Bilayer Structure*, IEEE Transactions on Magnetics **48**, 3051 (2012).

[300] O. Karlqvist, *Calculation of the magnetic field in the ferromagnetic layer of a magnetic drum*, Henrik Lindståhls Bokhandel i Distribution (1954).

[301] J. Gückelhorn, T. Wimmer, M. Müller, S. Geprägs, H. Huebl, R. Gross, M. Althammer, *Magnon transport in YIG/Pt nanostructures with reduced effective magnetization*, In preparation (2021).

[302] T. Wimmer, J. Gueckelhorn, M. Opel, S. Geprägs, R. Gross, H. Huebl, M. Althammer, *Analysis of Critical Behaviour and Electrical Annealing of Spin Current-Controlled Magnon Transistor Devices*, In preparation (2021).

[303] T. Wimmer, R. Schlitz, S. Geprägs, H. Huebl, R. Gross, S.T.B. Goennenwein, M. Althammer, *Electrical background signals between ferromagnetic metal electrodes deposited on a nonmagnetic substrate*, In preparation (2021).

[304] T. Wimmer, J. Gückelhorn, S. Wimmer, S. Mankovsky, H. Ebert, M. Opel, S. Geprägs, R. Gross, H. Huebl, M. Althammer, *Low Temperature Suppression of the Spin Nernst Angle in Pt*, arXiv:2103.12697, submitted to Physical Review Letters (2021).

[305] M. Althammer, A.V. Singh, T. Wimmer, Z. Galazka, H. Huebl, M. Opel, R. Gross, A. Gupta, *Role of interface quality for the spin Hall magnetoresistance in nickel ferrite thin films with bulk-like magnetic properties*, Applied Physics Letters **115**, 092403 (2019).

[306] K. Ganzhorn, T. Wimmer, J. Barker, G.E.W. Bauer, Z. Qiu, E. Saitoh, N. Vlietstra, S. Geprägs, R. Gross, H. Huebl, S.T.B. Goennenwein, *Non-local magnon transport in the compensated ferrimagnet GdIG*, arXiv:1705.02871 (2017).

Acknowledgements - Danksagung

Die Anfertigung einer Doktorarbeit bedarf neben einer Menge Zeit (4,5 Jahre), ***Leiden***schaft, Frustrationstoleranz, Glück und Hingabe (sowie genügend Forschungsmittel), vor allem die tatkräftige Unterstützung einer Vielzahl an Menschen, denen ich zu großem Dank verpflichtet bin. Insbesondere möchte ich den folgenden Menschen persönlich *danken*:

- Professor Dr. Rudolf Gross zuallererst für das Vertrauen und die Möglichkeit, meine Doktorarbeit am WMI antreten zu dürfen. Des Weiteren für sein messerscharfes und bemerkenswert rasches Verständnis beliebig komplexer physikalischer Sachverhalte, welches die Qualität der aus dieser Arbeit stammenden Publikationen sichergestellt hat. Die Arbeitsatmosphäre und zugleich Produktivität, die unter seiner Leitung herrscht, sucht seinesgleichen.

- Dr. Matthias Althammer für die unvergleichliche Betreuung dieses Projekts. Dafür, mein erster Ansprechpartner für Angelegenheiten aller Art zu sein, sei es bezüglich Probleme im Labor, physikalischer Fragestellungen oder jeglicher Unklarheiten organisatorischer Art. Weiterhin möchte ich dir auch dafür danken, mir das Gefühl gegeben zu haben, auch *dumme* Fragen stellen zu können, für dein aufmerksames Interesse an meinen teils wilden und hoch spekulativen Interpretationen und deiner ruhigen Art, mich danach wieder auf den Boden der Tatsachen zurückzuholen. Darüber hinaus für die unzähligen Diskussionen über die Unmengen an Daten, deinen extrem hilfreichen Hinweisen und deiner physikalischen Intuition, die mich oft in die richtige Richtung gelenkt haben. Und zu guter Letzt auch für deinen lockeren Führungsstil, der auf den nicht-wissenschaftlichen Veranstaltungen des WMI sowie der Abendgestaltung auf diversen Konferenzen für eine lockere Atmossphäre gesorgt hat.

- Dr. Hans Hübl für die Co-Betreuung dieses Projekts, dein stets offenes Ohr bezüglich jeglicher festkörperphysikalischer Fragestellungen und vor allem dafür, dass du deine kostbare Zeit für diese Interaktionen so großzügig zur Verfügung stellst. Insbesondere auch für deinen besonderen Einsatz für unser (vermeintliches) Magnon Bose-Einstein Kondensat Projekt, das uns allen viel Nerven gekostet hat (und manchmal sogar die ein oder andere Umarmung zur Folge hatte). Deine sehr kritische Hinterfragung jeglicher

physikalischer Interpretation meiner Messdaten hatte einen großen Einfluss auf die Qualität unserer wissenschaftlichen Arbeiten. Insbesondere danke ich dir auch für eine sehr entspannte Zeit in Denver, wo wir aufgrund der kurzfristigen Absage des APS March Meetings *gestrandet* sind. Ich denke, wir haben das Beste daraus gemacht!

- Dr. Stephan Geprägs für deine unverzichtbare Expertise in der Herstellung magnetischer Dünnfilmkristalle, welche von essentieller Bedeutung für meine Arbeit waren. Weiterhin auch für deine Mühen in der Charakterisierung der besagten Dünnfilme und deinen wertvollen Kommentare zu meinen Messdaten in den DC-Meetings. Insbesondere möchte ich dir auch für deine generell positive Austrahlung danken, die die gute Arbeitsatmossphäre am WMI signifikant prägt.

- Dr. Mathias Weiler für deine sehr wichtigen Beiträge zu unserem 'zero effective damping' Projekt und deinem damit verbundenen großen Einsatz für den Erfolg der Publikation. Weiterhin für dein stets offenes Ohr für meine Fragen und deiner Expertise in der Hochfrequenzmesstechnik sowie Magnetisierungsdynamik, welche mir einige wichtige Konzepte näher gebracht hat.

- Dr. Matthias Opel für deine verantwortungsvolle Arbeit und Problembehebung in der EDV und deiner Bereitschaft, mir auch mal sonntags mit einem derartigen Problem zu Hilfe zu eilen, sowie für deine immer wieder wichtigen Hinweise zu unseren Messdaten in den zahlreichen DC-Meetings. Auch dir möchte ich für deine immer positive Art danken, die für eine entspannte Atmosphäre gesorgt hat. Zu guter Letzt auch für unsere gute Zeit auf den zwei JEMS Konferenzen in Mainz und Uppsala.

- Dr. Akashdeep Kamra for the great collaboration on the antiferromagnetic pseudospin project. Also I like to thank you for your great and intuitive insights into physics and for being the smartest and simultaneously most chill *theoretician* I have came to know.

- Prof. Dr. Hubert Ebert von der LMU München für die sehr unkomplizierte Kollaboration und die theoretische Unterstützung bezüglich unserer Arbeit zum transversen Spin Nernst Effekt.

- Allen meinen mitleidenden Doktoranden-Kollegen für die schöne Zeit am WMI. Darunter einerseits diejenigen, die (zum Teil zeitweise, zum Teil über die komplette Zeit) das Büro mit mir geteilt haben und die vielen Stunden und Tage sehr viel erträglicher gemacht haben: Stefan Klingler, Alma Dorantes Palacios, Qi Ming Chen, Daniel Schwienbacher, Luis Flacke. Hier möchte ich insbesondere Daniel und Luis herausheben, mit denen ich mich das ein oder andere Mal mit nicht-wissenschaftlichen, tiefgreifenden,

dämlichen sowie manchmal sogar mit physikalischen Diskussionen aufhalten konnte und welche den Arbeitsalltag erst interessant gemacht haben. An Daniel sei insbesondere gerichtet: *Septimana Vergens. Potatio!*

Andererseits natürlich ein großer Dank an all diejenigen Doktoranden, die ich außerhalb meines Büros von ihrer Arbeit abhalten konnte: Lukas Liensberger für unsere (leider erfolglosen) Versuche ein BLS Signal von (vermeintlichen) Magnon Bose-Einstein Kondensaten rauszukitzeln sowie deine häufige Hilfe bei der Bedienung von Hochfrequenz Messaufbauten. Philip Schmidt für eine interessante Tour in den fernen Osten Berlins. Manuel Müller für seine FMR Charakterisierung vieler meiner YIG Filme. Janine Gückelhorn für deine tatkräftige Unterstützung durch die Herstellung einer Vielzahl von YIG und Hämatit Filmen, die Fortführung des Magnon Transport Projektes, sowie deiner enormen Hilfe für mein MMM 2020 Poster. Gabriele Rager, Qi Ming Chen und Yuki Nojiri für eine gute Zusammenarbeit bei der Organisation des FOPRA Versuchs. Lukas Liensberger, Thomas Luschmann, Daniel Schwienbacher, Philip Schmidt und allen anderen die dabei waren ein fettes Danke für einen berauschenden Abend auf dem Oktoberfest 2019 (mit kostenlosem Hendl, *bester Tag meines Lebens!*).

- Kathrin Ganzhorn für ihre exzellente Betreuung meiner Masterarbeit, die mir den Erfolg dieser Dissertation erst ermöglicht hat.

- Meinen Bachelor-Studenten Johannes Schirk und Thomas Narr für eure schnelle Auffassungsgabe und euer gutes, selbstständiges Arbeiten. Ein besonderer Dank geht hier an Thomas, den ich während seiner Zeit als Werkstudent mit verschiedensten Arbeiten quälen durfte.

- Meiner ersten Master Studentin Birte Cöster, welche einen enorm wichtigen Beitrag für die Funktionalität der Magnon Transport Strukturen mittels Lift-Off Fabrikation geleistet hat, ohne die ich nicht so weit gekommen wäre. Weiterhin ein großes Dankeschön für deine *gute Laune* und einigen guten Lachern.

- Meinem Master Studenten Emir Karadža für seinen unermüdlichen Einsatz in der Fabrikation einer Vielzahl an Proben, dessen Funktionalität leider durch viele unvorhergesehene Hindernisse geprägt waren (ein gutes Beispiel für Murphy's law). Deine Hingabe hat sich ausgezahlt und wir konnten wichtige Ergebnisse aus dem Projekt ziehen, die ein wichtiger Schritt für unser Verständnis darstellen. Neben deines wissenschaftlichen Erfolgs, hast du mir gezeigt was *balkanische* Freundschaft und Fürsorge bedeutet, und ich durfte daher nicht nur einmal von köstlicher bosnischer Küche profitieren. Wenngleich sich unsere Weltanschauungen recht fundamental unterscheiden, danke ich dir auch für unsere längeren Diskussionen über religiöse und

weltliche Themen. Insgeheim hoffe ich ja, dich irgendwann überzeugen zu können, bis dahin können wir ja bei Schokolade und Tee/Kaffee bleiben, statt Schweinebraten und Bier.

- Meinem Master Studenten Korbinian Rubenbauer, der früh bewiesen hat, sehr gute Arbeit zu leisten und mir eine große Hilfe in einem wichtigen Projekt ist. Ich bin mir sicher, dass deine sehr strukturierte Arbeitsweise ein Erfolgsgarant für deine Masterarbeit ist.

- Simon Mendisch, Valentin Ahrens und Martina Kiechle für eine gute Zeit auf der JEMS 2019 in Uppsala.

- Unseren unverzichtbaren Reinigungskräften Sybilla Plöderl und Maria Botta für ihre positive Art und den zahlreichen "zwischen Tür und Angel" Gesprächen, die für einen kleinen Ausgleich in den manchmal sehr stressigen Tagen gesorgt haben.

- Der kompletten technischen Belegschaft des WMI, darunter alle Mitarbeiter der Werkstatt, der Helium-Halle und der Labortechniker. Ein riesengroßes Danke für eure Hilfsbereitschaft in allen Belangen, sowie eure essentiellen Beiträge zur Aufrechterhaltung des wissenschaftlichen Betriebs am WMI. Zudem ein weiteres großes Danke für eure wichtigen Beiträge zu den festlichen Anlässen des WMI, ohne euch würde das Ganze wahrscheinlich *sehr trocken* ausfallen.

- Dem Ganzen Team des Kickbox-Vereins (KBV) Erding und allen tollen Menschen, die ich dort kennenlernen durfte. Am Ende gibt es ja doch nichts Schöneres, als sich *gepflegt zu verdreschen*.

- Meinen engsten Freunden Franz (groß), Franz (alt), Jonas, Manuel, Christian, Jakob, Daniel, Simon, Max und Georg alias "Fron', "Schwäääänz", "Buabbe", "Mabbe", "Griese", "Blase", "Stobbe", "Simmal", "Mäx" und "Schorsch" für die nötige *Ablenkung* vom stressigen Wissenschaftsalltag.

- Meiner Band *the Djingerbread experience* für den perfekten Ausgleich auf musikalischer Ebene.

- Meinen Geschwistern Jutta, Martin und Christine dafür, immer an mich geglaubt zu haben und dafür, die besten Geschwister zu sein, die man sich wünschen kann.

- Meiner Freundin und Liebsten "Kleinen" Malin. Für deine unendliches Verständnis in den stressigsten Momenten dieser PhD-Zeit, für deine Ehrlichkeit, deinen Frohsinn und deine Unkompliziertheit. Ich will dir dafür danken, dass du mich während der extremen Schreibphase vor dem Hungertod bewahrt hast und mir gezeigt hast, dass man manchmal auch Kunstpausen

einlegen sollte. Danke, dass du mir so viel Liebe zeigst und mir ein gutes Gefühl dabei gibst, zu sein wer ich bin. Kurz gesagt: *Ich liebe dich*.

- Meinen Eltern Heidi und Alfons, die mir diesen Weg erst geebnet haben. Ich danke euch, für eure immerwährende Unterstützung und dafür, mich zu der Person gemacht zu haben, die ich heute bin. Ohne eure Liebe und Hingabe für das Wohlergehen von mir und meinen Geschwistern, wäre ich nicht so weit gekommen. Euch soll diese Arbeit gewidmet sein.

Zu guter Letzt ein bayrisches Sprichwort, das für die nötige Ruhe auch in Momenten größter Belastung sorgt: *"Schau ma moi, dann sengmas scho!"*.